Physical Environment of Large-scale High-latitude and Polar Crown Filaments

Univ.-Diss.
zur Erlangung des akademischen Grades
doctor rerum naturalium
(Dr. rer. nat.)
in der Wissenschaftsdisziplin Astronomie und Astrophysik

eingereicht an der
Mathematisch-Naturwissenschaftlichen Fakultät
Institut für Physik und Astronomie
der Universität Potsdam
und
Leibniz-Institut für Astrophysik Potsdam

Andrea Diercke

Abgabe: 16. Dezember 2020
Disputation: 10. Juni 2021 in Potsdam

Leibniz-Institut für Astrophysik Potsdam
An der Sternwarte 16
14482 Potsdam

Universität Potsdam
Institut für Physik und Astronomie
Karl-Liebknecht-Straße 24/25
14476 Potsdam-Golm

Erstbetreuer/Gutachter: apl. Prof. Dr. Carsten Denker
Zweitbetreuer/Gutachter: Prof. Dr. Klaus Strassmeier
Externe Gutachterin: Prof. Dr. Lucie Green
Mentorin: Prof. Dr. Claudia Stolle

Published online on the
Publication Server of the University of Potsdam:
https://doi.org/10.25932/publishup-51130
https://nbn-resolving.org/urn:nbn:de:kobv:517-opus4-511301

Table of Contents

Abstract

Filaments are omniprent features in the solar chromosphere, one of the atmospheric layers of the Sun, which is located above the photosphere, the visible surface of the Sun. They are clouds of plasma reaching from the photosphere to the chromosphere, and even to the outer-most atmospheric layer, the corona. They are stabalized by the magnetic field. If the magnetic field is disturbed, filaments can erupt as coronal mass ejections (CME), releasing plasma into space, which can also hit the Earth. A special type of filaments are polar crown filaments, which form at the interface of the unipolar field of the poles and flux of opposite magnetic polarity, which was transported towards the poles. This flux transport is related to the global dynamo of the Sun and can therefore be analyzed indirectly with polar crown filaments. The main objective of this thesis is to better understand the physical properties and environment of high-latitude and polar crown filaments, which can be approached from two perspectives: (1) analyzing the large-scale properties of high-latitude and polar crown filaments with full-disk Hα observations from the Chromospheric Telescope (ChroTel) and (2) determining the relation of polar crown and high-latitude filaments from the chromosphere to the lower-lying photosphere with high-spatial resolution observations of the Vacuum Tower Telescope (VTT), which reveal the smallest details.

The Chromospheric Telescope (ChroTel) is a small 10-cm robotic telescope at Observatorio del Teide on Tenerife (Spain), which observes the entire Sun in Hα, Ca II K, and He I 10 830 Å. We present a new calibration method that includes limb-darkening correction, removal of non-uniform filter transmission, and determination of He I Doppler velocities. Chromospheric full-disk filtergrams are often obtained with Lyot filters, which may display non-uniform transmission causing large-scale intensity variations across the solar disk. Removal of a 2D symmetric limb-darkening function from full-disk images results in a flat background. However, transmission artifacts remain and are even more distinct in these contrast-enhanced images. Zernike polynomials are uniquely appropriate to fit these large-scale intensity variations of the background. The Zernike coefficients show a distinct temporal evolution for ChroTel data, which is likely related to the telescope's alt-azimuth mount that introduces image rotation. In addition, applying this calibration to sets of seven filtergrams that cover the He I triplet facilitates determining chromospheric Doppler velocities. To validate the method, we use three datasets with varying levels of solar activity. The Doppler velocities are benchmarked with respect to co-temporal high-resolution spectroscopic data of the GREGOR Infrared Spectrograph (GRIS). Furthermore, this technique can be applied to ChroTel Hα and Ca II K data. The calibration method for ChroTel filtergrams can be easily adapted to other full-disk data exhibiting unwanted large-scale variations. The spectral region of the He I triplet is a primary choice for high-resolution near-infrared spectropolarimetry. Here, the improved calibration of ChroTel data will provide valuable context data.

Polar crown filaments form above the polarity inversion line between the old magnetic flux of the previous cycle and the new magnetic flux of the current cycle. Studying their appearance and their properties can lead to a better understanding of the solar cycle. We use full-disk data of the ChroTel at Observatorio del Teide, Tenerife, Spain, which were taken in three different chromospheric absorption lines (Hα λ6563 Å, Ca II K λ3933 Å, and He I λ10830 Å), and we create synoptic maps. In addition, the spectroscopic He I data allow us to compute Doppler velocities and to create synoptic Doppler maps. ChroTel data cover the rising and decaying phase of Solar Cycle 24 on about 1000 days between 2012 and 2018. Based on these data, we automatically extract polar crown filaments with image-processing tools and study their properties. We compare contrast maps of polar crown filaments with those of quiet-Sun filaments. Furthermore, we present a super-synoptic map summarizing the entire ChroTel database. In summary, we provide statistical properties, i.e. number and location of filaments, area, and tilt angle for both the maximum and declining phase of Solar Cycle 24. This demonstrates that ChroTel provides a promising dataset to study the solar cycle.

The cyclic behavior of polar crown filaments can be monitored by regular full-disk Hα observations. ChroTel provides such regular observations of the Sun in three chromospheric wavelengths. To analyze the cyclic behavior and the statistical properties of polar crown filaments, we have to extract the filaments from the images. Manual extraction is tedious, and extraction with morphological image processing tools produces a large number of false positive detections and the manual extraction of these takes too much time. Automatic object detection and extraction in a reliable manner allows us to process more data in a shorter time. We will present an overview of the ChroTel database and a proof of concept of a machine learning application, which allows us a unified extraction of, for example, filaments from ChroTel data.

The chromospheric Hα spectral line dominates the spectrum of the Sun and other stars. In the stellar regime, this spectral line is already used as a powerful tracer of magnetic activity. For the Sun, other tracers are typically used to monitor solar activity. Nonetheless, the Sun is observed constantly in Hα with globally distributed ground-based full-disk imagers. The aim of this study is to introduce Hα as a tracer of solar activity and compare it to other established indicators. We discuss the newly created imaging Hα excess in the perspective of possible application for modelling of stellar atmospheres. In particular, we try to determine how constant is the mean intensity of the Hα excess and number density of low-activity regions between solar maximum and minimum. Furthermore, we investigate whether the active region coverage fraction or the changing emission strength in the active regions dominates time variability in solar Hα observations. We use ChroTel observations of full-disk Hα filtergrams and morphological image processing techniques to extract the positive and negative imaging Hα excess, for bright features (plage regions) and dark absorption features (filaments and sunspots), respectively. We describe the evolution of the Hα excess during Solar Cycle 24 and compare it to other well established tracers: the relative sunspot number, the F10.7 cm radio flux, and the Mg II index. Moreover, we discuss possible applications of the Hα excess for stellar activity diagnostics and the contamination of exoplanet transmission spectra. The positive and negative Hα excess follow the behavior of the solar activity over the course of the cycle. Thereby, positive Hα excess is closely correlated to the chromospheric Mg II index. On the other hand, the negative Hα excess, created from dark features like filaments and sunspots, is introduced as a tracer of solar activity for the first time. We investigated the mean intensity distribution for active regions for solar minimum and maximum and found that the shape of both distributions is very similar but with different amplitudes. This might be related with the relatively stable coronal temperature component during the solar cycle. Furthermore, we found that the coverage fraction of Hα excess and the Hα excess of bright features are strongly correlated, which will influence modelling of stellar and exoplanet atmospheres.

High-resolution observations of polar crown and high-latitude filaments are scarce. We present a unique sample of such filaments observed in high-resolution Hα narrow-band filtergrams and broad-band images, which were obtained with a new fast camera system at the VTT. ChroTel provided full-disk context observations in Hα, Ca II K, and He I 10830 Å. The Helioseismic and Magnetic Imager (HMI) and the Atmospheric Imaging Assembly (AIA) on board the Solar Dynamics Observatory (SDO) provided line-of-sight magnetograms and ultraviolet (UV) 1700 Å filtergrams, respectively. We study filigree in the vicinity of polar crown and high-latitude filaments and relate their locations to magnetic concentrations at the filaments' footpoints. Bright points are a well studied phenomenon in the photosphere at low latitudes, but they were not yet studied in the quiet network close to the poles. We examine size, area, and eccentricity of bright points and find that their morphology is very similar to their counterparts at lower latitudes, but their sizes and areas are larger. Bright points at the footpoints of polar crown filaments are preferentially located at stronger magnetic flux concentrations, which are related to bright regions at the border of supergranules as observed in UV filtergrams. Examining the evolution of bright points on three consecutive days reveals that their amount increases while the filament decays, which indicates they impact the equilibrium of the cool plasma contained in filaments.

This doctoral thesis is based on three refereed articles (two published, one accepted for publication), one submitted articles, which is currently under review, and material for a forthcoming refereed article (Chapter 5). The cross-references between thesis chapters and refereed journal articles are provide in the list below. Formatting of these articles (including the figures) were adapted to give this doctoral thesis a uniform layout. Some text of the articles was used for the abstract of this thesis deviating from the structure of the original articles. In the following, I outline my contributions and those of the co-authors.

- ☐ Z. Shen, **A. Diercke**, C. Denker, *Calibration of Full-disk He* I *10830 Å Filtergrams of the Chromospheric Telescope*, Astron. Nachr. 339, 661, 2018AN....339..661S (Abstract and Chapter 3)
  This project and the subsequent publication were part of a student internship with Mrs. Zili Shen, who was supervised by myself and apl. Prof. Dr. C. Denker. The conception of the study was developed by apl. Prof. Dr. Denker and me. The data reduction was performed by Mrs. Shen and me together. The method is based on previous work from apl. Prof. Dr. C. Denker and was adapted for the current application by Mrs. Shen and me. Mrs. Shen prepared most of the figures, consulting me for guidance. The manuscript was written together, whereby apl. Prof. Dr. Denker provided guidance during this study, critically read the manuscript and offered comments and suggestions to improve the manuscript.

- ☐ **A. Diercke**, & C. Denker, *Chromospheric Synoptic Maps of Polar Crown Filaments*, Solar Physics, 294, 152, 2019SoPh..294..152D (Abstract and Chapter 4)
  My contribution to this article were data reduction and calibration, the scientific analysis of the data, writing the manuscript, and preparing the figures, among others. apl. Prof. Dr. C. Denker provided guidance during this study, critically read the manuscript, and offered comments and suggestions improving the manuscript.

- ☐ **A. Diercke**, C. Kuckein, M. Verma, C. Denker, *Filigree in the Surroundings of Polar Crown and High-latitude Filaments*, Solar Physics, accepted for publication, 2020arXiv201204349D (Abstract and Chapter 7)
  The article is based on data obtained during an observing campaign, where I was the principle investigator (PI). The observational setup of the M-lite cameras was done by apl. Prof. Dr. C. Denker and Dr. M. Verma. The data was observed by Dr. C. Kuckein and me. Dr. C. Kuckein carried out the data reduction and reconstruction. I was performing the data analysis, provided the figures, and wrote the manuscript with help of Dr. C. Kuckein. Figure 7.1 was created by Dr. C. Kuckein. Dr. C. Kuckein, Dr. M. Verma and apl. Prof. Dr. C. Denker provided guidance during this study, critically read the manuscript and offered comments and suggestions to improve the manuscript.

- ☐ **A. Diercke**, C. Kuckein, P. W. Cauley, K. Poppenhäger, J. D. Alvarado-Gómez, E. Dineva, C. Denker, *Solar Hα Excess during Solar Cycle 24 with Data from Full-disk Filtergrams of the Chromospheric Telescope*, Astron. & Astrophy., submitted. (Abstract and Chapter 6)
  The idea of this study was developed by Dr. P. W. Cauley, Dr. C. Kuckein, Prof. Dr. K. Poppenhäger, and me. The data reduction and analysis, the preparation of the figures, as well as writing the main parts of the text was done by me. Figure 6.4 was created by Prof. Dr. K. Poppenhäger. The stellar perspective and discussion of the stellar interpretation in this study was provided by Dr. P. W. Cauley, Prof. Dr. K. Poppenhäger, and Dr. J. D. Alvarado-Gómez. apl. Prof. Dr. C. Denker provided guidance during this study, critically read the manuscript, and offered comments and suggestions improving the manuscript.

- ☐ **A. Diercke**, R. Jarolim, C. Kuckein, S. J. González Manrique, M. Ziener, A. M. Veronig, and C. Denker, *Automatic Extraction of Polar Crown Filaments Using Machine Learning Techniques*, in preparatopm (Abstract and Chapter 5)
  This study was part of a five-weeks research project, which included a research visit of the University of Graz, Austria, organized by the SOLARNET Mobility Program. I was able to secure a research visitor grant of the Mobility Program enabling me to carry out this research project. The data reduction and preparation for this project was done by me. The labeling of the dataset was obtained

by Dr. C. Kuckein, Dr. S. J. González Manrique, and me. First feasibility tests were performed by M. Ziener. R. Jarolim and me refined the method and performed most of the data analysis under supervision of Prof. Dr. A. M. Veronig. apl. Prof. Dr. C. Denker provided guidance during this study.

My second supervisor Prof. Dr. K. G. Strassmeier and my mentor Prof. Dr. C. Stolle provided guidance on the doctoral project as members of my PhD committee. Abstracts of peer-reviewed articles and conference proceedings, which were published during the doctoral project, but are not included in the doctoral thesis, are presented in Appendix A.

Chapter 1

Introduction

Solar prominences are
beautiful and mysterious creatures
whose basic properties are far from understood.

Priest, van Ballegooijen, and Mackay (1996)

Our society relies strongly on the technological achievements of the last decades. The Sun has a large impact on the Earth and strong solar activity phenomena can affect our technological society. The steady solar wind is always interacting with the Earth's magnetic field, which is visible as aurora during the night in polar regions. Large solar eruptions, such as flares (high-energetic particle events) and coronal mass ejections (CME), release large amounts of fast and high-energetic particles and enormous amounts of plasma into space. Reaching Earth, satellites can be damaged, which will disturb signals of the global positioning system (GPS). Geomagnetic storms are induced by the interaction of particles with Earth's magnetic field, which interrupt radio communication and are responsible, for example, for corrosion of pipelines or interruptions of power grids. Furthermore, humans can be affected directly by high-energetic solar particles, not only as astronauts in space, but also as flight crews on polar routes, where long exposure to these particles can be dangerous. This is commonly referred to as Space Weather. It is of the utmost importance to understand the origin and behavior of space weather events and to foresee and to prepare for such events. The Sun is driven by its dynamo, which is responsible for the cyclic changes of solar activity, which is clearly evident in solar features such as photospheric sunspots and chromospheric filaments. A special form of filaments are polar crown filaments, an indirect tracer of the global dynamo action, which allows us to study the high-latitude component of the dynamo. In the following work, I will introduce the main features of the solar dynamo, followed by an introduction of the atmospheric regions of the Sun. The main focus is on one of the most prominent solar features in the solar chromosphere, i.e., on-disk filaments and their counterparts, prominences, above the solar limb.

1.1 Brief History of Solar Observations and the Solar Dynamo

Magnetic fields are omnipresent in the universe and everything therein, i.e., galaxies, stars, or planets. Our very own star, the Sun, has a magnetic field, as well as many other stars. Understanding the solar dynamo is important to understand solar activity, which drives solar phenomena observed in the solar atmosphere. While multiple theories were established, which explain certain aspects of the solar dynamo, a universal dynamo theory describing the entire system is still subject of scientific studies and debates. I briefly discuss this topic and present some basic ideas about the solar dynamo, which will help to understand the complex topic of filaments and their origin.

In order to select a proper solar dynamo model, I will shortly introduce the observational evidence of the solar dynamo, which such a model has to reproduce. The Sun has been observed almost daily since the invention of the telescope early in the 17^{th}, century. This led to a large collection of sunspot drawings covering hundreds of years of solar activity. Systematic observations by Samuel H. Schwabe

indicated a periodic appearance of sunspots (Schwabe, 1844; Arlt et al., 2013). Further systematic sunspot observations revealed a relationship between the location of the sunspots in a periodic manner. This was first described by the British astronomer Richard Carrington (Carrington, 1858) and was ascertained by the German astronomer Gustav Spörer (Spörer, 1879), who observed the Sun regularly from 1861 to 1894 (Diercke, Arlt, and Denker, 2015). In the minimum of the solar cycle, sunspots are reported at mid-latitudes of around $\pm 30°$. The number of single sunspots and sunspot groups is still small. In the progression of the solar cycle, sunspots appear closer to the equator and at higher latitudes of up to $\pm 50°$. In this time, more and more sunspots emerge. When the sunspots finally appear close to the equator, their number reduces to a new minimum. At the beginning of a new cycle, new sunspot groups can already occur at the mid-latitudes. This relation is called Spörer's law (Diercke, Arlt, and Denker, 2015; Cameron, Dikpati, and Brandenburg, 2017). Another relation regarding sunspot groups is Joy's law, which states that most sunspot groups are tilted in a certain angle (Hale et al., 1919; Senthamizh Pavai et al., 2016; Cameron, Dikpati, and Brandenburg, 2017). With the invention of the magnetograph at the beginning of the 20$^{\text{th}}$ century, it was possible to infer the line-of-sight (LOS) magnetic field of the Sun, and further relations were discovered. In addition to Joy's law of the tilt of sunspot groups, it was soon uncovered that the leading and the following spots of a sunspot group have opposite polarities: the majority of leading spots have the same polarity on the northern hemisphere, but the opposite magnetic polarity on the southern hemisphere, which is called Hale's law (Hale, 1908; Hale et al., 1919; Cameron, Dikpati, and Brandenburg, 2017). The polarity of the unipolar field at the poles is the same polarity as the leading sunspots. Around cycle maximum, the polar fields reverse their polarity (for details see Section 1.5). The polarity of the leading and trailing spots are reversed at the beginning of the next solar activity cycle. This results in an magnetic cycle of about 22 years. The solar activity cycle is not precise like an ideal pendulum, so the cycle length changes between 10 and 12 years (Cameron, Dikpati, and Brandenburg, 2017).

There are three main ingredients for a dynamo. The first is an electrically conducting fluid, which is the case in stellar plasma. The second ingredient is a complex motion, which the fluid has to perform. For stars, it can be a turbulent flow or differential rotation. In order to produce large-scale organized fields, the mirror symmetry has to be broken by the rotation. The third ingredient is that this complex motion has to be vigorous enough, which is measured with the magnetic Reynolds number (see Chapter 3 in Schrijver and Siscoe, 2009).

The dynamo has to fulfill the magneto-hydrodynamic (MHD) induction equation (Schrijver and Siscoe, 2010):

$$\frac{\partial \mathbf{B}}{\partial t} = \nabla \times (\mathbf{v} \times \mathbf{B} - \eta \nabla \times \mathbf{B}) \tag{1.1}$$

($\mathbf{B}$: magnetic field, η: magnetic diffusion, inversely proportional to the plasma's electrical conductivity, and the flow field $\mathbf{v}$ includes large-scale flows such as differential rotation as well as small-scale turbulence). The purpose of the current research in solar and stellar dynamo theory is to solve numerically the induction equation (Eq. 1.1). Furthermore, a suitably formulated evolution equation describing the turbulence and the thermally driven convection has to be taken into account. To simplify these complicated tasks, the mean-field theory was applied. Here, the focus is on processes, which are capable of maintaining a large-scale magnetic field (see Chapter 3 in Schrijver and Siscoe, 2009). In this process, the magnetic field is reduced to a large-scale mean field and the small-scale components are averaged. Hereby, two concepts are introduced: the α- and Ω-effect. The latter describes simply the conversion from poloidal flux into toroidal flux by differential rotation. The α-effect generates a poloidal field from the toroidal field by rising and twisting motions (Priest, 2014). The manifestation of the α-effect is seen in the tilt of sunspot groups, known as Joy's law.

One model considering the α- and Ω-effect is the Babcock-Leighton model (Babcock, 1961; Priest, 2014; Cameron, Dikpati, and Brandenburg, 2017). The model will be described in a simplistic way. Initially, we have the poloidal field at the surface layer, and the toroidal field production near the tachocline at the bottom of the convection zone (Fig. 1.1, upper panels). The tachocline is a boundary layer with a strong rotational shear $\partial\Omega/\partial r$ (Schrijver and Siscoe, 2010) at a height of about $r = 0.7\,r_\odot$ (Stix, 2004). It defines sharply the border between the radiative zone, where the rotation is uniform and the convection zone with its differential rotation (Stix, 2004; Miesch, 2005). The simple magnetic dipole configuration of the poloidal field is broken by adding a toroidal component to the field, which results from differential

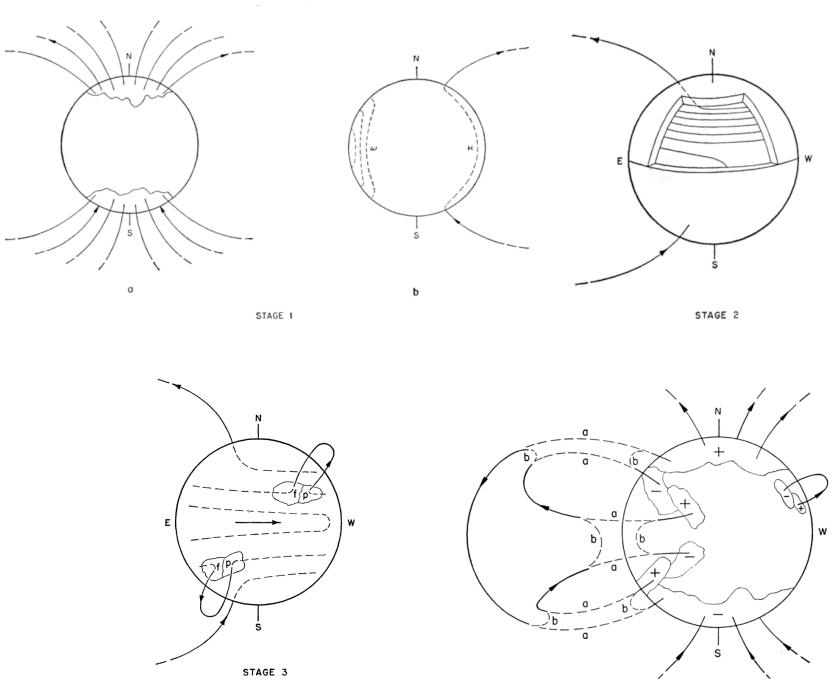

Figure 1.1: Sketch of the Babcock-Leighton Dynamo: (Stage 1 a, upper left panel): Initial poloidal field, (Stage 1 b, upper middle panel): the shallow, submerged part of each magnetic field line. (Stage 2, upper right panel): Effect of the differential rotation on submerged field lines, which wraps the magnetic field lines around the Sun, producing a toroidal component. (Stage 3, bottom left panel): Magnetic flux ropes emerge as bipolar regions. The submerged toroidal field emerges by buoyancy to the surface. (bottom right panel): The trailing flux of bipolar magnetic regions is transported towards the polar field, where they reconnect. (This Figure is a composite of Figures 1, 2, 3, and 8 in Babcock, 1961).

rotation (see Chapter 11 in Carroll and Ostlie, 2017). In the convection zone, the magnetic field lines are twisted by turbulent motion, which creates magnetic flux ropes. These flux ropes rise because of buoyancy, creating sunspot groups, whereby the magnetic polarity is along the flux ropes (Fig. 1.1, lower left panel). This already implies Joy's and Hale's law. These first sunspot groups appear at mid-latitudes, but the ongoing differential rotation leads to more sunspot groups at lower latitudes. The cancellation of flux close to the equator reestablishes the poloidal field with reversed polarity compared to the initial configuration (see Chapter 11 in Carroll and Ostlie, 2017). The poloidal flux of the decayed active regions is transported by the meridional flow towards the poles (Fig. 1.1, lower right panel). Here, it is dragged down to the tachocline, where the flux is sheared by the differential rotation. Thus, a new toroidal flux system is build-up which is the start of a new sunspot cycle.

In Babcock-Leighton-type dynamos, the differential shear of flux occurs at all latitudes, which makes it difficult to explain that sunspots only emerge at latitudes below $\pm 50°$. With the assumption that the toroidal flux is stored and produced in the tachocline, the emergence latitudes can be explained (Cameron, Dikpati, and Brandenburg, 2017). Here, the concept of unstable flux tubes is essential for the description. The flux tubes are considered to have field strength of above 10^5 G which leads to enough emergence at low latitudes as in the observations. The flux tubes are more unstable at low latitudes. In higher latitudes, the flux tubes are unable to escape to the surface.

The propagation of toroidal flux towards the equator is described by Spörer's law, which is explained in two possible ways (Cameron, Dikpati, and Brandenburg, 2017). The first involves dynamo waves as the reason for the equatorward propagation. The latitudinal propagation of the toroidal field is due to the radial differential shear, where the direction depends on the sign of the α-effect and the decreasing or increasing of the differential rotation rate with depth. In the case of the Sun, the α-effect favors an increase of the differential rotation with depth. Whereas the differential rotation decreases inwards near the tachocline at latitudes, where sunspots are formed (Brown and Morrow, 1987). The second explanation involves the meridional flow at the base of the tachocline, which has to be strong enough so that the advection of the toroidal flow by the meridional flow produces the equatorward propagation of sunspots, under the condition that the latitudinal transport due to diffusion is weak.

To summarize, the Babcock-Leighton-type dynamo is an easy approach, which reproduces the simple toroidal magnetic field during solar maximum and the poloidal field during solar minimum. Basic observational effects such as Spörer's law, Joy's law, and Hale's law are reproduced by the model, as well as the poleward propagation of low-latitude flux, which is important for the formation of polar crown filaments. This topic is discussed in detail in Section 1.5. Nonetheless, it does not reproduce all

observational evidence of the solar dynamo, e.g., the disappearance of polar crown filaments about six month after the magnetic field reversal (Webb, Davis, and McIntosh, 1984). For the scope of this thesis, the assumption of the Babcock-Leighton model is sufficient.

1.2 Radiative Transfer

The majority of radiation from the Sun originates in the photosphere. The German physicist Joseph Fraunhofer examined the spectrum of the solar light and observed more than 600 dark lines in the spectrum (Tull, 2001). For more than 300, he determined their position and gave letters to the most prominent lines, which are in some cases still in use, e.g., the Ca II H and K lines, the G-band, and Na I D doublet. These dark lines were later interpreted by Gustav Robert Kirchhoff as absorption lines (Tull, 2001), where certain atoms in the atmosphere of the Sun absorb the light at the respective wavelength of the spectrum. Absorption lines occur when a bound electron is excited by a photon in an unfilled higher orbit. Emission is the inverse process, when an electron releases a photon and returns to a lower state. The motion of a gas in a star is described by the Maxwell-Boltzmann velocity distribution. Assuming that absorption and emission of photons are balanced, we would have a thermodynamical equilibrium. Considering that we can observe the light of the Sun, shows us, that a star is not in the state of a perfect thermodynamical equilibrium, because photons can escape from the stellar surface. Nonetheless, in the photosphere, we can assume a local thermodynamical equilibrium (LTE, Carroll and Ostlie, 2017, Chapter 9) for regions small enough that the temperature is not changing. For the photosphere, this means that the temperature scale height is much smaller than the mean free path of the photons. In the following, I shortly introduce the absorption and emission processes on the Sun.

A photon traveling from the interior of the Sun outwards is scattered, absorbed, and emitted again and again. The distance a beam of photons can travel $\mathrm{d}s$, is characterized by the absorption coefficient κ_λ and the density of the gas ρ, which can be used to define the optical depth τ_λ:

$$\mathrm{d}\tau_\lambda = -\kappa_\lambda \rho \, \mathrm{d}s. \tag{1.2}$$

The probability that a photon escapes the Sun without being absorbed is $\mathrm{e}^{-\tau}$ (Spruit, 2001). The deeper layers of the Sun have a very high optical depth and the probability to escape without further absorption is very small. The photosphere of the Sun has an optical depth $\tau_\lambda = 0.1$ to $\tau_\lambda = 3$ (Spruit, 2001).

The decrease in intensity $\mathrm{d}I_\lambda$ of a beam of photons with wavelength λ, traveling through a gas caused by absorption is defined as:

$$\mathrm{d}I_\lambda = -\kappa_\lambda \rho I_\lambda \, \mathrm{d}s. \tag{1.3}$$

Besides absorption, we also have emission processes, which are balanced in LTE. The increase in intensity $\mathrm{d}I_\lambda$, traveling through a gas caused by emission is

$$\mathrm{d}I_\lambda = +j_\lambda \rho \, \mathrm{d}s, \tag{1.4}$$

whereby j_λ as the emission coefficient.

Combining both equations, we derive:

$$\mathrm{d}I_\lambda = -\kappa_\lambda \rho I_\lambda \, \mathrm{d}s + j_\lambda \rho \, \mathrm{d}s. \tag{1.5}$$

We can now introduce the ratio of absorption and emission as the source function $S_\lambda = j_\lambda / \kappa_\lambda$, which results in the radiative transfer equation (RTE):

$$-\frac{1}{\kappa_\lambda \rho} \frac{\mathrm{d}I_\lambda}{\mathrm{d}s} = I_\lambda - S_\lambda. \tag{1.6}$$

This function can now be solved using different assumptions regarding the atmosphere and the source function.

To formally solve the RTE in Eq. (1.6), we use the definition of the optical depth in Eq. (1.2). By multiplying the equation with e^{τ_λ} and integrating the integral between $\tau_\lambda = 0$ and $\tau_{\lambda,0} = \infty$, we derive (Böhm-Vitense, 1989; Stix, 2004):

$$I_\lambda = \int_0^\infty S_\lambda(\tau_\lambda) \exp(-\tau_\lambda) \, \mathrm{d}\tau_\lambda \tag{1.7}$$

With Eq. (1.7), the intensity can be calculated with a known source function. In the case of modeling the solar atmosphere, the reversed case of inferring the source function from the intensity at different heights of the atmosphere is more interesting.

In addition to the absorption coefficient κ_λ, which represents the absorption in the continuum, we can define the line absorption coefficient κ_l, which rapidly decreases from the line center with the distance $\Delta\lambda$. Combining both absorption coefficients, we define the optical depth for the line absorption χ_λ (adapted from Chapter 9 in Hanslmeier, 2020):

$$\chi_\lambda = \int_{-\infty}^{t} (\kappa_\lambda + \kappa_\mathrm{l}) \mathrm{d}t. \tag{1.8}$$

With this coefficient, we can define the intensity, which is radiating in an angle θ from the surface for the line $I_\lambda(0,\theta)$:

$$I_\lambda(0,\theta) = \int_0^\infty S(\chi_\lambda) e^{-\chi_\lambda/\cos\theta} \mathrm{d}\chi_\lambda / \cos\theta = F_\lambda \tag{1.9}$$

and for the continuum $I(0,\theta)$:

$$I(0,\theta) = \int_0^\infty S(\tau_\lambda) e^{-\tau_\lambda/\cos\theta} \mathrm{d}\tau_\lambda / \cos\theta = F_\mathrm{c} \tag{1.10}$$

For the optical depth of the continuum τ_λ and the optical depth for line absorption χ_λ the following relation can be defined (adapted from Chapter 19 in Unsöld, 1974):

$$\frac{\chi_\lambda}{\tau_\lambda} = \frac{\kappa_\lambda + \kappa_\mathrm{l}}{\kappa_\lambda}. \tag{1.11}$$

The depth of an absorption line r_λ is defined from Eqs. (1.9) and (1.10) as:

$$r_\lambda = \frac{F_\mathrm{c} - F_\lambda}{F_\mathrm{c}} = 1 - \frac{F_\lambda}{F_\mathrm{c}}. \tag{1.12}$$

The equivalent width W_λ of an absorption line is defined as an rectangle box reaching up to the continuum, with the same area as the spectral line:

$$W_\lambda = \int r_\lambda \mathrm{d}\lambda = \int \frac{F_\mathrm{c} - F_\lambda}{F_\mathrm{c}} \mathrm{d}\lambda. \tag{1.13}$$

Each absorption line seen in the solar spectrum contains information about, i.e., the chemical composition, magnetic field, Doppler velocities of solar features, which can be inferred from the shape of the spectral line profile and the location of its minimum. The spectral lines are formed at different heights in the solar atmosphere, which means, that with the help of these spectral lines, we obtain more information about the different solar atmospheric layers. To infer the characteristic parameters from the spectral line, we apply inversion codes, which attempt to find the solution for the integral of the RTE. The inversion starts with a guess of a model atmosphere and performs multiple iterations by modifying the model atmosphere until the synthetic profile matches the observed one. If they are similar enough, we assume that the atmospheric condition is derived, where the spectral line is formed. With this method, polarimetric data can be fitted and temperature, LOS velocity, source function, and components of the magnetic field can be inferred. Only few inversion codes are available, which can approximate the non-LTE (NLTE) conditions in the chromosphere.

1.3 Solar Atmosphere

We already introduced the photosphere as the surface of the Sun. In the following, we will provide a basic morphological description of this layer. Furthermore, we will briefly introduce three additional layers of the solar atmosphere: the chromosphere, the transition region, and the corona with the basic physical characteristics of each layer.

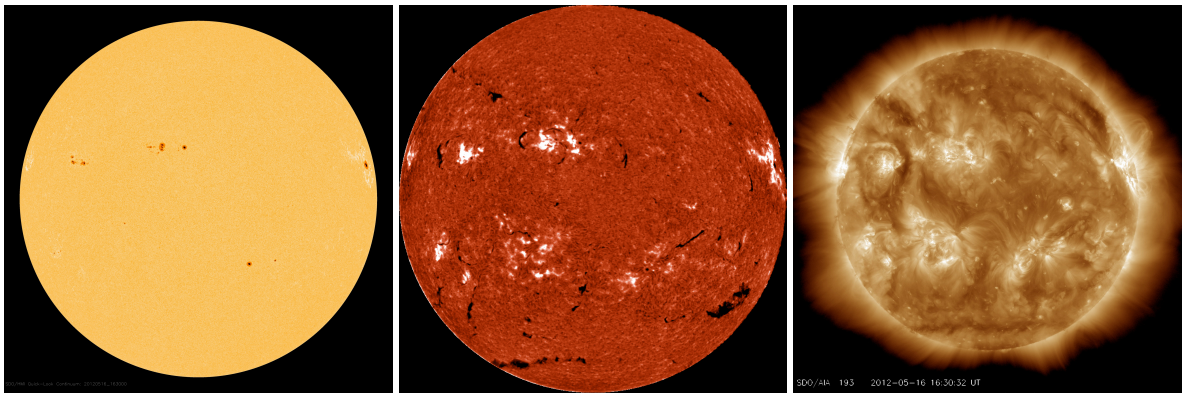

Figure 1.2: The solar atmosphere: photosphere (left), chromosphere(middle), corona (right) on 2012 May 16. The filtergram of the photosphere is obtained in the visible wavelength range with the Helioseismic and Magnetic Imager (HMI) onboard Solar Dynamic Observatory (SDO), The filtergram of the corona is obtained with the Atmospheric Imaging Assembly (AIA) onboard SDO at extreme ultraviolet (EUV) wavelength, using the Fe XII line at λ193 Å at characteristic temperatures of 1.25×10^6 K. The Hα filtergram at 6563 Å of the chromosphere is observed with the Chromospheric Telescope (ChroTel). The photospheric and chromospheric images are corrected for limb-darkening.

Photosphere. Observing the Sun from Earth, as white-light images, displaying the photosphere, which indicates that most of the visible light originates from this atmospheric layer, as already mentioned in Section 1.2. This layer defines the surface of the Sun and has an effective temperature of $T_{\rm eff} = 5777$ K (see Chapter 11 in Carroll and Ostlie, 2017). Its height only spans a few hundred kilometers (Stix, 2004). The most dominant features in the photosphere are sunspots and pores (Fig. 1.2, left panel). Furthermore, bright faculae in active regions, surrounding sunspots can be observed. In high-resolution solar images, we uncover the granulation pattern, which covers the solar photosphere (Fig. 1.3, left panel). The granules are a result of hot gas in the underlying convection zone, which rises to the surface in the middle of the granule and sinks back into deeper layers at the intergranular lanes, when it cools down due to radiative losses (Brandt, 2001). Granules are very dynamic with lifetimes of about six minutes (Stix, 2004) and have a diameter of about 150 km to 2500 km (Brandt, 2001). The granules are affected by the magnetic field. In strong magnetic flux concentrations above 100 G, i.e., in active regions, the granulation pattern is deformed and abnormal granulation can be observed (Dunn and Zirker, 1973; Sobotka, Bonet, and Vazquez, 1994; Beck et al., 2017). In the intergranular lanes, bright points become visible (Dunn and Zirker, 1973; Muller, 2001), which are connected to magnetic flux tubes rising in the atmosphere (Fig. 1.2, left panel). The magnetic field strength of bright points can reach values between 200 G to 1500 G, especially in high-resolution observations of the magnetic field, e.g., Beck et al. (2007), Utz et al. (2013), and Kuckein (2019).

Chromosphere. The chromosphere was first detected during a total solar eclipse, where a red shimmer appears around the occulted Sun, originating mainly from the dominant Hα line in emission. The total solar eclipse also revealed loops at the edge of the solar disk, which are called prominences. The appearance of the solar chromosphere changes completely, depending on the wavelengths, in which it is observed. The most prominent wavelengths are, e.g., the Fraunhofer lines Ca II H and K at λ3934 Å and λ3969 Å, respectively, Ca II λ8542 Å, He I λ10830 Å, and the hydrogen lines Hα at λ6563 Å and Hβ at λ4861 Å (Moore et al., 1966). In the following, I will introduce the Hα line, as the most prominent spectral line originating in the chromosphere (Fig. 1.2, middle panel). The chromosphere differs completely in its appearance from the photosphere. Most sunspots are still visible as dark features, but we observe them in a higher atmospheric layer. Around the sunspots, we see bright plage regions, indicating an enhanced line-core intensity in Hα, which can be used as a tracer for solar cycle activity (Chapter 6). The most prominent features in Hα are the dark, elongated filaments on the disk or bright prominences above the limb, which will be introduced in detail in Section 1.4). High-resolution observations of the Sun reveal the manifold fine structure of the chromosphere in Hα (Fig. 1.3, right panel). It is composed of small fibrils, which are connected to spicules observed at the limb. Fibrils are defined as fine structural patterns, which build up the chromosphere (Gaizauskas, 2001). Some fibrils are rooted in a bright core in a radial formation, which is called a rosette. The chromosphere is dominated by magnetic pressure

$\beta = 8\pi p/B^2 < 1$; it is variable and inhomogeneous, which is the reason, why the LTE assumption is not always possible (Schmieder, 2001). Therefore, a NLTE environment has to be assumed for modeling the chromosphere. Furthermore, the magnetic field cannot be neglected as for LTE models, because the chromosphere is structured by the magnetic field. Since, filaments are thin, leaf-like 3D structures, which receive non-isotropic radiation from all sides and from below, radiative transfer calculations have to be performed in 3D. The plasma is frozen in the magnetic field lines and outlines the magnetic field structure, which is visible in the fine structure of the chromosphere (Schmieder, 2001). The temperature of the chromosphere first decreases down to the temperature minimum of 4300 K at a height of about 500 km and increases afterward to a plateau between 1000 km to 2100 km with temperatures of 6000 K to 10 000 K (Schmieder, 2001).

Transition Region and Corona. The transition region is the layer between the chromosphere and the outermost region, the corona. Here, the temperature rises steeply from 10^4 K to 10^6 K. One concept to explain the steep temperature increase in this layer is by magneto-hydrodynamic waves such as transverse Alfvén waves (Stix, 2004). The waves are generated at the footpoints of magnetic flux tubes by photospheric motions or magnetic instabilities, like reconnection processes or nanoflares, and travel along the magnetic field lines without variations of pressure and density. Other models explain coronal heating by electric currents. The transition region can be observed in ultraviolet (UV) wavelengths between 500 Å and 1600 Å (Stix, 2004).

The corona becomes visible during total solar eclipses as an extended white shimmer like a crown around the solar disk. The temperature reaches values of 10^6 K. Beside solar eclipses, the corona can be observed from Earth with artificial eclipses, as implemented in coronagraphs, or by using narrow-band filters, e.g., tuned to the forbidden transitions Fe XIV at λ5303 Å and Fe XI at λ6374 Å (Del Zanna and Mason, 2018). In addition, the corona is constantly observed in extreme ultraviolet (EUV) between 13.7 Å and 1058.7 Å (Stix, 2004), e.g., the Solar Dynamics Observatory (SDO, Pesnell, Thompson, and Chamberlin, 2012) with the Atmospheric Imaging Assembly (AIA, Lemen et al., 2012) and in X-Ray, e.g, the Reuven Ramaty High-Energy Solar Spectroscopic Imager (RHESSI, Lin et al., 2002) and the Spectrometer/Telescope for Imaging X-Rays (STIX, Krucker et al., 2020; Warmuth et al., 2020) instrument onboard Solar Orbiter (Forveille and Shore, 2020). The corona can be divided into the active and quiet corona. However, bright features indicate active regions on the disk and prominences and coronal loops at the limb. The dark regions either indicate coronal holes or filaments.

1.4 Filaments

Filaments are elongated "clouds" of dense plasma, which are rooted in the photosphere and reach into the chromosphere and corona. In comparison with the surrounding plasma of the corona with a temperature of several millions of Kelvin, the plasma inside a prominence is cold with $T \approx 6000 - 8000$ K (Engvold, 1998). The low temperature can be explained by the high number density of the prominence ($N_e = 10^{10} - 10^{11}$ cm^{-3}, Malherbe, 1989) compared to coronal densities ($N_e = 10^9$ cm^{-3}, Malherbe, 1989), whereby, the energy loss in an optically thin medium is proportional to the density ρ^2 (Kippenhahn and Schlüter, 1957). Filaments are observed on the disk in absorption, and prominences when observed above the limb, appearing as bright loops in emission. Both objects have the same underlying physics.

Filaments or prominences reside between negative and positive polarities of the LOS magnetic field, the so-called polarity inversion line (PIL, Babcock and Babcock, 1955; Mackay et al., 2010). Above the PIL, a filament channel forms. The channel is defined as the region of axial aligned fibrils without fibrils crossing the PIL (Martin, 2001). The filament channel exists often for more than one rotation period. In a single filament channel more than one filament can form. This newly formed filament has different characteristics than its predecessor (Gaizauskas et al., 1997). The opposite polarities on each side of the PIL are connected by overlying arcades (Gaizauskas, 2001). The arcade plays an important role for the stability of the filament. Beneath the coronal arcades a twisted magnetic field or flux rope is formed (Lites, 2005). Different models were put forward to explain the formation of this helical field. One model explaining the formation and transportation of plasma into the flux rope has been proposed by

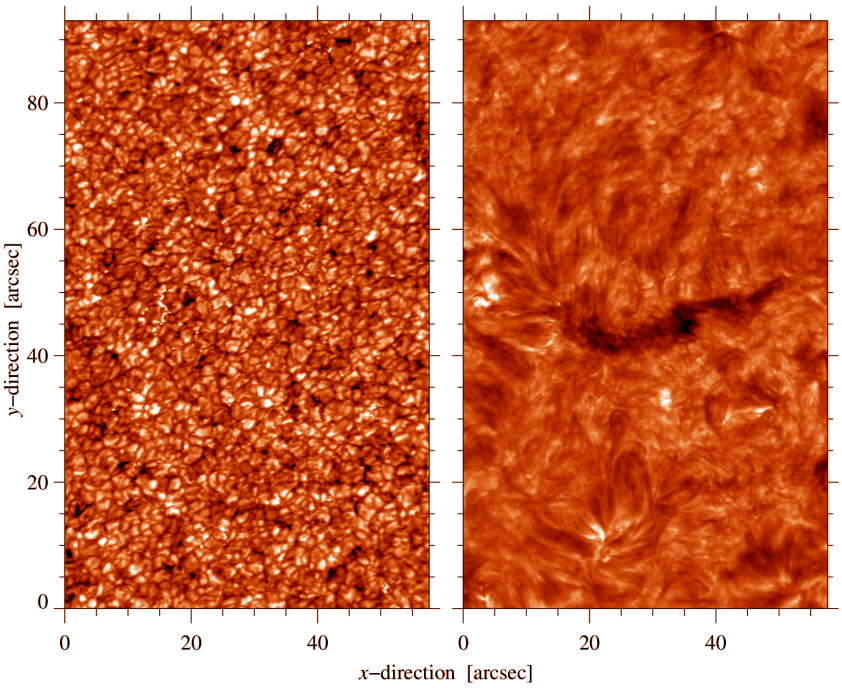

Figure 1.3: High-latitude filament observed in the Hα continuum (left), displaying the photosphere, and the Hα line core, displaying the chromosphere. In the photosphere, granulation is predominantly present, but in the intergranular lanes, we can determine bright points, which indicate strong concentrations of magnetic field. Putting these bright points into relation with the filament, we find that strong bright points are related to the footpoints of the filament. In the Hα line core image, we see next to the filament the chromospheric fine structures with fibrils and rosettes. The Figure is adapted from Chap. 7, Fig. 7.6 and Fig. 6 in Diercke et al. (2020).

van Ballegooijen and Martens (1989, see Section 1.6.1). Observations show that a filament is a dynamic object with a continual input of plasma.

The filament itself is composed of different components (Mackay et al., 2010). The main body, an elongated dark structure, is called a spine. Branching off from the spine, the barbs reach down to the footpoints in the photosphere. The extreme ends as well as the overlying arcades of the coronal loops are connecting the opposite polarities on each side of the filament channel (Martin, 1998). The whole filament is a collection of small threads, which are thought to be a bundle of magnetic field lines (Engvold, 2001; Lin et al., 2005).

In modern literature, filaments are categorized into three types (Engvold, 2015): (1) quiet-Sun, (2) active region, and (3) intermediate filaments. The active region filaments appear in the activity belt between $\pm 40^{\circ}$, reach only heights of about 10 Mm above the photosphere, and have lifetimes of a few hours to some days. Nevertheless, their magnetic field strength can reach values of up to 700 G (Kuckein et al., 2009). The quiet-Sun filaments are long-lived objects with lifetimes of up to several weeks appearing in the quiet Sun outside of the activity belts. If a filament does not belong to the class of either quiet-Sun or active region filaments, it is called an intermediate filament (Mackay et al., 2010). A special class of quiet-Sun filaments are polar crown filaments (PCF), which appear like an ornamental circlet or a crown around the polar caps. Leroy, Bommier, and Sahal-Brechot (1983) studied the properties of 120 polar crown prominences from 1976–1980. They determined heights from 20 Mm to 75 Mm above the photosphere and magnetic field strengths in the range of 2–20 G with average values of 8 G. Furthermore, these authors noted a gradient of the magnetic field B with height h of $\Delta B/\Delta h = 0.5 \times 10^{-4}$ G km^{-1}. A more recent study by Priest, van Ballegooijen, and Mackay (1996) deduced a length of 60–600 Mm, a height of 10–100 Mm above the photosphere, and a width of 4–15 Mm for quiet-Sun filaments. These filaments have a particle density of 10^{16}–10^{17} m^{-3} and a magnetic field of up to 40 G, which prevents the filament to be pushed down by gravity (Kippenhahn and Schlüter, 1957).

At the polarity reversal boundary the quiet Sun has a weak magnetic field, which causes the orientation of the fibrils above the PIL to become nearly random (Martin, 2001). Different theories explain, how the enormous filament channels of PCFs are formed. In one model (Gaizauskas, 2001), smaller channels of the same orientation link up and form larger channels. This happens at lower latitudes in the activity belt, where more emerging flux exists. The channels are then transported poleward by migrating flux, which is driven polewards by large-scale emergences of new flux combined with meridional flows. The polar crown is created when the poleward migrating flux reconnects with the fields in the polar caps (Gaizauskas, 2001). A detailed description is provided in Section 1.5.

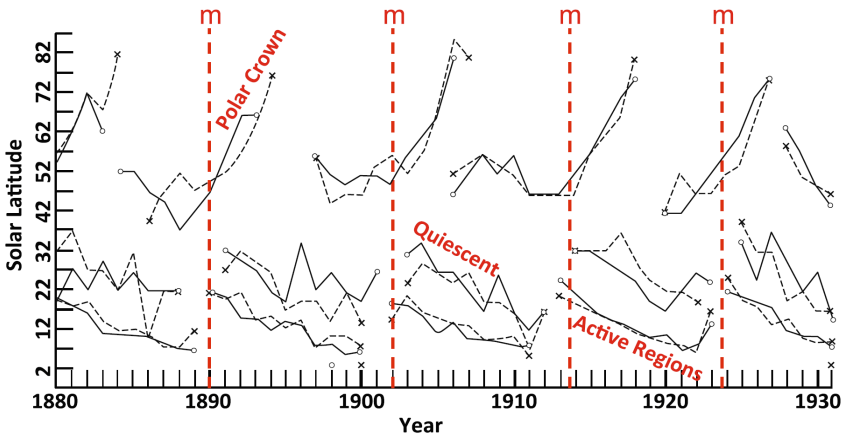

Figure 1.4: "Dash to the poles" of polar crown filaments in the solar cycles No. 12–15. Tracks are also given for quiet-Sun filaments near the activity belt and for active region filaments moving towards the equator for the northern and southern hemisphere (black solid and dashed line, respectively). Solar minima of each cycle are marked as dashed vertical red lines and designated with the letter m (Fig. 6 in Cliver, 2014).

1.5 Cyclic Behavior of Filaments

For filaments, a cyclic behavior similar to the Schwabe sunspot cycle is observed (Fig. 1.4). Active region filaments and quiet-Sun (or quiescent) filaments have a similar behavior as sunspots and appear closer to the equator around the minimum. The PCFs instead move towards the pole, which was known already since the end of the 19th century, when it was observed by the Italian astronomer Secchi and colleagues (Waldmeier, 1973; Cliver, 2014). This migration was studied and named "dash-to-the-poles" by John and Mary Ackworth Evershed during their observations from 1890 – 1914 (Evershed and Evershed, 1917; Cliver, 2014). Different studies report more than one "dash" or more recently "rush-to-the-poles" (Cliver, 2014).

The meridional flow and diffusion are causes the flux of the trailing part of active regions being transported towards the polar regions (Karna, Zhang, and Pesnell, 2017). Constant flux cancellation at its border results in the polar coronal hole beginning to shrink, which had their maximal area during solar minimum. The migration of the trailing flux to the poles lasts about 9 months. Polar crown filaments form at the boundary between the new-cycle polarity of the trailing flux and unipolar field of the polar coronal hole. At this region, a polar crown cavity is established. The ongoing flux transport towards the pole results in constant flux cancellation, which sustains the polar crown cavity and a shrinking of the polar coronal hole (Karna, Zhang, and Pesnell, 2017). Eventually, this leads to the reversal of the polar magnetic field around the time of the solar maximum. The polar crown filaments form in the polar crown cavity and appear close to the solar cycle maximum close to the pole and disappear with the reversal of the polar fields. When the polar crown cavity disappears at around solar activity maximum, it takes six months to $1^1/_2$ yrs for polar holes to redevelop with new-cycle polarity. After the disappearance of PCFs, a new high-latitude branch forms at about 50° in both hemispheres (Waldmeier, 1973; Cliver, 2014). There it resides until its migration to the pole near solar minimum. Waldmeier (1973) observed a second poleward migration in cycle 20 and mentioned the assumption that this second rush has escaped notice in earlier cycles.

A recent study by Xu et al. (2018), using full-disk Hα observations of the Big Bear Solar Observatory (BBSO, Denker et al., 1999) and the Kanzelhöhe Solar Observatory (KSO, Otruba and Pötzi, 2003; Pötzi et al., 2015), analyzed the migration of polar crown filaments between 1973 and 2018 for the Solar Cycles 21 to 24. The filaments were determined visually, whereby PCFs with a large negative tilt angle were excluded. They inferred the migration speed in each hemisphere and compared them among the four solar cycles. As indicated by previous studies (e.g., Sun et al., 2015; McIntosh et al., 2019), the magnetic field reversal and the accompanied disappearance of polar crown filaments, appears in most cycles first in the northern hemisphere and several months later in the southern hemisphere. Xu et al. (2018) found that the migration speed was higher in the northern hemisphere for Solar Cycles 21 and 23, and in Solar Cycle 22 the migration speed was almost identical. Only for Solar Cycle 24, the authors inferred a higher migration speed for the southern hemisphere. Additional solar cycles are need, where the migration rate can be inferred, to get a statistical significant relation.

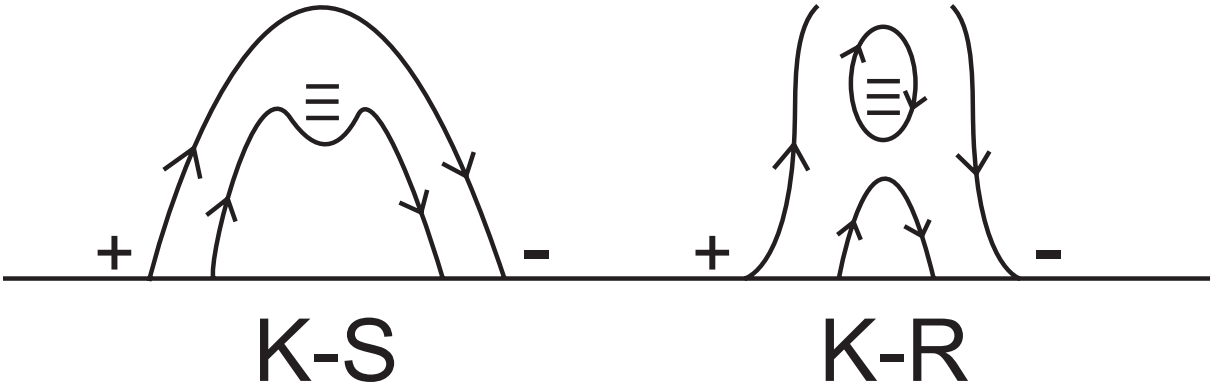

Figure 1.5: Magnetic field models: Kippenhahn and Schlüter (1957) model (K-S) and Kuperus and Raadu (1974) model (K-R) (Fig. 1.2 in Kuckein, 2012)

1.6 Filament Structure and Dynamic

The magnetic field supports the filament against gravity and thermal insulation from the surrounding corona (van Ballegooijen, 2001), because gas pressure and radiation pressure are not large enough to hold up the filament alone (Kippenhahn and Schlüter, 1957).

1.6.1 Magnetic Structure

Leroy, Bommier, and Sahal-Brechot (1984) report two types of prominences: (1) The first type of prominences have heights below 30 Mm and a transverse magnetic field, representing the Kippenhahn and Schlüter (1957, K-S) model. In these prominences, a magnetic field strength of $B \sim 20$ G was measured. (2) The prominences with heights above 30 Mm representing the magnetic field structures as described in the Kuperus and Raadu (1974, K-R) model with a magnetic field strength of $B \sim 5$ G–10 G. In addition, Leroy, Bommier, and Sahal-Brechot (1983, 1984) reported about polar crown prominences in a sample of 120 prominences with a magnetic structure as described in the model of Kuperus and Raadu (1974). The difference between these two models is the direction of the induced current flow along the filaments axis. Regarding Fig. 1.5 (left), in the K-S model the current would be directed out of the plane of the figure, towards the observer, where the transverse magnetic field points from positive polarity towards the negative polarity. This is called the normal polarity (NP) configuration. Whereas in the K-R model (Fig. 1.5 right) the current flow would be into the figure or away from the observer, representing the transverse magnetic field from negative polarity to positive polarity. This is called the inverse polarity (IP) configuration (van Ballegooijen, 2001).

Most quiet-Sun filaments show an inverse polarity configuration (van Ballegooijen, 2001), supporting the model of Kuperus and Raadu (1974) and the findings of Leroy, Bommier, and Sahal-Brechot (1984). This model allows the idea of a long twisted flux rope containing the filaments plasma, which is supported by observations (Kuckein, Martínez Pillet, and Centeno, 2012a; Yelles Chaouche et al., 2012; Kuckein et al., 2020). Here, the arched flux tube is anchored with the two ends in the photosphere and performs some revolutions around the flux tube axis, where a helical field is formed. One model, which describes the existence of a helical field, is the model of van Ballegooijen and Martens (1989). The model starts with an initial condition of a potential field where the magnetic field lines connect the two polarities separated by the PIL (see dashed line in Fig. 1.6a). By adding shear flows due to differential rotation or other shear flows, the footpoints are moved in different directions. Furthermore, converging flows are added to the model and the footpoints move toward the PIL (see Fig. 1.6a). The loops reconnect and the small loop CB and the long axial field line AD along the PIL arise (see Fig. 1.6b). The short and highly curved loop submerges through the surface, because their magnetic curvature force overcomes the buoyant forces (van Ballegooijen, 2001). Long loops with high curvature radii do not submerge. The whole process is repeated, whereby a new loop EH is wrapped around loop AD (see Fig. 1.6c and d). This newly developed twisted field is called the flux rope or flux tube. By repeating the process, the axis of the helical field rises. The cool plasma is trapped inside the helical field (van Ballegooijen and Martens, 1989). The source of the plasma is still unknown. One suggestion points to a siphon flow along the helical

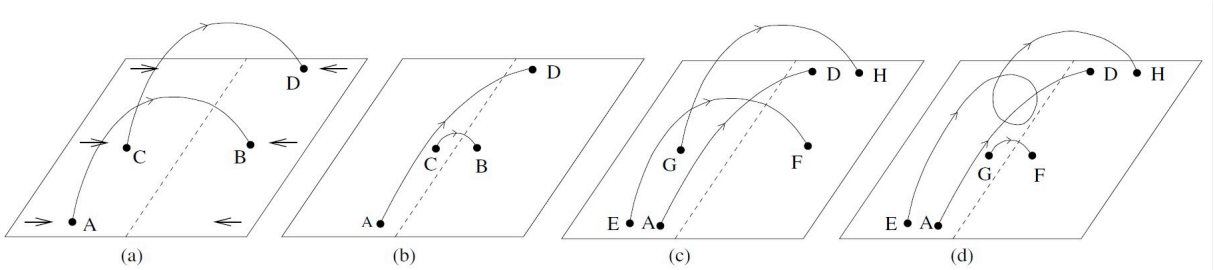

Figure 1.6: Formation of filaments according to the model of van Ballegooijen and Martens (1989). We see the photosphere connected by magnetic field lines. The dashed line denotes the PIL. (a) To the initial potential field, shear flows are added on both sides of the PIL and converging flows that the magnetic footpoints are pushed toward the PIL. (b) Magnetic reconnection produces the shorter loop CB and the longer loop AD. (c) The loops EF and GH start with an initial potential field configuration, and then shear flows start again. (d) After reconnection the loops EH and GF appear. The loop GF submerges below the photosphere. The loop EH wraps around the loop AD and forms a twisted field, which is called flux rope (see Fig. 3 in van Ballegooijen, 2001).

field lines transporting the plasma from the chromosphere up into the corona, which is driven by pressure differences between the chromosphere and the filament (van Ballegooijen, 2001). Observations show that a filament is a dynamic object with a continuous input of plasma. Other possible processes are described in detail in Section 1.6.2. Coronal arcades, connecting positive and negative magnetic field polarities, span over the helical field. They probably play an important role in the stability of the field (van Ballegooijen, 2001). Observations of erupting prominences support the idea of a twisted flux tube (Xue et al., 2016; Kuckein et al., 2020; Wang et al., 2020). There are also other explanations for a helical field. One involves vertical motions of the footpoints, but the necessary persistent motions over several revolutions are not observed (van Ballegooijen, 2001). Another possibility is that the twisted flux rope already exists when it emerges from the convection zone into the photosphere (MacTaggart and Hood, 2010; Okamoto et al., 2008, 2009; Kuckein, Martínez Pillet, and Centeno, 2012a).

1.6.2 Mass Supply in Filaments

The question, how the plasma is transported in the filament spine is still a matter of debate. In the literature, four main models try to explain, how the filament is supplied with plasma, driven by magnetic or/and thermal forces: the injection model, the levitation model, the evaporation-condensation model, and the newest is the magneto-thermal convection. Thereby, the models have to cover many different observed properties of filaments, since filaments and prominences appear in many different shapes and scales on the solar surface. From small-scale active region filaments, to large-scale quiet-Sun filaments, which can span over half the solar diameter and can be very dynamic. The supply with cool plasma at flow speed between 10–100 km s^{-1} has to be sufficiently explained by a model. Furthermore, a model explaining the plasma flow in filaments has to elucidate the origin of counter-streaming flows, which are found in all kind of filaments (e.g., Zirker, Engvold, and Martin, 1998; Alexander et al., 2013; Kuckein, Verma, and Denker, 2016; Diercke et al., 2018). However, most models cover some aspects of the observed parameters, but no model explains all processes.

Injection Model. In the injection model, the magnetic reconnection plays a key role to provide the energy to transport cool photospheric or chromospheric plasma directly into the corona Karpen (2015). This injection of plasma would be visible in high-resolution observations by upward jets (Wang, 1999) or upflows at the footpoints (including minority polarities forming a PIL) or close to the PIL of the filament channel (Karpen, 2015). Chae (2003) observed this process of cancellation, followed by upflows at the footpoints of an active region filament. How plasma is transported to heights of 100 Mm or larger, related to quiet-Sun filaments, with only reconnection processes without thermal heating of the plasma, remains a problem of the injection model. However, quasi-periodic upflows are reported by Li and Zhang (2016) for a large quiet-Sun filament observed with SDO. The authors found coronal bright points at the footpoints of the filament threads. The upflow was initialized by reconnection processes at the footpoints. For the injection model, it is not known how to explain the high dynamic process of plasma supply only

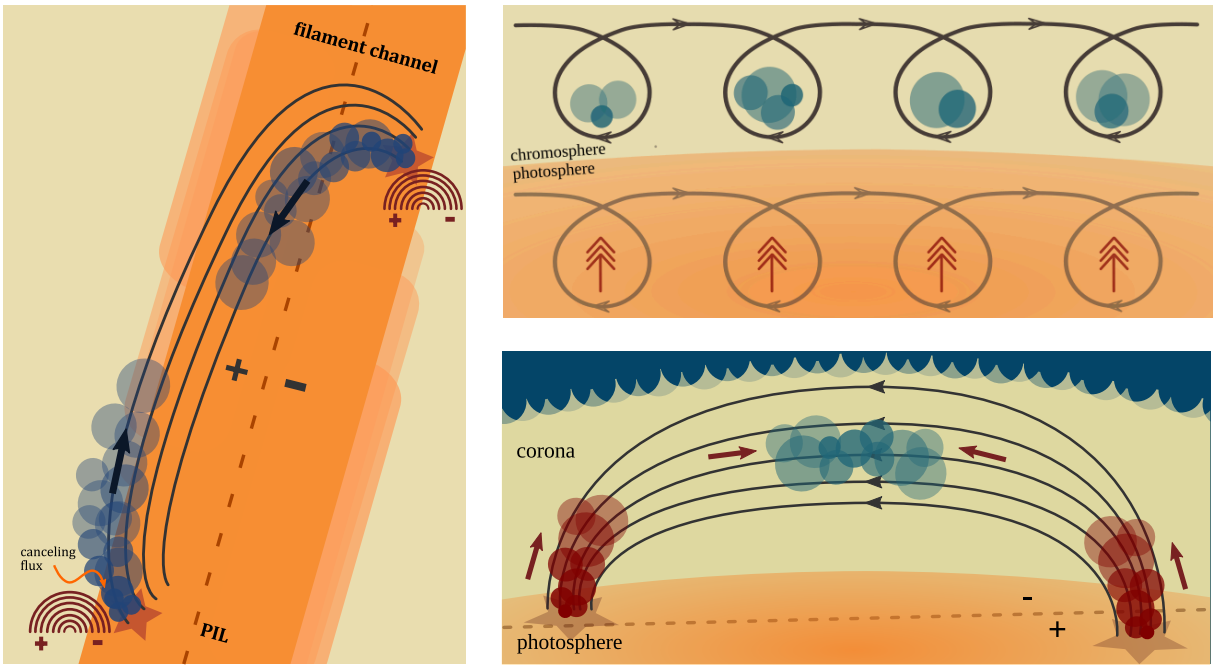

Figure 1.7: Composed figure illustrating three different plasma flow models: injection model (left panel), levitation model (upper right panel), evaporation-condensation model (lower right panel). The dashed line indicates the polarity inversion line (PIL). (Reproduced after inspiration from Figs. 1a, 3a, and 4 in Karpen, 2015, by S. Schrottke).

with reconnection at the footpoints. The injection model could simply explain counter-streaming flows through reconnection processes at both footpoints or alternating reconnection sequences between paired footpoints.

Levitation Model. The basic idea of the levitation model was already described in Section 1.6.1 and assumes that the cool plasma is lifted by rising twisted magnetic flux tubes (van Ballegooijen, 2001). This concave-upward formation was described by observations (e.g., Lites, 2005; López Ariste et al., 2006; Okamoto et al., 2008; Kuckein, Martínez Pillet, and Centeno, 2012a). Other explanations for the levitation of cool plasma involves the relaxation of the magnetic field, when U-loops emerge from the photosphere (Deng et al., 2000) or after reconnection and flux cancellation. If the U-loops change to arched loops, the uplifted plasma in the dipped magnetic field lines will flow down to the chromosphere along the magnetic field lines. These downflows were observed for erupting prominences and at the footpoints of quiet-Sun prominences (Okamoto, Tsuneta, and Berger, 2010). Nonetheless, simulations show the rise of U-loops into the chromosphere, but heights of quiet-Sun filaments can not be reached. In summary, the levitated material cannot travel as fast as injected plasma and usually is located above the PIL (Karpen, 2015).

Evaporation-condensation Model. The evaporation-condensation model is driven by thermal forces. The chromospheric plasma at the footpoints of a coronal loop is locally heated and evaporates into the coronal loops as hot upflows. The plasma condensates in the corona and forms the cool threads of the filament spine (Karpen, 2015). The main ingredient of the evaporation and condensation model is thermal non-equilibrium, which is the main driver that condensation can occur (Karpen, 2015). We assume that the chromospheric plasma is heated at both footpoints and evaporates along the magnetic field lines as hot upflows. The density increases at the location, where the upflows meet which causes an increase in the radiation of the plasma and the plasma cools. Once the plasma reaches a critical temperature of $T = 10^5$ K, a runaway situation develops, which forces the plasma to cool down to chromospheric temperatures in order to regain equilibrium, which is the condensation into filament threads. This process is caused by the peak of the optical-thin radiative loss function, which peaks at $T = 10^5$ K. An important factor to establish a thermal non-equilibrium is the heating scale h, which is proportional to the length of the loop L, whereby the length should be about one magnitude larger as the heating scale (Karpen, 2015). This is given for quiet-Sun filaments, which are more likely observed to have coronal loops, more aligned to the PIL and

form longer loops from weakly twisted flux ropes. The evaporation-condensation model is not suitable to explain the plasma flow in active region filaments with length $L < 80$ Mm and heat scales $h \approx 10$ Mm (Karpen, 2015), because here the thermal non-equilibrium can not be established. The main parts of the evaporation-condensation model were observed, such as the heating at the end of cool filament threads, which resulted in bright EUV emission at that location (Luna et al., 2014), as well as the condensation in filament threads, which was reported by several studies (e.g., Berger, Liu, and Low, 2012; Liu, Berger, and Low, 2012) with coronal data of SDO. Simulation with the evaporation-condensation model can reproduce condensation speeds, lifetime, size, and counter-streaming flows of quiet-Sun filaments.

Magneto-thermal Convection Model. The magneto-thermal convection model combines the influence of magnetic and thermal forces to explain the formation and evolution of filaments (Karpen, 2015). Magnetic bubbles form from twisted magnetic flux, which emerge into the chromosphere from beneath a filament. Because of internal reconnection or Alfvén dissipation, the bubble heats and is carried by buoyancy into coronal heights. The prominence plasma has a higher density than the plasma in the bubble and Rayleigh-Taylor instabilities (RTI, Müller, 2001) occurs. The hot plasma and magnetic flux are transported by a turbulent transport mechanism, caused by the RTI, into the corona. The condensed prominence plasma is divided into vertical spikes, as seen for hedgerow prominences, or flows back to the chromosphere. At the areas of strong gradients of flow speed, Kelvin-Helmholtz instability (KHI, Müller, 2001) can occur, which contributes to the mixing of cool and hot plasma. The model was developed by Berger et al. (2011) and explains hedgerow and polar crown prominences with vertical filamentary structures, where other models fail to explain the stable, extended cool plasma, which stretches out over several gravitational scale heights in these prominences. In SDO observations several prominences are reported with funnel-shape concentrations of hot plasma, which appear before a stable quiet-Sun prominence with vertical filamentary structures (e.g., Berger, Liu, and Low, 2012; Liu, Berger, and Low, 2012, 2014).

1.7 Activity Indices of the Sun

The solar activity can be monitored with different tracers, which change along with the solar cycle. Historically, the sunspot number was the first tracer, where the cyclic behavior the Sun was determined. Throughout the years, many other tracers were found which reflect the solar activity, e.g., Ca II K line, F10.7 cm radio flux, Mg II index, the magnetic field, and many more. Especially, chromospheric and coronal lines reflect the solar activity very well. In the following, I will introduce some of these tracers shortly.

Sunspot Number. I introduced in Section 1.1 that the sunspot number reflects the solar activity index. Until today, this is a widely used tracer for the solar activity. Still, also historical sunspot drawings can reveal new scientific insight in the history of the solar cycle. Beside the sunspot number, e.g., the sunspot area, the tilt angle, the north-south asymmetry, and many more quantities are analyzed (e.g., Hathaway, 2010; Diercke, Arlt, and Denker, 2015; Senthamizh Pavai et al., 2016; Arlt and Vaquero, 2020).

Ca II K Index. The chromospheric Ca II K line is sensitive to the magnetic field, but without a distinct Zeeman effect (Hale et al., 1919; Harvey, 1973). A very complete data collection of Ca II K full-disk images were recently presented in Chatzistergos et al. (2020), who combined around 290 000 full disk Ca II K observations from 43 datasets including observations between 1892 and 2019. They used the fractional plage area on the solar disk as an index for the solar activity. The spectral line of Ca II K exhibit line core emission, mainly reflecting regions of plage and the chromospheric network. The spectral index is a common tracer for the solar activity (Livingston et al., 2007; Bertello et al., 2016).

F10.7 cm Radio Flux. Since 1948, the disk integrated radio emission at 10.7 cm (2800 Hz) is monitored with daily observations (Tapping and Charrois, 1994). It is independent of weather conditions and therefore considered as an objective tracer of the solar activity (Hathaway, 2010). The telescope performs

several observations a day, whereby flaring events on the Sun are avoided. The correlation to the sunspot number is very high. Nonetheless, there is evidence that the radio flux follows the sunspot number by about 1-month (Hathaway, 2010).

Mg II Index. Another tracer for solar activity is the chromospheric Mg II index, which is derived from the core-to-wing-ratio of the Mg II doublet at 2795.6 Å and 2802.7 Å from space data since 1978 (Viereck and Puga, 1999). The advantage of this proxy is it considers both sunspot darkening and faculae brightening (Lean et al., 1997). The spectral Mg II index varies up to 20% between minimum and maximum (Viereck and Puga, 1999).

Total Solar Irradiance. The total solar irradiance (TSI) displays the entire radiant energy emitted from the Sun at all wavelengths (Hathaway, 2010) and is used to define the solar constant, which is the emitted energy per square meter at each second at one astronomical unit (AU). This quantity can only be measured outside of Earth's atmosphere and is therefore dependent on satellite observations. Therefore, a careful calibration of the data from the various instruments is required (Fröhlich, 2012). The behavior of sunspot number and TSI are strongly correlated, as well, but for Solar Cycle 23 the TSI did not reproduced the decrease of the peak of the solar cycle, as it was visible in the sunspot number (Hathaway, 2010).

Many more wavelengths in the solar spectrum can be related to the changes in activity. A large spectroscopic dataset of various chromospheric lines during Solar Cycle 23 is summarized by Livingston et al. (2007), including the Ca II K line, He I 10830 Å equivalent width, Ca II 8542 Å central depth, Hα central depth, or CN bandhead at 3883 Å. The conclusion from Livingston et al. (2007) that all spectral lines showed variations along the solar cycle, but with a lower relative amplitude as Ca II K.

1.8 Motivation

Polar crown filaments are astonishing features. They build at the border of the unipolar magnetic field of the polar region and the remnant trailing flux of bipolar regions from the activity belts, which was transported by meridional flows to the poles. The number of filaments, their length and lifetime, the appearance and disappearance of polar crown filaments, all are connected to the solar dynamo. Studying polar crown filaments means to study indirectly the actions of the solar dynamo. The large-scale properties, such as the migration of polar crown filaments ("rush-to-the-pole") and their disappearance, which is related to the magnetic field reversal at the poles, can be studied effectively by full-disk Hα observations of the Sun. In this thesis, I present an effective approach to data reduction (Chapters 3 and 4), which enabled the extraction of filaments, including polar crown filaments, with two different automatic methods (Chapters 4 and 5). A statistical analysis reveals the main properties of the filaments (Chapter 4). Moreover, I presented the capabilities of Hα observations as direct tracers of solar activity using bright plage regions and dark absorption features, including filaments (Chapter 6). In my doctoral thesis, the following questions will be addressed:

- ☐ Can the detection of filaments in full-disk data be improved?
- ☐ Which physical parameters of filaments can be inferred from full-disk observations?
- ☐ Does the rush-to-the-pole differ in Solar Cycle 24 from other cycles?
- ☐ What are the scientific capabilities of Hα full-disk observations?
- ☐ Can we relate Hα full-disk observations to chromospheric activity on other stars?

A detailed analysis of polar crown filaments is only possible with high-resolution observations. Only a few studies analyzed polar crown filaments in high-spatial resolution so far. In Chapter 7, we use high-resolution observations of the Hα spectral line in the line-core and in the continuum to study the connection of the filament to photospheric features, i.e., bright points in weak magnetic field close to the poles. Thereby, the following questions will be addressed:

- ☐ Differ polar crown filaments from filaments at lower latitudes?
- ☐ How can high-resolution solar observations advance our knowledge about polar crown filaments?
- ☐ How are bright points related to filaments?
- ☐ Are bright points connected to the mass supply of filaments?
- ☐ Does the weaker magnetic field close to the poles result in a different morphology of bright points?

Chapter 2

Observation and Instruments

In the thesis, we have used data from two telescopes. Full-disk observations of the Chromospheric Telescope (ChroTel) and high-resolution data of the Vacuum Tower Telescope (VTT), Observatorio del Teide, Tenerife, Spain. We will introduce both telescopes briefly in this section, as well as the very fast camera system, which was installed at the VTT in September 2018, to obtain high-resolution observations of polar crown and high-latitude filaments on the Sun. In addition, the data processing of the full-disk and high-resolution observations are briefly introduced. More detailed information on the data processing for the individual studies is given in the respective chapters.

2.1 Chromospheric Telescope

The Chromospheric Telescope (ChroTel, Kentischer et al., 2008; Halbgewachs et al., 2008; Bethge et al., 2011) is a full disk imager mounted on the telecope building of the Vaccum Tower Telescope (VTT, von der Lühe, 1998) at the Observatorio del Teide in Tenerife, Spain (Fig. 2.1). The robotic 10 cm-telescope takes images of the solar chromosphere in three different wavelengths: in the Ca II K line with a central wavelength at λ3934 Å, in Hα at λ 6562 Å, and in the He I line at λ10830 Å. In addition, the He I line is scanned at seven different wavelength posititions providing spectroscopic data. In principle, ChroTel can contribute to various scientific topics (Kentischer et al., 2008), i.e., the dynamic response of the chromosphere to the photospheric driving and the chromospheric source of the fast solar wind. For both topics the calculation of Doppler velocities from the spectroscopic He I data are required. The full-disk data of ChroTel are utilized for the understanding of large-scale structures and phenomena related to the solar dynamo. Furthermore, as a context imager, the chromospheric plasma can be tracked during and after eruptive events.

The telescope is enclosed in a metal housing on the terrace of the VTT to prevent dust on the mirrors (Fig. 2.1). The light is coming through the entrance window W1 and is guided by three mirrors (M1, M2, and M3) to the first lens L1. These three mirrors build up the turret system, whereby M1 and M2 are pointing the telescope towards the Sun. Mirror M3 reflects the light on the horizontal plane with achromat lens L1. Three guiding systems ensure the correct pointing of the telescope (Kentischer et al., 2008). The position of the Sun is calculated with an external program, which is integrated to the telescope control software, to achieve the correct pointing of the telescope (Halbgewachs et al., 2008). In total, the guiding accuracy is below 0.5″(Kentischer et al., 2008). One of the two independent image-stabilizing systems is installed behind lens L1. Behind lens L1 is the mirror M4 which feeds the coarse guider with light. The light is guided into the telescope building, where it is collimated by lens L4 and forms an image of 25 mm diameter of the telescope entrance aperture. At the location of the pupil image mirror M5 is installed. This mirror is a high-quality, fast tip-tilt mirror and reflects light to the fine guiding system. With this procedure fast image jitter introduced by strong wind is removed. With this, a maximum accuracy and high-quality solar images can be ensured. The achromat lens L5 in the following light path re-images the Sun and the achromat lens L6 collimates the light again. Here, the image has a approximate diameter of 24 mm. In the following path the light is transferred into the filter system. Since there is only one charged coupled device (CCD) camera, the light has to be distributed alternately to the three Lyot filter. This is

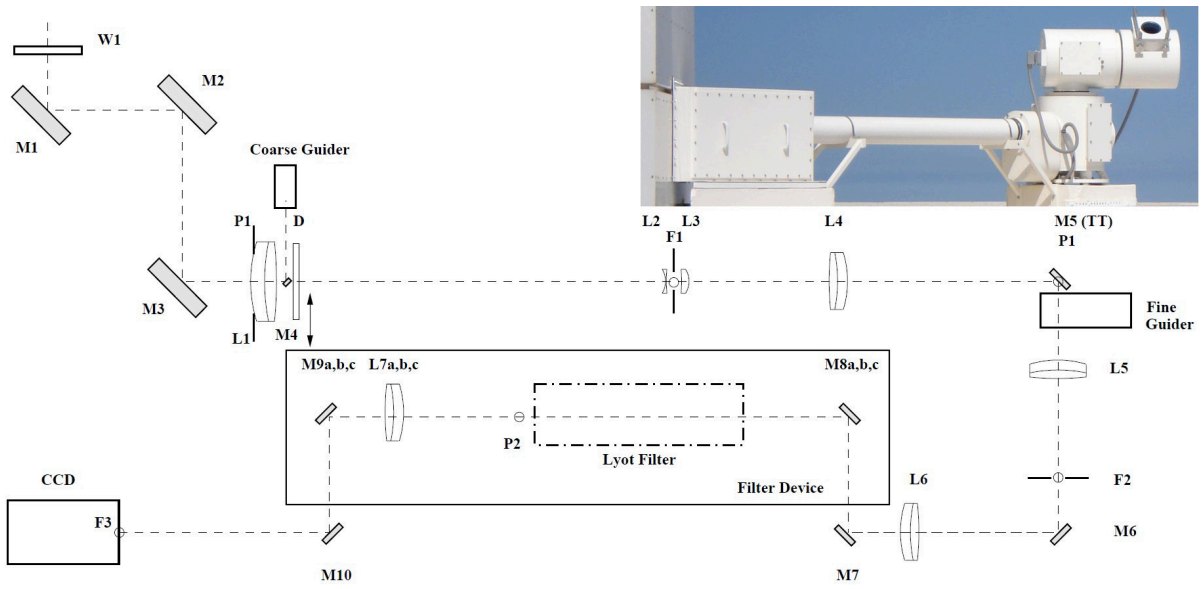

Figure 2.1: The view on ChroTel mounted on the VTT. The light comes through the entrance window and is guided with the turret system in the observing room inside of VTT, where the Lyot Filter are mounted. The telescope housing is made of stainless steel sheet metal (adapted from Figs. 1 and 2 in Kentischer et al., 2008).

performed with the mirrors M7 and M10, which rotate always in the same amount (Bethge, 2010). The achromat lens L7 projects then the image of the Sun on the CCD chip. Due to the large field-of-view (FOV), optical aberrations, like astigmatism and a field curvature are introduced to the image, which has to be removed after recording the data.

The filter system contains in total three Lyot filters with three different wavelengths (Bethge et al., 2011). The first Lyot filter with a central wavelength of 3934 Å and three different full width at half maximum (FWHM) at FWHM = 0.3 Å 0.6 Å, and 1.2 Å, covering the Ca II K line. The second Lyot filter at 6562 Å with FWHM = 0.5 Å and 1.0 Å contains the Hα spectral line. The default setting of this filter is FWHM = 0.5 Å. The third Lyot filter is centered at a wavelength of 10830 Å and a FWHM = 1.4 Å. This filter is a tunable filter and records data regularly at seven wavelength positions around the central wavelength. This rapid adjustment of the wavelength of the transmission peak is only possible with a liquid crystal variable retarders (LCVR). The change in position is done in 60 ms and all seven filtergrams are obtained in 8 s. The selected and fixed wavelength positions are non-equidistant at $\lambda_1 = 10\,827.45$ Å, $\lambda_2 = 10\,828.47$ Å, $\lambda_3 = 10\,829.60$ Å, $\lambda_4 = 10\,830.30$ Å, $\lambda_5 = 10\,831.00$ Å, $\lambda_6 = 10\,832.13$ Å, and $\lambda_7 = 10\,833.15$ Å. This wide wavelength range includes the complete He I-triplet and also parts of the Si I line close-by. Please note that the recorded images are stored in reversed order starting with λ_7 as the first filtergram (see Chapter 3 for details).

The telescope obtains full-disk filtergrams on a detector with 2048 $\times$ 2048 pixels. The large detector size results in an image scale of about $0\farcs96$ pixel^{-1}, which corresponds to a spatial resolution of $2\farcs5$ in Hα and $3''$in He I. The exposure times vary between the three channels with $t_{\rm exp} = 100$ ms for Hα, $t_{\rm exp} = 300$ ms for He I, and $t_{\rm exp} = 1000$ ms for Ca II K (Bethge et al., 2011). These different exposure times result from the diverse quantum efficiency for the three wavelengths, whereby the quantum efficiency is highest for Hα with 63% and reduces to 39% for Ca II K and only 2% for He I.

The instrument was designed to work autonomously without user interaction (Halbgewachs et al., 2008; Bethge et al., 2011). It should start to operate automatically in the morning and closes in the afternoon. During bad weather conditions, which are monitored by weather sensors, the telescope stops operating and starts again when the conditions are safe for operation. Unfortunately, since 2017 the telescope has to be started manually and requirres a technician on-side to be operated. Moreover, several failures of the telescope control software and in the data recording pipeline prevented regular observations. As a consequence, the data rate is lower since 2017. The regular operation of the telescope starts in March or April until December, in parallel to the operation of large high-resolution telescopes GREGOR (Schmidt et al., 2012) and VTT.

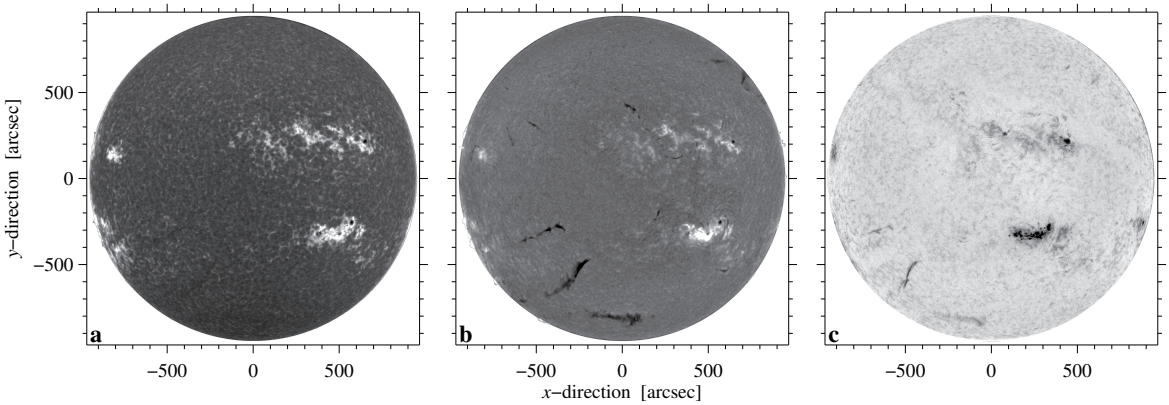

Figure 2.2: Sample images of the three chromospheric channels: Ca II K line (left) Hα (middle panel), and line core He I(right), after filtering with Zernike polynomials (see Chapter 3).

Since the regular start of observations on 13 April 2012, ChroTel observed on 1062 days with different amounts of data each day, ranging from single images to up to 200 images per day. On special request, observing modes with cadences of 10–15 s in Hα and Ca II K line and with 30 s cadence in He I are possible Bethge et al. (2011). In consequence, there are observing days with only a single or two wavelengths observed, whereby Hα was observed always, Ca II K was observed on 974 days and He I on 984 days. Nonetheless, the standard mode observing in all three channels obtains images with a cadence of 3 min.

The data are transferred every night to the data archive at Leibniz-Institut für Sonnenphysik (KIS) in Freiburg, Germany (formerly known as the Kiepenheuer Institut für Sonnenphysik). The basic image processing steps, such as correction for bias and gain and dark- and flat-field reduction, are applied instantly. A preview of the images with a lower resolution of 1024×1024 pixels in `jpg` format is available on-side a few minutes after recording, which can be used as context images for VTT and GREGOR observations. The scientific data are stored in the Flexible Image Transport System (FITS, Wells, Greisen, and Harten, 1981; Hanisch et al., 2001) format and should be available on the next day, as well as movies of the observing day. The level 1.0 data is available in the KIS Science Data Center[1] and in the Virtual Solar Observatory [2].

The level 1.0 data require further processing before they can be used for an analysis with routines included in the solar software package SolarSoft (SSW, Freeland and Handy, 1998; Bentely and Freeland, 1998) Interactive Data Language (IDL)[3]. First of all, the data are rotated to the solar north with the information about the rotation angle stored in the FITS header. The data are corrected for intensity spikes with routines of the data pipeline (sTools, Kuckein et al., 2017). In data observed in the early morning or afternoon, the solar disk appears oval because of differential refraction. This was corrected by fitting an ellipse to the solar disk. The entire data archive is limb darkening corrected, by fitting fourth-order polynomials to the intensity profile (Diercke et al., 2018). Recording the data with Lyot filters introduced a non-uniform intensity variation in the filtergrams, which was corrected with a method developed in the scope of this thesis (Chapter 3), which uses an approximation of this variation with Zernike polynomials to correct the filtergrams. Further details of the data reduction are described in Chapter 3 and Chapter 4.

[1] KIS Science data center: sdc.leibniz-kis.de:8080/
[2] Virtual Solar Observatory: sdac.virtualsolar.org/cgi/search
[3] www.harrisgeospatial.com

Figure 2.3: The coelostat mirrors of the the Vacuum Tower Telescope (VTT) at a height of 38 m in September 2018.

2.2 Vacuum Tower Telescope

The Vacuum Tower Telescope (VTT, Schmidt and Soltau, 1987; von der Lühe, 1998) is a 70-cm aperture tower telescope at the Observatorio del Teide, Tenerife Spain, which started operation in 1987 after an extensive site survey. The telescope is operated under the leadership of KIS in a consortium with the German institutes Leibniz-Insitut für Astrophysik Potsdam (AIP) and the Max-Planck-Institut für Sonnensystemforschung (MPS) in Göttingen. It is located at an altitude of 2390 m. On top of the tower at a height of 38 m, a coelostat system collects the light. It consists of two mirrors with a diameter of 80 cm. The light is directed through the entrance window of the vacuum tank to the primary mirror with a diameter of 70 cm, which is a mounted in a *Schiefspiegler* configuration. The vacuum tank is of cylindrical shape, while the cylinder has at the top a diameter of 75 cm, it widens to a diameter of about 1.5 m one floor below the dome. Since 2016, the vacuum window was broken and was replaced in 2020. The vacuum serves to avoid internal seeing during observations. Nonetheless, very good observations can be taken also without the vacuum, but the observation time is then reduced to observations in the early morning until the air in the tube was heated and the influences on the seeing were to strong. After closing the telescope for short time to cool down the air in the tube, a continuation of the observations is possible. The Kiepenheuer Adaptive Optics System (KAOS, van der Lühe et al., 2003) is integrated on the optical bench near the telescope focus. The optical bench is located in a metal tank, which can be evacuated. In the current state of the AO there is no vacuum in the tank. On this optical bench in the AO tank, the collimator, the deformable mirror, the tip-tilt mirror and a camera are located. A wheel with field stop and calibration targets is integrated on an intermediate focal plane in the tank. The collimator mirror transfers the light on the tip-tilt-mirror from where it is sent to the deformable mirror with 35 electrodes, arranged in three rings. The mirror is controlled by the signal from the wavefront sensor which is located outside of the tank. The wavefront sensor has 37 subapertures, whereby the central aperture is neglected, because of a shadow of a mirror which obstructs it. The adaptive optics system enables observations of small scale features, such as bright points, the smallest resolvable features on the solar surface (Chapter 7).

The focal length of the telescope is 46 m and the image scale at the primary focus is $4.59''$/mm. The main post-focus instrument of the VTT is the echelle spectrograph (von der Lühe, 1998; Löhner-Böttcher et al., 2017). A pre-disperser to select the required wavelength from a low-resolution spectrum. The echelle grating has a size of 220×440 mm and a blaze angle of $63°$. The spectral resolution $R = \lambda/\Delta\lambda$ is about 800 000 at a wavelength of 5500 Å. It is possible to observe in several different wavelengths simultaneously, which is in the current state three wavelength, due to the three CCD cameras available.

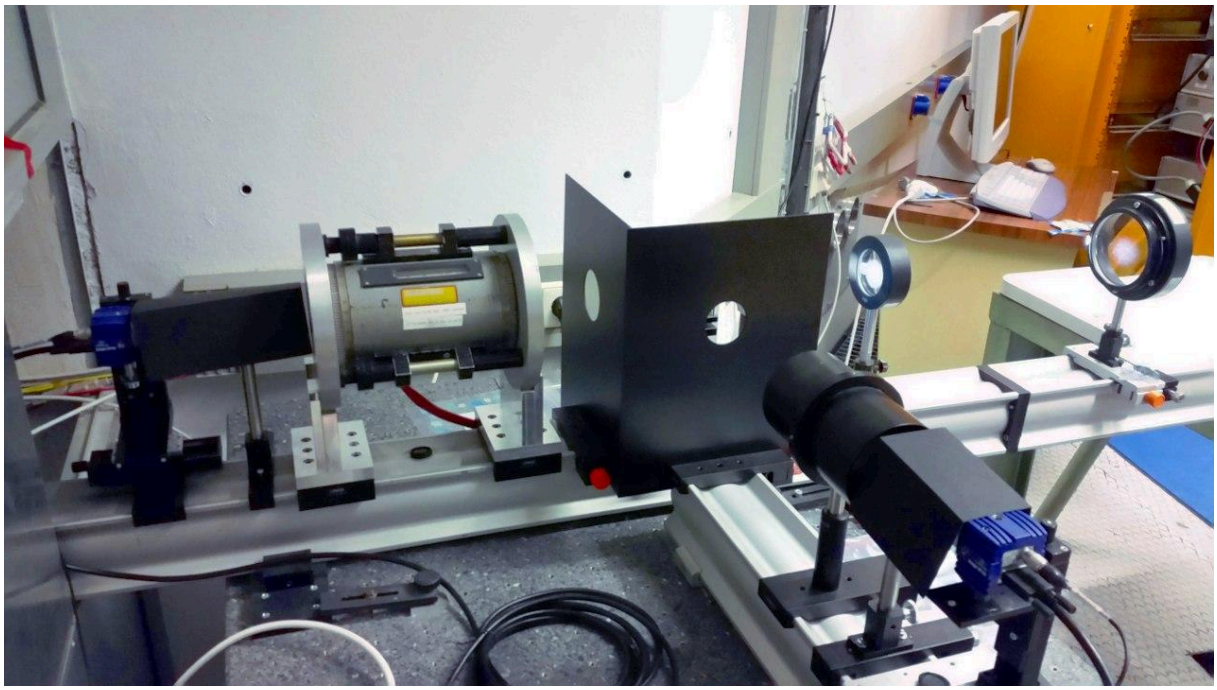

Figure 2.4: Setup of the M-lite camera system at the VTT in September 2018 (Fig. 1 in Denker et al., 2020). The light was distributed by a beamspliter to the Hα narrow- and broad band imager, whereby an interference filter selects the Hα broad-band wavelength range for both cameras. A Lyot filter is used for the narrow-band channel (left). Infront of the broad-band camera (middle) a neutral density filter limits the photon flux. Image courtesy of Christoph Kuckein.

A 45° fold mirror or beamsplitter can direct the light to additional instruments in the optical lab of VTT. Two of these instruments are permanent instruments. The Laser-based Absolute Reference Spectrograph (LARS, Löhner-Böttcher et al., 2017) supports the echelle spectrograph for ultra-high precision observations to calibrate the spectrum on an absolute wavelength scale. Thereby, the light to the spectrograph is directed with a single mode fiber towards the spectrograph. The second permanent instrument is the HELioseismological Large Regions Interferometric DEvice (HELLRIDE, Staiger, 2012), which is a Fabry-Pérot spectrometer. It allows quasi-simultaneous observations in several spectral lines with a 4-by-4 grid matrix and a field-of-view (FOV) of $100'' \times 100''$. The instrument will be available in the near future for regular observations.

In addition to the permanent instruments, there is space in the optical lab for visiting instruments, like the M-lite Camera System (LaVision, 2017; Denker et al., 2020), which was tested at the VTT before installing it at the GREGOR solar telescope (Schmidt et al., 2012) at Observatorio del Teide. The camera system was used to obtain high-resolution observations of polar crown and high-latitude filaments (Diercke et al., 2020). The 45° fold mirror guides the light through two achromatic lenses with focal lengths of $f_1 = 1500\,\mathrm{mm}$ and $f_2 = 800\,\mathrm{mm}$ to an Hα interference filter at $\lambda 6567$ Å with FWHM of $\Delta\lambda = 7.5$ Å and a transmission of 70%. A 70/30 gray beamsplitter divides the light to the narrow- and broad-band channel, respectively. In the broadband-channel, a neutral density filter reduced the photon flux. In the narrow-band channel a Hα Lyot filter is installed, observing at λ 6563 Å with a FWHM of (0.6 Å). This Lyot filter was manufactured in 1945 and modified later by Bernhard Halle Nachf. Berlin-Steglitz (Denker et al., 2020). Previously, it was installed at the Observatory on Telegrafenberg in Potsdam, Germany. It is temperature controlled and the wavelength can be tuned by adjusting the temperature. The M-lite cameras were used to record the high-resolution data with a high-temporal cadence. The M-lite cameras have a detector size of 1920×1280 pixels, which is corresponds to an aspect ratio of 16:10, whereby the pixel size is $5.86 \times 5.86\,\mu\mathrm{m}^2$. The cameras can be used in the spectral range from 4000 Å to 9000 Å with a peak quantum efficiency of 72 % at about 5000 Å, whereby the red spectral quantum efficiency is about 58% at $\lambda 6000$ Å. The cameras have a full well capacity of $32\,000\,\mathrm{e}^-$ with a low read-out noise of about $6.8\,\mathrm{e}^-$. The cameras are able to take fast time-series of images with a frame rate of up to 100 Hz at 12 bit. A programmable timing unit (PTU) is used to synchronize the cameras with an accuracy of about 10 ns. Thereby the cameras use a global shutter. Furthermore, the images are rapidly stored on the

Solid-State Drives, so that fast cadences of image sequences are possible. Exposure times between 34 μs and 10 s are possible, whereby 5–20 ms are typical for solar observations. The camera system should be used to observe a large variety of solar structures, including dark umbra of sunspots, filaments, as well as prominent absorption lines, such as the Hα line, where the intensity is reduced by a factor of five compared to quiet-Sun or continuum observations. Therefore, it is possible to add a gain of 0-24 dB to the cameras, to increase the digitized read noise signal. More detailed information on the cameras is found in Denker et al. (2020).

During the observations, we took sequences of 500 images with 10 or 20 repetitions, depending on the seeing conditions. The images were taken with an exposure time of $t_{\rm exp} = 20$ ms. The acquisition rate was $f_{\rm acq} = 46$ Hz. The diffraction limit of the VTT ($D = 0.7$ m) is for the Hα $\alpha = \lambda/D = 0.193''$. Therefore, the data were recorded with 2×2-pixel binning, which results in an image scale of $0.098''$ pixel^{-1}. This corresponds to 71.14 km on the solar surface for each pixel. The high full-well capacity is especially good for observations in the narrow-band with a Lyot filter. Nonetheless, we added in the narrow-band channel an additional gain of 18 dB, to have a similar amount of counts in both cameras.

The basic reduction was carried out with the "sTools" data-reduction pipeline (Kuckein et al., 2017), which included dark and flat-field correction, as well as proper alignment between both cameras. The pipeline carries out image selection, based on the 100 best images of each burst of 500 images using the Median Filter-Gradient Similarity (MFGS, Deng et al., 2015; Denker et al., 2018) image quality metric gauging the seeing quality. The images of both channels were aligned to perform the restoration. The channels are well aligned and just marginal shifts of 1–4 pixels, rotations of about -1°, and magnifications of about 1% were needed. The broad- and narrow-band images were restored together using Multi-Object Multi-Frame Blind Deconvolution (MOMFBD, Löfdahl, 2002; van Noort, Rouppe van der Voort, and Löfdahl, 2005).

Chapter 3

Calibration of Full-disk He I 10 830 Å Filtergrams of the Chromospheric Telescope

The Sun has been observed with telescopes for more than 400 years on a regular basis. Long-term observations of sunspots revealed a cyclic behavior of their appearance related to the solar dynamo (Cliver, 2014). Thus, long-term historical sunspot data are still an important part of present science (Diercke, Arlt, and Denker, 2015; Senthamizh Pavai et al., 2016). Nowadays, space observations monitor the Sun continuously with high cadence (tens of seconds) and high-spatial resolution (about one second of arc), e.g., the Solar Dynamic Observatory (SDO, Pesnell, Thompson, and Chamberlin, 2012) with the onboard instruments Atmospheric Imaging Assambly (AIA, Lemen et al., 2012) and Helioseismic and Magnetic Imager (HMI, Scherrer et al., 2012). In addition to space instruments, full-disk observations from Earth are crucial to understand solar dynamics and activity, e.g., the full-disk Hα λ6562.8 Å observations, which are part of the Global Hα Network (Steinegger et al., 2000). This network initially combined full-disk Hα observations from Big Bear Solar Observatory (BBSO, Denker et al., 1999) in California, Kanzelhöhe Solar Observatory (KSO, Otruba, 1999) in Austria, and Yunnan Astronomical Observatory (YNAO) in China. Today, a total of seven facilities around the Earth monitor the Sun in Hα as part of the network bridging the night gap. Furthermore, the Global Oscillation Network Group (GONG, Harvey et al., 1996) of the U.S. National Solar Observatory (NSO) hosts a similar network. This network consists of six facilities across the globe (Spain, U.S.A., Chile, Australia, and India) with the aim to study the internal structure of the Sun and its dynamics using helioseismology. GONG also provides full-disk Hα observations and magnetograms.

Along with Hα observations, KSO archives include full-disk images of the Sun in the continuum and the Ca II K line core, as well as drawings of sunspots. The Precision Solar Photometric Telescope (PSPT, Coulter, Kuhn, and Lin, 1996) at Mauna Loa Solar Observatory (MLSO) provides full-disk observations in the blue and red continuum, broad-band observations of the Ca II K λ3933.7 Å line, and narrow-band observations in the wings of this line. The Full-Disk Patrol (FDP, Keller, Harvey, and Giampapa, 2003) telescope provides full-disk observations at high-temporal cadence. Besides Hα images, observations in the Ca II K line, in the He I λ10 830 Å triplet, in the continuum, and at other photospheric wavelength positions are possible. Doppler velocity maps can be created as well using the Hα spectral information. The Chromospheric Helium Imaging Photometer (CHIP, Elmore et al., 1998) at Mauna Loa was operated from 1996 until 2013 by the High-Altitude Observatory (HAO). It recorded every 3 min full-disk observations of the Sun at seven wavelength positions around the He I λ10 830 Å.

This study concerns another full-disk imager, i.e., the Chromospheric Telescope (ChroTel, Kentischer et al., 2008; Bethge et al., 2011) on Tenerife, Spain, which is mounted on the terrace of the Vacuum Tower Telescope (VTT, von der Lühe, 1998). It is based on the model of CHIP and also a Lyot filter for He I was provided by HAO. ChroTel is a robotic telescope with an aperture of 10 cm and observes at three different chromospheric wavelengths: Hα λ6562.8 Å, Ca II K λ3933.7 Å, and He I λ10 830 Å. In proximity of the infrared He I line, the instrument is tuned to seven different filter positions around $\pm$3 Å centered on the He I line core. Thus, Doppler maps can be derived based on these filtergrams. The filter positions

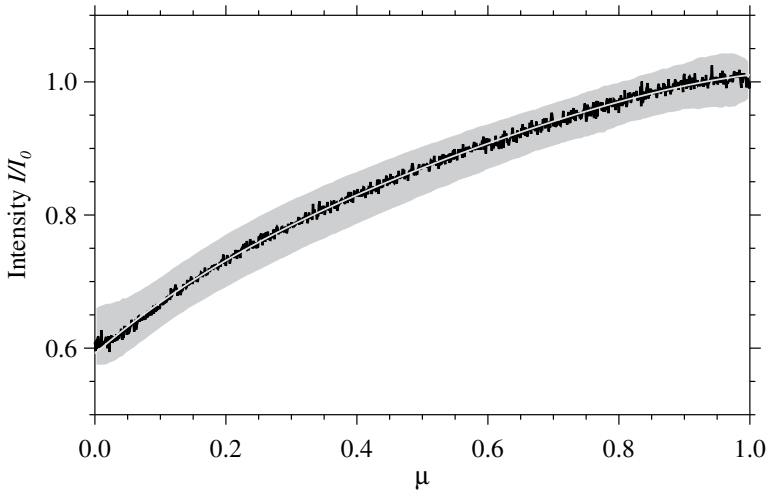

Figure 3.1: Intensity profile used for the limb-darkening correction of the He I filtergram at 10:09 UT on 2018 March 23. The intensity I/I_0, which was normalized to the quiet-Sun intensity at disk center I_0, is plotted against $\mu = \cos\theta$, where θ is the heliocentric angle. The mean local intensity is plotted in black and the area within three standard deviations of the mean local intensity is shaded in gray. A 4^{th}-order polynomial fit is overplotted as a white curve.

include the close-by photospheric Si I line and telluric lines. In the regular observing mode of ChroTel, the telescope records every three minutes an image in all three wavelength bands. Higher cadences of up to 10 s are possible in Hα and Ca II K, when continuous data acquisition is limited to a single channel.

Numerous previous studies highlight the importance of the triplet of neutral helium He I λ 10 830 Å which originates in the high chromosphere (Kuckein, 2012). It consists of a blue and red component, where the red component is a blend of two lines. The line is a primary choice to analyze the chromospheric magnetic field (see Kuckein, Martínez Pillet, and Centeno, 2012a) and the line-of-sight (LOS) velocities in filaments (see Kuckein, Martínez Pillet, and Centeno, 2012b). In both studies, the authors presented high-resolution spectral observations obtained with the Tenerife Infrared Polarimeter (TIP-II, Collados et al., 2007) at the VTT. A similar study of high-resolution spectroscopy was carried out with the GREGOR Infrared Spectrograph (GRIS, Collados et al., 2012) analyzing LOS velocities of arch filament systems (González Manrique et al., 2018). On the other hand, ChroTel observations were used to to analyze LOS velocities during a flare., which was triggered by a splitting sunspot (Louis et al., 2014). Compared to high-resolution instruments, ChroTel offers a unique advantage of full-disk Dopplergrams in the He I line, which allows us to relate the high-resolution observations with the surrounding structures. Furthermore, full-disk He I Dopplergrams enable us to study large-scale features such as polar crown filaments over several days continuously. Given the wealth of data that ChroTel provides, a method to calibrate the filtergrams and produce full-disk Dopplergrams is necessary to fully exploit this dataset.

In the following, we present a method to calibrate the ChroTel He I filtergrams, i.e., the removal of optical aberrations with the help of Zernike polynomials. The calibration is necessary because the filter transmission introduces a non-uniformity in the intensity distribution of each flat-fielded and limb-darkening-corrected filtergram. In Section 3.1, we introduce the ChroTel observations in the He I wavelength band along with the basic pre-calibration steps. In Section 3.2, we describe the method to calibrate the filtergrams yielding a uniform intensity background. In addition, we discuss the derived Doppler velocities from the ChroTel filtergrams and compare them with corresponding Doppler velocities from high-resolution observations of GRIS for a selected sample dataset followed by a discussion.

3.1 Observations

In the following sections, we introduce the datasets, which we used from ChroTel as well as the dataset from the high-resolution spectrograph GRIS, which was used to validate the results derived from the ChroTel observations. Furthermore, we discuss shortly the ChroTel image quality of the seven filtergrams in He I over the day for one dataset.

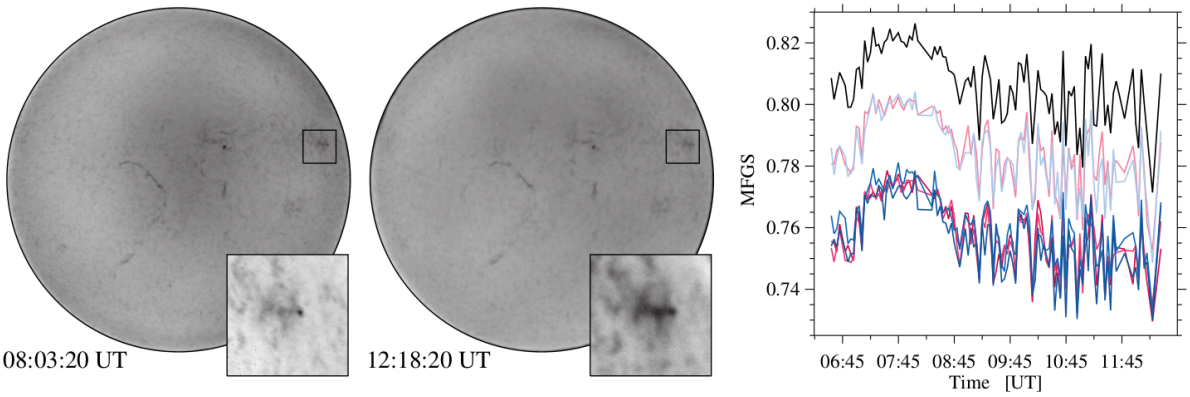

Figure 3.2: Image quality based on the Median Filter-Gradient Similarity (MFGS) method for the time-series on 2017 June 20. The best (*left*) and worst (*middle*) image of the time-series were recorded at 08:30:20 UT and 12:18:20 UT, respectively. Both images are corrected for limb darkening. Active region NOAA 12663 is marked with a black square and shown enlarged in the lower right corner. Here, the image quality between both images is also visibly different. The MFGS values between 06:33 UT and 12:30 UT (right) were plotted over time for all seven wavelength positions. The black profile represents the central filtergram, and blue and red colors correspond to filtergrams with shorter and longer wavelengths respectively. Lighter shades of blue and red indicate closer proximity to the He I line core. (different). For clarity, the MFGS curves for the central filtergram #4 is shifted up by an offset of $+0.1$, and the curves for filtergrams #1, #2, #6, and #7 are shifted down by an offset of -0.1.

3.1.1 Observations of the Chromospheric Telescope

We selected three datasets of ChroTel with different solar activity levels for the following investigation. Data representing the active Sun was taken on 2014 May 12, whereas low solar activity was encountered during quiet-Sun conditions on 2018 March 23. The data recorded on 2017 June 20 are a good example for typical activity levels.

ChroTel acquires filtergrams at seven wavelength positions in and around the He I triplet (Bethge et al., 2011). The filtergrams are numbered #1 – 7 in order of increasing wavelength, with #4 being the central filtergram. The central wavelengths for the seven filter position are 10 827.45 Å, 10 828.47 Å, 10 829.60 Å, 10 830.30 Å, 10 831.00 Å, 10 832.13 Å, and 10 833.15 Å. Level 1.0 data are available online, which are flat-field corrected and converted to FITS format (Wells, Greisen, and Harten, 1981; Hanisch et al., 2001). Each set of filtergrams in level 1.0 data is ordered with decreasing wavelength. However, we present all results #1 – 7 with increasing wavelength for consistency. The 2048×2048-pixel images are rotated and rescaled so that the radius corresponds to $r = 1000$ pixels, which yields an image scale of about $0.96''$ pixel^{-1}. To account for limb-darkening, we derive an average intensity profile for each image, as described in Diercke et al. (2018). The intensity values I for each pixel are plotted against $\mu = \cos\theta$, where θ is the heliocentric angle. The intensity profile is fitted with a 4$^{\text{th}}$-order polynomial

$$I(\mu) = c_0 + c_1 \cdot \mu + c_2 \cdot \mu^2 + c_3 \cdot \mu^3 + c_4 \cdot \mu^4. \tag{3.1}$$

In the next step, the profile is expanded to a 2D map containing the limb-darkening values for the whole solar disk. After division of the He I filtergrams by the 2D limb-darkening function, dark sunspots and bright areas are removed by masking these region. The 4$^{\text{th}}$-order polynomial fit is then repeated for quiet-Sun regions only. An example of the fitted profile is shown in Fig. 3.1. The 2D expansion of this profile is again used for the limb-darkening correction of the filtergrams.

3.1.2 Observations of GREGOR Infrared Spectrograph

On 2017 June 20, active region NOAA 12663 was observed with GRIS, which is located close to the west limb (Fig. 3.2). The slit length of GRIS corresponds to $66.3''$ with a sampling of $0.136''$ pixel^{-1} along the slit. The spectral window covers about 18 Å, which includes the chromospheric He I 10 830 Å line, the Si I, the Ca I, and several telluric lines. The dispersion is about 18 mÅ pixel^{-1}, and the number of spectral points is $N_\lambda = 1010$. The spatial scan was taken from 08:33 UT to 09:00 UT, covering a field-of-view (FOV) of $20'' \times 59''$. These data will be used in Section 3.2.3 to validate the Doppler velocities derived from ChroTel filtergrams.

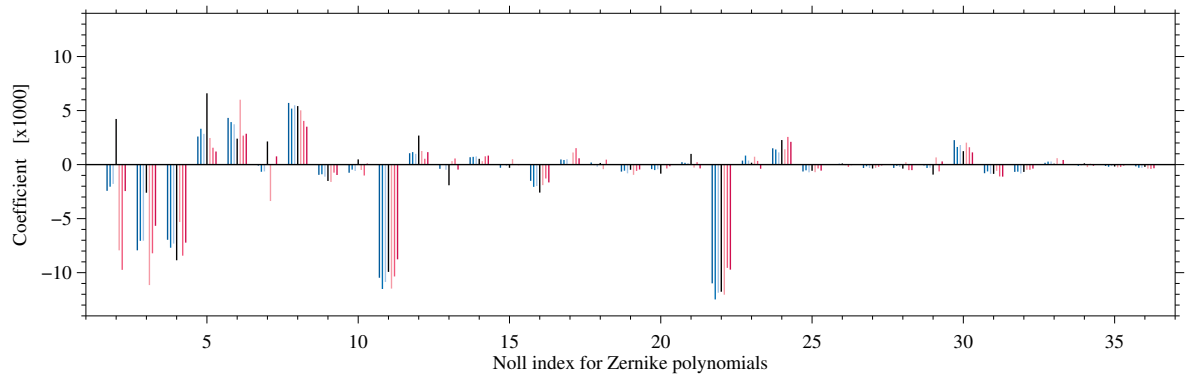

Figure 3.3: Coefficients of 36 Zernike polynomials fitted to He I filtergrams at seven wavelength positions for the best quiet-Sun dataset on 2018 March 23. For each position, the coefficients are displayed in increasing wavelength from left to right. Black refers to the line-core filtergram, while blue and red correspond to the red and blue line wings (see color-coding in Fig. 3.2).

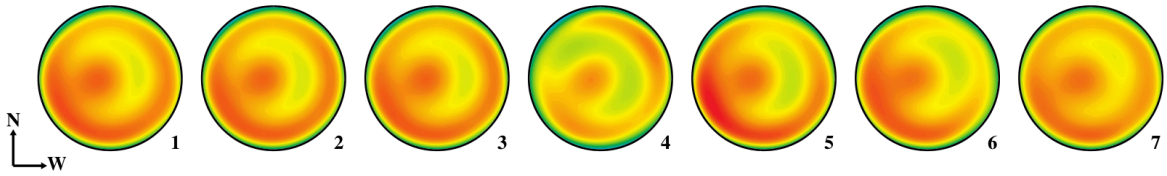

Figure 3.4: 2D reconstruction of the background based on the Zernike coefficients depicted in Fig. 3.3 for the best quiet-Sun dataset on 2018 March 23. Each filtergram is labeled #1 – 7 according to increasing wavelength. The images are scaled in the same interval [0.75, 1.07].

3.1.3 Image Quality

The best image in each dataset was identified with the Median Filter-Gradient Similarity (MFGS, Deng et al., 2015) method, which compares the magnitude gradient of the original image to that of its median-filtered counterpart. This metric is implemented in the sTools software package (Kuckein et al., 2017; Denker et al., 2018). The evolution of MFGS values with time over the course of an observing day is shown as an example in Fig. 3.2 for the dataset obtained on 2017 June 20. The best seeing conditions and thus the best images are encountered in the morning for all seven wavelength positions. The central filtergram has a maximum MFGS value of about 0.82 at 08:03:20 UT. The image is visibly sharper compared to the worst central filtergram at 12:18:20 UT with an MFGS value of only 0.76, which appears blurred and unsharp. Increasing turbulence, when the ground is heated by the Sun, and decreasing air mass are competing factors for the prevailing seeing conditions. Thus, mountain-island observatory sites such as Observatorio del Teide experience the best and most stable seeing conditions in the early morning hours. This applies to both synoptic full-disk observations with ChroTel and high-resolution observations with the VTT and the GREGOR solar telescope (Schmidt et al., 2012). Comparing MFGS values of filtergrams at different wavelength positions, the central filtergram reaches highest values (see black profile in the right panel of Fig. 3.2). The blue and red line-wing filtergrams (light blue and red profiles) exhibit the next highest MFGS values. The lowest values are encountered in the far line-wing and continuum filtergrams. The drop of MFGS values with distance from the He I line core can be explained by the diminishing fine-structure contents of the filtergrams, i.e., the MFGS method is structure dependent, which has to be considered when comparing different types of images. Nonetheless, all MFGS time profiles are tightly correlated with correlation values between 0.89 and 0.95 and display the same trend, i.e., improving seeing conditions until about 08:00 UT, followed by a decrease until 09:00 UT. This time interval clearly demonstrates the changing contributions of air mass and (ground-layer) turbulence to the prevailing seeing conditions. After 09:00 UT, larger MFGS variations on shorter time-scales are observed, which are likely linked to local seeing in the vicinity of ChroTel's roof-mounted turret.

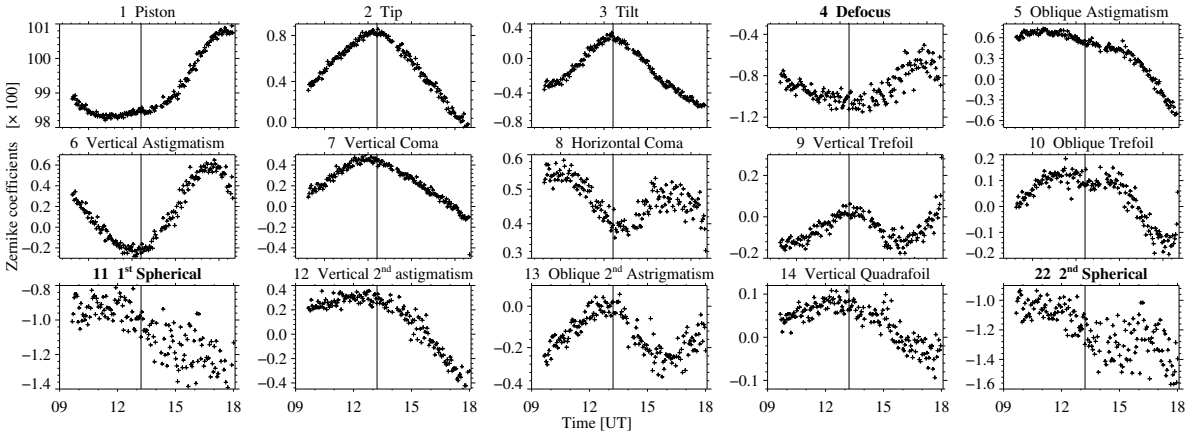

Figure 3.5: Temporal evolution of Zernike coefficients corresponding to the He I line-core filtergram. The images were taken from 09:39 UT to 17:57 UT on 2018 March 23. Noon local time at the Observatorio del Teide on Tenerife is marked with a vertical line. The title on each panel includes the Noll index j followed by the names of the corresponding optical aberrations. The radial polynomials $j = 4$, 11, and 22 are marked in bold.

3.2 Methods

3.2.1 Zernike Polynomials

The limb-darkening corrected filtergrams in Fig. 3.2 exhibit an uneven background, which is likely introduced by time-dependent filter transmission and image rotation caused by the alt-azimuthal mount of the turret system. The central part of the image is darker with a brighter ring surrounding it. The uneven background is visible in each filtergram and persists throughout the time-series but continuously changes its appearance. These intensity changes across the solar disk and from filtergram to filtergram hamper any efforts to reliably calculate Doppler velocities.

To remedy this shortcoming, we developed a calibration process for ChroTel He I filtergrams using Zernike polynomials to characterize this uneven background. Zernike polynomials are a sequence of orthogonal polynomials on the unit disk, which can be expressed in polar coordinates as a product of angular and radial functions. They are widely used to describe aberrations of optical systems. Since they are orthogonal, Zernike polynomials are often chosen as a basis to represent properties of a circular image with no redundancy. In the following, we will show that Zernike polynomials are well-suited to remove artifacts from solar full-disk images – with applications well beyond the ChroTel data at hand.

Noll (1976) modified the polynomials with a special normalization scheme and introduced a new index system. The mode-ordering number j is a function of the radial degree n and azimuthal frequency m. The filter transmission is expressed in terms of Zernike polynomials up to mode-ordering number $j = 36$, which corresponds to radial degrees $n \leq 8$ and azimuthal frequencies $|m| \leq 8$.

3.2.2 Calibration Process

Since the solar radius in ChroTel filtergrams is rescaled to 1000 pixels, we inscribe the circular Zernike polynomials in a square image with 2000×2000 pixels. Zernike polynomials are generated with routines written in the Interactive Data Language (IDL) included in the sTools software repository, which were originally developed by Denker and Tritschler (2005) for measuring the quality of Fabry-Pérot etalons. Fitting arbitrary intensity distributions across a disk, like those of ChroTel He I filtergrams, is also implemented in these IDL routines. Since the geometry of Zernike polynomials matches that of the solar disk in He I filtergrams, the pixel-to-pixel correspondence can be exploited. The intensity values of the limb-darkening-corrected filtergrams are placed in a column vector b with about 3.14×10^6 elements. Similarly, the first 36 Zernike polynomials form the 36 columns, with 3.14×10^6 elements each, of the matrix A. The intensity values in the solar disk are then fitted with a linear combination of 36 Zernike polynomials, which becomes a linear least-squares problem $A \cdot x = b$ using matrix-vector multiplication. Finally, singular value decomposition (SVD, Press et al., 2002) and back-substitution is used to obtain the 36 coefficients x of the Zernike polynomial fit. This calibration has one caveat because it applies

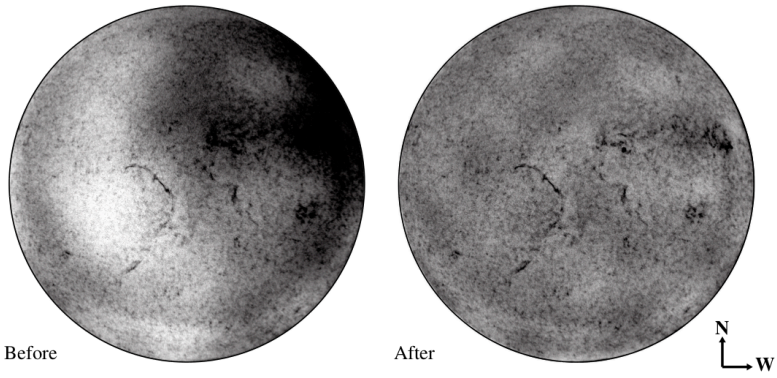

Figure 3.6: Comparison of a ChroTel filtergram before (*left*) and after (*right*) calibration using the Zernike reconstruction of the background. The He I filtergram was taken in the red line wing (#5) at 08:03:20 UT on 2017 June 20 at a time of average solar activity.

only to quiet-Sun regions, where He I absorption profiles are not present. Consequently, active regions and filaments with strong He I absorption features have to be excluded from the fitting procedure. This can be accomplished by masking these regions in He I line-core filtergrams using intensity thresholds and morphological image processing. This process is carried out in three steps. First, the background is computed, including the active regions and filaments, and removed from the line-core filtergram. Second, the corrected filtergram is used to determine the mask for active regions and filtergrams. Third, the background is computed excluding active regions and filaments. The mask determined in the second step is applied to all filtergrams at the seven wavelength positions.

To determine the optimal number of Zernike polynomials to be used in the fit, we tested the calibration method on the best quiet-Sun filtergrams which were taken at 10:09 UT on 2018 March 23. On this day, no active regions or filaments were present and thus all pixels in the solar disk were used in the fitting procedure. Figure 3.3 displays the coefficients for each Zernike polynomial for the set of seven filtergrams. The piston term $j = 1$, representing the average intensity, is not shown. The strongest modes are $j = 4$, 11, and 22. These Zernike polynomials have only a radial component. In optical terminology, $j = 4$ refers to the defocus term, $j = 11$ represents the primary and $j = 22$ the secondary spherical aberration (Noll, 1976). Most sets of the seven Zernike coefficients are similar but not identical for each Noll index j. This points to a common origin for the observed variation of the filter transmission. The variation is sufficient in magnitude to necessitate calibrating the filtergrams individually for each wavelength position. Figure 3.4 displays the 2D reconstruction of the background using the Zernike coefficients plotted in Fig. 3.3.

The Zernike reconstructions of the background identify a dark circle near the center and an asymmetrical ring-shaped structure on the disk, both of which correspond to strong radial modes. Attempts to fit more Zernike polynomials reveal higher-order radial modes, while the non-radial polynomials become increasingly smaller. These higher-order polynomials characterize small-scale structures near the edge of the disk or high-frequency radial variations. However, only broad trends across the whole disk are subject of the calibration process. Thus, the limit is appropriately set at $j = 36$, which is also supported by visual inspection of the corrected filtergrams. The orthogonality of Zernike polynomials ensures that the first 36 coefficients will not be affected if higher order terms are neglected. The Zernike fits identify different structures in each filtergram, even though similarities prevail on larger scales. Filtergram #4 refers to the core of the He I line, so that the disk has a lower average intensity than the other filtergrams. The filtergrams were taken with tunable Lyot-type filters, which means that the wavelength position of the transmission peak is shifted very rapidly by applying a variable voltage to liquid crystal retarders between the birefringent stages (Bethge, 2010). This may introduce additional changes between filtergrams, which become visible in the Zernike reconstructions of the background.

In addition, we investigated the evolution of the Zernike coefficients, again using the complete quiet-Sun dataset on 2018 March 23. Figure 3.5 shows the time-dependent variation of the first 14 Zernike coefficients, as well as the coefficients of the radial mode $j = 22$. We only display the coefficients for the time-series of the He I line-core filtergrams because they are representative for the other filter positions as well. The three radial modes $j = 4$, 11, and 22 show a large scatter, while the non-radial coefficients exhibit a clear trend as the day progressed. The piston term $j = 1$ characterizes the average intensity of the solar disk, which is close to unity after limb-darkening correction. Most coefficients, e.g. $j = 2$,

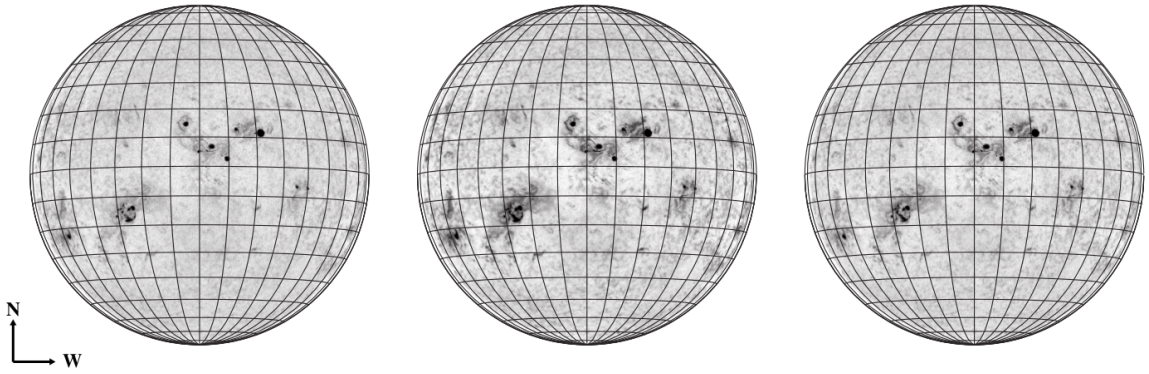

Figure 3.7: Calibrated ChroTel He I filtergrams taken on 2014 May 12: blue line-wing #3, line-core #4, and red line-wing #5 filtergram (*from left to right*), respectively. The image intensity was scaled in the interval [0.86, 1.03] and a Stonyhurst grid was superposed on the solar disk.

3, and 7, peak at local noon. This suggests that either changes in the light level or elevation of the Sun are responsible for the observed time dependence. ChroTel has an alt-azimuth mount that introduces image rotation, which is however corrected as part of the data reduction. The Lyot filter is mounted in the collimated beam, which results in a stationary pupil. More importantly, the two mirrors of the turret introduce linear polarization, which changes over the day. This influences strongly the transmission of the Lyot filter. A time-lapse movie covering the whole observing period reveals that the central dark spot (Fig. 3.2) moves across the solar disk. The temporal evolution of the coefficients quantitatively describes how transmission artifacts evolve over time. In principle, the time dependence of the Zernike coefficients can be modeled since the shape of the profiles are rather simple. However, analyzing a large sample of daily He I time-series is beyond the scope of this study. Applying the corrections to a single filtergram takes only about 180 s on a modern desktop computer so that processing time-series data is feasible.

To validate the background calibration procedure employing Zernike polynomials, we evaluate the statistical moments of the intensity distributions on the solar disk. Since strong He I absorption features are absent in quiet-Sun filtergrams, the intensity values are expected to have a symmetrical distribution. Skewness, i.e., a measure of the asymmetry of the intensity distribution, is mainly introduced by variations in filter transmission. We compare the skewness of the best quiet-Sun filtergrams from 2018 March 23 before and after calibration. The calibration reduces the skewness in most filtergrams. Relevant for determining Doppler velocities (see Section 3.2.3) are the blue and red line-wing filtergrams, where the skewness is reduced from $+0.17$ to $+0.12$ and from -0.10 to -0.02, respectively. The variance of the intensity distribution is also reduced for all seven filtergrams. The average variance is 2.1×10^{-4} before and 0.67×10^{-4} after calibration. The intensity distributions of the calibrated filtergrams are visually more symmetrical and the tails of the distribution are more confined. This raises our confidence that large-scale variations introduced by the filter transmission were significantly reduced in the filtergrams, resulting in a flat background across the solar disk.

Displaying the calibrated quiet-Sun filtergrams is not very instructive because they are void of any significant absorption structures such as active regions and filaments. Therefore, the best He I red line-wing filtergram on 2017 June 20 was chosen for the direct comparison. Figure 3.6 clearly demonstrates the improvements after limb-darkening correction and calibration of the background. The intensity was clipped tightly to display the background variations more prominently. The calibration process removed the gradient towards the upper left corner of the image and results in an image with even background. The slightly brighter areas in the center of the solar disk surrounding the active regions are real and were observed in Hα line-wing filtergrams as well (Marquette and Denker, 1999). Finally, the calibrated filtergrams #3 – 5 on 2014 May 12 in Fig. 3.7 are displayed in a broader intensity range to bring forth details within the active regions. Properly calibrated line-wing and line-core filtergrams are the basis for the derivation of Doppler velocities in the following section.

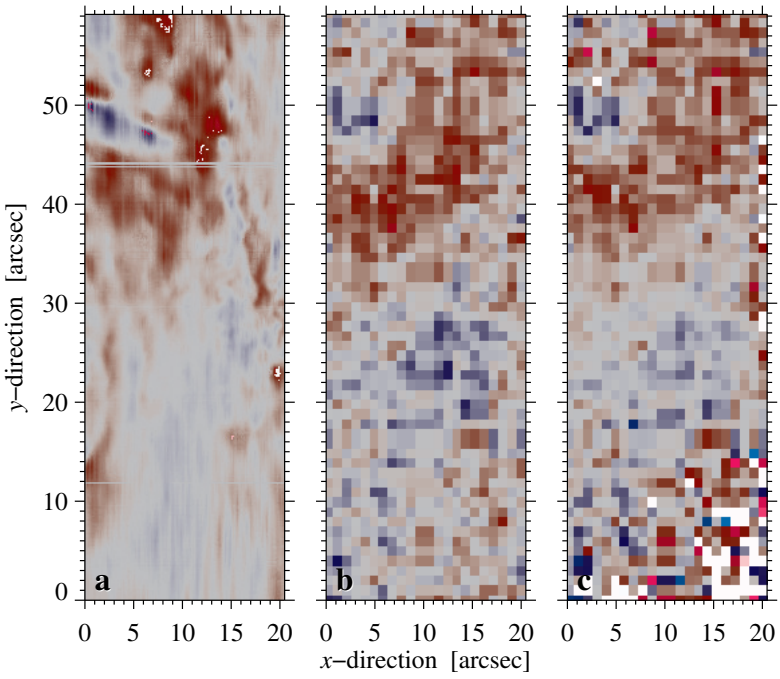

Figure 3.8: Doppler velocity maps obtained with (a) GRIS and ChroTel, which were derived with (b) the difference method and (c) a parabolic fit to the central three filtergrams. The difference map is scaled between ±0.1 in terms of the normalized quiet-Sun intensity, whereas the other two maps are scaled between ±20 km s^{-1}. The ChroTel maps appear pixelated due to the considerable difference in image scale.

3.2.3 Doppler Velocity

Bethge et al. (2011) produced Doppler maps from ChroTel filtergrams using a center-of-gravity (COG) method to identify the line center. Their COG formula contains arbitrary coefficients to account for filter transmission, blending of different components of the He I line, and other factors that affect real data. These coefficients are optimized for each dataset by comparing ChroTel Doppler maps to co-spatial, high-resolution observations of the TIP-II instrument at the VTT. They concluded that for velocities up to about 20 km s^{-1} the inner three filtergrams are sufficient, but the coefficients are not universally applicable. New datasets may require re-calibration with near-infrared spectrographic scans. Because of the scarcity of near-infrared spectrographic data, the synoptic observations from ChroTel cannot be fully exploited. Furthermore, the time dependence of the Zernike coefficients (see Section 3.2.2 and Fig. 3.5) implies that such a cross-calibration is only valid for a short period of time (tens of minutes).

The calibration of the He I filtergrams with the help of Zernike polynomials allows us to test two methods to derive Doppler velocities. The first method is a simple difference map, where the red line-wing filtergram is subtracted from the blue line-wing filtergram. The second method is a parabolic fit to the "line profile" of the inner three filtergrams. The reference Doppler velocities are obtained with GRIS from a high-resolution spectrograph scan taken on 2017 June 20 between 08:33 UT and 09:00 UT. The scan covers parts of active region NOAA 12663 near the west limb. The Doppler shift map from GRIS is compiled by fitting the He I line core in each pixel with a parabola and determining its minimum position. The corresponding Doppler velocity map is shown in Fig. 3.8a, scaled between ±20 km s^{-1}.

Multiple ChroTel filtergrams were taken during the scanning period of GRIS, and we chose the filtergram with the best seeing conditions at 08:33 UT for comparison. The GRIS scanning time is around half an hour, shorter than the time scale of the temporal evolution of the Zernike coefficients of about 2–3 hours. The region scanned with GRIS is extracted from the ChroTel filtergrams and carefully aligned to the GRIS map. In addition to the continuum image, the Doppler maps from ChroTel and GRIS are also aligned with respect to each other. Figure 3.8 compares the GRIS Doppler map to ChroTel velocities determined with the two different methods.

After the calibration, the quiet-Sun intensity in areas with no He I absorption is close to unity. The intensity difference between the blue line-wing filtergram #3 and the red line-wing filtergram #5 is directly related to the line shift because of the normalization across the filtergrams. This normalized intensity difference $\delta I = I_r - I_b$ is proportional to the Doppler velocity $v' = C \cdot \delta I$, which is similar as described in the method of Padinhatteeri, Sridharan, and Sankarasubramanian (2010). The factor C will be derived from the comparison with the GRIS Doppler velocities and can then be extended to the full-disk dataset.

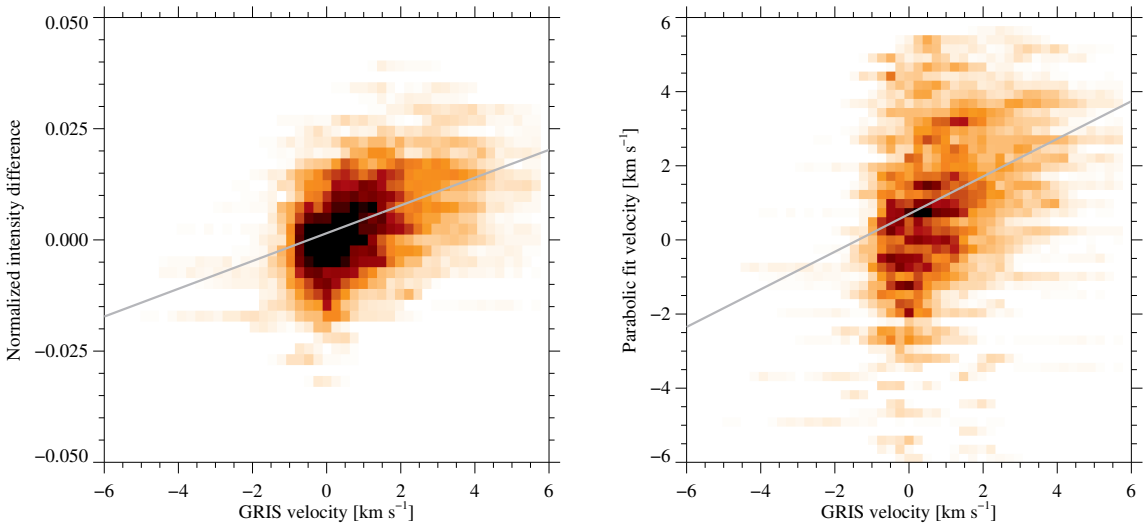

Figure 3.9: (*left*) Reference velocity (GRIS) vs. velocity analogue v' (ChroTel). The light grey line depicts a linear regression with a slope of $m = 0.0031$ s km^{-1} and a vertical intercept of 0.0015. The background image is a color-coded 2D histogram. (*right*) Reference velocity (GRIS) vs. velocity derived with a parabolic fit (ChroTel) in the velocity range of ± 6 km s^{-1}. The light grey line depicts a linear regression with a slope of 0.51 and a vertical intercept of 0.70 km s^{-1}. The background image is a color-coded 2D histogram.

The Dopplergrams from the Michalson Doppler Imager (MDI, Scherrer et al., 1995) on board the Solar and Heliospheric Observatory (SoHO, Domingo, Fleck, and Poland, 1995) are produced similarly with a modified difference method using four filtergrams in the wing.

Since the intensity difference is a proxy for line shift, the resulting velocities should be proportional to the reference LOS velocity. This difference map is presented in Fig. 3.8b, scaled between ± 0.1. This normalized intensity difference has the advantage that it is defined across the entire solar disk. In regions without He I absorption, the intensity of both line-wing filtergrams is normalized to unity, and any background artifacts have been removed by the Zernike fitting. Thus, the difference is close to zero as is the Doppler velocity. This is confirmed in the full-disk difference map in Fig. 3.10. On the other hand, the line shift in regions with He I absorption is due to both differential rotation and the local plasma motion.

For regions with He I absorption, the contribution from differential rotation results in a broad trend across the solar disk. The Zernike polynomials can identify and remove this from the final calibrated filtergram. The caveat is that large active regions with strong absorption are excluded from the Zernike polynomial fit. In addition, co-temporal GRIS scans cover an area too small to determine differential rotation effects. We need to compare the obtained Doppler velocities to other full-disk He I Doppler maps in order to identify whether differential rotation has been removed.

For the second method, the intensity trace of the inner three filtergrams can be treated as a low-resolution line profile for each pixel location. For pixels with He I absorption as determined from the line-core filtergram, a parabolic fit allows us to compute more accurately the line center and thus the Doppler velocity. We have to exclude some pixels with a negative coefficient for the quadratic term, i.e., where the vertex of the parabola is on the top. The resulting map is shown in Fig. 3.8c, where the excluded pixels are displayed in white. The map is scaled between ± 20 km s^{-1}.

The reference map obtained with GRIS is dominated by stronger red-shifted profiles, representing down-streaming flows in the upper part of the Doppler map (Fig. 3.8a). In the lower part, weaker blue-shifted profiles are encountered, which represent up-streaming flows. The spatial resolution of GRIS is $0.13''$ pixel^{-1}, i.e., roughly ten times better than the ChroTel resolution. As expected from the low spatial and spectral resolution, the ChroTel maps lack fine structure compared to the GRIS map and thus appear pixelated in a direct comparison. More importantly, for each ChroTel velocity value, about 100 GRIS measurements are available, representing different physical conditions in the chromosphere. In consequence, a very tight correlation of the ChroTel and GRIS velocity measurements is not expected. However, the overall structure is recovered in the ChroTel maps, especially in regions with large velocities.

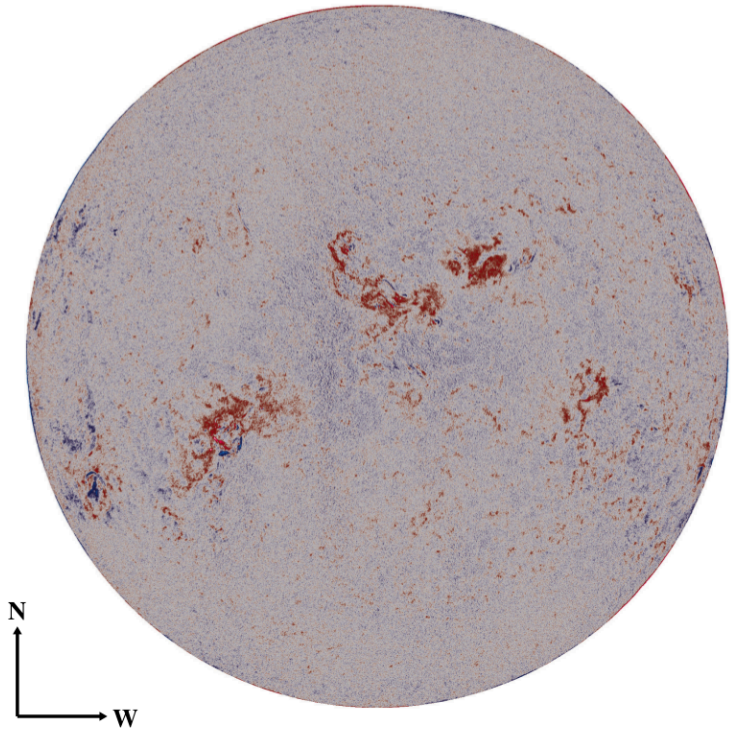

Figure 3.10: ChroTel full-disk difference maps (red minus blue line-wing filtergram) for the best He I dataset on 2014 May 12. The effects of solar differential rotation were removed in the Zernike fitting process. The normalized intensity difference was multiplied by the factor $C = 320\,\mathrm{km\ s^{-1}}$.The images are scaled between $\pm 35\,\mathrm{km\,s^{-1}}$. The median velocities is about $\pm 1.6\,\mathrm{km\,s^{-1}}$ and the velocity outside the active regions is between $\pm 15\,\mathrm{km\,s^{-1}}$.

Furthermore, the two ChroTel Doppler maps in Fig. 3.8 are very similar. Next, we will analyze scatter plots of GRIS and ChroTel Doppler velocities for both methods to validate the velocity values in the ChroTel maps.

Figure 3.9 (left panel) shows the velocities from the difference map plotted against the reference velocities from the GRIS Doppler map. In the original calibration runs, Bethge et al. (2011) found that reconstructed velocities fall into two regimes: $-5 < v < 5$ km s^{-1} and $|v| \geq 5$ km s^{-1}. In our analysis, we find that a similar separation occurs at 6 km s^{-1}. Thus, the following scatter plots will focus on the velocity regime $-6 < v < 6$ km s^{-1}. From the best linear fit, overplotted in gray, we obtain a slope of m = 0.0031 s km^{-1} and a vertical intercept of 0.0015. The factor C determines to $C = 1/m = 320$ km s^{-1}, which is used to calculate Doppler velocities from the difference map. Linear fits to smaller velocity intervals show the same slope, which indicates that a linear model is appropriate for this relationship. Pearson's linear correlation coefficient between the reconstructed and reference velocities in this regime is $\rho = 0.48$. In comparison, Bethge et al. (2011) found a correlation coefficient of $\rho = 0.45$ using the central three filters in the $-5 < v < 5$ km s^{-1} regime. Thus, a simple difference map with the Zernike-calibrated filtergrams yields comparable results, without resorting to external calibration.

Figure 3.9 (right panel) shows the reconstructed velocity from the parabolic fit vs. the GRIS velocity in the $-6 < v < 6$ km s^{-1} regime, and the linear fit with a slope of 0.51. The vertical intercept of 0.70 reflects a difference in the rest wavelength. As seen in the scatter plot, the parabolic fit velocities show a larger scatter around the linear trend line, and the correlation coefficient is only $\rho = 0.27$. In both scatter plots, the horizontal striation is a result of enlarging ChroTel data to match the resolution of GRIS. Each pixel in ChroTel data covers many pixels in GRIS data and consequently a range of GRIS velocities. As a sanity check, we computed the linear correlation between the two types of ChroTel Doppler velocities. The high correlation of $\rho = 0.77$ suggests that these two methods deliver consistent results. Finally, a full-disk Doppler map is displayed in Fig. 3.10 as an example, which corresponds to the best set of filtergrams on 2014 May 12.

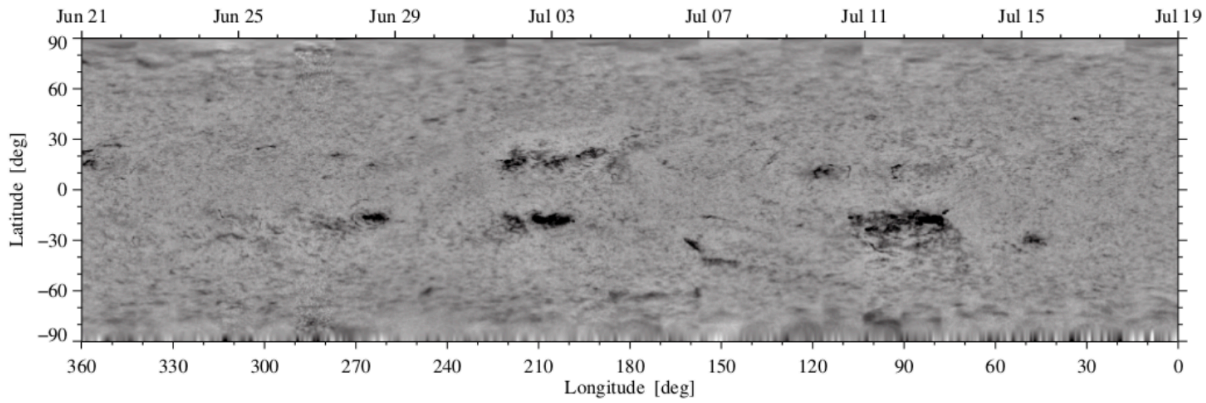

Figure 3.11: Carrington map (rotation No. 2125) derived from calibrated ChroTel He I line-core images covering the time period from 2012 June 21 to end of July 18. The Carrington map comprises one calibrated full-disk image per day, which was derotated to the respective Carrington latitude with a sampling of 0.1°.

3.3 Discussion and Conclusions

The difference method is more suitable for producing full-disk maps than the parabolic fit method. In regions with low or no He I absorption, spectral line fitting is not an option. In our sample datasets, the parabolic fit is only possible in regions with strong He I absorption, i.e., active regions and filaments. Thus, full-disk Doppler maps are produced with the difference method. We present the parabolic fits for active-region data mainly as a cross check for the consistency of the results. Compared to the COG method provided in the original work of Bethge et al. (2011), the difference map from Zernike-calibrated filtergrams does not require each time an external calibration with a co-temporal spectrograph scan.

Re-calibrating the entire ChroTel archive requires considerable computational resources. In the Zernike calibration procedure, the most computationally intensive part is performing a singular value decomposition on each image. Therefore, modeling the long-term temporal evolution of the Zernike coefficients could minimize computation time. It is possible to avoid repeated fitting procedures if the daily and annual variations of the coeffients can be modeled.

With this new method, ChroTel dopplergrams will no longer be limited by the availability of high-resolution spectrographic data to calibrate the data. Using this method, we are able to produce synoptic maps with ChroTel He I filtergrams as shown in Fig. 3.11. It uniformly re-normalizes all filtergrams across different days. Synoptic ChroTel data allows studies of solar cycle variations and for solar activity monitoring. Solar features can be identified with digital image processing in ChroTel filtergrams. The same method can be employed to reduce the Hα and Ca II K data from ChroTel. In addition, the high-resolution observations of GRIS and other high-resolution spectrographs can be embedded in the large-scale context with full-disk He I filtergrams and Doppler maps. The ChroTel data complements SDO data with data in three chromospheric wavelength.

The calibration method developed in this paper can potentially be applied to other full-disk images. As an example, images from the the Narrowband Filter Imager (NFI) on board the Hinode Solar Optical Telescope (Tsuneta et al., 2008) contain artifacts which are caused by air bubbles in the fluid inside the tunable filter. They distort and move when the filter is tuned, and then usually drift toward the edges of the field of view over time (Tsuneta et al., 2008). Zernike polynomials may be appropriate to model these image artifacts and remove them. Similarly, the Zernike method can be used to characterize background trends and optical artifacts in other solar full-disk images.

Chapter 4

Chromospheric Synoptic Maps of Polar Crown Filaments

Polar crown filaments (PCFs) form at the intersection of old flux from the previous cycle in the polar region and new flux of the present cycle, which is transported out of the activity belts toward the Poles. The flux of opposite polarity builds a neutral line above which a filament channel can form (Martin, 1998; Mackay et al., 2010). The PCFs appear inside the filament channel. They are usually long-lived structures and can last over several days up to weeks. The PCFs appear shortly after the magnetic-flux reversal around the maximum of the solar cycle at mid-latitudes. During the course of the solar cycle, PCFs form closer to the Pole as the neutral line shifts closer to the Pole. Around the time of magnetic polarity reversal, PCFs disappear from the solar surface (Leroy, Bommier, and Sahal-Brechot, 1983, 1984). This cyclic behavior has been known since the beginning of the 20th century (Cliver, 2014). However, studies covering the current cycle are still rare (Xu et al., 2018). This propagation toward the Pole throughout the cycle is known as the "dash-to-the-Pole" (Evershed and Evershed, 1917; Cliver, 2014).

The PCFs belong to the category of quiet-Sun filaments, which appear outside of the activity belts. Another class of filaments are active-region filaments, which reside in the vicinity of active regions. Filaments that cannot be assigned to either active-region or quiet-Sun filaments are called intermediate filaments (Martin, 1998).

To study the cyclic behavior of PCFs, a more global view of the Sun is needed for which regular long-term observations of the solar chromosphere are necessary. From these observations, synoptic maps can be produced, which allow us to study large-scale patterns over a longer periods of time. Carrington (1858) first created synoptic maps of sunspot observations from which a cyclic behavior could be determined, *i.e.* most prominently Spörer's Law (Cameron, Dikpati, and Brandenburg, 2017). The variety of synoptic maps nowadays increased in the last 150 years, and many more physical parameters are available to be studied. One well-known example of synoptic maps is the hand-drawn McIntosh maps (McIntosh, 2005; Gibson et al., 2017), which allow us to determine a relation between open magnetic structures (coronal holes) and closed magnetic structures (filaments or active regions). Another example are long-term studies of filaments with full-disk images from the *Kodaikanal Observatory* (KO) of the Indian Institute of Astrophysics (IAA) from 1914 – 2007 (Chatterjee et al., 2017). The work of Hao et al. (2015) shows a detailed study of filaments and their statistical properties for the years 1988 – 2013 for Hα observations of the *Big Bear Solar Observatory* (BBSO) in California. Finally, Xu et al. (2018) extracted the positions of PCFs for four cycles (1973 – 2018) from Hα observations at BBSO and at the *Kanzelhöhe Solar Observatory* (KSO) in Austria, which are directly relevant to the present work.

Morphological image processing is a powerful tool for automatically analyzing images and is widely used in solar physics. Robbrecht and Berghmans (2004) carried out a study on the automatic recognition of coronal mass ejections (CME) by using the Hough transform (Gonzalez and Woods, 2002), and in addition, they used morphological closing to separate different CMEs. Another application is soft morphological filters to reduce noise in images as presented by Marshall, Fletcher, and Hough (2006) for the reduction of cosmic-ray induced noise in images of the *Large Angle Spectroscopic Coronagraph* (LASCO: Brueckner et al., 1995). Morphological image processing using the blob analysis (Fanning, 2011), to select connected regions in an image, enabled for example a statistical analysis of pores (Verma and Denker, 2014) and

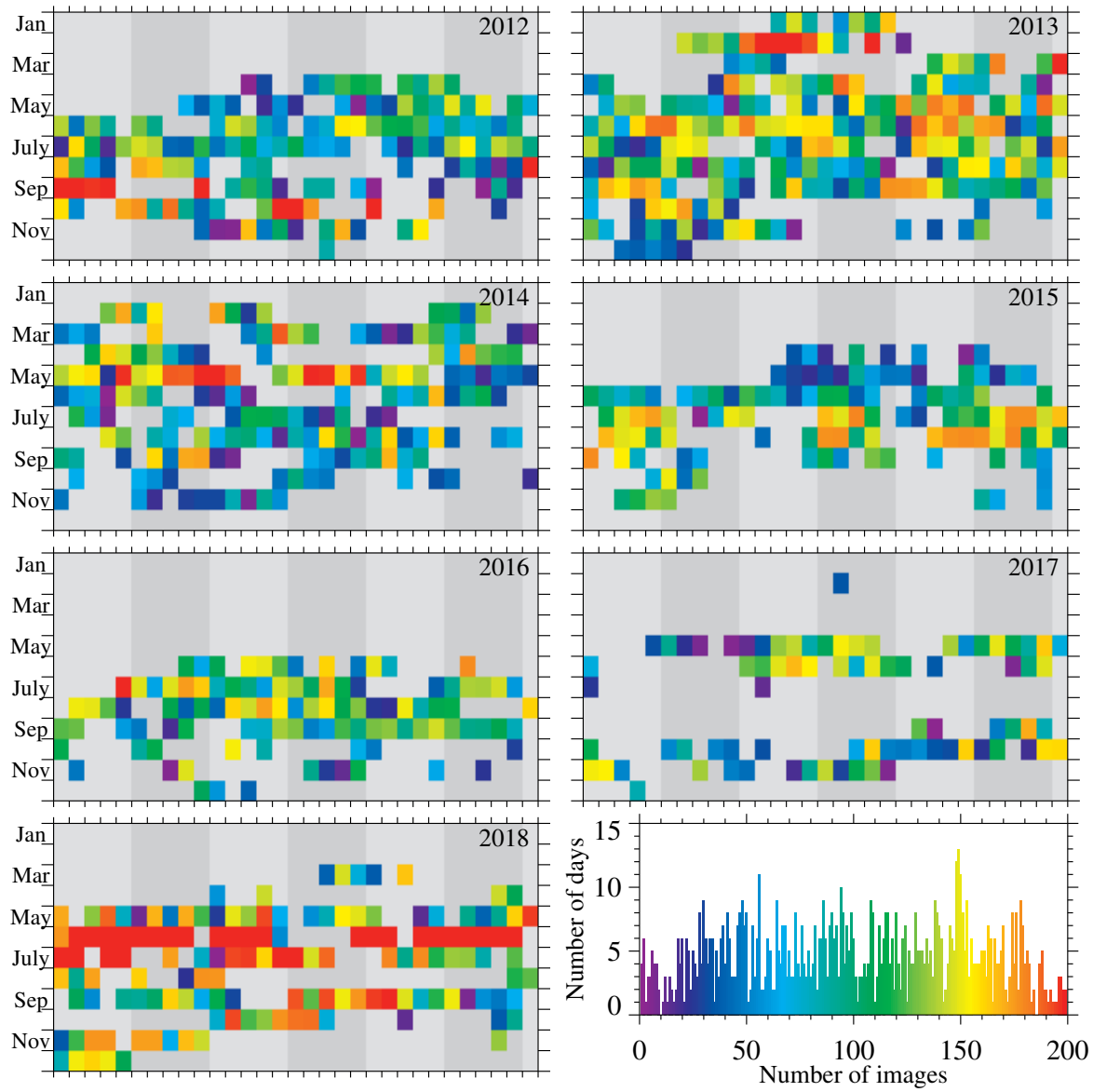

Figure 4.1: Overview of all data between 2012 and 2018. The number of images per day is color-coded. The *gray-shaded areas* indicate a time interval of five days during a given month. The *histogram in the lower right corner* indicates the number of images for all days between 1 – 199 images per day. More than 200 images per day were recorded on 46 days, which are indicated in *red*.

of historical sunspot drawings of the years 1861–1894 from Spörer (Diercke, Arlt, and Denker, 2015). Qu et al. (2005) used morphological image processing for automatic threshold extraction to select dark objects in Hα line-core images based on a Support Vector Machine (SVM: Cortes and Vapnik, 1995) to identify the spines and footpoints of filaments and to recognize the disappearance of filaments.

In Section 4.1, we give an overview of the database of the *Chromospheric Telescope* (ChroTel: Kentischer et al., 2008; Bethge et al., 2011), and we present synoptic maps of three different chromospheric spectral lines, which will be used to study the poleward migration of high-latitude filaments during Solar Cycle 24, as well as the He I λ10830 Å Doppler velocity. We introduce the data handling and a reduction method for the ChroTel data, as well as a method to extract filaments from the synoptic maps based on morphological image processing (Section 4.2). Basic physical parameters, *i.e.* area, tilt angle, and location on the disk, are extracted automatically with morphological image processing tools (Section 4.3). We separated the high-latitude filaments into different categories, *i.e.* quiet-Sun filaments and PCFs, where we study their different appearances and compare their intensity variations in Hα λ6563 Å and He I λ10830 Å. The categorization of different objects on the Sun will be discussed in the context of future labeling approaches with neural networks (Goodfellow, Bengio, and Courville, 2016).

Table 4.1: Summary of ChroTel observations in different spectral lines between 2012 and 2018

Spectral line	Days of observations	Number of images
Hα	974	111,633
He I	916	94,670
Ca II K	899	90,353

4.1 Observations

ChroTel is mounted two levels above ground on a projecting roof of the *Vacuum Tower Telescope* (VTT: von der Lühe, 1998) at the *Observatorio del Teide* on Tenerife, Spain. It is a ten-cm aperture full-disk telescope operating automatically since 2011. It records chromospheric images with 2048 $\times$ 2048 pixels using three Lyot-type birefringent narrow-band filters in Hα λ6562.8 Å with a FWHM of 0.5 Å, Ca II K at λ3933.7 Å with a FWHM of 0.3 Å, and He I λ10830 Å with a FWHM of 0.14 Å. In the He I line, the instrument scans seven non-equidistant filter positions within $\pm$3 Å around the line core of the red component, whereby liquid-crystal variable retarders allow a rapid adjustment of the seven wavelength points (Bethge et al., 2011). The quantum efficiency is highest for Hα at 63 % and reduces for Ca II K to 39 % and for He I to 2 % (Bethge et al., 2011). The exposure time in Hα is 100 ms. Because of the low quantum efficiency of the other two channels, the exposure time was selected to be higher with 300 ms for each filter position around the He I line and 1000 ms for Ca II K.

ChroTel contributes to a variety of scientific topics (Kentischer et al., 2008; Bethge et al., 2011), *e.g.* statistical studies of filament properties, supersonic downflows, and chromospheric sources of the fast solar wind, among others. For the last two topics, the calculation of Doppler velocities from the spectroscopic He I data is required. In addition, ChroTel full-disk images monitor large-scale structures and give an overview of chromospheric structures in the vicinity of solar eruptive events. The cadence between images of the same filter is three minutes in the standard observing mode. Higher cadences of up to ten seconds for Hα and Ca II K and 30 seconds for He I are possible with single-channel observations (Bethge et al., 2011).

Between 2012 and 2018, ChroTel took Hα data of the Sun on 974 days. For each day, we downloaded all recorded images but kept only the best image of the day. The images were selected by calculating the Median Filter-Gradient Similarity (MFGS: Deng et al., 2015; Denker et al., 2018), which computes the similarity of the gradients of the original images and those of median-filtered images. Along with the Hα images, we downloaded the images closest in time for Ca II K and He I. There are some days when ChroTel observations covered only Hα but with a higher cadence of one minute.

The total amount of data in the ChroTel archive is visualized in Figure 4.1. We display in rainbow colors the number of images in Hα for each day in the year. Usually, observations commence in April and last until November. In some years, the observations started already in January and continued until December. In 2017, less data were taken because of technical problems. The regular automatic observations started again in mid-2018. In that year, some days contained observations with more than 200 images, which implies time-series of more then ten hours. The ChroTel archive is hosted by the Leibniz Institute for Solar Physics (KIS) in Freiburg, Germany (ftp://archive.leibniz-kis.de/archive/chrotel). Table 4.1 gives an overview of the total number of images in the ChroTel archive for each spectral line.

4.2 Methods

Level 1.0 data, which are available in the ChroTel archive, went through the standard dark- and flat-field correction and were converted to the format of the Flexible Image Transport System (FITS: Wells, Greisen, and Harten, 1981; Hanisch et al., 2001). In preprocessing, we rotated and rescaled the images, so that the radius corresponds to $r = 1000$ pixels, which yields an image scale of about $0.96''$ pixel^{-1}. A constant radius rather than a constant image scale makes it easier to construct synoptic maps in an automated way. The images were corrected for hot pixels by removing these strong intensity spikes from the image by replacing them with the local median value using routines from the sTools library (Kuckein et al., 2017). We noticed that in images that were recorded early in the morning and late in the afternoon, the

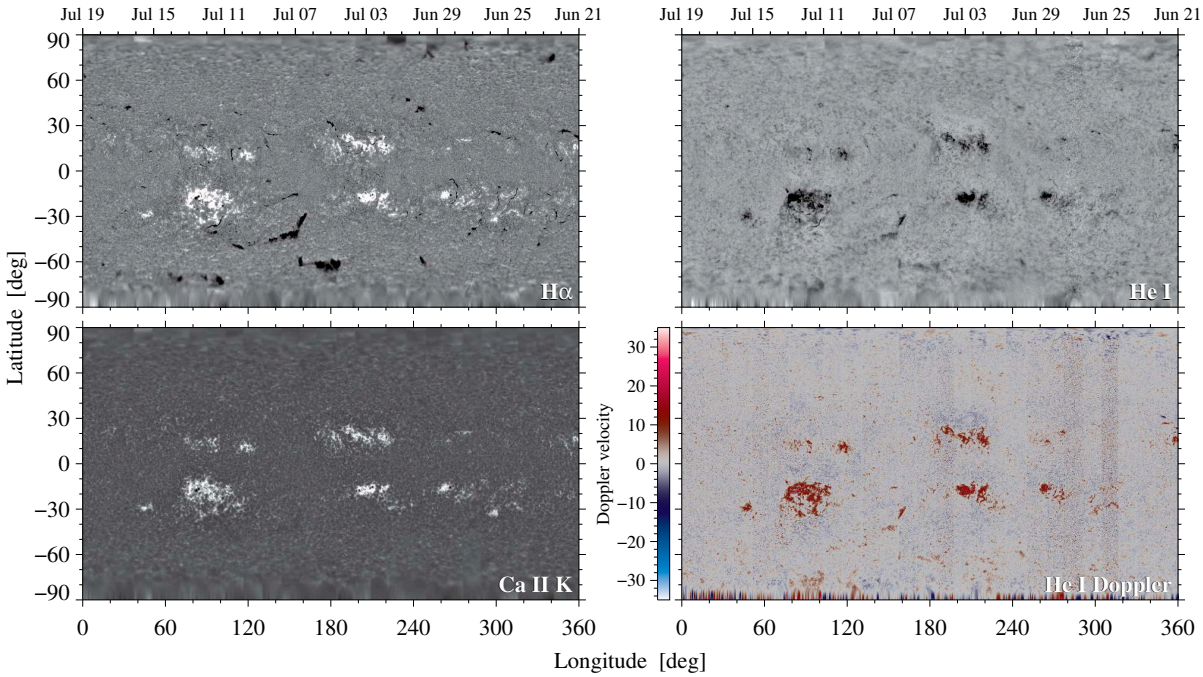

Figure 4.2: Synoptic line-core intensity maps of the strong chromospheric absorption lines Hα λ6563 Å, Ca II K λ3933 Å, and He I λ10830 Å including a He I Doppler map (*top-left to bottom-right*), which cover Carrington rotation No. 2125 from 21 June to 19 July 2012. The Doppler velocities were derived with the method explained by Shen, Diercke, and Denker (2018) and were scaled between $\pm$35 km s^{-1}, where red and blue indicate down- and upflows, respectively.

solar disk appeared deformed and had the form of an ellipse. This is caused by differential refraction because of significantly varying air mass across the solar disk. Thus, we fitted an ellipse to the solar disk and stretched the solar disk to the theoretical value of the solar radius recorded in the FITS header. For the Ca II K images, we observed that the solar disk was not centered in the images such that in these images a geometrical distortion is visible at the limb. Furthermore, all images were corrected for limb-darkening by fitting a fourth-order polynomial to the intensity profile. In a second step, bright areas and dark sunspots were excluded from the intensity profile and the polynomial fit was repeated (*e.g.* Diercke et al., 2018; Denker et al., 1999). The images were corrected by dividing the images with the resulting center-to-limb-variation profile. Because of intensity variations introduced by non-uniform filter transmission, we corrected all images with a recently developed method by Shen, Diercke, and Denker (2018) using Zernike polynomials to yield an even background by dividing the images by their intensity-variation profile. First, we created a mask, where we excluded bright and dark areas. The resulting intensity profile was fitted with a linear combination of 36 Zernike polynomials. The resulting linear least-square problem was solved with singular value decomposition. From the back-substitution, we obtained 36 coefficients for Zernike polynomials.

To create the Carrington maps, one image per day was rotated to the corresponding longitudinal positions on a Carrington grid using the mapping routines of SolarSoftWare (SSW: Freeland and Handy, 1998; Bentely and Freeland, 1998) for differential rotation correction. These image slices were merged creating a Carrington map for each solar rotation with a longitudinal sampling of 0.1°. The image slices of one day were overlapping with the previous and following day by two hours. If an image of the previous or following day were missing, the input image was rotated that it covered in total 48 hours of solar rotation. Longer gaps were not covered with data and were left blank. Finally, the grid was transferred to heliographic coordinates and converted to an equidistant grid, which caused noticeable stretching at the polar regions. The process was repeated for all three chromospheric lines (Figure 4.2). In the case of the He I filtergrams, we created a synoptic map individually for each filtergram. As a result, we can produce synoptic Doppler maps (Figure 4.2d) by subtracting the two line-wing filtergrams as described by Shen, Diercke, and Denker (2018). In the Hα data (Figure 4.2a), we clearly recognize the filaments as elongated black structures, whereby the active-region plage areas appear bright. The sample map of Carrington rotation 2125 also contains PCFs (Figure 4.2). In the He I data, active regions and filaments

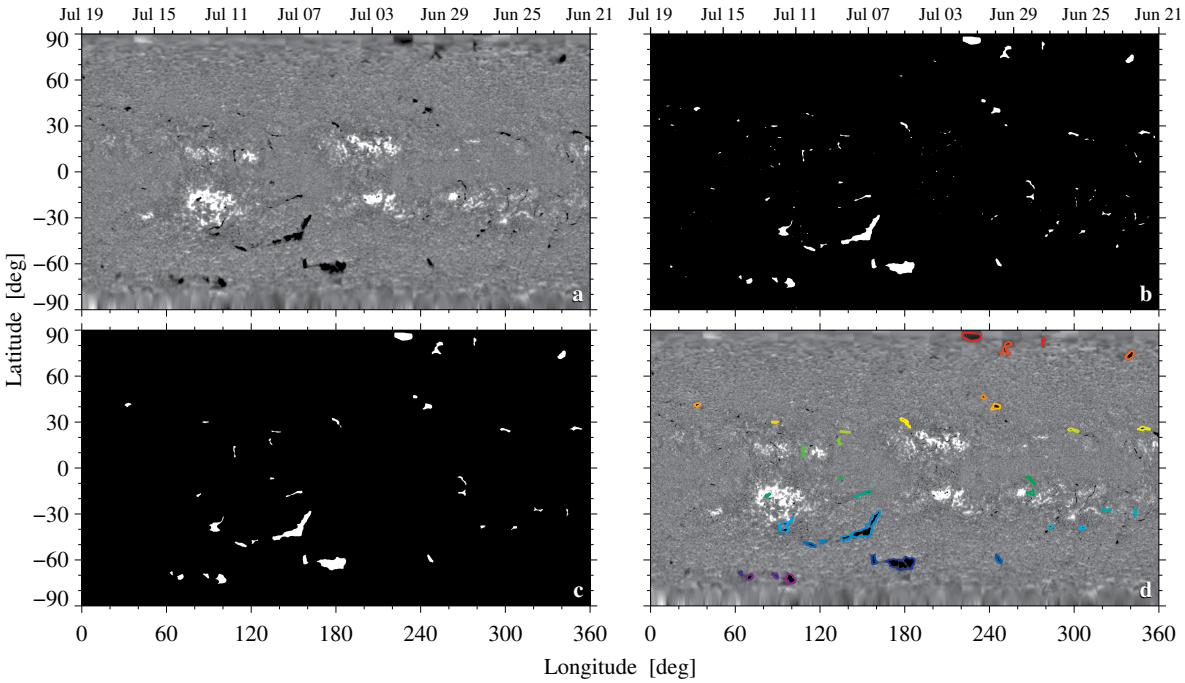

Figure 4.3: Morphological filament extraction from an Hα synoptic map. **(a)** Hα synoptic map after application of the Perona–Malik-filter. **(b)** Mask of dark structures after morphological closing. **(c)** Mask after removal of small dark regions. **(d)** Resulting map with color-coded contours of extracted filaments, indicating the different detected objects.

appear dark. The chromospheric emission of the Ca II K line is greatly enhanced in locations, where the magnetic field is strong, *i.e*, in plage regions and the chromospheric network. The filaments are, however, not recognizable in the line core of the Ca II K line. In the Doppler maps, plage regions exhibit downflows, whereas regions with stronger upflows are located in the surroundings.

The synoptic ChroTel maps contain, among others, information about the number, area, location, and orientation of filaments. We apply basic morphological image processing tools to Hα maps, which will be outlined in the following, to extract this information for further analysis. Figure 4.3 shows as an example the procedure for Carrington rotation 2125, which was used to extract the filaments. The background of the images was perfectly flat because the non-uniform background was removed by dividing individual full-disk images with the intensity variation expressed by Zernike polynomials. The images were normalized with respect to the quiet-Sun intensity. We used the Perona–Malik filter (Perona and Malik, 1990), an anisotropic diffusion algorithm, to smooth structures while preserving the borders of elongated dark structures such as filaments (Figure 4.3a). The filter was used with the gradient-modulus threshold controlling the diffusion $\kappa = 30$ and with 15 iterations in the exponential implementation, which favors high-contrast over low-contrast structures. Thus, we used a global threshold to extract dark structures, which was selected by visual inspection. The thresholds were 0.3 and 0.9 times the average quiet-Sun intensity. In addition, we applied morphological closing with a circular kernel with a diameter of 56 pixels to close small gaps between connected structures (Figure 4.3b). We used a blob analyzing algorithm (Fanning, 2011), which selects connected regions called "blobs" in the image based on the four-adjacency criterion, and applied it to a binary mask containing pixels belonging to dark structures. Because we only want to analyze large-scale PCFs and quiet-Sun filaments, dark structures with a size of 500 pixels or smaller, which include sunspots and small-scale active region filaments, were excluded from further analysis (Figure 4.3c). The remaining structures are shown in Figure 4.3d.

Several properties follow from the blob analysis such as the location of the detected filaments and their area in pixels. Other properties of filaments can be determined from fitting an ellipse to the structure, such as the tilt-angle, as well as semi-major and semi-minor axis, which gives a first approximation of the length and width of the filament. The location of filaments enables us to study the cyclic behavior of PCFs.

We focus in the following analysis on PCFs and other high-latitude filaments. We categorize PCFs as high-latitude filaments if their center-of-gravity is located at latitudes above/below $+50°/-50°$, as in

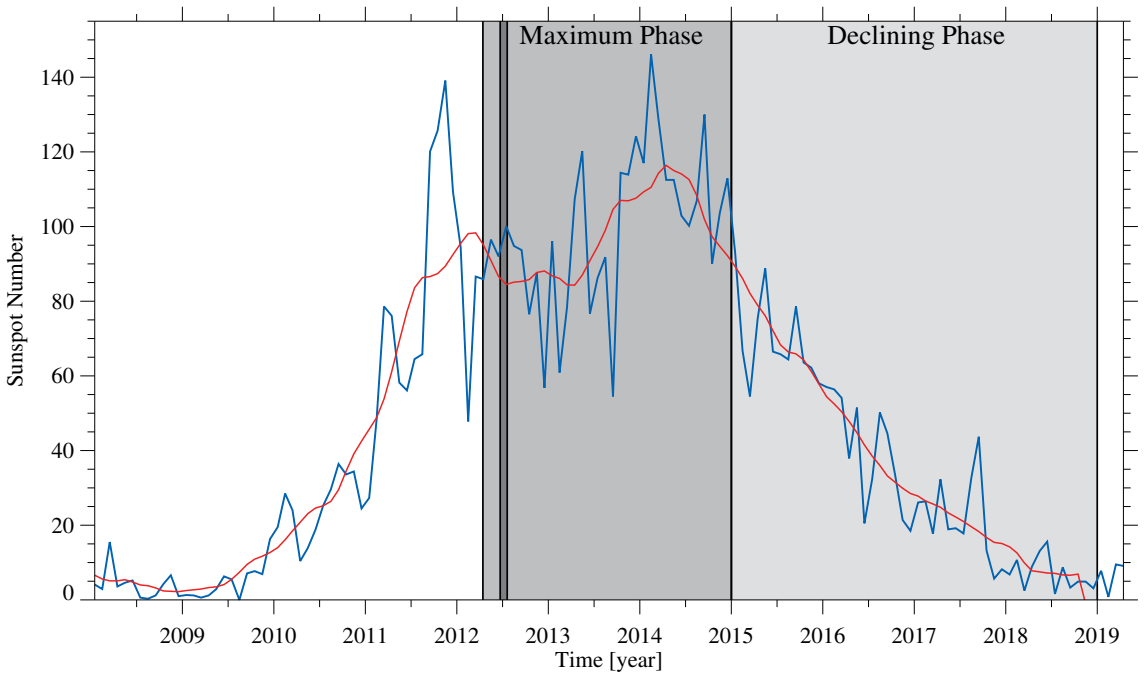

Figure 4.4: Monthly mean total sunspot number (*blue*) and 13-month smoothed monthly total sunspot number (*red*) for Solar Cycle 24 (SILSO World Data Center, 2008 – 2019). The *gray areas* indicate the two observing periods in which the ChroTel data were divided. The maximum phase starts on 13 April 2012 and lasts until the end of 2014. The declining phase covers the years 2015 – 2018. The *small dark gray region* indicates Carrington rotation 2125, which is displayed in Figure 4.2.

the work of Hao et al. (2015). Because of strong geometric distortions in synoptic maps near the Poles, structures above/below $+85°/-85°$ are excluded. Additional quiet-Sun filaments are selected if their center-of-gravity is located between $\pm 30°$ and $\pm 50°$.

4.3 Results

The current Solar Cycle 24 (Figure 4.4, the sunspot data for Solar Cycle 24 were provided by SILSO World Data Center (2008 – 2019), www.sidc.be/SILSO/) started in late 2008. In 2011 and 2014 two maxima were reached. Sun et al. (2015) date the polar magnetic-field reversal for the northern and southern hemisphere in November 2012 and March 2014, respectively. The minimum is expected by the end of 2019 or the beginning of 2020. The regular ChroTel observations started 2012, after the first maximum in 2011. They cover the second maximum in 2014 with a large number of observing days in that year, and monitor the decreasing phase of the cycle between 2015 and 2018. In the following analysis, we split the dataset in two parts: the maximum phase contains the observations around the maximum between 2012 – 2014 (dark gray in Figure 4.4, 528 observing days). The declining phase contains the observations between 2015 – 2018 after the magnetic polarity reversal (light gray in Figure 4.4, 434 observing days).

4.3.1 Global Distribution of Filaments in Latitude

The number of detected structures in each latitude bin is displayed in Figure 4.5 for both the maximum and declining phase. For the maximum phase, most detected filaments are located in the mid-latitudes between $\pm 20°$ and $\pm 50°$, where intermediate and quiet-Sun filaments are located. Fewer filaments are detected in the higher latitudes above/below $+60°$ and $-60°$, where more filaments appear in the southern hemisphere. This can be explained with the delayed polar magnetic field reversal in the southern hemisphere. In the declining phase, fewer filaments are detected because of lower solar activity but also because of the sparser coverage of ChroTel data. Nonetheless, we recognize fewer detected filaments at high latitudes, which is expected following the polar magnetic field reversal in both hemispheres.

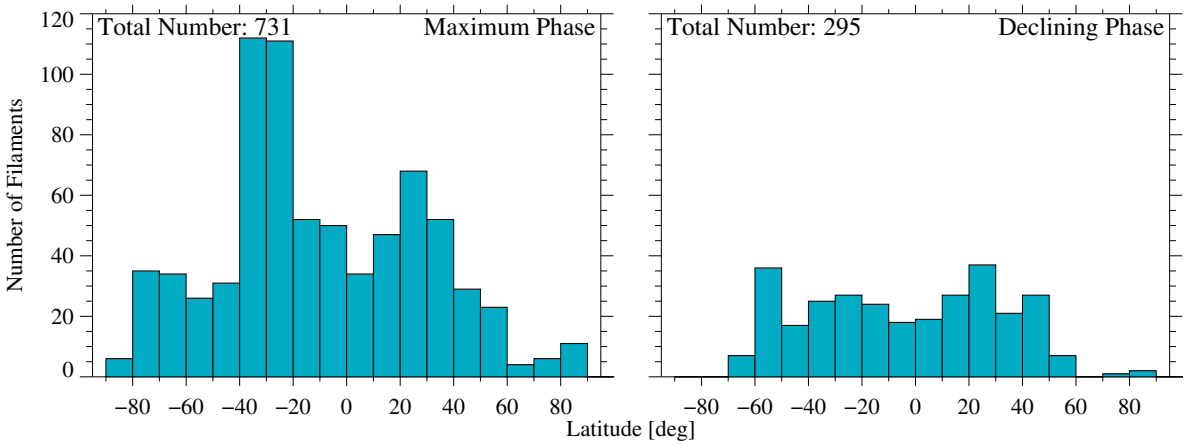

Figure 4.5: Distribution of detected filaments per latitude bin for the maximum (*left*) and the declining (*right*) phase. Each bin has a size of 10°.

4.3.2 Latitude Dependence of Filaments across the Solar Cycle

We derived the location of the center-of-gravity for each detected object using blob analysis. In Figure 4.6, we display the location with respect to the corresponding Carrington rotation for the entire dataset. The black line indicates the split into the maximum phase on the left and the declining phase on the right. In the maximum phase, we have more observations and therefore more detected filaments. Higher latitudes are more interesting for this study. Thus, we display in Figure 4.7 only the higher latitudes above/below $+50°/-50°$. The gray regions indicate the polar magnetic-field reversal in the northern and southern hemisphere as described in Sun et al. (2015). In the upper panel, we recognize structures at high latitudes above 70°. After the polar magnetic field reversal, no structures at latitudes above 75° are identified in the northern hemisphere. In the southern hemisphere, the polar magnetic field reversal occurred 16 months later, *i.e.* in March 2014 (Sun et al., 2015). After the reversal, we detect only filaments that do not reach latitudes of $-75°$. These structures appear at around $-60°$.

The dash-to-the-Pole of polar crown filaments in the southern hemisphere started at approximately Carrington rotation 2115 and lasted until approximately Carrington rotation 2140 (Xu et al., 2018). The ChroTel observations start at the Carrington rotations 2122 and cover about 75 % of the dash-to-the-Pole. This allows us to estimate a rough migration rate for the PCFs for the southern hemisphere, which we compare with the migration rate given in Xu et al. (2018). Cluster analyses was used to ensure that quiet-Sun filaments are not erroneously mixed with PCFs, which yields four clusters in the maximum phase (Figure 4.7). Clusters I and II (blue and green crosses) belong to the year 2012. They are clearly connected and represent the migration of the PCFs. Cluster III (orange crosses) also belongs to the migration of the PCFs and is a continuation of the migration of the PCFs from Cluster I and II only separated by the gap of observations between 2012 and 2013. Cluster IV (violet crosses) is excluded from the calculation of the migration rate, because it is clearly separated from cluster III and represents ordinary quiet-Sun filaments. In order to verify the exclusion of Cluster IV, we derived the distance of all data points to the line of best fit. All points from Cluster IV have a significantly larger distance of more than 10° per rotation than the other detected PCFs of the other clusters. Ordinary quiet-Sun filaments are also excluded from the calculation of the migration rate in Xu et al. (2018) for Solar Cycles 21 – 23, as well. The derived migration rate from Clusters I – III is $0.79° \pm 0.11°$ per rotation. An estimate of the migration rate for PCFs in the northern hemisphere is not possible based on ChroTel data due to the lack of observations in this phase.

4.3.3 Size Distribution of Filaments in Latitude

Blob analysis facilitates extracting the area in pixels of detected filaments. The grid in the synoptic maps has an equidistant spacing between ±90° along the ordinate. Along the abscissa, each pixel corresponds to 0.1°. Thus, we calculated the area in megameters-squared and differentiated the filaments in three categories: i) $<1000\,\mathrm{Mm}^2$, ii) $1000\,\mathrm{Mm}^2 - 2500\,\mathrm{Mm}^2$, and iii) $>2500\,\mathrm{Mm}^2$. In Figure 4.8, we display

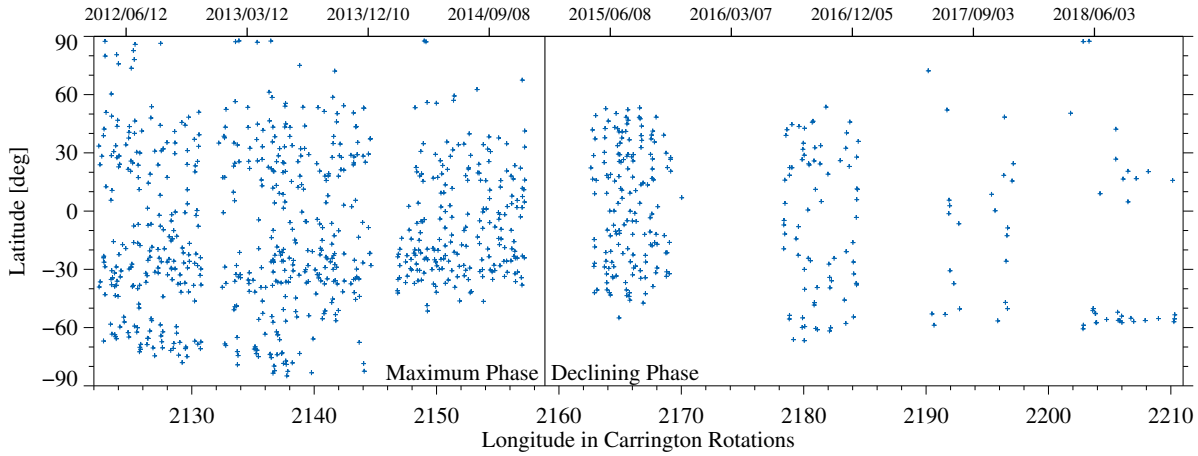

Figure 4.6: Position of identified filaments for 90 Carrington rotation periods between 2012 and 2018. The line indicates the split of the dataset in maximum and declining phase. The maximum phase includes the years 2012 – 2014 and the declining phase includes the years 2015 – 2018.

a histogram of the three different size categories as a function of latitude. In the maximum phase (top panel in Figure 4.8), the distribution across latitudes is imbalanced between the northern and southern hemisphere, *i.e.* the northern hemisphere is dominated by the small and mid-sized filaments. The few detected filaments at high latitudes in the northern hemisphere belong to Category ii). In the southern hemisphere, many large filaments are present. In the declining phase (bottom panel Figure 4.8), most of the detected filaments are smaller in both the northern and southern hemisphere, and only a few large filaments appear without any clear latitude dependence.

4.3.4 Tilt Angle Distribution of Filaments

Fitting an ellipse to the detected filament yields the approximate orientation of the filaments relative to the Equator. We present in Figure 4.9 the orientation of the detected filaments for different latitudes and for the maximum and declining phase. Essentially, we sorted the filaments according to their orientation in two categories: i) North-West (NW) or South-East (SE) orientation and ii) North-East (NE) or South-West (SW) orientation. According to Joy's Law the majority of active regions, and filaments as well, are orientated in the NW/SE direction in the northern hemisphere and in the NE/SW direction in the southern hemisphere (Cameron, Dikpati, and Brandenburg, 2017). In the maximum phase of Solar Cycle 24, the same relationship holds true for ChroTel data. Most of the detected filaments in the southern hemisphere have a NE/SW orientation, and in the northern hemisphere most of the objects have a NW/SE orientation. However, in the higher latitudes of the southern hemisphere, the NW/SE orientation is dominating. In the declining phase, the aforementioned relationship is again confirmed by the histogram for the northern hemisphere, whereas in the southern hemisphere, the relationship remains ambiguous. At mid-latitudes, both orientations turn up with the same frequency for bins between $-10°$ and $-40°$. However, the NW/SE orientation is more common in the bin $-60°$ to $-50°$.

4.3.5 Distribution of Hα and He I Line-Core Intensities

Figure 4.10 shows scatter plots of Hα and He I line-core intensities for PCFs covering the maximum and declining phase, respectively. In addition, the individual histograms of the line-core intensities for Hα and He I are provided. The images are normalized with respect to the mean quiet-Sun intensity [I_{qs}], which was derived by creating a mask, which excluded dark and bright regions and computing the mean of the remaining values. The typical line-core intensity of the Hα line is 16 % and for He I it is about 90 % of the continuum intensity in the quiet-Sun. Taking into account the FWHM of 0.5 Å of the Hα Lyot filter, we would end up with a line-core intensity of 19 % for Hα with respect to the continuum intensity. The values were obtained from a disk-integrated reference spectrum taken with the Kitt Peak Fourier Transform Spectral (FTS: Brault, 1985) atlas.

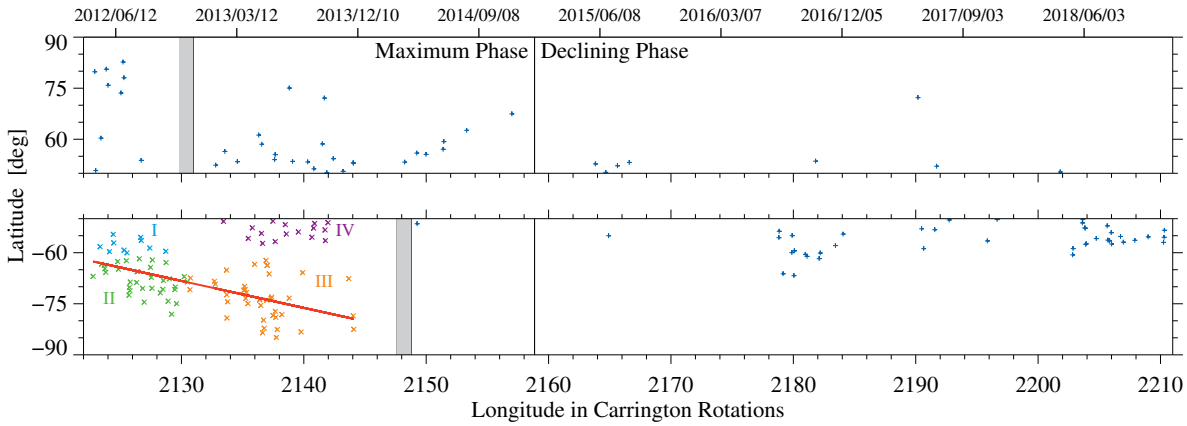

Figure 4.7: Butterfly diagram of high-latitude filaments above/below $+50°/-50°$. The *gray areas* indicate the time of the polar magnetic field reversal in November 2012 for the northern hemisphere (*top*) and March 2014 for the southern hemisphere (*bottom*). The filaments of the southern hemisphere of 2012 and 2013 are divided in four clusters. The filaments belonging to Cluster I (*blue crosses*), Cluster II (*green crosses*), and Cluster III (*orange crosses*) were used to calculate the migration rate. The red line indicates the migration of polar crown filaments toward the Pole. Filaments belonging to Cluster IV (*violet crosses*) are quiet-Sun filaments and were not used in the computation of the migration rate. The *vertical black* line indicates the the split of the dataset into maximum and declining phase.

Comparing the histograms in the maximum phase and declining phase (Figure 4.10) for PCFs, the Hα histograms show that they cover a broader intensity range compared to the He I histograms but with a steeper negative slope toward higher intensities. The He I histograms show a Gaussian distribution and are more symmetric. Therefore, we fitted Gaussians to the He I histograms and derived a FWHM of 0.014 for both maximum and declining phase.

The two-dimensional histogram of the Hα and He I line-core intensities of the maximum phase shows random structures at large He I intensities. This is likely caused by artifacts related to strong geometric distortions at very high latitudes close to the Poles. Another effect is introduced by the mask, which was derived from the Hα images during the blob analysis. However, the filaments in He I are smaller than in Hα. Thus, structures of the surrounding quiet-Sun are included in the He I histogram.

The histogram in Hα for the declining phase differs from the one for the maximum phase. The slope toward the lower intensities is less steep and almost linear. This may be caused by the absence of erroneously detected structures close to the Pole. The slope toward brighter structures is instead much steeper, which can be also seen in the two-dimensional histogram. In total, there are fewer PCFs at higher latitudes in the declining phase. Only in the He I histogram, we recognize that the automatic detection found structures at lower He I intensities, which could be caused by geometric distortions close to the Pole.

4.4 Discussion

We presented an overview of the ChroTel dataset for the years 2012 – 2018 and created synoptic maps for each of the 90 Carrington rotation periods. With morphological image-processing tools, such as blob analysis, we automatically extracted dark objects, where we concentrated on elongated, large-scale objects, *i.e.* various types of filaments. We carried out a statistical analysis and presented initial results based on the catalogue of detected filaments.

In the first part of the analysis, we focused on the locations of the filaments as a function of time (Figure 4.6). The observations included the time of the polar magnetic field reversal for Solar Cycle 24 in both northern and southern hemispheres (Figure 4.7). We identified PCFs close to the Poles before the reversal, and we established their absence after the reversal. Up until the end of 2018, very few filaments were detected at high latitudes. For the southern hemisphere, we derived the migration rate of PCFs in Solar Cycle 24, *i.e.* a rate of $0.79° \pm 0.11°$ per rotation. The study of Xu et al. (2018) gives a rate of $0.63° \pm 0.08°$ per rotation, which is smaller than our value. However, we have to take into account that our

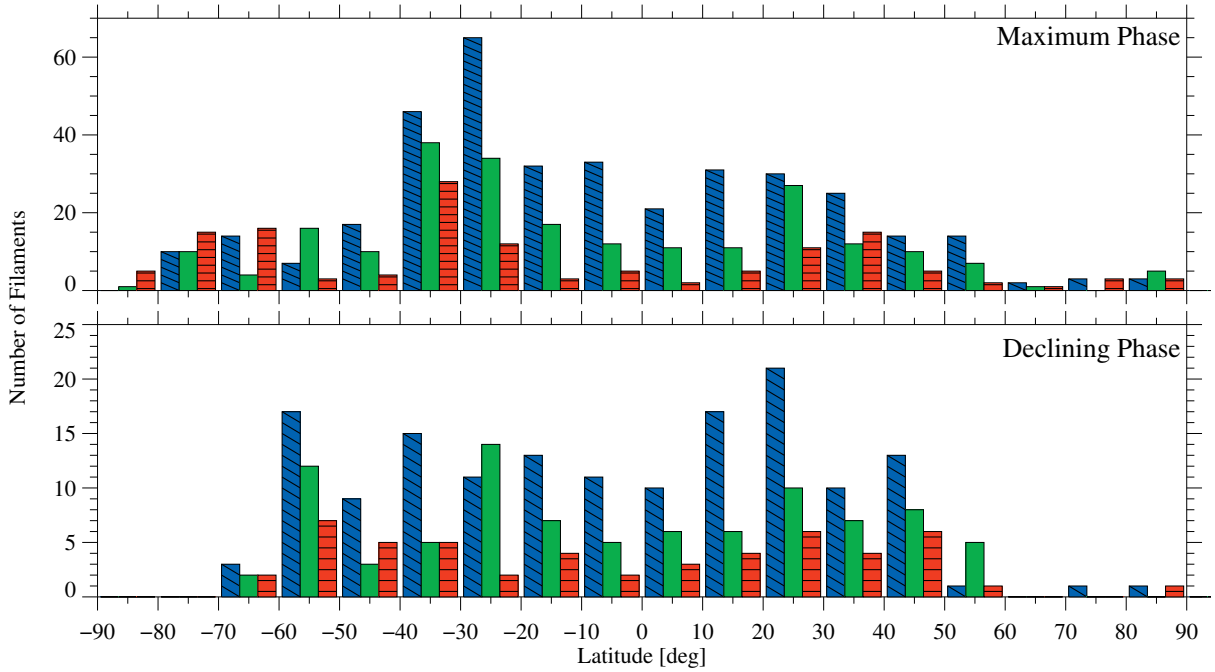

Figure 4.8: Distribution of filaments per area bin for the maximum (*top*) and declining (*bottom*) phase. The first area bin (*filled blue with diagonal lines*) refers to filaments with an area smaller than 1000 Mm^2, the second bin (*filled green*) comprises areas between 1000 Mm^2 and 2500 Mm^2, and the third bin (*filled red with horizontal lines*) contains areas larger than 2500 Mm^2.

observations started after PCFs began migrating toward the Pole. Therefore, our estimate of the migration rate is based on incomplete data. Additional observations will increase the reliability of the migration rate. In addition, Figure 4.7 illustrates the asymmetry of the northern and southern hemisphere in Solar Cycle 24, which was reported by Svalgaard and Kamide (2013) and Sun et al. (2015) for this cycle. Yet, an asymmetric behavior has been known since Spörer (1889) who studied the appearance of sunspots in both hemispheres.

With upcoming observations in the next years, we can continue monitoring the propagation of high-latitude filaments toward the Pole, starting after the solar minimum (Hao et al., 2015; Xu et al., 2018). This behavior of PCFs was expected and studied over several decades. Nonetheless, our work demonstrates that the ChroTel dataset can be used for the analysis of the cyclic behavior of PCFs and their "dash-to-the-Pole". However, the ChroTel dataset is relatively small compared to other full-disk Hα surveys, *i.e.* those of BBSO, KSO, or the Global Oscillation Network Group (GONG: Harvey et al., 1996), but it can complement the datasets of the other surveys. Similar to ChroTel, the full-disk telescopes at BBSO and KSO have a ten-centimeter aperture. The Lyot-type filter at BBSO has a bandpass of 0.25 Å and that of KSO a bandpass of 0.7 Å, whereas ChroTel's bandpass is 0.5 Å. All three surveys utilize a 2048×2048-pixel detector size and contain images with a cadence as short as one minute. In addition, ChroTel provides Ca II K λ3933 Å and He I λ10830 Å filtergrams, whereby the He I spectroscopic data facilitate obtaining Dopplergrams. Full-disk data at KSO also include Ca II K and continuum images. For filament research, which is the focus of our study, only Hα and He I filtergrams are relevant. All instruments are ground-based facilities and are exposed to adverse weather conditions and periods of poor or mediocre seeing. Therefore, the Hα data of all three surveys complement each other very well and partly bridge the day–night cycle for continuously monitoring solar activity.

Blob analysis provided the area for the detected filaments. We divided the dataset chronologically according to the maximum (2012 – 2014, 528 observing days) and declining phase (2015 – 2018, 434 observing days) of Solar Cycle 24. In the maximum phase, the number of detected filaments is much larger than for the declining phase (Figure 4.5), which is related to higher levels of solar activity but also related to the better coverage with ChroTel observations in this phase. For both phases, small filaments are more common at mid-latitudes below/above $+50°/-50°$ than filaments with an area greater than 1000 Mm^2 (Figure 4.8). In the maximum phase, we detected in general more filaments in the southern

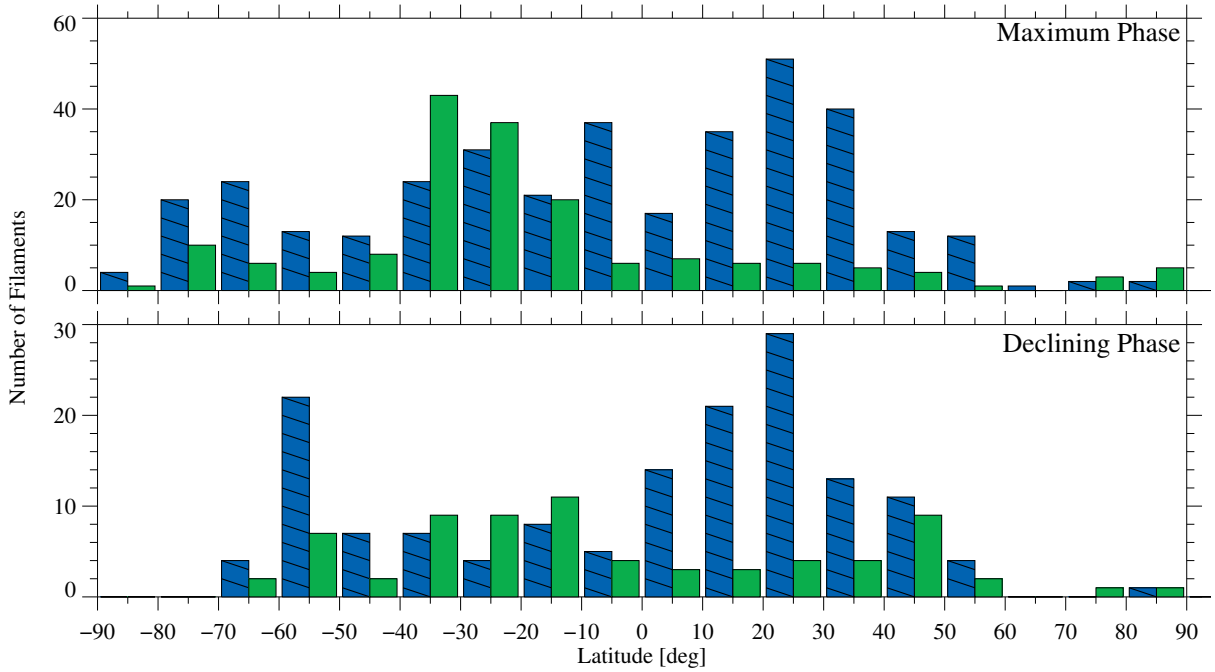

Figure 4.9: Distribution of filament tilt angles, which are either directed to the NW/SE (*filled blue with diagonal lines*) or NE/SW (*green*) direction for the maximum (*top*) and declining (*bottom*) phase.

hemisphere between $-50°$ and $-30°$ as compared to the northern hemisphere or around the Equator. On the other hand, we find more large filaments ($>2500\,\mathrm{Mm}^2$) at high latitudes as compared to small filaments. In addition, the number of filaments at high latitudes is smaller compared to mid-latitudes.

Hao et al. (2015) compare the area of filaments for Solar Cycles 23 and 24 between 1996 and 2013 based on BBSO data. Both cycles show a symmetric increase of the number of filaments between $\pm 40°$ and $\pm 20°$ and a few filaments close to the Equator and the Poles. In our dataset, we do not cover the activity maximum in the northern hemisphere, but only the maximum in the southern hemisphere, which explains the asymmetric histogram obtained from the ChroTel observations. In polar regions, Hao et al. (2015) did not find many PCFs with large areas. The automatized detection method applied to the ChroTel data found proportionally more filaments with larger areas in these regions. Nonetheless, large-scale filaments are not unusual close to the Poles and may be attributed to the later start of ChroTel observations during Solar Cycle 24 so that a number of larger filaments is better seen in our dataset because of the smaller total number of detected filaments.

The prevailing orientation of filaments in the northern (southern) hemisphere is north-west (north-east) (Tlatov, Kuzanyan, and Vasil'yeva, 2016; Cameron, Dikpati, and Brandenburg, 2017). This was confirmed with the ChroTel observations for both maximum and declining phase of Solar Cycle 24 at mid-latitudes between $\pm 20°$ and $\pm 50°$. In polar regions, the orientation seems to be reversed with a NE/SW orientation. The few detected filaments in the declining phase make it difficult to recognize a dominant orientation in the southern hemisphere, but in the northern hemisphere, a clear dominance of the NW/SE orientation is visible in the histogram. The studies of Hao et al. (2015) and Tlatov, Kuzanyan, and Vasil'yeva (2016) confirm the dominant orientation of mid-latitude filaments taking into account more solar-cycle observations. Tlatov, Kuzanyan, and Vasil'yeva (2016) observe a negative tilt angle for the polar regions, which is also visible in the ChroTel data of the maximum and declining phase.

Finally, we inspected the line-core intensity distribution of filaments in Hα and compared it to that of He I line-core intensities for the same regions. The distribution in Hα is broader and resembles a bimodal distribution with a strong declining slope toward high intensities and a shallow slope toward low intensities, in both maximum and declining phase. The He I distribution is well-represented by a Gaussian distribution. We have to take into account that high-latitude filaments are located between $\pm 50°$ and $\pm 70°$. In addition, we recognize either lower or higher intensities, which do not belong to the overall

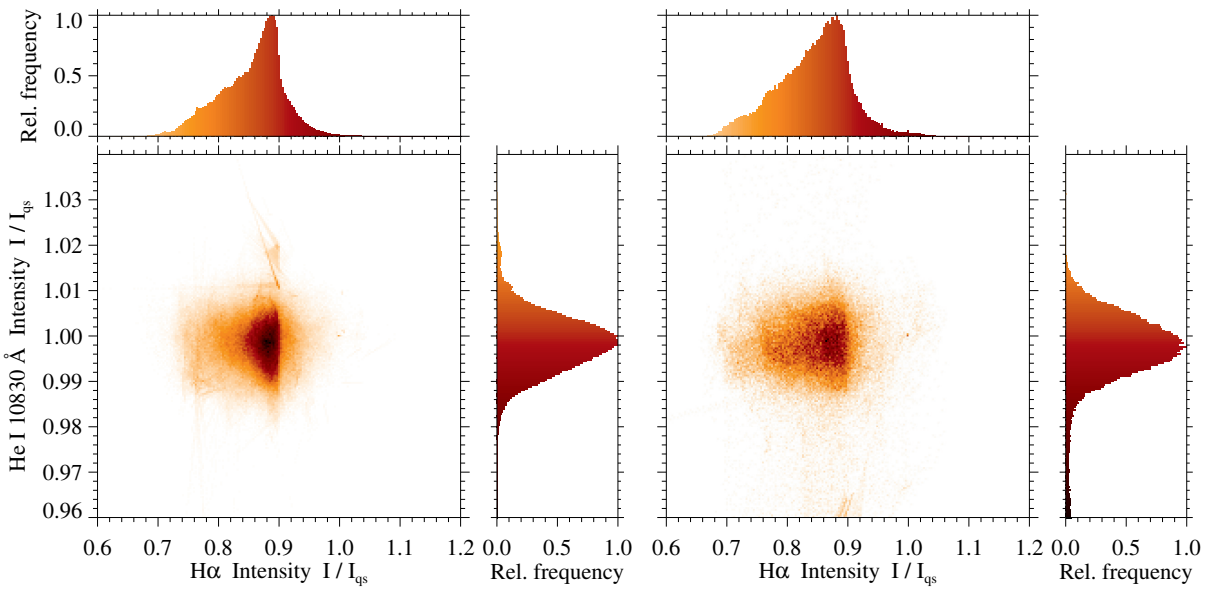

Figure 4.10: Scatter plot of Hα and He I line-core intensities [I/I_{qs}] derived from synoptic maps covering the maximum (*left*) and declining (*right*) phase for PCFs. In addition, we provide the respective histograms of the line-core intensities for each spectral line and phase of the cycle.

intensity distribution in He I, which indicates that the filaments in He I have a smaller extent than in Hα. Thus, intensities of the surrounding quiet-Sun are erroneously included in the intensity distribution.

The study of Xu et al. (2018) focused on the location of filaments in the BBSO and KSO data for Solar Cycles 21 – 24. The ChroTel dataset complements the data of BBSO and KSO. Information about tilt angles and size distribution is not yet available for BBSO and KSO data of Solar Cycle 24, which would be helpful for a more robust determination of PCF properties. Additional data of other Hα surveys, *e.g. Kodaikanal Observatory* (Chatterjee et al., 2017), would allow us to cover more than a century of filament observations. An automatic data extraction approach with machine learning tools would facilitate an analysis of the lifetime and proper motions of the filaments. Space-based observations with, *e.g.* the *Solar Dynamics Observatory* (SDO: Pesnell, Thompson, and Chamberlin, 2012), would complement such a study with observations of the upper chromosphere, transition region, and corona.

4.5 Conclusions

In this work, we demonstrated the value of the small-aperture synoptic solar telescopes such as the ten-cm aperture ChroTel. In 2012, the telescope started to take data on a regular basis, covering the maximum and declining phase of Solar Cycle 24. In total, it observed on almost 1000 days in seven years and recorded chromospheric images in three strong chromospheric absorption lines: Hα, Ca II K, and near-infrared He I, whereby the He I line was scanned at seven different wavelength positions around the line core. We presented the image reduction pipeline, including limb-darkening correction, a non-uniform brightness correction with Zernike polynomials, and a geometric stretching to an equidistant graticule, which finally led to synoptic maps in all wavelengths. In this work, we concentrated on the automated extraction of filaments and their statistical analysis based on the Hα data, *i.e.* the number of filaments, their location, area, and tilt angle. Furthermore, we compared the line-core intensity distribution of filaments in Hα with He I line-core intensities extracted from synoptic maps. Finally, we determined the appearance and disappearance of PCFs around the time of the polar magnetic field reversal, which enabled us to study the long-term evolution of PCFs in more detail. Other typical properties of filaments such as the tilt angle were derived from ChroTel observations. Hence, ChroTel can complement larger surveys, *i.e.* those of BBSO, KSO, GONG, and many others (Pevtsov, 2016). Nonetheless, in contrast to the aforementioned observatories, ChroTel only started observations during the maximum of Solar Cycle 24 and has consequently a relatively smaller database. A significant advantage of ChroTel is

that it observes the Sun regularly every three minutes in the three different wavelengths. Furthermore, high-temporal-resolution observations with a one-minute cadence are possible in Hα, which facilitates detailed studies of selected PCFs.

The automated detection of filaments with morphological image processing tools, still contains false detections of small dark structures, which may not be related to filaments. We eliminated these structures in the present study with a rough threshold. Non-contiguous parts of filaments or small-scale active region filaments are also sorted out. In a forthcoming study, detection and recognition of filaments will be improved and automated with object detection methods based on neural networks. Thus, filaments can be analyzed in more detail revealing their physical properties, *e.g.* class membership, length, and width. Furthermore, the rapid cadence of ChroTel observations enables us to study the temporal evolution of individual filaments and examining their horizontal proper motions. One future goal is to search for counter-streaming flows, which are ubiquitously present in all kinds of filaments. The high quality of the ChroTel dataset facilitates the analysis of a large number of filaments in Hα but also in He I. The latter provides line-of-sight velocities, which were not exploited so far. Structures such as plage regions appear bright in Hα but dark in He I. The different morphologic and photometric properties of solar objects in the three wavelength bands of ChroTel are an excellent starting point for object tracking, identification, and classification using machine learning techniques and novel neural network routines.

Chapter 5

Automatic Extraction of Polar Crown Filaments Using Machine Learning Techniques

Observing the Sun in Hα, the omnipresent features are solar filaments. These are structures of dense, cool plasma, which reach from the chromosphere into the corona, stabilized by the magnetic field. They appear above and along the polarity inversion line (PIL), which separates opposite polarities (Martin, 1998; Mackay et al., 2010). Filaments can be very dynamic objects, which change their appearance in only a few hours. If the magnetic field is destabilized, the filaments can erupt, e.g., as coronal mass ejections (CMEs), and the plasma stored in them is ejected into space. We differentiate between three kinds of filaments: active region filaments, which are smaller, more dynamic, and rooted at large magnetic field concentrations of active regions; quiet-Sun filaments, which appear at all latitudes and are usually larger and more stable; and the category of intermediate filaments, where filaments are subsumed, if they do not fit to the aforementioned classes (Mackay et al., 2010). A special type of quiet-Sun filaments are polar crown filaments, which appear at high-latitudes above 50° (Leroy, Bommier, and Sahal-Brechot, 1983). They form at the border of the unipolar field at the poles and the trailing magnetic flux of active regions of opposite polarity, which is transported towards the poles by meridional flows (Karna, Zhang, and Pesnell, 2017). The appearance of polar crown filaments at mid-latitudes at the time of the activity minimum and their migration towards the poles is called "rush-to-the-pole" (Cliver, 2014). Studying polar crown filaments gives indirect evidence on the solar dynamo. The change of the migration rate, the onset of the propagation, and the timing of the magnetic field reversal at the poles with whom these filaments disappear from the solar disk until the next cycle, is analyzed in several studies (e.g., Cliver, 2014; Chatterjee et al., 2017; Xu et al., 2018; Diercke and Denker, 2019). Systematic filament studies are performed on all kinds of filaments, as in the statistical studies of, e.g., Hao et al. (2015) or Diercke and Denker (2019, see Chapter 4). The key ingredient of all these studies is an effective extraction of the location, length, width, and other statistical properties of filaments from full-disk observations.

Xu et al. (2018) resorted to a visual inspection of the location of polar crown filaments, because they could not find a satisfactory method to extract all filaments automatically. Hao et al. (2015) applied an adaptive threshold, which is based on the Otsu (1979) threshold, but with a modification, which takes into account the mean intensity on the solar disk to improve the automatic detection of filaments. Diercke and Denker (2019, see Chapter 4) extracted filaments automatically at all latitudes from synoptic charts based on Hα full-disk images by applying morphological image processing techniques. To avoid the extraction of sunspots from the data, they excluded small-scale features, which eliminated small-scale filaments as well. Moreover, the algorithm encountered problems extracting filaments at the poles, in particular, because in the geometrical conversion to an equidistant grid with heliographic coordinates the filaments were stretched resulting in some artifacts in the maps.

Object identification in solar physics is also attempted using machine learning techniques. One example is the detection algorithm of Qu et al. (2005), who used an adaptive threshold to extract the candidates for filaments from Hα full-disk images and used a support vector machine (SVM, Cortes and Vapnik, 1995) to differentiate between sunspots and filaments. The filament is then extracted with

morphological image processing. In the last few years, applications of deep neural networks became popular in astrophysics for image classification, object detection, or segmentation of solar objects. One application in solar physics is the classification of solar images, where the objects were separated into five classes: filaments, flare ribbons, prominences, sunspots, and quiet Sun, if no object was detected in the image (Armstrong and Fletcher, 2019). To train the convolutional neural network (CNN, e.g., LeCun and Bengio, 1995; Lecun, Bengio, and Hinton, 2015; Elgendy, 2020), Armstrong and Fletcher (2019) used high-resolution Hα data of the Solar Optical Telescope (SOT, Tsuneta et al., 2008) onboard the space mission Hinode (Kosugi et al., 2007). In addition, transfer learning (Taylor and Stone, 2009) was performed to classify images from SDO. In particular, filaments are difficult targets to extract from Hα full-disk observations with classical image processing tools, because it is complicated to differentiate them from other dark objects like sunspots. Zhu et al. (2019) presented an approach to extract filaments from full-disk Hα images (Denker et al., 1999) obtained at the Big Bear Solar Telescope (BBSO), using the fully convolutional neural network (FCN) U-Net (Ronneberger, Fischer, and Brox, 2015), which was modified to enable image segmentation to extract filaments. The authors train the network with semi-manual computed ground-truth using image manipulation software and classical image processing. The results show an efficient segmentation compared to classical image processing, with reduced false detection of small-scale dark objects. Nonetheless, the exclusion of sunspots is not effective in this method. Another recent approach to segment filaments is presented by Ahmadzadeh et al. (2019), who used an off-the-shelf model, Mask Region-Based Convolutional Neural Network (R-CNN, Girshick et al., 2014; He et al., 2017) and applied it to BBSO Hα full-disk data. The training data are created from maps, which are also used as input for the Heliophysics Events Knowledgebase (HEK, Hurlburt et al., 2012). In the data, non-filament regions are removed with classical morphological image processing, whereby the accuracy is estimated to be about 72% compared to manually labeled data (Ahmadzadeh et al., 2019). The network is trained and validated on two years of data and tested on three years. The segmentation results are comparable to the ground-truth labels and the network identified filaments that were missing in the original HEK database.

Extraction of filaments for statistical studies can be tedious. Morphological image processing is very effective, but a differentiation with other dark features on the Sun is very difficult. We decided to train an off-the-shelf deep neural network, i.e., YOLOv5 (Jocher et al., 2020), with the labeled data of the Chromospheric Telescope (ChroTel, Bethge et al., 2011) to detect filaments in Hα filtergrams. Besides detecting filaments in Hα images, we will extract the filaments with a standard deep learning segmentation model, i.e., DeepLabv3 (Chen et al., 2017). This model is trained with masks created from the labeled ChroTel data. In addition, we can create labels with YOLOv5 for the complete ChroTel dataset, including years, where the data was not yet labeled. The entire dataset can then be used to train the segmentation algorithm. In the end, we obtain the masks predicted by the segmentation model, where we can extract filaments and use them as input for a statistical study, similar to the study by Diercke and Denker (2019, see Chapter 4). The goal of this study is to provide a tool to extract filaments from any full-disk Hα data source. These filaments could then be used, e.g., for statistical studies with multiple applications or simply as input data for global databases such as HEK. The schematic outline of the present study is displayed in Figure 5.1.

5.1 Data

In order to train a neural network to perform object detection of filaments, we had to label these filaments in Hα full-disk filtergrams. For this purpose, we decided to use the dataset of ChroTel (Kentischer et al., 2008; Bethge et al., 2011). The 10-cm aperture telescope mounted at the terrace of the VTT (von der Lühe, 1998) observes in three different wavelengths Hα, Ca II K, and He I λ10830 Å with a cadence of 3 min. The observations are carried out with three Lyot filters, whereby the Hα filter has a FWHM of 0.5 Å. All three wavelengths display the chromosphere, but Hα is the best wavelength to study filaments. In addition, plage regions appear bright, while sunspots are dark. In the Ca II K filtergrams, filaments are not visible, but bright plage regions become visible. The He I triplet is observed at seven spectral positions $\pm$3 Å. The wide range includes filtergrams of the continuum and of the near-by Si I line. In the line-core He I filtergrams, filaments become visible, but with a reduced optical thickness. Furthermore, in He I the

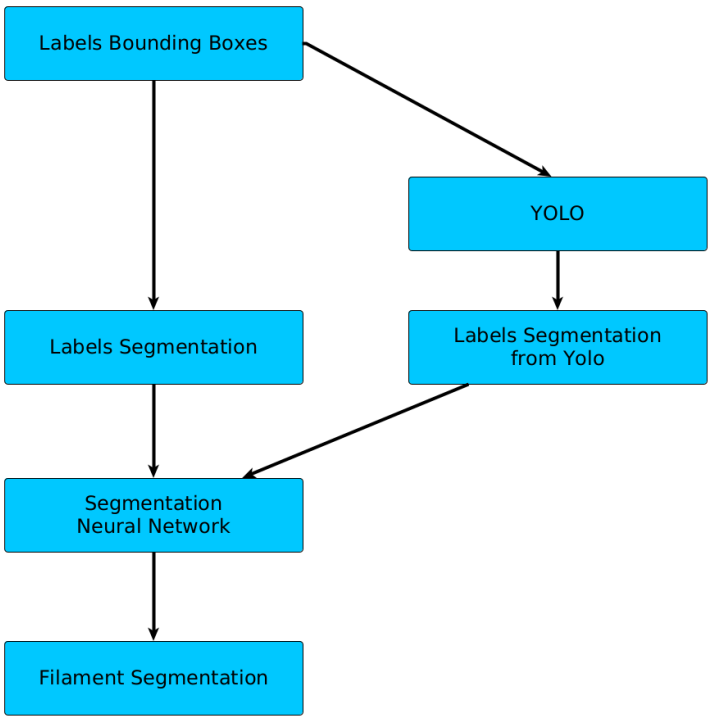

Figure 5.1: Schematic outline of filament detection and segmentation with neural networks.

plage region in the surroundings appear also dark, which complicates the differentiation of filaments from other structures.

The regular ChroTel observations started in 2012 and are ongoing. The dataset contains 1056 days of observations until September 2020, whereby on each day the qualitatively best filtergram was selected with the Median Filter-Gradient Similarity (MFGS, Deng et al., 2015; Denker et al., 2018) method. In this method, the similarity between the original image and the median-filtered image is evaluated. The basic data reduction includes dark- and flat-field correction, as well as rotation to the solar north and geometric correction of solar images with an oval appearance, which is caused by the low elevation of the Sun in the early mornings or late evenings. Furthermore, the images are normalized to the median intensity of the solar disk and are limb darkening corrected. The Lyot filter introduced a non-uniform intensity variation, which is corrected by approximation with Zernike polynomials (Shen, Diercke, and Denker, 2018, see Chapter 3). Further details of the image processing are given in Shen, Diercke, and Denker (2018) and Diercke and Denker (2019). All filtergrams are scaled to a solar radius of $r = 1000$ pixels, which results in an image scale of about $0\farcs96$ with an image size of 2000×2000 pixels.

We manually labeled one image of each day from the entire ChroTel dataset between 2012 and 2018, which includes 955 observing days. The images are displayed at a lower resolution with an image size of 1000×1000 pixels and a rectangle is drawn around each filament of the images, by determining the upper left and bottom right corner. In some cases the filament is split in several parts, whereby we labeled each part individual with a bounding box. The labeled data cover observations from the maximum and minimum of Solar Cycle 24. The labels of the bounding boxes and the images with a resolution of 1000×1000 are used as ground-truth input data for the training of the deep neural network. Three examples of such an input image with the corresponding labels are displayed in the left panels of Figure 5.3. Each bounding box contains the information on the central coordinate of the box, its width and height, and the information for the class. In this study, we only have one class, i.e., filaments, which has the class identifier 0.

We used additional Hα observations of the Kanzelhöhe Solar Observatory (KSO, Otruba and Pötzi, 2003; Pötzi et al., 2015; Jarolim et al., 2020) to validate the training of the object detection algorithm with an additional data source. Moreover, the training should be extended with a combined dataset of ChroTel and KSO Hα data. The KSO is observing in three wavelengths: white-light, Ca II K, and Hα. In addition, hand-drawn sunspot observations are provided by KSO. The Hα observations are part of the Global Hα Network (GHN, Steinegger et al., 2000), providing Hα full-disk images on a daily basis with a cadence of about 1 min. The regular Hα observations started in 1973 with photographic plates and since 2000

the digital image acquisition system is operating regularly (Otruba and Pötzi, 2003). The light passes through a 100 Å bandpass filter to reduce the thermal stress on the system. A tunable polarizer with a step motor changes the wavelength of the Hα line to observe the line-wing. The temperature-controlled Zeiss Lyot filter was build in 1960 and has a FWHM = 0.7 Å (Otruba and Pötzi, 2003). By adjusting the temperature a wavelength shift between -0.35 Å and $+0.4$ Å is possible. A beamsplitter sends the light to two charged-coupled device (CCD) cameras, one for low-speed observations and one for high-speed observations. The low-speed camera provides high-resolution observations with 2k$\times$2k pixels and 12-bit, but with an image cadence of 1 min, which is used for the Global Hα network. The frame rate is seven images per second, which facilitates frame selection, resulting in an observing cadence of 6 s in the standard observing mode. The exposure time is determined automatically using a control system, so that exposure times between 2.5 ms and 25 ms are possible. The image scale is about 1″, equivalent to 720 km on the Sun (Pötzi et al., 2015).

5.2 Methods

5.2.1 Object Detection

In this section, we will briefly introduce object detection with deep neural networks (Elgendy, 2020) and specifically the object detection algorithm You Only Look Once (YOLO, Redmon et al., 2016; Redmon and Farhadi, 2016, 2018; Jocher et al., 2020). Object detection algorithms localize an object in an image, classify each object based on the trained examples, and try to determine an optimal bounding box around the object. The difference to image classification is that the image classification algorithm only gives the classes contained in an image. The standard object detection algorithms consists of four different steps. First, the algorithm proposes regions of interest (ROI) where a bounding box might contain an object. The probability is given with the objectness score. The second step is the feature extraction and the prediction of the network. As a third step, the object detection algorithm selects from multiple bounding boxes, which are predicted for one object, a single bounding box using the non-maximum suppression (NMS, e.g., Neubeck and Van Gool, 2006; Elgendy, 2020). This method selects one bounding box with the maximum prediction probability, to avoid a repeated detection of the same object. The last step is the evaluation of the results, which is performed with two main methods, which are introduced in the following: frames per second (FPS) and mean Average Precision (mAP). The evaluation of FPS is giving the speed of the network detection, whereas the mAP score gives the precision of the object recognition. First, we introduce the evaluation method Intersection over Union (IoU), which can be defined for each bounding box. The fraction of the overlap and the union of the bounding box of the ground-truth B_{GT} and the bounding box of the prediction B_{Pred} is calculated as (Elgendy, 2020):

$$\mathrm{IoU} = \frac{B_{\mathrm{GT}} \cap B_{\mathrm{Pred}}}{B_{\mathrm{GT}} \cup B_{\mathrm{Pred}}}. \tag{5.1}$$

The IoU defines the correct number of predictions, the True Positives (TP). Therefore, a threshold is used when a bounding box is defined as a correct prediction. If we have an mAP@0.5, the threshold for a true positive detection of a bounding box is above an IoU of 0.5, otherwise the bounding box is considered as a false positive (FP) prediction. If an object is not detected, we have a false negative prediction (FN). Along these, we define the precision and recall (Elgendy, 2020):

$$\mathrm{Recall} = \frac{\mathrm{TP}}{\mathrm{TP} + \mathrm{FN}} \tag{5.2}$$

$$\mathrm{Precision} = \frac{\mathrm{TP}}{\mathrm{TP} + \mathrm{FP}} \tag{5.3}$$

By plotting both values, we can define the Precision-Recall curve and the area below this curve is the Average Precision (AP). The mean over all classes in the problem is finally the mAP, which is always given at a certain threshold for the IoU score.

The most common object detection algorithms are Region-Based Convolutional Neural Network (R-CNN, Girshick et al., 2014), Single-Shot Detector (SSD, Liu et al., 2016), and YOLO. The R-CNN algorithm was the first large application of convolutional neural networks (CNN), which was successfully

localizing and detecting objects in images. It is a multi-stage detector, which means that in the detection process three different modules have to be trained. The multiple training is computationally expensive and very slow. The second and third generation Fast R-CNN (Girshick, 2015) and Faster R-CNN (Ren et al., 2017) perform much faster and with a higher accuracy. Nonetheless, the R-CNN network does not perform real-time detection and the training is longer because of the different phases involved. In contrast, SSD is a single-stage detector, where the prediction is directly made by the convolutional layer in one shot. Another single-stage detector is YOLO, which performs real-time detection with an end-to-end training. In YOLO the region proposal step is omitted and instead the image is split into grids, where for each cell a bounding box is predicted. Non-maximum suppression allows us to extract from the large number of candidates the final bounding box. There are three detection layers for detection on large-, medium-, and small-scale. For this purpose, the image is divided into three grids of different sizes.

The algorithm of YOLOv3 is refined by Ultralytics[1] to its newest and more flexable version YOLOv5[2] (Jocher et al., 2020) using the Python library for deep learning applications `PyTorch` (Paszke et al., 2019). The model architecture is built-up of three main parts: the backbone, the neck, and the head of the model. The backbone mainly extracts the important features form the input image. The neck is responsible to detect features in the images in different scales and to generalize the model, which is performed in YOLOv5 with a feature pyramid. The model head performs the final detection. It decides on the bounding boxes, the class probabilities, and objectness of the detection. For evaluation of the bounding boxes, YOLOv5 uses a special form of IoU, the Generalized IoU (GIoU, Rezatofighi et al., 2019). In this method, the smallest convex hull C of the ground-truth bounding box and the predicted bounding box is calculated and subtracted from the IoU in Eq. (5.1):

$$\mathrm{GIoU} = \mathrm{IoU} - \frac{C/(B_{\mathrm{GT}} \cup B_{\mathrm{Pred}})}{C}. \tag{5.4}$$

Especially, in cases where the ground-truth and predicted bounding box do not overlap, the standard IoU performance is very poor, but GIoU can address this problem by introducing the convex hull C. The performance of GIoU is compared to the standard IoU and show an improvement in the performance of object detection algorithms.

In YOLOv5, five pre-trained models are available in different sizes. The model "YOLOv5l" is the reference model with a parameter size of 47.8 million parameters. The largest model is "YOLOv5x" with about 89 million parameters, which achieved the highest mAP on a reference dataset, but it is slower than the smaller models.

5.2.2 Segmentation

Image segmentation is a computer vision task, which in case of grid-based images, aims to assign each pixel a label (Russell and Norvig, 2010). In classical digital image processing segmentation is based on the discontinuity or similarity of intensity values in the image (Gonzalez, Woods, and Eddins, 2009). The edge detection is based on the discontinuity of an object to separate objects in images, whereby methods such as thresholding or the watershed algorithms use similarities in the intensity values for image segmentation. Image segmentation has a broad range of applications reaching from medical images, where it is used to determine, e.g, boundaries of tumors; autonomous driving, e.g. to detect pedestrians; to astronomy.

The performance of classical image segmentation methods, such as thresholding or edge detection, can be challenging depending on the given data sources and objects, which should be segmented and extracted. In the last few years, deep learning models performed image segmentation applications with a remarkable high precision rate (see Minaee et al., 2020, for review). The segmentation can be divided into two basic approaches: semantic segmentation, where all pixels are classified into respective classes, e.g., sky, tree, car, or pedestrian; and partitioning of objects (also known as instance segmentation), where the objects are classified to objects of interest. The development of different deep learning models resulted in the last few years until 2020 in over 100 deep learning models for image segmentation, which can be divided into about 10 classes based on their model architecture (Minaee et al., 2020). We will shortly

[1] https://www.ultralytics.com/
[2] https://github.com/ultralytics/yolov5

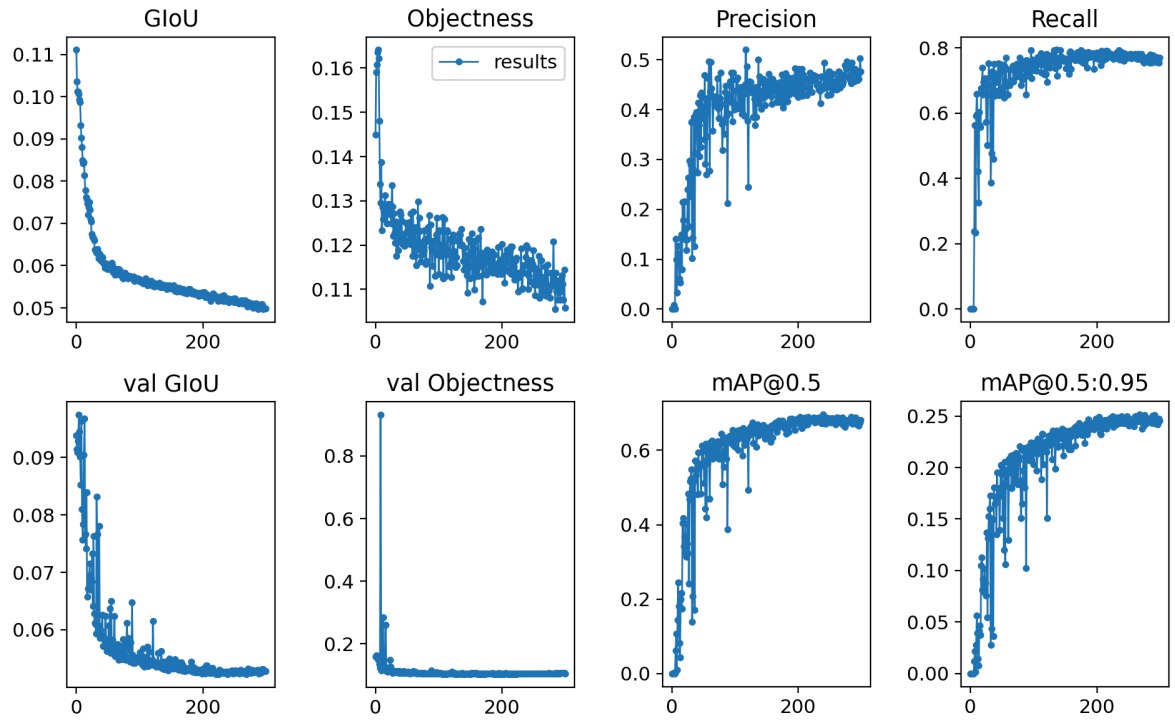

Figure 5.2: Evaluation metrics during the training of YOLOv5: Generalized Intersection over Union (GIoU) for the trainings set (upper left panel) and validation set (lower left panel), Objectness for the trainings set (second upper left panel) and validation set (second lower left panel), precision and recall (upper right panels), and the mean Average Precision (mAP) for a threshold of the IoU of 0.5 (second lower right panel) and at threshold of 0.95 (lower right panel).

introduce one of these models, the DeepLabv3 (Chen et al., 2017) model, which will be used in the later application. The model is based on dilated convolution, also known as atrous convolution (Chen et al., 2017; Minaee et al., 2020). The challenge of segmentation models is to segment objects on multiple scales. For dilated convolutions, another parameter is introduced to the convolutional layer, the dilation rate. For a feature map $x(i)$ at each location i, the output $y(i)$ is defined as (Chen et al., 2017; Minaee et al., 2020):

$$y_i = \Sigma_{k=1}^{K} x(i + r \cdot k)\, w(k), \tag{5.5}$$

whereby r is the dilation/atrous rate, which defines a spacing between the weights of the kernel w. With this, the respective field of the kernel can be enlarged without additional computing cost. This approach is mainly used in semantic segmentation.

5.3 Results

5.3.1 Filament Detection with a Deep Neural Network

The off-the-shelf YOLOv5 algorithm is tested on reference datasets containing images of, e.g., cats, dogs, trees, and many other objects of more than 80 classes, from which pre-trained weights are available. To use the model for solar physics applications, we have to use a customized training of YOLOv5 from scratch, whereby the weights of the algorithm are randomly initialized, hence no transfer learning is used. For the training we use the full-disk ChroTel Hα filtergrams. The dataset is split in a test set, a training set, and a validation set. The training set is the largest with 680 images (70%) and the validation set contains 85 images (10%). The test set contains the remaining 190 images (20%), whereby we select for each year one continuous block of 20% of images for the test set. The image and the corresponding file containing the coordinates of each bounding box are the input for the training of the neural network.

First, we perform some tests, if the detection of filaments with YOLOv5 works on the filament dataset and to set a baseline for further improvements of the detection method. The image size is reduced to 512×512 pixels, because of the memory of the graphics card, which is in this case a GeForce RTX 2080

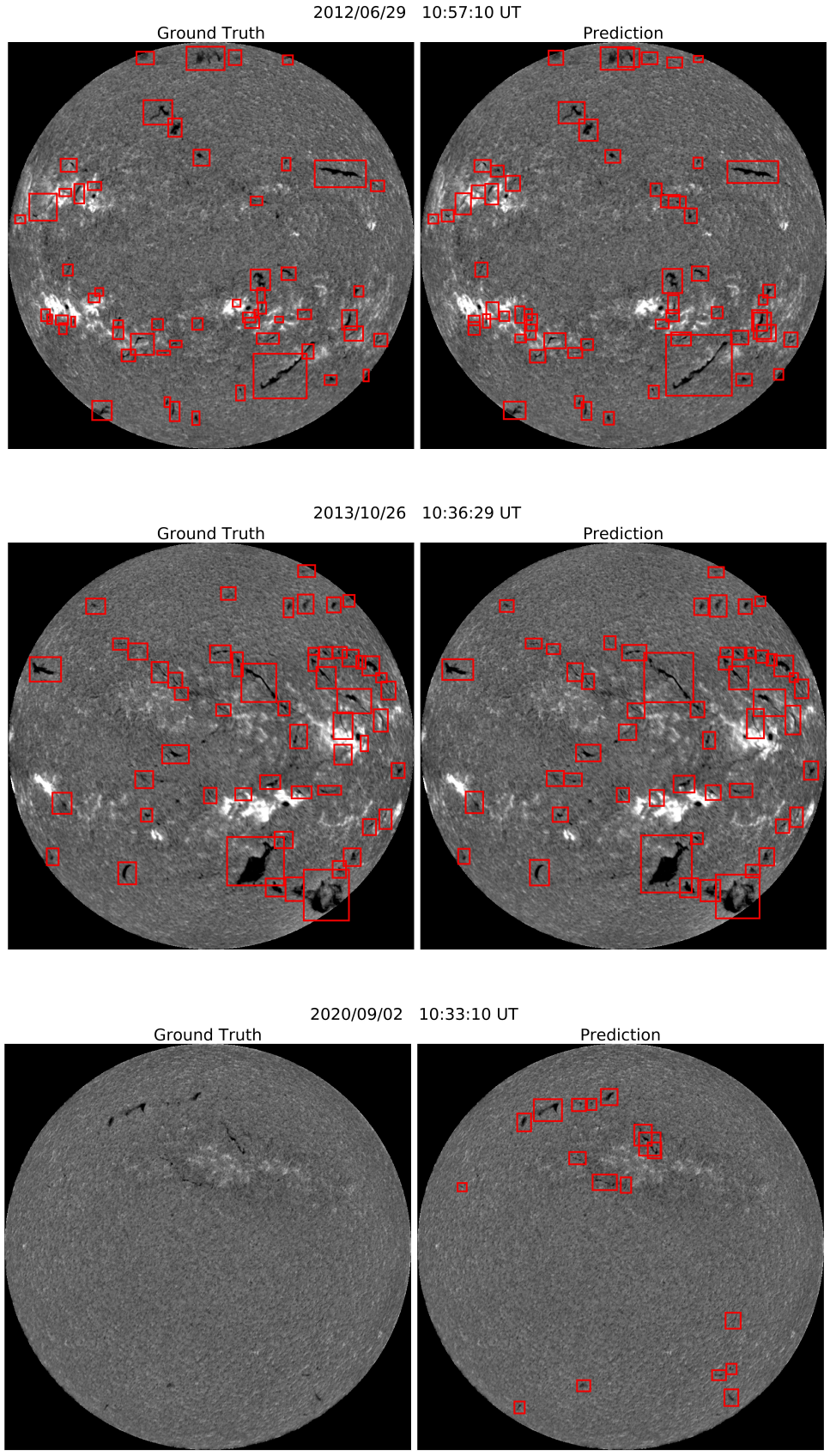

Figure 5.3: Sample Hα filtergrams from ChroTel for three different days: 2012 June 29 (upper panels), 2013 October 26 (middle panels), and 2020 September 2 (lower panels). The input image with the ground-truth bounding boxes (red) is displayed in the left panels. For 2020, the data is not labeled. In the right panels, the predicted bounding boxes by YOLOv5 are displayed. The coordinates of the ground-truth bounding boxes are the input features for the training of YOLOv5.

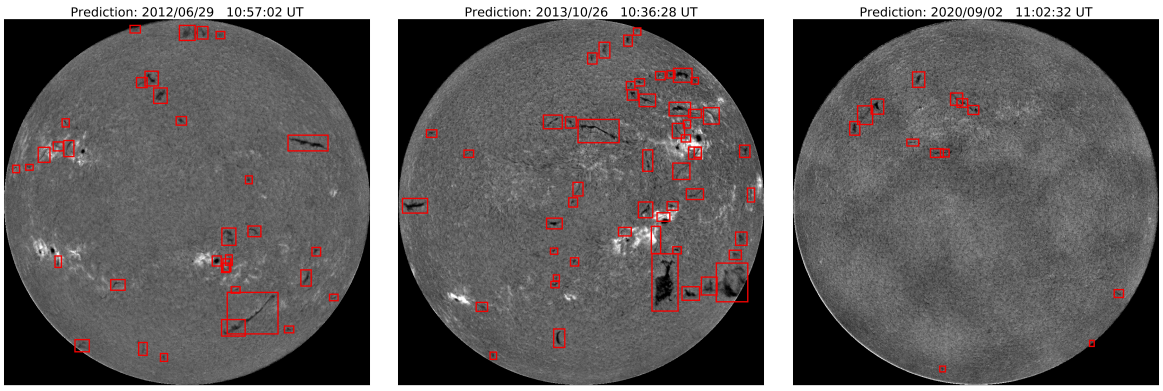

Figure 5.4: Sample Hα filtergrams of KSO with the predicted bounding boxes from YOLOv5 trained on ChroTel data for different years: 2012 June 29 (left), 2013 October 26 (middle), and 2020 September 2 (right). The rotation of the images were not corrected.

Ti with 11 GB Memory, which is used for training. We select the "YOLOv5x" model with the highest mAP score on a reference dataset. The first training is performed with 60 epochs and lasted 26 minutes. The predictions already show many detections of filaments, but not all filaments were found, yet. The evaluation scores, including GIoU, precision, recall, and mAP, do not converge at this point. The test is repeated with the pre-trained weights from the reference dataset, to evaluate, if transfer learning generates a higher prediction of filaments. The results are nearly identical.

After setting the baseline, we adjust the training setup. In order to better detect small-scale filaments, we train the neural network with image patches of the full resolution image. We implement the selection of randomly located patches from the input images with a resolution of 1024×1024 pixels, on which the dataset was labeled. The patches have a size of 512×512 pixels. The labels for the bounding boxes in each patch were selected accordingly. The training of 300 epochs lasted two hours. The resulting evaluation metrics are displayed in Figure 5.2. The GIoU score gradually converged to zero as well as the objectness, which indicate a very good overlap of the ground-truth and predicted bounding boxes. The precision and recall reached values of about 0.47 and 0.77, respectively. The recall indicates that there are few false negative detections. The mAP@0.5 reached a score of 0.68, which is already very high. The mAP@0.95 of 0.25 after 300 epochs. The values for precision, recall, and mAP show convergence.

The comparison of the ground-truth bounding boxes (left panels) and the predicted bounding boxes (right panels) is displayed for three examples in Figure 5.3. The examples show different activity levels during the solar cycle. The observations of 2012 June 29 and 2013 October 26, shortly before and around the solar maximum, show a high level of activity with many active regions and filaments, whereas the observation from 2020 September 2 shows the activity condition during the solar minimum, where only a few filaments and active regions are present on the Sun. From the examples, we can see that almost all labeled filaments were predicted by the object detection algorithm and that even very small filaments and an erupting filament (2013 October 26) were successfully detected. Our method shows a high stability and frequently identifies filaments that were missing in the original labels (filaments close to disk center in Fig. 5.3, upper row). The bottom row of Fig. 5.3 shows a direct comparison of an observation without labels and the neural network predictions. When a filament is separated into several smaller structures, the separation is sometimes different (Fig. 5.3, upper row, large filament close to the southern pole). The trained model is used to predict the bounding boxes for the full ChroTel dataset and also on the additional data of 2020, which is possible in few seconds. The visual inspection of the results showed remarkable good results in the detection of filaments.

For additional tests of the model, we use KSO Hα filtergrams. Therefore, we used the same data processing steps as for the ChroTel images, i.e., normalization to the median intensity of the solar disk, limb darkening correction, and correction of non-uniform intensity changes with Zernike polynomials, but the images were not rotated to solar north. The results are shown in Figure 5.4 for three samples in different states of the solar cycle with high activity in 2012 and 2013, and minimum activity in 2020 with only small-scale filaments. Moreover, in 2020 the solar disk is covered by clouds, which shows that the neural network is even stable during bad observing conditions.

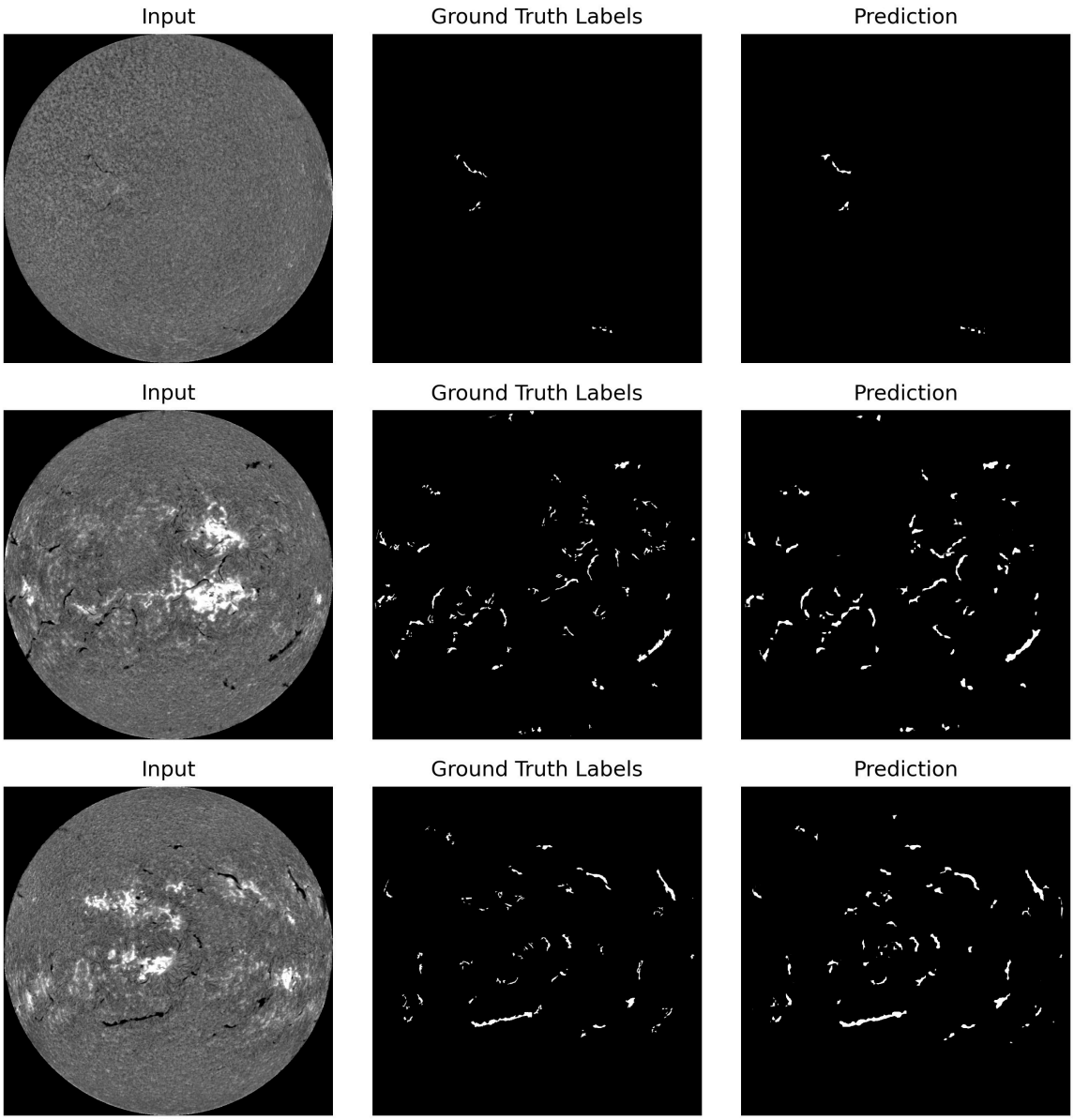

Figure 5.5: Three examples of filament segmentation. The input image of ChroTel (left), the ground-truth mask created from the labeled ChroTel images (middle), predicted segmentation mask from DeepLabv3 (right).

5.3.2 Segmentation of Filaments Using a Deep Neural Network

The next step is to extract filaments from the locations found with the object detection algorithm. Therefore, we choose a deep learning segmentation approach: DeepLabv3. The DeepLabv3 model is available as a standard model in the `torchvision` library of `Pytorch`. DeepLabv4 uses Residual Network-101 (ResNet-101, He et al., 2016) as a backbone. In addition, we use as an optimizer stochastic gradient descent (SGD, Goodfellow, Bengio, and Courville, 2016) and a binary crossentropy (BCE, Goodfellow, Bengio, and Courville, 2016) as the loss function. The model is trained with the labeled ChroTel images from 2012 to 2018. As an input for the training of the segmentation model, we use the ChroTel images with a resolution of 1024×1024 pixels and the corresponding binary masks with the locations of the filaments. The labeled bounding boxes assist in creating the binary mask, whereby we determine a threshold for each part of the image located in a boundary box, based on the mean intensity of this image part subtracted by its standard deviation. This threshold showed the best results in generating the binary masks. All objects with less than this threshold are included in the mask. Some examples of the ChroTel images and the generated ground-truth binary masks are displayed in Figure 5.5 (left and middle panels).

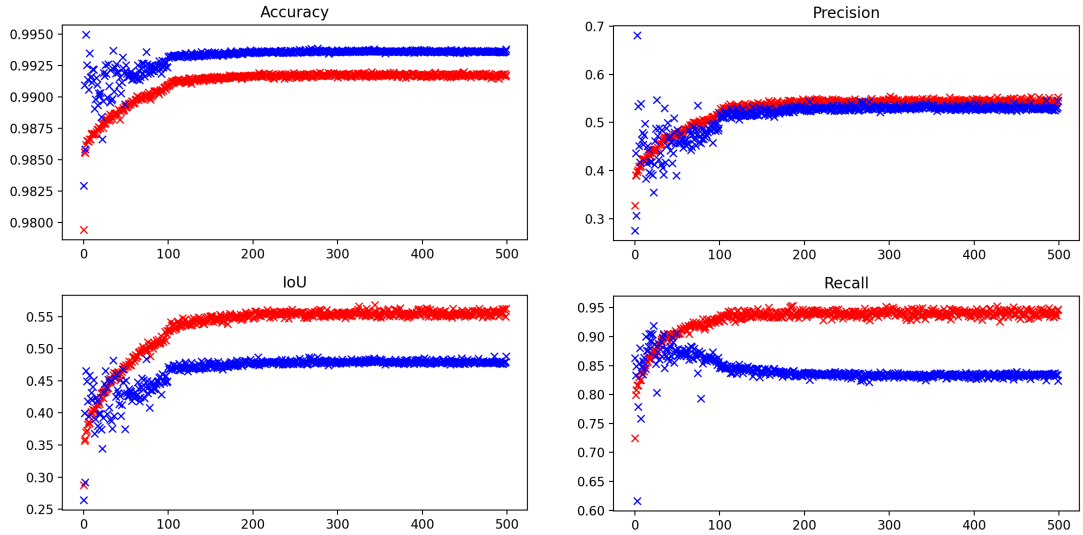

Figure 5.6: Evaluation parameters from the training of the segmentation model DeepLabv3 with ChroTel data: accuracy (upper left panel), intersection over union (IoU, lower left panel), precision (upper right panel), and recall (lower right panel), for training set (red) and validation set (blue).

The labeled data are separated into a training and validation data, whereby ten percent of the data is used for validation. As for the object detection algorithm, we define image patches of 512×512 pixels, but for the validation set, we pass the image with a size of 1024×1024 pixels. The evaluation of the results is performed with accuracy, IoU, precision, and recall, which are also used as direct input to the model to improve the results of the training as well as the loss function. The accuracy compares the ground-truth segmentation mask with the predicted mask. A sample of the evaluation parameter for one sample training with 500 epochs is displayed in Figure 5.6 for the training and validation dataset. All four parameters converged. The IoU reached a value of 0.56, the precision of about 0.55, and recall of 0.95, for the training dataset. The validation dataset reaches smaller values for the IoU and recall, but in this case also much less data are used. The accuracy is very high with values of over 0.99 for both datasets. The predicted masks are almost identical with the ground-truth masks or even show additional filament detections and extractions than the ground-truth mask (Figure 5.5, right panels). The most important part of the training is that sunspots are not segmented in the data, which is clearly the case for most maps. Figure 5.7 displays a sample image with the overlying location of the labeled bounding boxes for ChroTel and the results from the segmentation on 2012 June 29. Most filaments located in the bounding boxes are detected and segmented by the model.

These are just the first results of the segmentation algorithm, further development is still ongoing. The first approach was to use the already labeled data of ChroTel from 2012 to 2018. Using the object detection with YOLOv5, more labeled data of comparable quality can be automatically created. This can be an additional input for the training of the segmentation model. Two more years of data can be included. In addition, we want to use the KSO data as an additional training input. From a first comparison we showed that the object detection with YOLOv5 on an unknown data source is working. Including KSO in the training, would improve the stability of the detections for both YOLOv5 and the segmentation model DeepLabv3. Moreover, we can test both methods on yet unknown data sources, e.g., BBSO, the Uccle Solar Equatorial Telescope (USET, Clette et al., 2002), and the Global Oscillation Network Group (GONG, Harvey et al., 1996). We will include in the pipeline an automatic image reduction standardized to use it on different data sources. The pipeline including YOLOv5 and DeepLabv3 trained for filament detection and segmentation will be publicly available on GitHub.

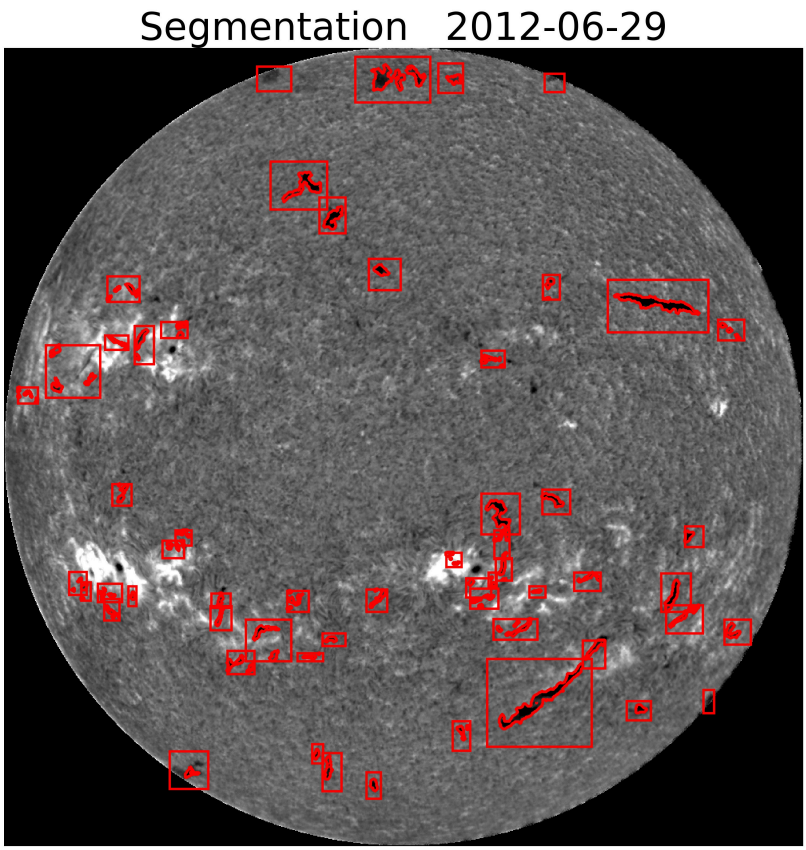

Figure 5.7: The predicted segmentation (red contours) from the segmentation model DeepLabv3 for a sample ChroTel image on 2012 June 29. The bounding boxes (red squares) display the labeled bounding boxes.

5.4 Discussion

From a qualitative evaluation we conclude that the filament detection using the object detection algorithm YOLOv5 is very fast and we obtain very good results in the detection of filaments at all scales and independent of the location, including small active region filaments located in bright plage regions or close to the solar pole. Even filaments, very close to the limb and erupting filaments are identified by the neural network. The main driver for this study was to differentiate between filaments and sunspots, which cannot be trivially solved with morphological image processing as seen in Chapter 4, where we excluded small-scale structures to avoid sunspots in the data, but excluded small-scale filaments, as well. As we will discuss in Chapter 7, there is a large number of polar crown filaments of small-scale. Often a larger polar crown filament is visible as many small-scale structures. In order to infer basic physical properties of filaments, e.g, location, length, width, connectivity to other layers; and to perform effective statistical studies with these properties, in particular of polar crown filaments and their migration, an effective localization of filaments is of utmost importance.

The YOLOv5 is an out-of-the-shelf detection algorithm, which is easily installed, and trained very fast. The detection process is possible in real-time, once the network is trained. This gives a very fast possibility to create a labeled dataset with a very high precision of filament detections. The model training was only performed with observations from ChroTel. The evaluation of Hα filtergrams from KSO, shows that our method can be directly applied to new datasets without any additional labeling or model training. In order to further increase the performance, a training with different data sources would be necessary.

The segmentation allows us to extract the filaments directly from the images by using the predicted masks generated by the network. In the study of Zhu et al. (2019), the trained U-Net efficiently segmented filaments, but sunspots were not excluded. The major problem was the use of a semi-manual ground-truth, which contained already sunspots. Other methods were developed to separate filaments and sunspots using SVMs (Qu et al., 2005), but this needs an additional training and computation. The approach of Ahmadzadeh et al. (2019) used a different approach for the training data with ground-truth masks created from the HEK database, which have an accuracy of 72% compared to hand-labeled data (Ahmadzadeh

et al., 2019). In our approach, we used manually labeled data and created the binary input masks from the labeled data. Sunspots are in most cases excluded, while small-scale filaments and filaments close to the limb are included in the annotations. This results in an optimal precondition for an effective training of the network for the segmentation of filaments. The results justify the initial effort in labeling.

5.5 Conclusions and Outlook

The filament detection and segmentation approach was very successfully applied to the ChroTel database. The object detection algorithm was even tested on previously unknown KSO data and detected effectively filaments. Further tests will be carried out to optimize the segmentation algorithm for the ChroTel dataset. We also want to test the segmentation algorithm on the KSO data. Further tests will reveal, if a training of ChroTel and KSO data together will improve the detection and segmentation of filaments. A large-scale data integration from different telescopes will be then possible. Further applications could be the automatic detection of eruptive filaments in real-time, which is relevant for the forecast of coronal mass ejections (CME) and space weather events, which could hit Earth. The Sun is observed by many telescopes from all over the world in Hα. Ground-based solar telescopes are restricted to observations during the day. Automated and reliable detection is required to analyze the data stream from multi-site observatories.

The training can also be extended by using other wavelengths. In the case of ChroTel, the Ca II K observations can be used for a better differentiation between filaments and sunspots, because in the Ca II K filtergrams sunspots are better visible. Some remnant filamentary structures are still visible in filtergrams of the Ca II K line (Kuckein, Verma, and Denker, 2016; Diercke et al., 2020, see Chapter 7). The He I λ 10830 Å give a further opportunity, because the spectroscopic data allow us to use continuum observations, which only show sunspots, whereas the line-core filtergrams display sunspots and filaments, as well as plage regions as dark structures.

Moreover, the data can be used as an input for the HEK database, but utilizing not only BBSO data (Ahmadzadeh et al., 2019), but of several instruments with nearly real-time detection. Furthermore, the segmented filaments can be used as input data for another detection algorithm, e.g., to detect coronal holes (Hofmeister et al., 2019; Palacios et al., 2020; Illarionov, Kosovichev, and Tlatov, 2020) in EUV data of SDO. Both filaments and coronal holes are visible as dark objects in the solar corona, i.e. in SDO observations at 193 Å. Therefore, often filaments are detected incorrectly as coronal holes. If the network learns to differentiate filaments from coronal holes, the detection of coronal holes can be improved as well. In addition, the training can be extended by not only giving the location of filaments in the EUV maps, but by training the data with Hα full-disk observations.

Beside filaments other structures can be detected with these methods. Other classes can easily added, for example, sunspots, which are omnipresent in full-disk observations of the photosphere and chromosphere. This would require a labeled dataset of sunspots to start the training, which can be created from morphological maps of dark objects, excluding the already detected filaments. Going from full-disk images to high-resolution ground-based observations enables many new applications of object detection and segmentation approaches based on deep learning. High-resolution observations of the High-resolution Fast Imager (HiFI, Kuckein et al., 2017; Denker et al., 2018) at the GREGOR solar telescope (Schmidt et al., 2012) are collected in a large data archive with observations in G-band (3500 images), blue continuum (2100 images), and Ca II H (2800 images) on about 110 observing days in 2016. The labeling of the data is in progress and implementing object detection with YOLOv5 is planned in the framework of the SOLARNET project. Starting 2021, the world's largest solar telescope, the Daniel K. Inouye Solar Telescope (DKIST, Tritschler et al., 2016) with a primary mirror of 4 m-diameter, observes regularly the Sun. A large amount of data is collected every day with high frame rates and petabytes of solar data. Deep learning algorithms for classification, object detection, and segmentation will be of utmost importance for the new era of solar observations.

Chapter 6

Solar Hα Excess during Solar Cycle 24 with Data from Full-disk Filtergrams of the Chromospheric Telescope

The first record of a varying sunspot number throughout a solar cycle was found in systematic sunspot observations by S. H. Schwabe in the 19th century (Schwabe, 1844; Hathaway, 2010; Arlt et al., 2013; Arlt and Vaquero, 2020). This was followed in systematic observations by R. Carrington (Carrington, 1858) and G. Spörer (e.g., Spörer, 1879; Diercke, Arlt, and Denker, 2015). R. Wolf established the relative sunspot number, counting the spot groups and individual sunspots (Hathaway, 2010). This method is still used nowadays to determine the International Sunspot Number provided by the Solar Influences Data Analysis Center (SIDC) of the Royal Observatory of Belgium, which is used to monitor the 11-year activity cycle of the Sun.

Throughout the years, many other wavelengths were used to monitor solar activity, e.g., the chromospheric Ca II K line, which is sensitive to the magnetic field. Livingston et al. (2007) summarized the results from three solar cycles where they analyzed spectroscopic data of different chromospheric lines. The spectral Ca II K index showed the highest variations throughout the cycle with amplitudes of about 25%. Other chromospheric line indicators including He I 10830 Å equivalent width, Ca II 8542 Å central depth, Hα central depth, or CN bandhead at 3883 Å, all showed variations with the solar cycle, but with a lower relative amplitude as compared to Ca II K. Full-disk Ca II K measurements show an average increase of 30% of the central intensity between minimum and maximum of the solar cycle (White and Livingston, 1981), whereby the increase is associated with solar plages. The authors suggest that the variability of the quiet-Sun network is negligible in the rising phase of the solar cycle. A more recent study by Bertello et al. (2016) combines measurements of the disk integrated Ca II K emission index of the Synoptic Optical Long-term Investigations of the Sun (SOLIS, Keller, Harvey, and Giampapa, 2003; Bertello et al., 2016) facility with measurements of the Ca II K emission from full-disk images of the Kodaikanal Observatory of the Indian Institute of Astrophysics in Bangalore. Naqvi et al. (2010) used average full-disk images of the Big Bear Solar Observatory (BBSO, Denker et al., 1999), to calculate an index using an adaptive intensity threshold to extract the bright plage regions from Ca II K full-disk images (Johannesson, Marquette, and Zirin, 1998). With this index they characterized the solar activity of Solar Cycle 23 for different thresholds in comparison with other solar indices. A very complete data collection of Ca II K observations was recently presented in Chatzistergos et al. (2020), who collected around 290 000 full disk Ca II K observations from 43 datasets including observations between 1892 and 2019. They used the fractional plage area on the solar disk as an index for the solar activity. Further chromospheric spectral indices from high-resolution solar spectra obtained utilizing the Potsdam Echelle Polarimetric and Spectroscopic Instrument (PEPSI, Strassmeier, Ilyin, and Steffen, 2018), whereby the light is collected by the Solar Disk-Integrated (SDI) telescope, is currently studied by Dineva et al. (2020b).

Other well established solar indices include Mg II and F10.7 cm radio flux. The chromospheric Mg II doublet at 2795.6 Å and 2802.7 Å is used since 1978 as a proxy for solar activity (Viereck and Puga, 1999). The index is calculated from the core-to-wing ratio of the spectral line. This spectral Mg II index

varies up to 20% between minimum and maximum. It is especially good in monitoring solar faculae, as Lean et al. (1997) determined from solar irradiance models, which consider both sunspot darkening and faculae brightening. The F10.7 cm solar flux index monitors the disk integrated radio emission at 10.7 cm or 2800 MHz since 1946 (Tapping and Charrois, 1994; Hathaway, 2010). Several measurements a day are obtained, whereby periods of flares are avoided. The radio flux is strongly correlated with the relative sunspot number but with a lag time of about one month (Hathaway, 2010).

Toriumi et al. (2020) studied transiting active regions with space-borne data of the Helioseismic and Magnetic Imager (HMI, Scherrer et al., 2012) and the Atmospheric Imaging Assembly (AIA, Lemen et al., 2012) onboard the Solar Dynamics Observatory (SDO, Pesnell, Thompson, and Chamberlin, 2012) as well as data of the Hinode X-Ray Telescope (XRT, Golub et al., 2007). The continuum observations showed that the light curves of the active region's intensity decrease when the sunspot is at disk center, while the light curve increases when the active region is close to the limb. This effect is well known from observations of the total solar irradiance (TSI, Fröhlich, 2012) and shows that the effects of the umbra and penumbra of the active region dominates close to disk center. The LOS magnetic flux as well as the UV irradiance (1600 Å and 1700 Å) show an bell-shaped (or mountain-shaped) light curve. In case of the UV irradiance, the bandpass is sensitive to faculae regions rather than to sunspots (Simões et al., 2019; Toriumi et al., 2020).

The Sun is regularly observed in another prominent chromospheric line, i.e., the Hα spectral line at 6562.8 Å. Several observatories form the Global Hα Network (Steinegger et al., 2000), including the BBSO and the Kanzelhöhe Solar Observatory (KSO, Otruba, 1999), and take regular full-disk images in the line core of Hα. In total, seven facilities around the world are part of this network, which continuously observe Hα line-core filtergrams. Similarly, the Global Oscillation Network Group (GONG, Harvey et al., 1996) of the U.S. National Solar Observatory (NSO) consists of six facilities observing, which produce, among other data products, time series of full-disk Hα filtergrams and magnetograms. In addition, other observatories provide regular full-disk Hα observations, e.g., the Chromospheric Telescope (ChroTel, Kentischer et al., 2008; Bethge et al., 2011). The large number of ground-based facilities all around the world facilitate almost continuous coverage of the Sun with full-disk Hα filtergrams, bridging bad weather locally and the day-night cycle.

The variation of Hα throughout the solar cycle is known from disk- integrated observations (Livingston et al., 2007; Maldonado et al., 2019). The Hα line has the advantage of displaying two main contrast features: bright plage regions around active regions and dark filaments and sunspots. Especially, filaments of all sizes dominate the solar disk in this spectral line, ranging from small scale active region filaments to large scale polar crown filaments.

Another advantage of using Hα as a solar activity indicator is that Hα spectra are easily obtainable for stars other than the Sun. Thus, activity metrics and cycle information based on Hα variations on the Sun can potentially be used to infer stellar activity properties for which Ca II H & K diagnostics, for example, are not obtainable.

The Sun is the only star for which we can obtain spectra of active regions at high spatial resolution. As a result, there is an inherent degeneracy for other stars between the projected area and intrinsic emission strength of their active regions (e.g., Cauley, Redfield, and Jensen, 2017). This degeneracy makes it difficult to measure such properties for other stars, which is important when trying to quantify and remove the contamination of stellar activity from exoplanet transmission spectra (Cauley et al., 2018; Rackham, Apai, and Giampapa, 2018). It is also important from the view of stellar physics: what are the intrinsic emission strengths in individual active regions for different chromospheric lines for stars of varying spectral type and magnetic activity level? Empirical constraints on these quantities will provide guidance for sophisticated 3D MHD radiative transfer models of stellar atmospheres (Leenaarts, Carlsson, and Rouppe van der Voort, 2012; Holzreuter and Solanki, 2015; Štěpán et al., 2015).

The aim of this study is to explore the capabilities of spatially-resolved Hα excess as a tracer of solar activity. Bright and dark regions, each at different thresholds, are identified in ChroTel full-disk Hα filtergrams. We compare the positive and negative imaging Hα excess with established solar activity tracers such as the relative sunspot number, the F10.7 cm radio flux, and the Mg II index (Section 6.3.1). One goal is to determine the contribution of low-activity regions to solar cycle variations of the Hα spectral irradiance and to relate it to stellar cycles for modelling the X-ray emission of stars (Section 6.3.2).

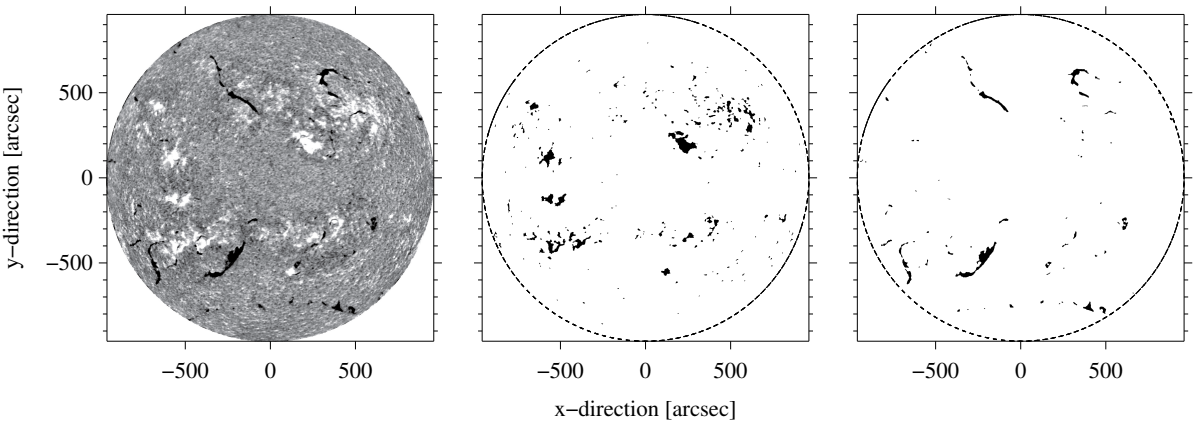

Figure 6.1: ChroTel Hα filtergram (left) and the corresponding mask for bright (middle) and dark features (right). The solar disk is indicated as a dashed circle.

The second driver is to answer the questions, if the Hα activity level is dominated either by changes of active region emission or by the coverage fraction of Hα emitting regions on the solar disk (Section 6.3.3 and Section 6.3.4). This is especially important for modelling exoplanet atmospheres, disentangling the star's surface from the planet's atmosphere.

6.1 Observations and Data Processing

The Chromospheric Telescope is a robotic ground-based 10-centimeter telescope, located at the Observatorio del Teide, Tenerife, Spain, which observes the Hα line with a Lyot-type narrow-band filter at 656.2 nm with a full width at half maximum (FWHM) of $\Delta\lambda = 0.05$ nm and a cadence of three minutes. The recorded images have a size of 2048×2048 pixels. Regular observations started in April 2012. Technical problems resulted in larger data gaps of several months, i.e., in 2017 and 2019. For an overview of the acquired data between 2012 and 2018 see Fig. 1 in Diercke and Denker (2019). In Table 6.1, we present the number of observing days per year. The ChroTel observations cover the maximum of Solar Cycle 24 and the declining activity phase until the minimum of solar activity. Therefore, we have a representative statistical sample of the different activity phases within Solar Cycle 24.

To study long-term solar activity, we selected one Hα filtergram per day by calculating the Median Filter-Gradient Similarity (MFGS, Deng et al., 2015; Denker et al., 2018), where magnitude gradients of an input image and its median-filtered companion are compared. We selected the image with the highest MFGS value for each observing day. All images underwent basic data processing steps, including flat-field and dark corrections. Level 1 data were rotated so that solar north is on top and east to the left, and the elliptical shape of the Sun was corrected for early morning and late evening data. All images were scaled so that the solar radius equals $r_\odot = 1000$ pixels, which results in an image scale of about $0\farcs96\,\mathrm{pixel}^{-1}$. Moreover, the Lyot-filter introduced a non-uniform intensity pattern across the solar disk, which was corrected by approximating the pattern with Zernike polynomials (Shen, Diercke, and Denker, 2018). All images are limb-darkening corrected, normalized to the median value of the quiet-Sun intensity, and centered. Details of the data processing are described in Diercke and Denker (2019).

6.2 Method

In order to explore the capabilities of Hα as a proxy for solar activity, we will use the Hα excess calculated for bright regions and dark (absorption) features at different thresholds. To extract bright regions, related to plage, we created a mask with a dynamic threshold T_k related to intensities with 0%, 2.5%, 5%, 7.5%, and 10% above the median intensity I_{med}:

$$T_k = I_{\mathrm{med}} + [0.0, 0.025, 0.05, 0.075, 0.1] \times I_{\mathrm{med}}. \tag{6.1}$$

Table 6.1: Overview of Hα observations with the Chromospheric Telescope in 2012 – 2020.

Year	Number of observing days
2012	146†
2013	210
2014	172
2015	115
2016	102
2017	76
2018	141
2019	38
2020	56*

† starting 13 April
* until 2 September

We used morphological image processing to extract these regions more efficiently. First, we applied morphological closing on the masks using a circular structuring element with a radius of ten pixels. We excluded small areas with less than 20 pixels and removed border effects at 0.99 $r_{\odot}$ (Fig. 6.1). From all pixels R_{ij}, we calculated the positive imaging Hα excess E_k of the bright regions, similar to the method described in Naqvi et al. (2010):

$$E_k = \frac{1}{1000} \sum_{ij} f_{ij} \quad \text{with} \quad \begin{cases} f_{ij} = |R_{ij} - T_k| & \text{if } R_{ij} \geq T_k \\ f_{ij} = 0 & \text{if } R_{ij} < T_k \end{cases} \tag{6.2}$$

This results in the positive imaging Hα excess E_0, E_{25}, E_{50}, E_{75}, and E_{100} at thresholds T_k as defined in Eq. (6.1) for additional 0%, 2.5%, 5%, 7.5%, and 10% above the median intensity, respectively. The same procedure is repeated for the absorption features, including sunspots and filaments, whereby the threshold is defined as:

$$T_k^- = I_{\text{med}} - [0.0, 0.025, 0.05, 0.075, 0.1] \times I_{\text{med}}. \tag{6.3}$$

from which we create the negative imaging Hα excess E_k^- for each threshold T_k^-: E_0^-, E_{25}^-, E_{50}^-, E_{75}^-, and E_{100}^-. We will compare the imaging Hα excess for dark and bright regions with the mean intensity I_{mean} of all bright regions (Section 6.3.1). Moreover, the mean intensity is calculated for all identified Hα excess regions. In Section 6.3.2, we calculate their distribution as a function of the normalized Hα intensity for a certain time span during minimum and maximum.

6.3 Results

6.3.1 Imaging Hα Excess

We will discuss in this section the positive and negative imaging Hα excess for bright and dark regions, respectively, at various thresholds and compare both to the mean intensity of the bright regions. The Hα excess will be also compared to other activity indices.

Figure 6.2 displays the monthly average of the Hα excess for different thresholds T_k for the bright (top left) and dark (top middle) solar features. The observations started in April 2012, shortly before the maximum of Solar Cycle 24 on the northern hemisphere in November 2012, which is followed by the maximum on the southern hemisphere about 16 month later in March 2014 (Sun et al., 2015). The magnetic field reversal at the poles, which occurs around the time of the maximum, is marked with vertical gray bars for each hemisphere (Sun et al., 2015). The recorded data cover the activity minimum in 2018/2019 and the start of Solar Cycle 25 in 2019/2020.

The shape of the average monthly Hα excess for the different thresholds is very similar but with an offset in intensity, which results from the high number of pixels close to the median intensity and is related to the quiet-Sun, which shifts the curve along the ordinate. These pixels influence the amplitude of the curve, which is highest for the threshold equal to the median E_0 with an amplitude of about $A_{E_0} = 40$ and lowest for the Hα excess with the highest threshold E_{100} with an amplitude of about $A_{E_{100}} = 20$. In the following, we will use the Hα excess with the highest threshold E_{100}, because at this threshold only

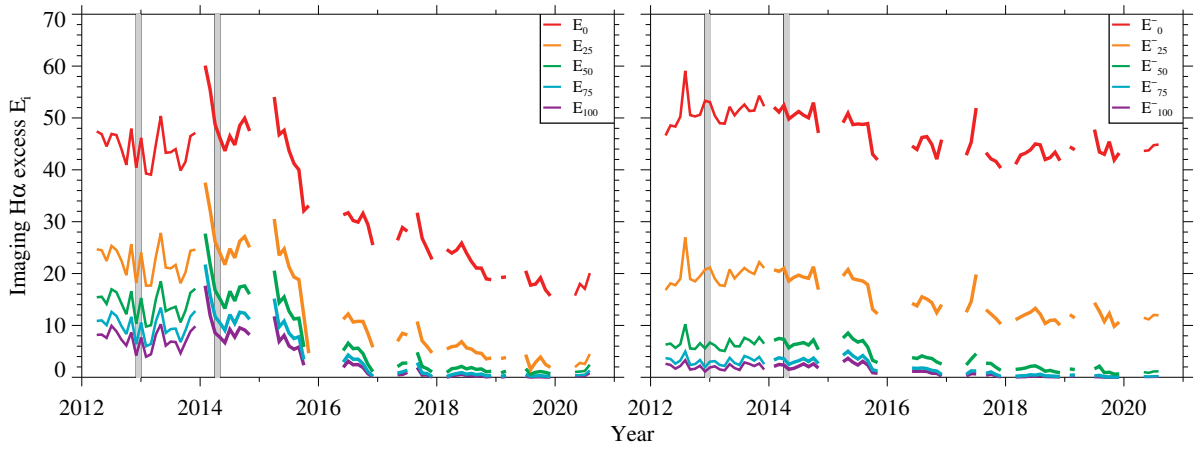

Figure 6.2: ChroTel imaging Hα excess in 2012 – 2020 of bright features (left) and of dark features (right) for different thresholds (from top to bottom): E_0, E_{25}, E_{50}, E_{75}, and E_{100}. The gray areas in the background indicate the northern and southern magnetic field reversal in November 2012 and March 2013, respectively.

plage regions are taken into account and most of the "quiet-Sun" pixels are neglected. We clearly see that the Hα excess is highest around maximum and decreases towards the minimum when the number of active regions and the related bright plage regions is lower. The motivation of this study is to characterize the intensity excess from the bright regions for possible relations to stellar activity studies. The negative Hα excess might help the solar-stellar connection community to quantify how much the Hα intensity decreases across the solar or stellar disk because of absorption features in the atmosphere. The curve of the negative Hα excess for the absorption features (right panel in Fig. 6.2) shows overall a similar shape as the positive Hα excess for the bright regions, but with smaller amplitudes. In general, the Hα excess follows the global evolution of the solar activity. A detailed comparison is provided in Fig. 6.3 for the individual positive and negative Hα excess E_{100} and E^{-}_{100}, respectively.

The vertical gray bars in Fig. 6.2 indicate the magnetic field reversal in the northern (left panel) and southern hemisphere (right panel) during the maximum of Solar Cycle 24 (Sun et al., 2015). Especially, before the magnetic field reversal in the southern hemisphere, we see a strong peak in the positive Hα excess. The negative Hα excess of absorption features exhibits only a relatively small peak before the magnetic field reversal in the northern hemisphere. We will discuss this in detail for individual observations in Fig. 6.3.

In Fig. 6.3, we compare the positive Hα excess E_{100} (top left panel) directly with the negative Hα excess of the absorption features E^{-}_{100} (top middle panel). Both indices are set against with the mean intensity I_{mean} of Hα excess regions throughout Solar Cycle 24 (top right panel). The daily Hα excess values (cyan asterisks) as well as the monthly average (white curve) are displayed.

The changes between the maximum and minimum of the solar cycle are best visible in the positive Hα excess E_{100}. Here the values vary between $E^{\mathrm{max}}_{100} \approx 20$ around the activity maximum and $E_{100} \approx 1$ around in the activity minimum. The spread of the daily Hα excess around the maximum varies between $E_{100} \approx 5$ and $E_{100} \approx 20$, whereas around the minimum the variations are much smaller between $E_{100} \approx 2$ and $E_{100} \approx 0$. This is related to the very small number of active regions during the minimum. We can see that the positive and negative Hα excess is increasing shortly before the magnetic field reversal in the northern hemisphere (left gray bar). For the magnetic field reversal in the southern hemisphere (right gray bar), the positive Hα excess increases just before the magnetic field reversal to its maximum and stays high for several months.

For the negative Hα excess of absorption features, the values vary between $E^{-}_{100} \approx 7$ and $E^{-}_{100} \approx 0$ between maximum and minimum, respectively. The variation is much stronger in the maximum, covering the full range from maximum values to low values of about $E^{-}_{100} \approx 1$ in just a few days, while variations of the daily Hα excess are very small during the minimum. This indicates that absorption features such as filaments are reduced in number during the solar minimum. Just before the magnetic field reversal in the northern and southern hemispheres, the negative Hα excess is high and drops after the reversal, which could indicate the disappearance of polar crown filaments after the magnetic field reversal at the end of

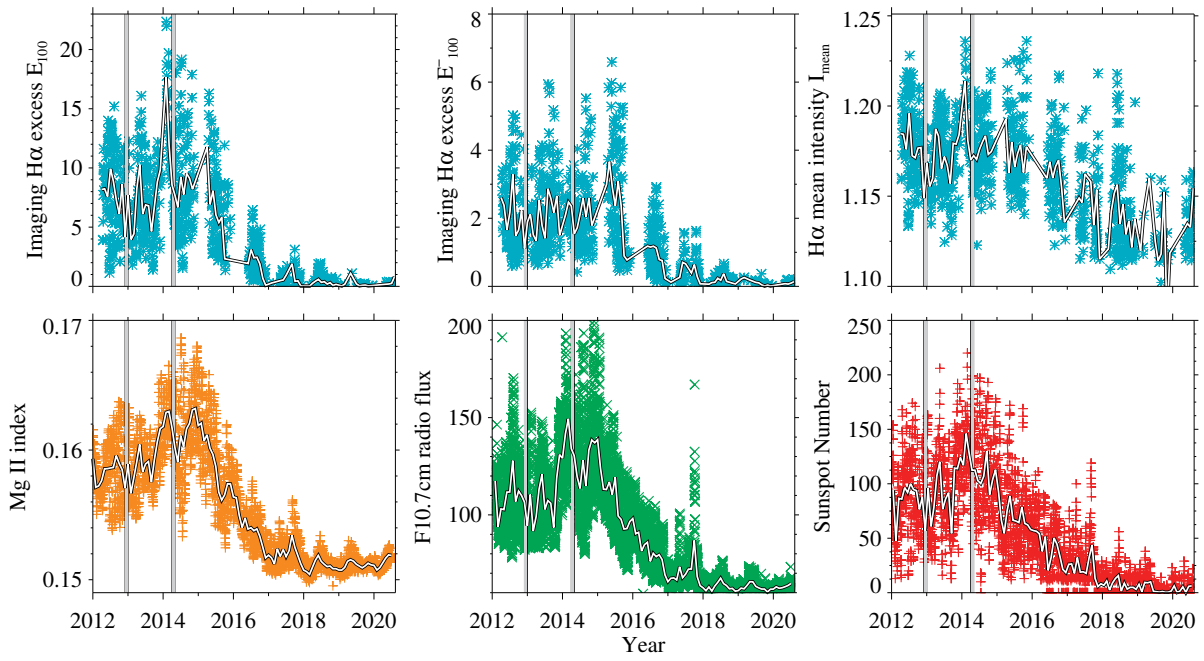

Figure 6.3: Comparison of the imaging Hα excess with different solar activity indices during Solar Cycle 24 in 2012 – 2020. Upper panel: imaging Hα excess E_{100} of bright features (left), imaging Hα excess E^{-}_{100} of dark features (middle), and mean intensity of Hα excess regions (right). Lower panels: Mg II index (left), F10.7 cm radio flux (middle panel), and relative sunspot number (right) for daily observations. The monthly average for all proxies is shown as a white line. The gray areas in the background indicate the northern and southern magnetic field reversals in November 2012 and March 2013, respectively.

the "rush-to-the-pole" of polar crown filaments (Cliver, 2014; Xu et al., 2018; Diercke and Denker, 2019). Nonetheless, the number of absorption structures increases to an even higher level after the magnetic field reversal, which can be a joint effect of an increased number of sunspots and filaments in the activity belt close to active regions. A second "rush-to-the-pole" is not observed (Diercke and Denker, 2019). The drop from a high number of absorption features towards the minimum is steeper than for the bright regions.

The variations of the mean intensity of Hα excess regions (top right panel in Fig. 6.3) are large throughout the entire cycle but decrease towards the minimum. The daily variations decrease in the minimum and the intensity level is clearly reduced.

Several established solar activity tracers are commonly used in the solar community. To study the value of the positive and negative Hα excess as a tracer of solar activity, we compare in the following the Hα excess with three established proxies (lower panels in Fig. 6.3): spectral magnesium Mg II index,[1] the solar radio flux at F10.7 cm,[2] and the sunspot number.[3] We display the daily observations for each activity tracer as single points and their monthly average as a solid white line. The trend of the positive Hα excess is very similar to the other three proxies throughout the solar cycle. Towards the maximum the daily variations are high but in the monthly average much higher then in the minimum, where also the daily variation is reduced. To compare the positive Hα excess with the other tracers, we interpolated the monthly variation of the positive Hα excess to the other tracers and calculated the Spearman correlation σ_S for the monthly variation for each tracer. The correlation of the positive Hα excess is lowest for the smoothed sunspot number with $\sigma_S = 0.88$ and $\sigma_S = 0.91$ with the mean monthly sunspot number. The correlation to the F10.7 cm radio flux is $\sigma_S = 0.93$. The highest correlation is with the Mg II index with a correlation of $\sigma_S = 0.95$. The positive Hα excess and the Mg II index display both the solar activity of the chromosphere.

The high increase of the excess in Hα shortly before the magnetic field reversal in the southern hemisphere (right gray bar) is similar to the sunspot number and the F10.7cm radio flux, whereby the

[1] https://www.iup.uni-bremen.de
[2] https://spaceweather.gc.ca
[3] http://www.sidc.be

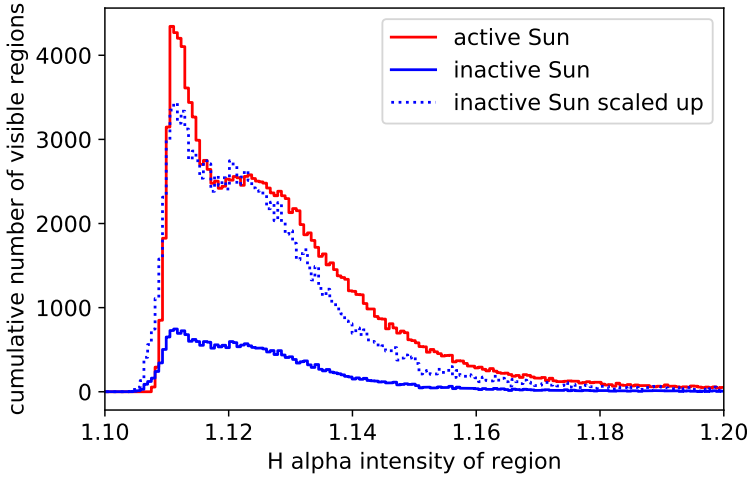

Figure 6.4: Intensity distribution of individual Hα excess regions shown as a histogram for the active Sun (red) and the inactive Sun (blue). A scaled-up histogram of the inactive Sun is provided for an easier visual comparison with the active Sun (light blue).

latter stays on a high level for several month after the reversal, whereas the Hα excess decreases in a similar manner as the Mg II index. The maximum of the Mg II index is shortly after the magnetic field reversal in the southern hemisphere. Direct comparisons of single peaks in the positive Hα excess during the minimum is difficult, because of the sparse observations from ChroTel during this time. Nonetheless, the overall decrease of activity is visible.

The Hα excess is calculated from solar Hα full-disk filtergrams for both bright and dark features, whereby the positive Hα excess for bright features is very similar to the chromospheric Mg II index and the F10.7 cm radio flux. Not only the positive Hα excess reflects the solar activity, but also the negative Hα excess of absorption features, which was never studied before. If we want to compare solar activity variations with solar-like stars, the typical solar activity indices such as the Mg II index and the F10.7 cm radio flux are not available on a regular basis. For stars, a typical activity tracer is the spectroscopic Hα index, defined by a line-to-continuum flux ratio around this spectral line (see e.g., Alvarado-Gómez et al., 2018). For the Sun, daily Hα full-disk observations are recorded with synoptic facilities. To effectively compare the solar activity with other stars, a database of the Hα excess is important. In the following, we discuss selected applications of the positive Hα excess to better understand the Hα bright and to improve modelling of stellar atmospheres.

6.3.2 Intensity Distribution of Active Regions

In the context of solar and stellar activity, not only the number of active regions, but also the distribution of Hα intensities of the observed regions is of interest. To investigate how the active and inactive parts of the solar cycle differ in the Hα properties of active regions, we selected individual Hα excess regions observed on the Sun in 330 days each around the solar minimum and maximum, as described in Section 6.2. We produced a histogram of the number of observed regions as a function of the normalized Hα intensity (Fig. 6.4). The total number of bright regions between solar maximum (red histogram) and minimum (blue histogram) differs by a factor of about four. The shape of those two distributions is almost the same, as can be seen when scaling the distribution for the inactive Sun up to the level of the active Sun (light blue histogram). Both distributions resemble a skewed Gaussian, with a longer tail towards higher intensities. The tail is slightly more extended for the active Sun.

The distribution of Hα intensities on the solar disk can be linked to our knowledge of other stars that display activity cycles. Stellar activity cycles are studied in various observables, i.e., from chromospheric emission (Noyes et al., 1984; Baliunas et al., 1995; Hall and Lockwood, 2004; Metcalfe et al., 2010) over white light modulation (Reinhold, Cameron, and Gizon, 2017; Nielsen et al., 2019) to X-ray emission (Hempelmann, Schmitt, and Stępień, 1996; Sanz-Forcada, Stelzer, and Metcalfe, 2013). We focus here on a particularly useful comparison to findings about stellar coronae during stellar activity minima and maxima, which are hypothesized to correspond to the underlying surface structures present on stars.

Coronal changes over a stellar activity cycle can be observed in soft X-rays, and a small number of cool stars have been monitored over more than a decade for their coronal cycles (Hempelmann et al.,

2006; Favata et al., 2008; Robrade, Schmitt, and Favata, 2012; Orlando et al., 2017). When analysing soft X-ray spectra with moderate resolution, such as they are provided by the current large X-ray observatories XMM-Newton (Jansen et al., 2001) and Chandra (Weisskopf et al., 2002), the data quality typically allows for two to three temperature components of the stellar corona to be fitted simultaneously. Robrade, Schmitt, and Favata (2012) showed that for the two stars 61 Cyg A and α Cen B, the coronal spectra in both the high and low activity states can be fitted with three temperature components each. When letting the temperatures of the three components free to fit, they found that the fitted temperatures are virtually the same, and only the emission measure of each component changes over the course of the cycle. This is in line with our finding that the distribution of mean intensities of individual regions retains basically the same shape between solar minimum and maximum, and only the number of regions that are present changes.

6.3.3 Rotational Modulation of the Positive Hα Excess

In this section, we inspect in detail solar rotation over a two-months period, both during the maximum and minimum phases (Fig. 6.5). We compare the Hα excess E_{100} of bright regions with their mean intensity and their surface coverage fraction as a percentage. During the maximum of the solar cycle (upper panel), we selected observations in August and September 2013, because we had consecutive observations with only six days missing. Here, we see a very strong correlation between the positive Hα excess (black curve) and its coverage fraction (blue curve). The Hα excess depends not only on the intensity in each region relative to the threshold but also on the number of pixels used for its calculation. This results in very high correlations of the Hα excess and the coverage fraction, i.e., $\sigma_S = 0.96$ for the Spearman correlation. Nonetheless, the correlation of the coverage fraction of the Hα excess (blue curve) and the mean intensity (red curve) is very high, i,e., $\sigma_S = 0.77$ for the Spearman correlation. The Hα excess varies between $E_{100}^{\min} = 1.4$ and $E_{100}^{\max} = 10.8$ on a time-scale of about 25 days, which is roughly the length of a solar rotation period at the solar equator (Balthasar, Vazquez, and Woehl, 1986; Arlt and Vaquero, 2020). The coverage fraction of the Hα excess covers the range 0.9 – 3.1%. The mean intensity varies only in the range $1.15 - 1.22\, I/I_{\rm med}$.

During the minimum of the solar cycle (lower panel of Fig. 6.5), we selected the observations of May and June 2018, because they were the most continuous observations with only 11 days missing due to bad weather conditions. Interestingly, the same similarities in the behavior of the coverage fraction of Hα excess to the mean intensity and Hα excess can be found. The Spearman correlation between the coverage fraction of Hα excess and the mean intensity is $\sigma_S = 0.85$, which is higher than the values for the maximum phase. The Spearman correlation between the Hα excess and the coverage fraction is $\sigma_S = 0.98$, which is comparable to the values from the maximum phase. The fluctuations of the Hα excess are much smaller compared to the maximum with variations from $E_{100}^{\min} = 0$ to $E_{100}^{\max} = 1.9$. In addition, the coverage fraction of the Hα excess is significantly smaller than for the maximum phase with values in the range 0.02 – 0.48%. The mean intensity is in the range $1.13 - 1.24\, I/I_{\rm med}$. We find a cyclic variation of about 14 days in all three variables. In the Hα filtergrams, we recognize that this effect was caused by one to three major active regions, which were present during the phases of enhanced activity. During the days of low activity, no major active region is visible on the solar surface.

6.3.4 Hα Excess of Active Regions

In this section, we discuss the variation of the mean intensity and Hα excess during the passage of three different active regions in 2013 around the solar maximum. We selected active regions NOAA 11818 (2013 August 9 – 20, 12 days), NOAA 11835 (2013 August 25 – September 4, 11 days), and NOAA 11850 (2013 September 19 – October 1, 13 days). We chose these active regions because their disk passages were almost completely covered by ChroTel observations with only one observing day missing for NOAA 11818 on 2013 August 12. A comparison to the minimum phase was not possible, because active regions were too small and did not survive an entire disk passage. Furthermore, the ChroTel data coverage was sparse during this time due to technical problems. The length of the disk passage of the three selected active regions varied because of size and compactness of the active regions. Active region NOAA 11850

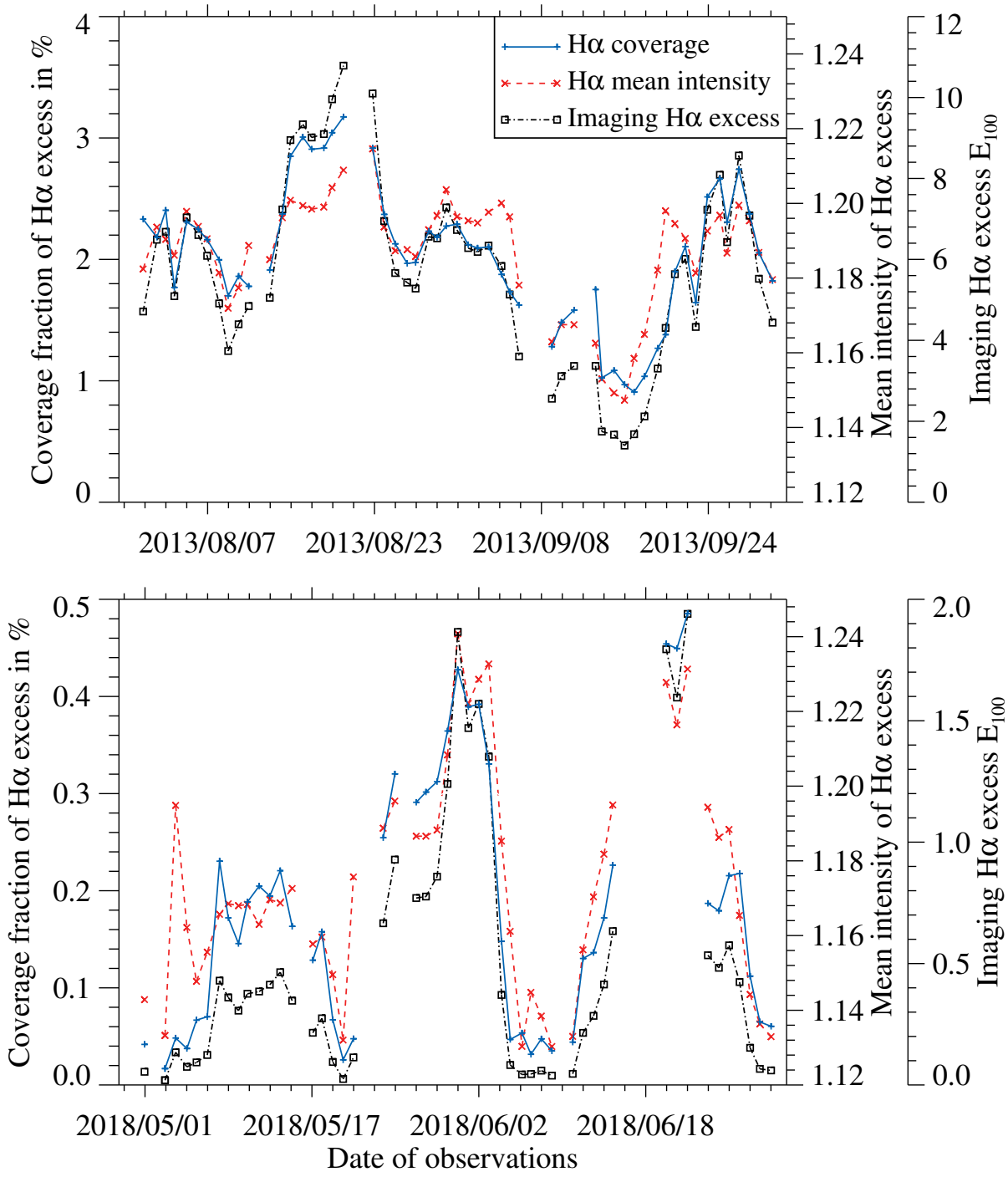

Figure 6.5: Coverage fraction of Hα emitting regions in percent (solid blue line), the mean intensity of the Hα emitting regions (dashed red line), and the Hα excess E_{100} of Hα emitting region (dash-dotted black line) in August and September 2013 around the maximum of Solar Cycle 24 (upper panel) and May and June 2018 around the minimum of Solar Cycle 24 (lower panel).

was very large and reached a length of almost 450″. It lasted thirteen days on the solar disk. Active region NOAA 11835 lasted eleven days and NOAA 11818 lasted twelve days. An overview of the disk passage of the active regions is presented in Fig. 6.6. For the sake of clarity, we concentrated on the eight central days (days 4 – 11) and discarded the limb observations. However, Fig. 6.7 displays the whole disk passage.

In Fig. 6.7, we display the Hα excess (black curve) during the passage over the solar disk of the three active regions, and we compare this with the mean intensity of each region (red curve) and with the number of pixels included in each active region (blue curve). As defined in Eq. (6.2), the Hα excess is a function of the number of pixels in each mask and the intensity. NOAA 11850 (left panel) is the largest active region and has the longest disk passage. The Hα excess at the east limb of the Sun is very

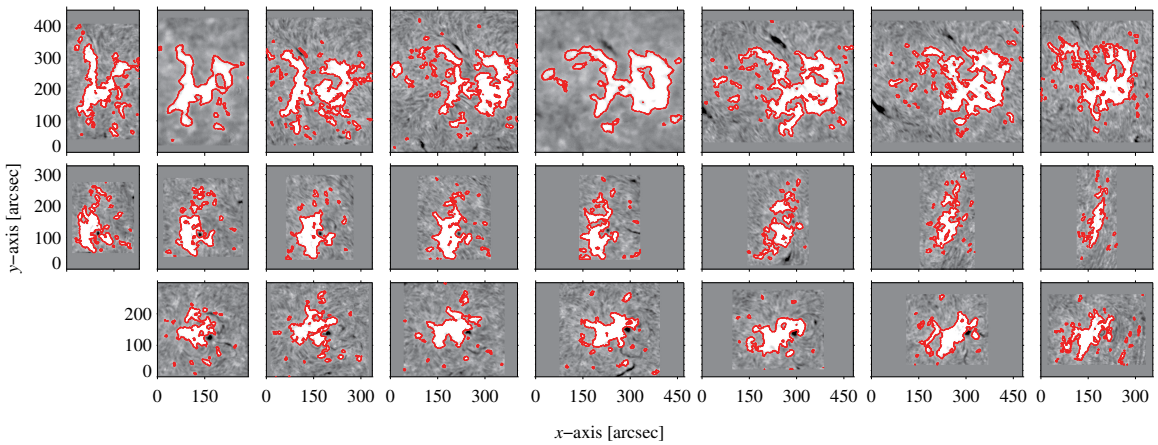

Figure 6.6: Regions of interest extracted from ChroTel Hα full-disk filtergrams, displaying the disk passage (days 4 – 11) of three active regions in 2013 during the maximum of Solar Cycle 24: NOAA 11850 (top), NOAA 11835 (middle), NOAA 11818 (bottom). The respective mask for each active region is displayed with red contours.

small, i.e., $E_{100} \approx 0.2$, and increases until day nine when the Hα excess reaches its maximum of $E_{100} \approx 5$. Towards the western limb, the Hα excess decreases again to a small value of $E_{100} \approx 0.4$. In contrast, the mean intensity is already high at the limb with an intensity of about $1.28\,I/I_{\mathrm{med}}$. Afterwards, the mean intensity decreases to an intensity of about $1.22\,I/I_{\mathrm{med}}$ until day four and stays on roughly the same level until the region disappears rotates off the solar disk. We assume that the active region was already fully developed when it rotated onto the solar disk. This may explains, why the mean intensity is already high at the beginning of observations. The lifetime of active regions vary from few hours for small ephemeral regions to months for large active regions (van Driel-Gesztelyi and Green, 2015). Projection effects at the solar limb cause a detector pixel to cover different fractions of an active region as compared to a pixel at disk center. Hence, the Hα excess is influenced because the coverage fraction at the limb is smaller than at disk center. Therefore, a correlation of the mean intensity with the Hα excess is absent as indicate by a comparably Spearman correlation of $\sigma_{\mathrm{S}} = 0.01$. Here, the evolution of the Hα excess is mainly dominated by the size (number of pixels) and not by its mean intensity.

On the other hand, for the smaller active regions NOAA 11835 (middle panel) and NOAA 11818 (right panel), the mean intensity increases during the disk passage and decreases towards the limb, which correlates well with the Hα excess. Especially in the case of active region NOAA 11818, the influence of the mean intensity on the imaging Hα excess becomes clear. For this active region, between days six and eleven, the size of the active region remains constant but the mean intensity sharply increases, which results in an increase of the Hα excess. The Spearman correlation between Hα excess and mean intensity is $\sigma_{\mathrm{S}} = 0.86$ for NOAA 11818, pointing to a very close relation of both parameters. In case of NOAA 11835, the Spearman correlation between Hα excess and mean intensity is $\sigma_{\mathrm{S}} = 0.82$, which is slightly reduced because of the large increase in intensity on day three. Nonetheless, in all three active regions the correlations of the number of pixels with the Hα excess is very high with a Spearman correlation of $\sigma_{\mathrm{S}} = 0.97$ for NOAA 11818, $\sigma_{\mathrm{S}} = 0.89$ for NOAA 11835, and $\sigma_{\mathrm{S}} = 0.98$ for NOAA 11850.

Mean intensity (red curve) and Hα excess (black curve) show a similar temporal profile for active regions NOAA 11818 and NOAA 11835, which resembles the bell-shaped profiles of the UV irradiance for active regions presented in Toriumi et al. (2020), where the 1600 Å and 1700 Å images display the transition region and (upper) photosphere. The UV intensity profiles represent mainly signals from bright plage regions, which is also the case for the positive Hα excess.

6.4 Discussion

6.4.1 A New Tracer of the Solar Activity: Imaging Hα Excess

The prominent Hα spectral line is commonly known to reflect the solar activity but it is rarely used as such. The work by Livingston et al. (2007) is one of the very few studies that analyzed the evolution of the Hα

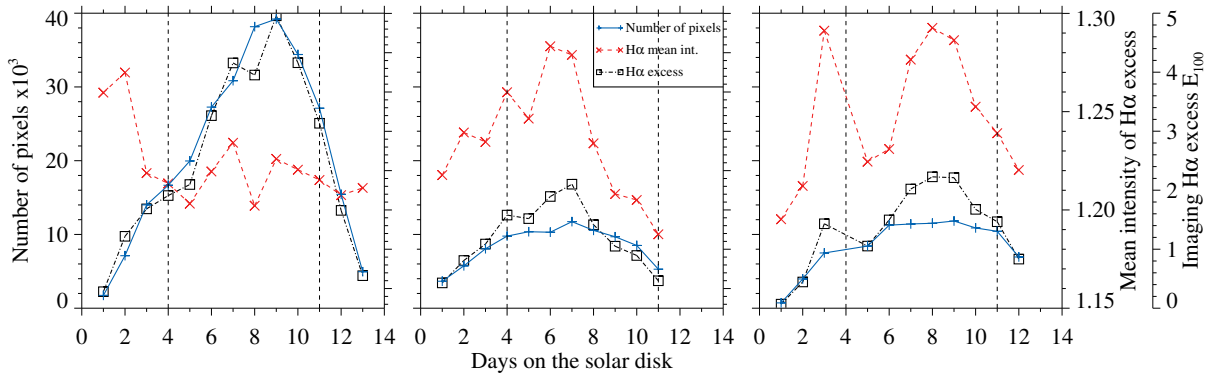

Figure 6.7: Hα excess (dash-dotted black line), mean intensity (dashed red line), and numbers of pixels in mask (solid blue line) for three active regions during their disk passage: NOAA 11850 on 2013 September 19 (left), NOAA 11835 on 2013 August 25 (middle), and NOAA 11818 on 2013 August 9 (right). The vertical dashed lines indicate the images displayed in Fig. 6.6.

line-core intensity for Solar Cycle 22 and 23 in comparison to many other spectral indices. The authors conclude that Hα and other chromospheric lines such as He I 10830 Å, Ca II 8542 Å, and the CN band head at 2883 Å are very similar to the Ca II K index but with a reduced amplitude. Nonetheless, the Global Hα Network and GONG provide on a daily basis time series of full-disk Hα filtergrams, which can be used to provide a continuous Hα excess rate for the Sun. In this study, we explored possibilities to use Hα full-disk filtergrams to create a tracer for the solar activity, i.e., the imaging Hα excess. The positive Hα excess of bright regions displays the strongest variations in amplitude, because bright regions disappear nearly completely from the solar disk during solar minimum. The negative Hα excess of absorption features is also a suitable parameter to monitor solar activity. Dark features are associated with the solar cycle, for example, sunspots and filaments. Moreover, polar crown filaments – large-scale filaments in polar regions – start to appear in a large number around and after the minimum of the solar cycle until they reach a peak shortly before the magnetic field reversal, i.e., around solar maximum, when they disappear from the solar disk (Cliver, 2014). In the master thesis of Le Phuong (2016), an Hα spectral index from spectra of the Integrated Sunlight Spectrometer (ISS, Keller, Harvey, and Giampapa, 2003) of SOLIS was derived based on the intensity enhancement in the line core. However, the variations during the solar cycle were weak, as indicated in the study of Maldonado et al. (2019). In any case, solar activity is small compared to stellar activity, which might be a limiting factor for spectral indices, while disk-resolved indices may perform better.

Hα synoptic charts of filaments from several Hα surveys were used by Makarov and Tlatov (2000) and Makarov et al. (2001) to calculate an activity index for the large-scale magnetic field indicating a cyclic behavior for several solar cycle (Ermolli et al., 2014). In contrast to this, we extracted the Hα excess of dark features directly from Hα full-disk filtergrams and showed that it can be used as a tracer for solar activity. Its capabilities have to be further explored.

We compared the positive and negative Hα excess with already established solar indices: relative sunspot number, F10.7 cm radio flux, and Mg II index. The highest correlations were found with the Mg II index, which originates in the chromosphere, just like the Hα spectral line. We also investigated the Hα mean intensity of the bright regions, which showed that the mean intensity of active regions also changes with the solar cycle. We analyzed this behavior in detail for two consecutive solar rotation periods during the minimum and maximum phases of the solar cycle and compared them with the coverage fraction of Hα excess regions and with the positive Hα excess. Moreover, we studied these parameter for the disk passages of a sample of three active regions. These results will be discussed in the context of modelling stellar atmospheres and exoplanet characterization.

6.4.2 Activity Contamination in Exoplanet Transmission Spectra

The Sun has frequently been used in case studies to understand how exoplanet properties can be affected by surface features of their host stars (e.g., Meunier, Desort, and Lagrange, 2010; Llama and Shkolnik, 2015; Haywood et al., 2016). Detections of molecules and atoms in exoplanet atmospheres can be contaminated by stellar active regions, which has been variously coined the *transit light source effect* or *contrast effect*

(Cauley et al., 2018; Rackham, Apai, and Giampapa, 2018). Indeed, transits of active latitudes can entirely mimic an absorption signal in the planet's atmosphere for strong chromospheric lines such as Hα (Cauley, Redfield, and Jensen, 2017; Cauley et al., 2018). While broadband variability and/or multi-component spectral fitting can place strong limits on star spot coverage fraction (Gully-Santiago et al., 2017) and, in some cases, bright faculae and plage coverage fractions (Morris et al., 2017), these techniques provide little information concerning the emission line flux from individual bright active regions. Being able to constrain the strength of active region emission for individual stars will allow us a much more precise contamination estimate of exoplanet atmospheric absorption, i.e., how much of the observed signal is due to the occultation of active regions by the planetary disk?

The Hα data presented here offers some insight into this problem. Figure 6.5 demonstrates that the mean intensity of Hα excess on the Sun strongly correlates with the coverage fraction of Hα emitting regions. In other words, as the coverage fraction increases, so does the Hα excess in those active regions. This suggests that both changes in active region coverage fraction and emission strength would be required to model Hα rotational modulation of the Sun-as-a-star, as opposed to, for example, fixing the emission strength as a constant and varying the coverage fraction.

Active region contamination of transmission spectra is only a problem for planets transiting active stars. One group of systems for which this is particularly important is short-period planets transiting very young stars, e.g., V1298 Tau (David et al., 2019), AU Mic (Plavchan et al., 2020), and DS Tuc (Newton et al., 2019). UV and Hα transmission spectra for these targets can be used to search for signatures of extended atmospheres and evaporation, which requires an understanding of the degree to which stellar active regions are affecting the planetary signal. Although a functional form for the relationship between emission line strength and active region coverage derived for the Sun may not be directly applicable to pre-main sequence stars or different spectral types, the underlying relationship is likely correct: as the coverage fraction of magnetic bright regions increases, the average intensity of the emission from those active regions increases. This relationship could be included in models of the rotational modulation of these young stars in order to provide constraints on the two model parameters. This method is especially applicable to young stars given their relatively short rotation periods, which makes it possible to collect data across many rotations.

6.5 Conclusions

This study showed the value of the Hα spectral window to derive a tracer for solar activity. The imaging Hα excess created from Hα emitting regions in full-disk filtergrams is closely related to other chromospheric tracers such as the Mg II index. Especially for comparisons with other stars, the Hα excess is of direct use because the Hα spectral line is commonly observed to characterize the activity of a star. Exploring the capability of this tracer will provide new insight in modelling stellar atmospheres and detecting exoplanet atmospheres. We investigated three possible applications. In the first, we analyzed the Hα mean intensity distribution of active regions for the active and inactive Sun, which emphasizes the role of low-intensity active regions for a stable coronal temperature during the solar cycle. The second application was the analysis of the Hα excess for two consecutive solar cycles in the maximum and minimum phases and its comparison to the coverage fraction and mean intensity, which are strongly correlated. A strong temporal correlation was also found for the Hα excess and its mean intensity for a sample of three active regions during solar maximum. These results impact modelling of stellar active regions, where the coverage fraction and the intensity of Hα emitting regions are required to accurately represent chromospheres of solar-like stars.

Chapter 7

Filigree in the Surroundings of Polar Crown and High-latitude Filaments

Filaments are common chromospheric and coronal phenomena, which appear at all latitudes. They form at the borders of opposite-polarity magnetic fields (Babcock and Babcock, 1955), *i.e.*, at the polarity inversion line (PIL). The plasma inside the twisted loop-like structures is relatively cool compared to its surrounding. A typical filament has an elongated spine with two extreme ends. The ends of the filaments reach down to the photosphere, where they are rooted in concentrations of magnetic flux. Barbs branch from the central spine and build footpoints in the photosphere (Martin, 1998; Li and Zhang, 2013). Spine and barbs are built up from individual threads tightly packed parallel to each other. Concerning their location on the Sun, we distinguish three types of filaments (Mackay et al., 2010): quiet-Sun filaments, intermediate filaments, and active region filaments. The first type appears outside of the activity belt and is rooted in the weak magnetic field of the quiet Sun. The sizes range from very small (*e.g.,* Wang et al., 2000; Kontogiannis et al., 2020) to very large scales spanning over more than half a solar diameter (*e.g.,* Iazev and Khmyrov, 1988; Kuckein, Verma, and Denker, 2016; Diercke et al., 2018). Active region filaments develop in the vicinity of active regions and are usually smaller, have shorter lifetimes, and possess a stronger magnetic field than the other types (Mackay et al., 2010; Kuckein, Martínez Pillet, and Centeno, 2012a), whereas intermediate filaments are filaments which cannot be categorized according to one of the other two groups. Polar crown filaments (PCFs) are a special type of quiet-Sun filaments (Leroy, Bommier, and Sahal-Brechot, 1983). They are tracers of the global solar dynamo and follow the solar cycle in the "rush-to-the-pole" (Xu et al., 2018; Diercke and Denker, 2019). These filaments indicate areas of weak background fields in polar regions (Li et al., 2008; Li, 2010; Panesar et al., 2014). Typical PCFs form as large structures along the PIL in the filament channel and appear as extended and elongated absorption structures on the solar disk (Gaizauskas, 2001). Nonetheless, smaller filaments also appear in filament channels. They are fragments of larger filaments, where only the extreme ends of the filaments are visible and the rest of the spine remains not traceable because of weak density and high latitudes (Schmieder et al., 2010; Dudík et al., 2012).

Granulation predominantly covers the solar photosphere. The chromosphere above shows more diverse structures, especially in the dominant absorption line of Hα. Beside filaments, we find fine structures in form of dark, elongated mottles or fibrils, when longer than a few seconds of arc (Dunn and Zirker, 1973; Schmieder, 2001; Rutten and Hagenaar, 2001; Tsiropoula et al., 2012). Mottles form a network above or around supergranular cells. If they appear radially around a prominent bright core, the structure is called rosettes, whereby the bright core is related to the underlying magnetic field (Schmieder, 2001). In the wings of Hα, mottles and fibrils are still visible. Far in the wings, where the typical filamentary structures disappear, photospheric granulation becomes visible, but often with a network of bright points within the intergranular lanes. This pattern was first described by Dunn and Zirker (1973) and named "filigree", where individual elements were referred to as "crinkles". Nowadays, the term bright points is more established (Muller, 2001). They are the smallest, resolvable features on the Sun. The majority appears in a more circular shape, but many have an elongated appearance (Dunn, Zirker, and Beckers, 1974; Muller, 2001). Typical bright points have a width of about $0\farcs3-0\farcs35$ (Dunn and Zirker, 1973; Kuckein, 2019) and the elongated ones have a length of up to $1\farcs0-2\farcs5$ (Dunn and Zirker, 1973; Tarbell

et al., 1990), which represents likely a chain of bright points but appears as a single structure because of insufficient spatial resolution.

Immediately after discovering these small-scale structures in the Hα line wings, a connection was postulated that they are manifestations of magnetic footpoints (Mehltretter, 1974; Wilson, 1981). Bright points represent single magnetic elements, which are characterized by strong concentrations of magnetic flux, even though there is no one-to-one relation between their brightness and the magnetic flux density (Leenaarts et al., 2006). Each bright point represents an elementary flux tube, which is believed to reach nearly vertically from the photosphere to the corona (Tarbell et al., 1990; Muller, 2001). They are observed in different lines and are mostly studied in the Fraunhofer G-band with a central wavelength of $\lambda_G = 4305.5$ Å (Muller, 2001). The connection between bright points in the Ca II H & K lines and Hα filigree was already known since shortly after the first description of filigree and was confirmed in other studies since then (Mehltretter, 1974; Wilson, 1981; Leenaarts et al., 2006). Bright points may not spatially coincide exactly at different wavelengths, *e.g.*, G-band and Ca II bright points (see Zhao et al., 2009), but they are physically the same phenomenon in G-band, Ca II H & K, Hα, and other molecular bands or spectral lines (Muller, 2001). Kuckein (2019) compared the appearance and properties of bright points in several wavelength bands covering the blue continuum at 4505 Å, Ca II H, Ca I λ10839 Å, Na I D_2, and Si I λ10827 Å. Bright points were detected in all wavelengths, expanding in size with height along the magnetic field lines.

Dunn and Zirker (1973) found bright points are best observed about +2 Å from the line core of Hα, while Leenaarts et al. (2006) report that bright points are especially well identified in the blue wing of H$\alpha - 0.8$ Å. According to the latter authors, bright points are less sharp as in G-band but the Hα blue wing has a better contrast compared to the surroundings because of line formation properties of the Hα line in the photosphere. In other lines, the bright points were also best seen in the blue wing, *i.e.*, Na I D_2 and Si I λ10827 Å (Kuckein, 2019).

Only few studies of filaments exist with high-resolution observations from ground-based telescopes (*e.g.*, Chae et al., 2000; Kuckein, Martínez Pillet, and Centeno, 2012a), in particular for quiet-Sun filaments (*e.g.*, Engvold, 2004; Lin et al., 2005; Kuckein, Verma, and Denker, 2016) and polar crown filaments (*e.g.*, Lin, Engvold, and Wiik, 2003). To the best of our knowledge, no high-resolution studies attempted to connect photospheric bright points in the quiet-Sun at high-latitudes to processes in the chromosphere related to filaments. Throughout the manuscript, we use the term "bright point" when we refer to crinkles, *i.e.*, the single elements of filigree. The goal of the present study is to examine bright points in the vicinity of eight polar crown filaments and study their morphology. Do high-latitude and active-region bright points differ? Does the weaker magnetic field close to the poles result in a different morphology of bright points? Will the interface between mixed-polarity and more unipolar fields have an impact on where PCFs form? Finally, how are bright points related to filaments?

First, we introduce briefly the new synchronized CMOS cameras and the observations of polar crown and high-latitude filaments in the Hα narrow-band filtergrams and broad-band images (Section 7.1). We refer to observations in the narrow- and broad-band channels as Hα filtergrams and Hα images, respectively. In the latter, filigree in the surroundings of high-latitude and polar crown filaments are visible. We examine filaments in Hα filtergrams, where they are visible in great detail (Section 7.3.1) and we describe their evolution with context observations in Hα and He I 10830 Å. The morphological appearance of bright points close to the filament is described in Section 7.3.2. We relate the bright points to concentrations of the magnetic field in the quiet-Sun using line-of-sight (LOS) magnetograms and scrutinize their upper atmospheric response in UV 1700 Å and Ca II K images (Section 7.3.3). In the Discussion (Section 7.4), we contrast quiet-Sun bright points with those found in the activity belt, which are associated with stronger magnetic field concentrations.

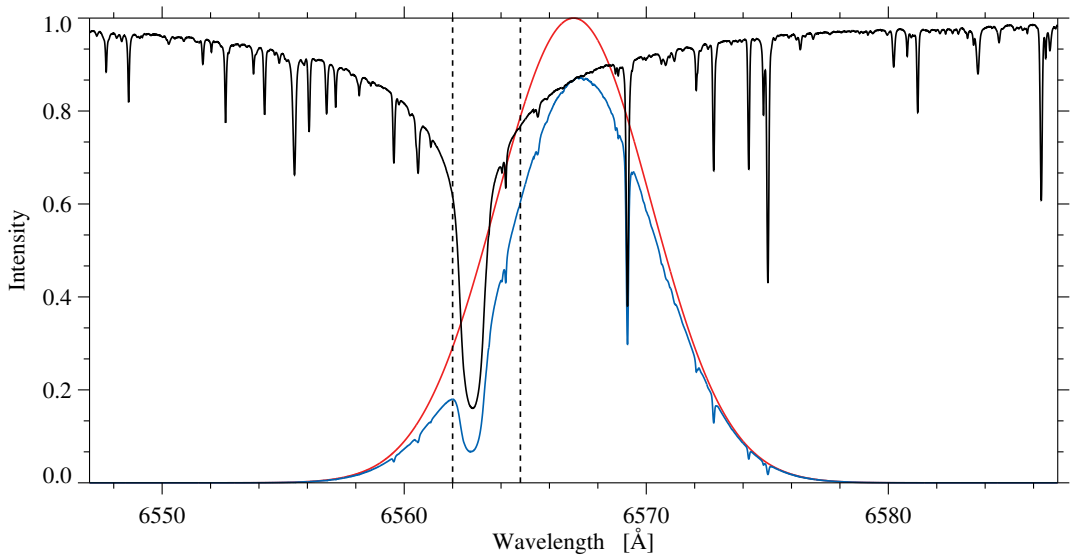

Figure 7.1: Transmission curve of the Hα broad-band filter. Atlas spectrum of the Kitt Peak Fourier Transform Spectrograph (*black*), broad-band filter transmission (*red*), and convolution of both curves (*blue*). The dashed line indicate the positions of H$\alpha - 0.8$ Å and H$\alpha + 2$ Å.

Table 7.1: Overview of the date, time, and location of the observed high-latitude and polar crown filaments. The labels 'a' and 'b' refer to the location of the filaments in Figure 7.2. The filament type refers to polar crown (P) and high-latitude (H) filaments.

Date	Time [UT]	Coordinates [arcsec]		Filament		Index
		x	y	Label	Type	
21 Sept. 2018	08:33:58 – 08:39:16	−172.0	47.2	A	P	a
21 Sept. 2018	08:44:00 – 08:45:45	−81.6	47.2	B	P	b
22 Sept. 2018	09:05:36 – 09:09:45	14.4	97.2	C	H	–
24 Sept. 2018	08:33:34 – 08:39:49	−624.0	−364.8	D	H	a
24 Sept. 2018	08:40:01 – 08:41:35	01.6	99.2	E	P	b
25 Sept. 2018	08:40:47 – 08:42:33	84.0	28.0	E	P	a
25 Sept. 2018	08:49:19 – 08:51:05	−422.4	−374.4	D	H	b
26 Sept. 2018	09:37:46 – 09:39:55	18.4	37.6	E	P	–

7.1 Observations

Two new synchronized high-cadence CMOS M-lite 2M cameras manufactured by LaVision GmbH Göttingen (Germany) were tested in September 2018 at the *Vacuum Tower Telescope* (VTT: von der Lühe, 1998). They replaced the old cameras of the GREGOR *Fabry Pérot Interferometer* (GFPI: Denker et al., 2010; Puschmann et al., 2012) at the GREGOR solar telescope (Schmidt et al., 2012). During the tests, a large variety of polar crown and high-latitude filaments were recorded. We used for the observations a broad-band Hα filter 6567 Å with a full width at half maximum (FWHM) of 7.5 Å and a transmission of $T_{\max} = 70\,\%$. The transmission curve of the interference filter is plotted in Figure 7.1 at its nominal central wavelength, which is displaced from the Hα line core towards the red. The same interference filter served as a prefilter for the narrow-band Lyot filter at (6562.8±0.3) Å for the second camera. The light was distributed between both cameras by a 70/30 beamsplitter cube. The Lyot filter was manufactured by Bernhard Halle Nachf. Berlin-Steglitz (Künzel, 1955) and is temperature controlled. The wavelength can be tuned by changing the temperature and the entrance polarizer. The interference filter was somewhat tilted to avoid retro-reflections from its front side, which shifts the transmission peak towards the blue. Thus, the convolution of the filter curve with the spectrum yields higher line-core intensities than those depicted in Figure 7.1. The spectrum was taken from the spectral atlas of the Kitt Peak Fourier Transform Spectrograph (Brault, 1985). In general, the line wings contribute significantly more to the broad-band intensity than the line core so that filigree can be detected. However, the contrast of bright points will be

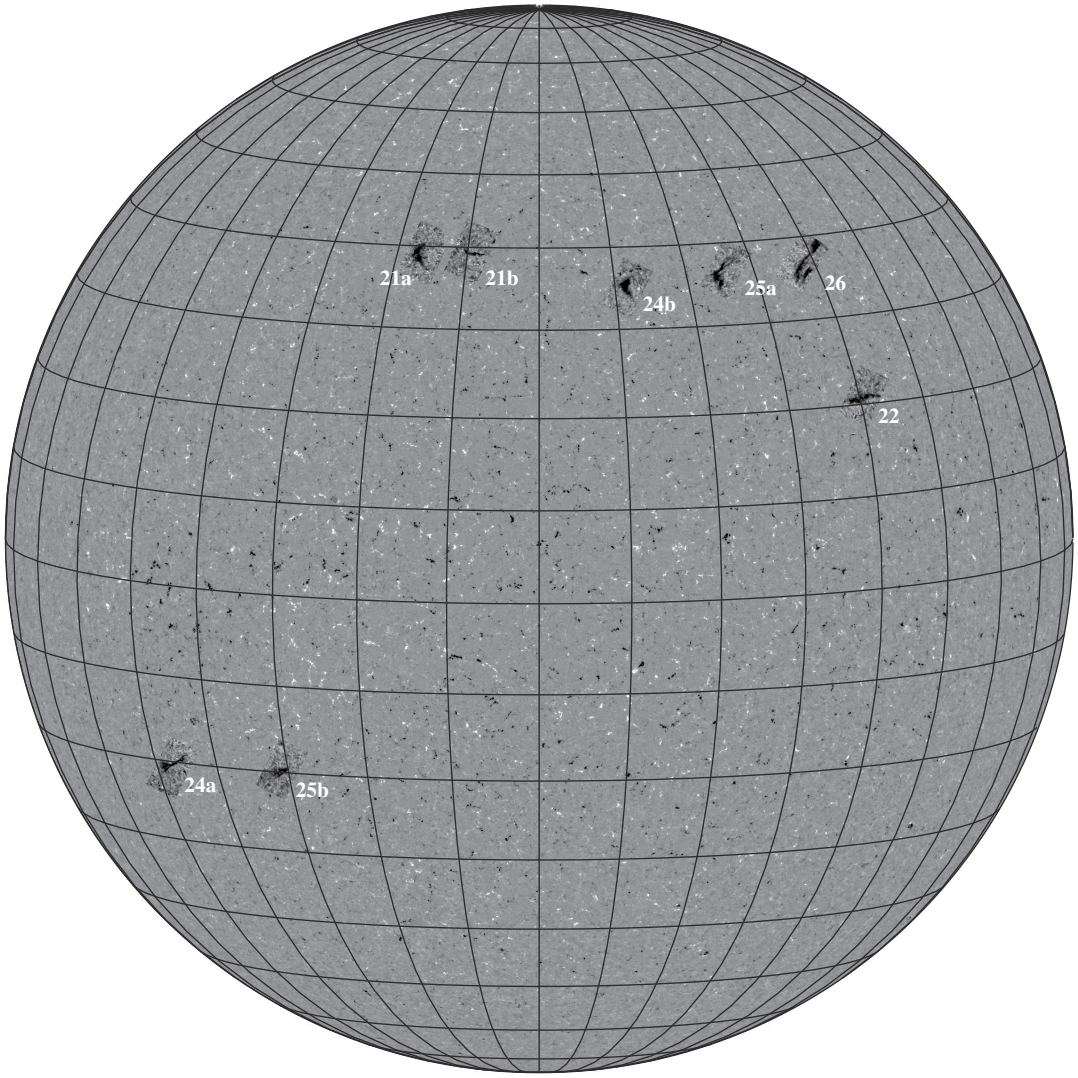

Figure 7.2: Composite image of a magnetogram and Hα filtergrams illustrating the locations of the observed high-latitude and polar crown filaments across the solar disk observed between 21 and 26 September 2018. The corresponding dates and times are collected in Table 7.1. Multiple observations on a day are labeled 'a' or 'b'. The background image is a "deep" magnetogram, averaged over 12 min, observed around 08:34:00 UT on 24 September 2018, which is scaled between $\pm$80 G. Lines of longitude and latitude are separated by 10°.

lower compared to more discriminate filters in the line wings, *e.g.*, H$\alpha-0.8$ Å or H$\alpha+2$ Å as suggested by Dunn and Zirker (1973) and Leenaarts et al. (2006), respectively.

The M-lite 2M cameras have a detector size of 1920×1280 pixels with a pixel size of $5.86\times5.86\,\mu\mathrm{m}^2$. The quantum efficiency is about 48% at Hα. The cameras are able to take fast time-series of images with a frame rate of up to 100 Hz at 12 bit. A programmable timing unit (PTU) was used to synchronize the cameras with an accuracy of about 10 ns. Furthermore, the images were rapidly stored on Solid-State Drives (SSDs) facilitating image sequences with fast cadence. Details of the camera system are given in Denker et al. (2020, submitted). During the observations, we took sequences of 500 images with 10 or 20 repetitions, depending on the seeing conditions. The images were taken with an exposure time of $t_{\mathrm{exp}}=20$ ms and an acquisition rate of $f_{\mathrm{acq}}=46$ Hz. The data were recorded with 2×2-pixel binning, which results in an image scale of $0.098''$ pixel^{-1} and corresponds to about 71 km on the Sun.

Using this setup, we observed eight PCFs for five days between 21 and 26 September 2018. The observations were mainly performed in the morning, when seeing conditions are better and more stable. An overview of the location of the filaments is given in Figure 7.2 and the corresponding Table 7.1. The

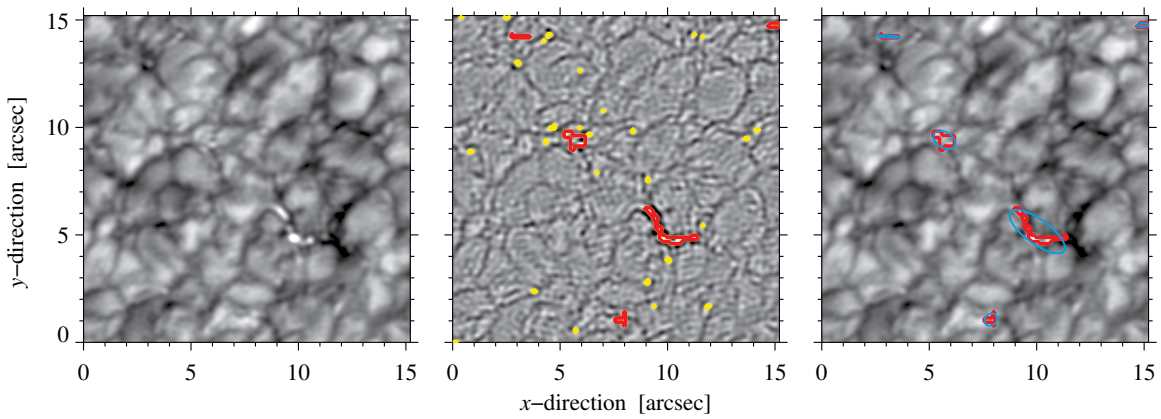

Figure 7.3: Identification of filigree. Input Hα broad-band image on 21 September 2018 at 08:34:10 UT (Filament A) for a central region of about $15'' \times 15''$ (*left*). Hα broad-band image after applying a Laplacian filter with the contours of the pixels above the threshold of three standard deviations in yellow and the contours of the extracted filigree after applying dilation and erosion and removing small-scale features in red (*middle*). Hα broad-band image with the contours of the extracted filigree in red (*right*). In addition, we display an example for the ellipse fitting, approximating the shape of the bright point (*blue contours*).

dataset consists of five different filaments (labeled from 'A' to 'E'), two of which were observed on several days. Most filaments were recorded in the northern hemisphere, and only Filament D was observed in the southern hemisphere. The locations of the filaments imply that most of the filaments are PCFs, with the exception of Filaments C and D, which belong to the category of high-latitude filaments.

As a context imager, we use the *Chromospheric Telescope* (ChroTel: Bethge et al., 2011) with an aperture of 10 cm, which provides full-disk Hα, Ca II K, and He I 10830 Å images with a cadence of three minutes. All images went through basic image processing including dark, flat-field, and limb-darkening corrections (Diercke and Denker, 2019) and were corrected with Zernike polynomials, removing a non-uniform background introduced by the Lyot filters (Shen, Diercke, and Denker, 2018). We aligned the high-resolution VTT images with the ChroTel Hα images and used the ChroTel Ca II K images to align the data with the UV 1600 Å and 1700 Å filtergrams of the *Atmospheric Imaging Assembly* (AIA: Lemen et al., 2012), which in turn were used to align them with the LOS magnetograms of the *Helioseismic and Magnetic Imager* (HMI: Scherrer et al., 2012) on board the *Solar Dynamics Observatory* (SDO: Pesnell, Thompson, and Chamberlin, 2012). The HMI magnetograms were used to compare the location of bright points, which were derived from the high-resolution broad-band Hα images, with their counterparts in the photospheric magnetic field. The SDO data were rescaled and derotated with standard SDO and image processing routines as described in Diercke et al. (2018).

7.2 Methods

Aligning data from different instruments is difficult due to large differences in image scale. In consequence, we cannot rely on pixel-to-pixel alignment. We have to take into account the differences in image scale for VTT images ($0.098''$ pixel^{-1}), ChroTel images ($0.96''$ pixel^{-1}), and SDO magnetograms and UV filtergrams ($0.6''$ pixel^{-1}). The low-resolution data were resampled to the same image scale as the VTT data using linear interpolation.

We created "deep" magnetograms by averaging 16 magnetograms around the central magnetogram of the time series. Individual HMI magnetograms have an average noise level of about 10 G with a gradual increase of noise towards the limb (Liu et al., 2012). Considering only photon statistics, the signal-to-noise ratio improves by a factor of four, which is, however, somewhat lower in reality and approaches a limit when the evolution time scale of magnetic features can no longer be neglected. The 12-minute averages are a good compromise between magnetic sensitivity and temporal evolution of small-scale magnetic features in the quiet Sun.

The first step in extracting filigree from broad-band Hα images is to normalize the data by dividing the images by the median intensity of the quiet Sun (left panel in Figure 7.3). For identification of bright points, we followed the method presented by Feng et al. (2012) who identified G-band bright points. A

Laplacian filter, utilizing the second derivative of the image, helps to obtain candidates for the filigree (middle panel in Figure 7.3). For these candidates, we applied an intensity threshold, which is the mean intensity plus three times the standard deviation of the image (yellow contours in the middle panel of Figure 7.3). We applied morphological dilation to the mask with a cross-shaped structuring element $s = [[0, 1, 0], [1, 1, 1], [0, 1, 0]]$. After applying morphological closing to the mask with a 5×5-pixel circular kernel, we removed small-scale features with less than five contiguous pixels. The thus extracted filigree are shown as red contours in the middle and right panels of Figure 7.3.

A blob finding algorithm (Fanning, 2011) identifies contiguous regions based on the four-adjacency criterion. Several properties follow from the blob analysis, for example, the location of the bright points and their perimeter length and area in pixels. Other properties of bright points can be determined from fitting an ellipse to the structure, for example, the tilt-angle and the semi-major and -minor axis, which gives the eccentricity of the bright points. In the following, we will divide filigree in three classes: bright points in the surroundings of the filaments (Type I), bright points at the location of the filament (Type II), and bright points at the footpoints of the filaments (Type III). The footpoints were determined manually by utilizing Hα filtergrams of the narrow-band channel and magnetograms. The corresponding locations of the footpoints are marked in subsequent figures by red circles.

7.3 Results

7.3.1 Morphology of the Filaments in Hα

All observed filaments are either small-scale polar crown or high-latitude filaments (see Table 7.1 and Figure 7.2). We could not record longer time series of PCFs because of unstable seeing conditions. They are small enough to fit into the field-of-view (FOV) of the detectors and are therefore not longer than 80″ (Figure 7.4). The morphology of the filaments is clearly seen in high-resolution filtergrams with single threads forming the spines. Some of the filament spines appear as the typical dark elongated structures, *e.g.*, Filament B in the middle of the FOV. Some filaments are thicker and more diffuse, namely Filaments A and E. For both filaments, both extreme ends could not be clearly determined, which could be an indication that these were fragments of a larger filament (Schmieder et al., 2010), where only the extreme ends were visible and the rest was not sufficiently dense to be observed in Hα. Especially strong is this impression for Filament E on 24 and 25 September. Examining the ChroTel full-disk Hα filtergrams (not shown), we see the filament ends for Filament A and E about 27″ to 10″ outside the high-resolution FOV. Filament A covers about 45 % of the complete filament, whereas the fraction in the FOV increases for Filament E from about 15 % on 24 September and about 25 % on 25 September to about 50 % of the complete filament on 26 September. The diffuse impression of these two filaments can be explained by assuming that they are only fragments of a larger filament, whereby for Filament E on 25 and 26 September single threads become visible along the spine of the filament.

Filament A is only visible on 21 September. During this short period, it is very dynamic. The complete spine between both footpoints becomes visible and we can observe plasma flows from the spine towards the second footpoint in full-disk context observations of the *Kanzelhöhe Solar Observatory* (KSO: Otruba and Pötzi, 2003; Pötzi et al., 2015). Furthermore, the filament starts to erupt but fails in the process. Afterwards, the filament is only visible as a small-scale structure and dissolves completely. In contrast, Filament E is visible for five days. On the first day, 24 September, the eastern part (Figure 7.4) is very dynamic and changes completely over the course of a day. The small-scale structure develops in an elongated structure, where half of the filament spine becomes visible. Around 14:00 UT, the filament dissolves again into a small-scale structure. On the second day, 25 September, the spine is more opaque and changes are only small. After 26 September, the filament begins to dissolve. The other filaments B, C, and D are very stable with short lifetimes of one to two days.

In the surroundings of the filaments (Figure 7.4), we see in the filtergrams typical chromospheric fine structures made up of single threads. Some pronounced rosettes, which are formed by radial dark mottles, are anchored in bright cores. Some of these bright cores are related to filigree and strong concentrations of magnetic field. The mottles build a network, which is located around supergranular cells (Schmieder, 2001), which is also seen in the Hα filtergrams, *i.e.*, Filament A on the right side of the filament at (x, y) coordinates (30″ – 55″, 20″ – 60″), where the mottles are located around a supergranular cell. Some

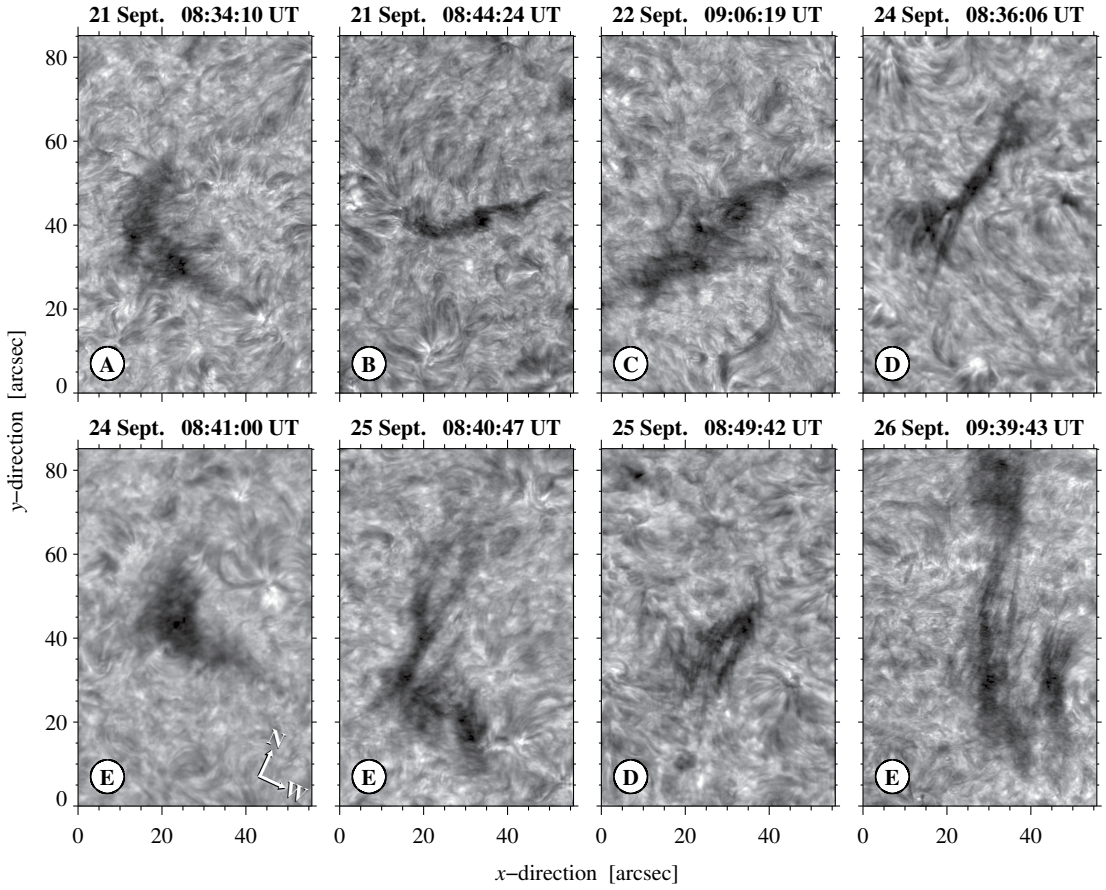

Figure 7.4: High-resolution Hα filtergrams of the polar crown and high-latitude filaments observed with the narrow-band Lyot filter at the VTT. The label of the filaments is noted in a black circle in the lower left corner (see Table 7.1). The arrows indicate the direction of solar north and west.

longer mottles or fibrils are anchored in bright cores and even mini-filaments are seen in the surroundings of the larger polar crown and high-latitude filaments, *i.e.*, Filaments C and E on 22 and 24 September, respectively.

We compare the appearance of the filaments in the three ChroTel filtergrams using Filament E as an example (Figure 7.5). In the ChroTel Hα filtergrams (upper row in Figure 7.5), Filament E has a similar morphology as in the high-resolution Hα filtergrams but lacks the high contrast fine-structure such as mottles, fibrils, or mini-filaments. The background is uniform and does not provide many details. The shape of the filament is, however, the same when compared to the high-resolution images. On 25 September, we see an extended faint absorption structure in the upper part of the filtergram continuing beyond the contour of the filament between coordinates ($20'' - 50''$, $60'' - 90''$).

All filaments are visible in the He I λ10830 Å line-core filtergrams (middle row in Figure 7.5). The filaments appear overall very similar as in Hα but differences become apparent in a detailed comparison. Strong absorption is encountered in different parts of the filament in He I as in the ChroTel Hα filtergrams. For example, on 25 September, Filament E has a stronger absorption in the elongated upper part of the filament in He I at coordinates ($10'' - 25''$, $35'' - 60''$) but in Hα the absorption of the lower, compact part is higher at coordinates ($5'' - 35''$, $5'' - 35''$). In addition, on 24 & 25 September, we see dark, faint absorption structures above Filament E between coordinates ($20'' - 55''$, $60'' - 90''$), which are much fainter in the Hα full-disk filtergrams. This strengthens the supposition that these filaments are fragments of larger structures.

The ChroTel full-disk Ca II K filtergrams (bottom row in Figure 7.5) show a different chromospheric layer. Nonetheless, some small absorption features are also visible in the Ca II K filtergrams at the location of the filaments, for example, Filament E on 24 and 25 September. This faint Ca II K absorption in filaments is also reported in, e.g., Kuckein, Verma, and Denker (2016). On 26 September, the ChroTel

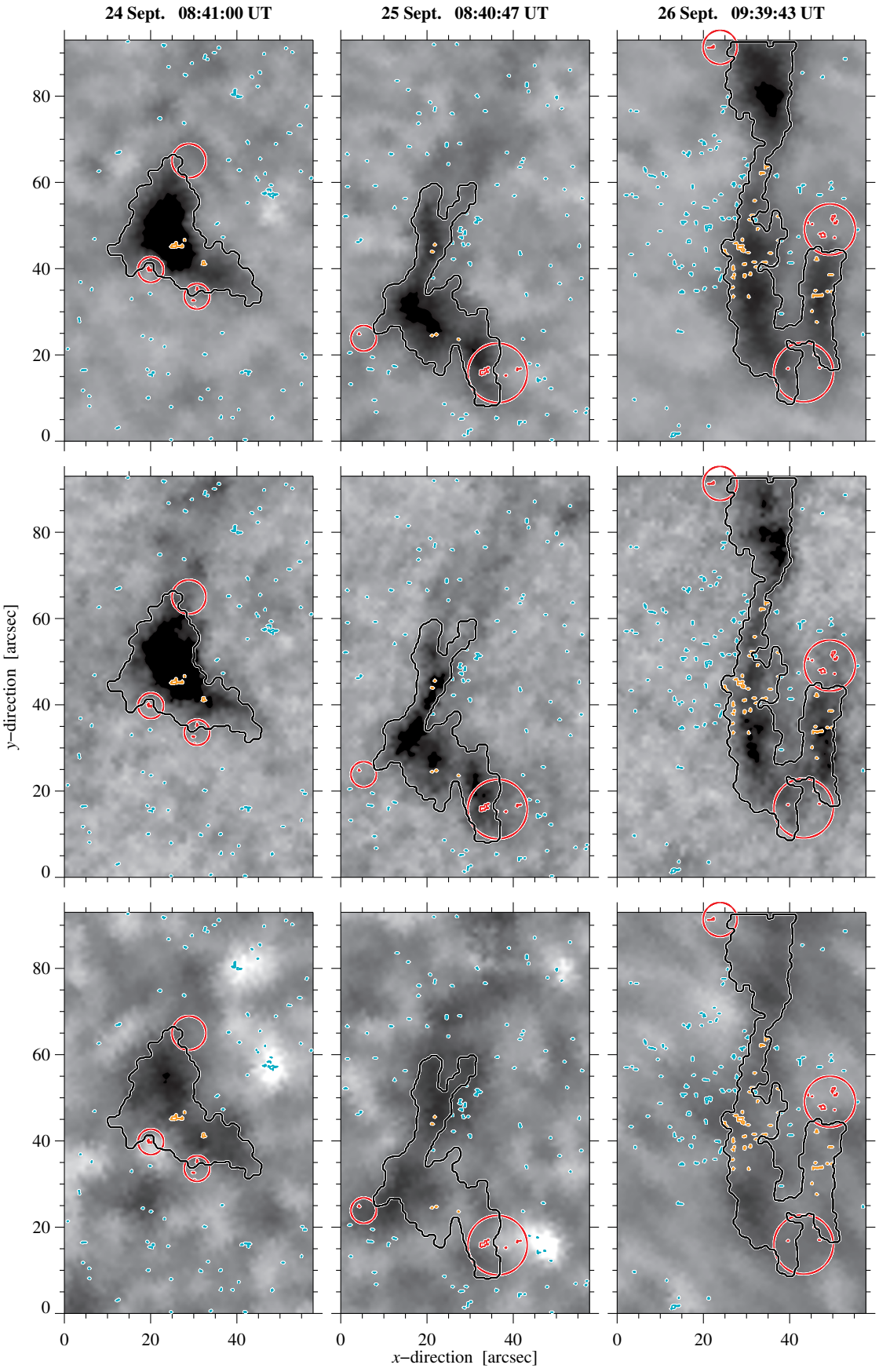

Figure 7.5: Filament E observed 24 – 26 September 2018 with ChroTel in Hα (*top*), in the red line core of the He I λ10830 Å triplet (*middle*), and in Ca II K (*bottom*) with the contours of the filaments derived from the Hα filtergrams (*black*) and of filigree in the three categories: Type I (*cyan*), Type II (*orange*), and Type III (*red*). In addition, the footpoints of the filaments are marked with red circles.

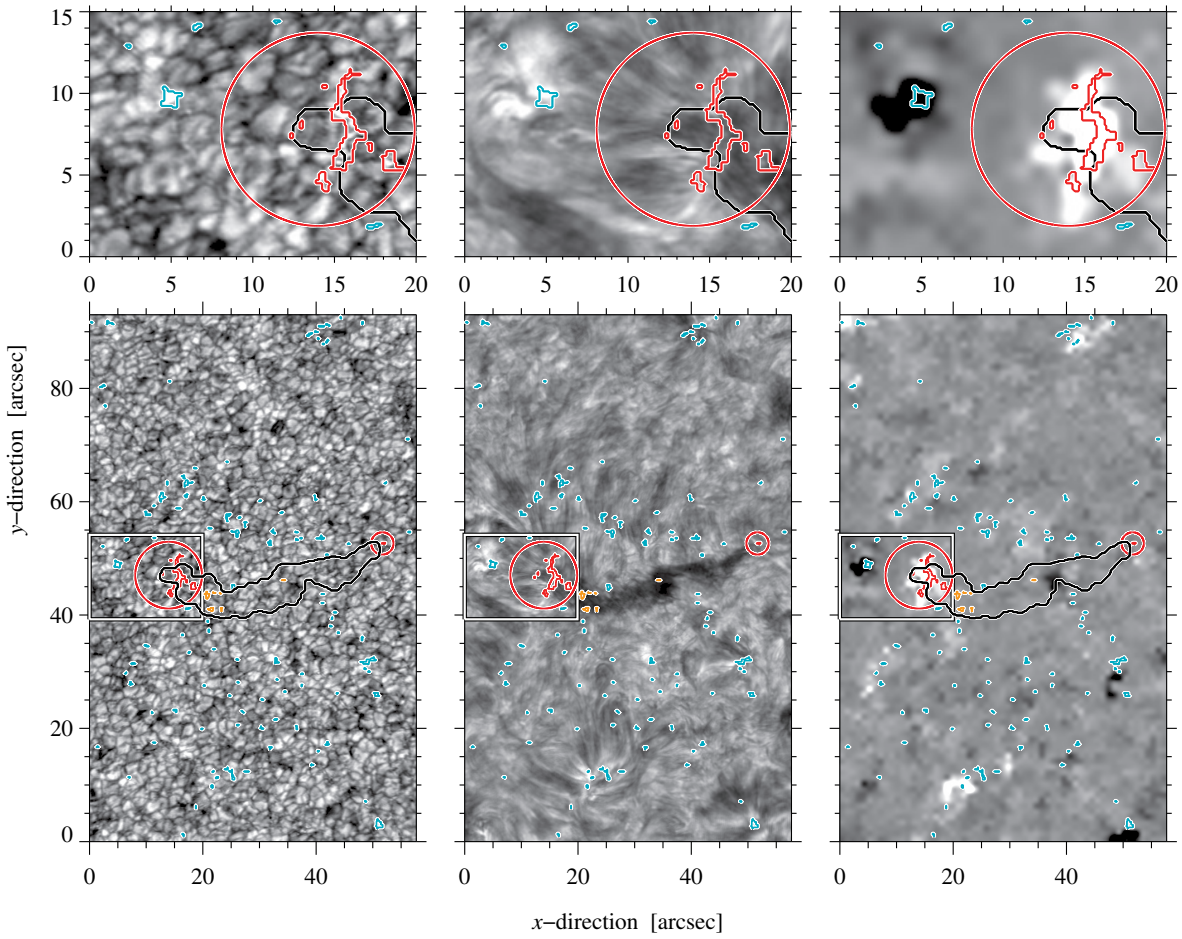

Figure 7.6: Identified filigree of Type I (*cyan*), Type II (*orange*), and Type III (*red*) for the Filament B on 21 September 2018 superposed on a high-resolution Hα image (*left*) and filtergram (*middle*) and on a corresponding magnetogram (*right*). The deep HMI magnetogram was averaged over 12 minutes and is displayed between $\pm$40 G. For clarity, we display the contours of the filament (*black*) and the footpoint regions (*red*). The white rectangle indicates a region-of-interest, which is displayed in the top row at a higher magnification.

Ca II K filtergram is washed-out, *i.e.*, mediocre seeing conditions prevent a detailed discussion. The network of bright points is associated with supergranular cell boundaries, which are slightly visible around the filaments as bright regions. The enhanced brightness in Ca II K filtergrams is closely related to the magnetic field strength (Rutten and Uitenbroek, 1991), and the magnetic field converges at the boundaries of supergranular cells, which are outlined as bright regions in the Ca II K filtergrams. In addition, the filigree in the surroundings of the filaments are located close to these regions. This will be discussed in more detail in Section 7.3.3 based on UV 1700 Å filtergrams.

7.3.2 Morphological Description and Statistics of Filigree

The broad-band Hα images (left panels in Figure 7.6) show photospheric granulation on 22 September above which Filament B is suspended. The magnified left footpoint region establishes the location of Type I and II bright points in the high-resolution image of granulation. The granulation exhibits an irregular brightness distribution, *i.e.*, some very bright granules and some darker areas with the size of a granule. Some of these dark areas are likely remnants of strong absorption structures leaving imprints in the broad-band Hα images. The bright points are located at the border of the granules, *i.e.*, along the intergranular lanes. Inspecting the Hα filtergram (middle panel in Figure 7.6), we recognize that bright points are located near the footpoints of the filaments (red circles) but also coincide with bright cores of rosettes at coordinates (25″, 15″). Fibrils extend between the footpoint of the filament and the bright point to its left. Mapping bright point positions onto magnetograms (upper right panel in Figure 7.6) reveals that both bright points are rooted at opposite polarities, crossing the polarity inversion line. The larger

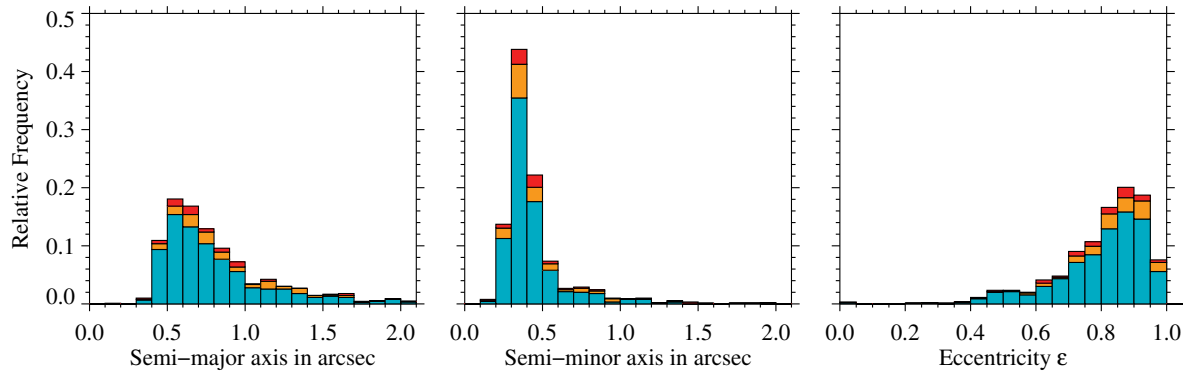

Figure 7.7: Histogram of semi-major axis (*left*), semi-minor axis (*middle*), and eccentricity (*right*) of bright points. The histogram bins are divided into the three different classes: Type I (*cyan*), Type II (*orange*), and Type III (*red*). The bins are normalized to the total number of bright points ($n = 897$).

FOV depict that many, but not all, bright points are associated with strong magnetic field concentrations. Magnetic field observations with higher spatial resolution may even yield a closer association. Moreover, some bright points are very close to strong magnetic fields but do not exactly match their positions. This may be due to alignment and projection errors, and differences in the three instruments. However, this behavior was also noted in other studies, *e.g.*, for G-band and Ca II bright points (Zhao et al., 2009). The magnetograms will be analyzed in more detail in Section 7.3.3.

In this example, we already encounter different shapes and sizes of bright points. Visually, the large majority is small and has a more roundish form but some are larger and either roundish or elongated. Some bright points are located in clusters, as seen for Filament B (right panel in Figure 7.6) at the upper footpoint, where no single bright point can be distinguished. In the following, we will determine area distribution, perimeter length, and eccentricity of bright points based on the entire dataset.

Size Distribution of Filigree

The filigree in this study are close to the solar polar regions. To study their properties such as length, width, or area, we have to correct the images geometrically by resampling the pixels to a regular grid with a pixel size of 71 km, similar to the method described in Verma and Denker (2011) for *Hinode* images (Kosugi et al., 2007). This facilitates a more accurate estimation of the statistical parameters and makes it possible to compare our results with those obtained on other locations on the solar disk. To analyze the size distribution of filigree, we fit an ellipse to individual bright points and estimate their length and width based on the semi-major and -minor axis, respectively (right panel in Figure 7.3). The corresponding distributions are displayed in the left and middle panels of Figure 7.7 for each of the three types of filigree (see Section 4.2).

The distribution of the semi-major axis of bright points is displayed in the left panel of Figure 7.7. The peak of the distribution is between $0\farcs5$ and $0\farcs6$ for Type I bright points, whereas Type II and III bright points peak at about $0\farcs6 - 0\farcs7$. The respective median values and related standard deviations for each type are $0\farcs7 \pm 0\farcs5$ (Type I), $0\farcs8 \pm 0\farcs7$ (Type II), and $0\farcs7 \pm 1\farcs0$ (Type III). Higher values are reached only by few bright points with maximum values for of $5\farcs1$, $5\farcs4$, and $7\farcs9$ for Type I, II, and III, respectively. These large values are likely related to (unresolved) cluster of bright points in each category. The minimal values are about $0\farcs3$ for Type I and II and about $0\farcs2$ for Type III. The shape of the distributions indicates that most bright points are spatially resolved.

The histogram of the semi-minor axis shows a similar distribution (middle panel of Figure 7.7), but the distribution is shifted towards lower values with a peak between $0\farcs3 - 0\farcs4$. The median and standard deviation for the three types are very similar with $0\farcs38 \pm 0\farcs21$ (Type I), $0\farcs39 \pm 0\farcs28$ (Type II), and $0\farcs41 \pm 0\farcs33$ (Type III). Only a few bright points have a semi-minor axis above $1''$ and reach maximum values of $2\farcs6$ (Type I) and about $1\farcs9$ for Type II and III. The minimum values for the semi-minor axis are $0\farcs18$ for Type I and III and $0\farcs19$ for Type II. The minimum size of the bright points is limited by the selection procedure of bright points, where we excluded all structures with less than five pixels.

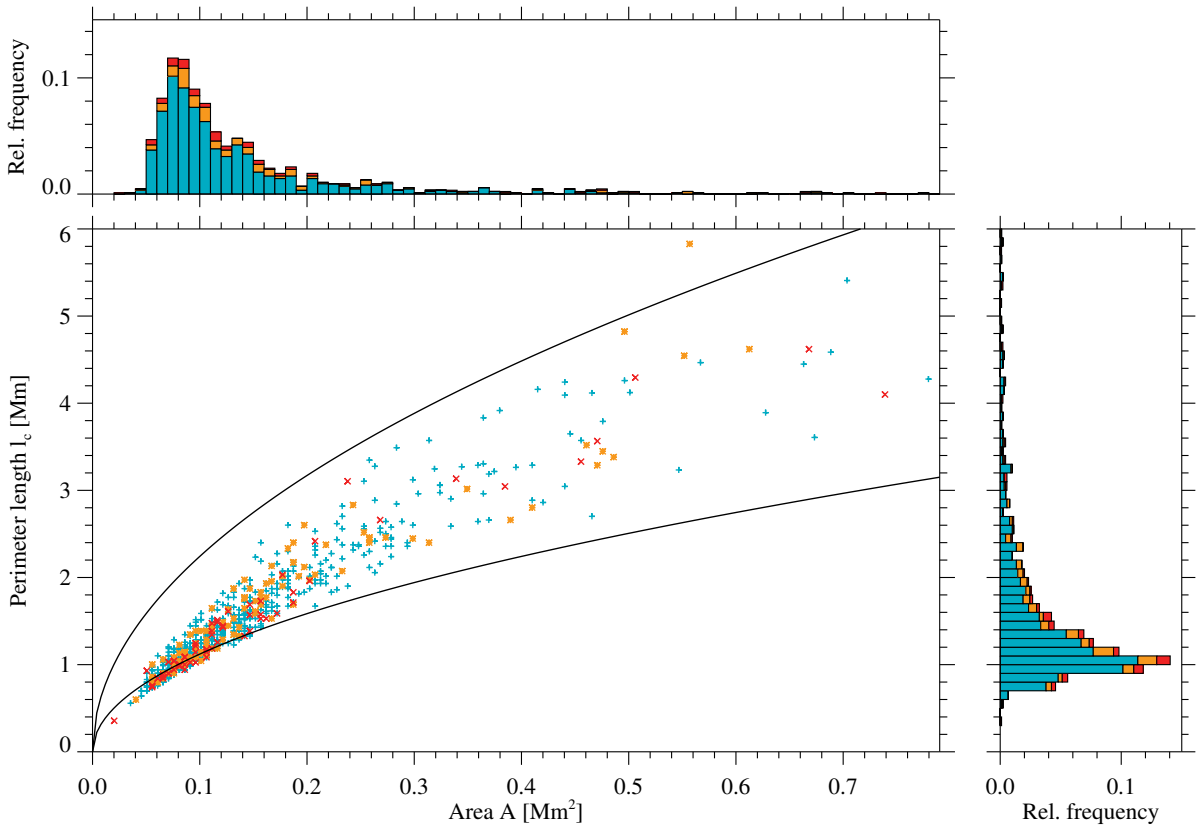

Figure 7.8: Area *vs.* perimeter length and the respective histograms for bright points of Type I (*cyan* '+'), Type II (*orange* '∗', and Type III (*red* '×'). The envelope functions (*black*) indicate $\alpha = 1$ and $\alpha = 2$ in Equation (7.2) for the lower and upper curve, respectively.

Eccentricity of Filigree

The majority of bright points are best described by a circular shape but some bright points appear to have an elongated shape (Muller, 2001). In the following, we present a quantitative description of the bright points' shape approximated by the eccentricity ε of an ellipse following the approach of Verma and Denker (2014)

$$\varepsilon = \frac{e}{a} = \frac{\sqrt{a^2 - b^2}}{a}, \tag{7.1}$$

where e represents the linear eccentricity or distance of the focus points from the center, a the semi-major axis and b the semi-minor axis (right panel of Figure 7.3).

In the right panel of Figure 7.7, a histogram of the eccentricity of bright points is shown. If the eccentricity is $\varepsilon = 0$, the object has a circular shape and the semi-major and -minor axis are equal. Only three bright points have an $\varepsilon = 0$ and 3.5 % of the bright points have an eccentricity of $\varepsilon < 0.5$. The median eccentricity is 0.84, 0.86, and 0.83 with standard deviations of 0.14, 0.13 and 0.17 for Types I, II, and III, respectively. This relates to an aspect ratio of about 2:1.

Area Distribution of Filigree

We displayed the area distribution of filigree, converted from pixels to megameters squared, in relation to the perimeter length in megameters after geometric correction of the images (Figure 7.8). In addition, we display the corresponding histograms differentiating the three categories of bright points discussed. The bright points have a median area of about 0.11 Mm^2 with a standard deviation of 0.21 Mm^2. The peak of the area distribution is about 0.08 Mm^2 for the three types of bright points. The smallest area is 0.036 Mm^2 (Type III) and the largest bright point or cluster thereof reaches an area of 3.5 Mm^2 (Type III). The perimeter length is increasing with increasing area. The median of the perimeter length is 1.24 Mm

with a standard deviation of 1.17 Mm. The peak of the distribution of the perimeter length is between 1.0 and 1.2 Mm for the three types. The minimal value for the perimeter length is reached for a Type III bright point with 0.34 Mm. The maximum perimeter length is 17 Mm for a single very elongated bright point or cluster of bright points at a footpoint (Type III). The majority of filigree have small areas and perimeter length and only few develop large areas with corresponding large perimeter length.

The following relation was defined for pores by Verma and Denker (2014)

$$l_c = 2 \cdot \alpha \cdot \sqrt{\pi \cdot A}, \tag{7.2}$$

where c is the perimeter length of the pore, A is the area, and α is a constant, which describes how elliptical and jagged is a feature. The functions for $\alpha = 1$ (assuming a circular object) and $\alpha = 2$ (describing an elliptical or more rugged border) are displayed in Figure 7.8. In most cases, Equation (7.2) describes the relation of the area to the perimeter length for bright points, but some outliers with very large perimeter length disturb the relation. This shows that some bright points have a very complex shape. For the lower approximation of $\alpha = 1$, the relation of area and perimeter length is not well approximated. The objects are too small, *i.e.*, contain too few pixels for accurate ellipse fitting.

The three different groups of filigree are shown in Figure 7.8 with different symbols and colors. In general, the distribution of the bright points of Type I is large, whereas the other two types cluster more in the lower end of the distribution with smaller areas and perimeter lengths. Nonetheless, there are individual Type II and III bright points which also possess large areas and moderate perimeter lengths.

7.3.3 Filigree and Their Relation to Magnetic Field and UV Intensity

The relationship between bright points and the magnetic field was discussed since the first description of filigree by Dunn and Zirker (1973). We compare the location of the three types of filigree with the magnetic flux density (Figure 7.9). Most of the footpoint regions coincide with areas of enhanced magnetic flux density such as the left footpoint region of Filament B in Figure 7.9. The footpoint is rooted in a positive-polarity patch, which is accompanied by a negative-polarity patch to the left (see also the magnified views in Figure 7.6). In time-series of deep magnetograms, we observe that small-scale negative flux elements detach from the negative patch, which subsequently travel to the positive patch at the filament footpoint leading to flux cancellation. This occurs five times over a period of 10 hours. However, both the negative- and-positive polarity patch remain the dominant magnetic features in this region-of-interest over this 10-hour period, which indicates that the magnetic flux is intermittently replenished. We surmise that such a mechanism can provide the energy required to maintain and/or renew the cool plasma contained in the filament. We find also Type I bright points (cyan contours in Figure 7.9) in the surroundings of the filaments, which coincide with concentrations of magnetic flux. Not all bright points are located in concentrations of magnetic flux but most are close to these areas. Filaments are located above the PIL and rooted in concentrations of magnetic field. Thus, we do not expect high photospheric magnetic flux density for Type II bright points inside the filament contours.

Filaments D and E (Figure 7.9) were observed on consecutive days and give some insight into the evolution of the photospheric magnetic field below the filaments over the course of two and three days, respectively. Filament D is fully evolved on 24 September and decays on the following day. On the first observing day, the spine and three footpoints, rooted in strong concentrations of magnetic field, are clearly defined, whereas on the second day, the spine is not any longer elongated and distinct footpoints can no longer be recognized. Only the footpoint on the left is rooted in a region of high magnetic flux but no bright points are related to this footpoint region. The number of bright points at the location of the spine clearly increased on the second day. Filament E significantly evolved during 24 – 26 September. On the first day, the filament has a more clumpy appearance, with three footpoints rooted in strong magnetic flux concentrations. On the second day, the footpoints are more difficult to define. In addition, a clear relation to high magnetic flux concentrations is missing. On the third day, the filament is more elongated, covering the entire FOV, and the single structure splits into two filaments, stretched out next to each other but connected by some threads (best seen in Figure 7.4). The footpoints are not clearly visible in magnetograms. Not many bright points are found along the filament on the first two observing days but on the last observing day, their number increases. In full-disk observations (not shown), we see that Filament E is decaying in the following days. The large number of bright points at the location of the

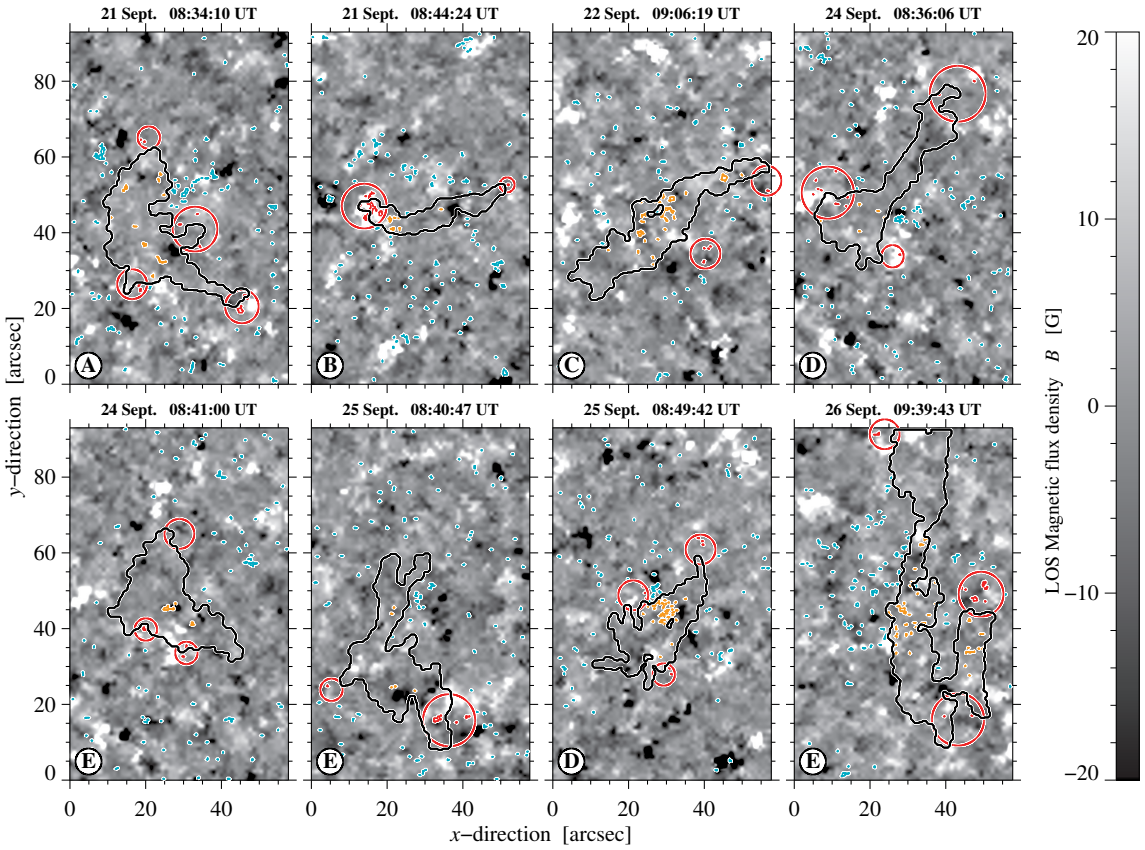

Figure 7.9: Deep HMI magnetograms, where the flux density is scaled between ±20 G with contours of filaments (*black*) and filigree categorized as Type I (*cyan*), Type II (*orange*), and Type III (*red*). In addition, the footpoints are marked with red circles. The label of the filaments is noted in a black circle in the lower left corner of each panel (see Table 7.1).

filament can be taken as an indication that the filament starts to decay. However, to verify this hypothesis, more samples of filaments and bright points are needed on several observing days.

In addition to magnetograms, we display the UV 1700 Å intensity (Figure 7.10), which we examine based on the position of bright points in Hα images. The UV 1700 Å filtergrams are normalized to the median value of the quiet-Sun intensity I_c derived from the full-disk images, excluding bright and dark structures. Bright points are located close to intensity-enhanced regions in the UV 1700 Å filtergrams. The location of the bright points is related to the magnetic network in UV 1700 Å filtergrams. On 21 September, on the right side of Filament A, bright points are clearly located at the border of a supergranular cell, including the bright points associated with the footpoints of the filament. Supergranular cell boundaries can also be determined for other filaments, *e.g.*, on 24 September for Filament D (lower left corner) and on 25 September for Filament E (upper right corner). A similar behavior as for the UV 1700 Å is evident in Ca II K filtergrams (Figure 7.5) and AIA UV 1600 Å filtergrams (not displayed).

We determined the intensity in the Hα images and UV 1700 Å filtergrams as well as the magnetic flux density of the three types of bright points and display their statistics as a box-and-whisker plot (Figure 7.11). Filigree are very bright in Hα images but vary in intensity (left panel in Figure 7.11). The intensity, normalized by the median value of the quiet-Sun intensity I_c, is in the range $0.96-1.17\,I/I_c$ with a median and standard deviation of $1.04\,I/I_c$ and $0.03\,I/I_c$, respectively, for all bright points. Type II bright points reach the lowest intensities of $(1.026\pm0.027)\,I/I_c$ while Type III bright points exhibit the highest intensities of $(1.049\pm0.023)\,I/I_c$. For all three types, mean and median values are very similar, and the scatter is also insignificant. Most bright points are clearly brighter than unity, *i.e.*, the median intensity of the quiet Sun that was used in the normalization.

The magnetic flux density (middle panel in Figure 7.11) of individual bright points was averaged across all pixels belonging to the bright point. The median values of the three types are very similar, *i.e.*, around 6.0 G, whereas the mean value varies more from 12.1 G for Type III, over 8.6 G for Type I, to 6.9 G for Type II. The scatter in the values is highest for Type III bright points at the footpoints, which

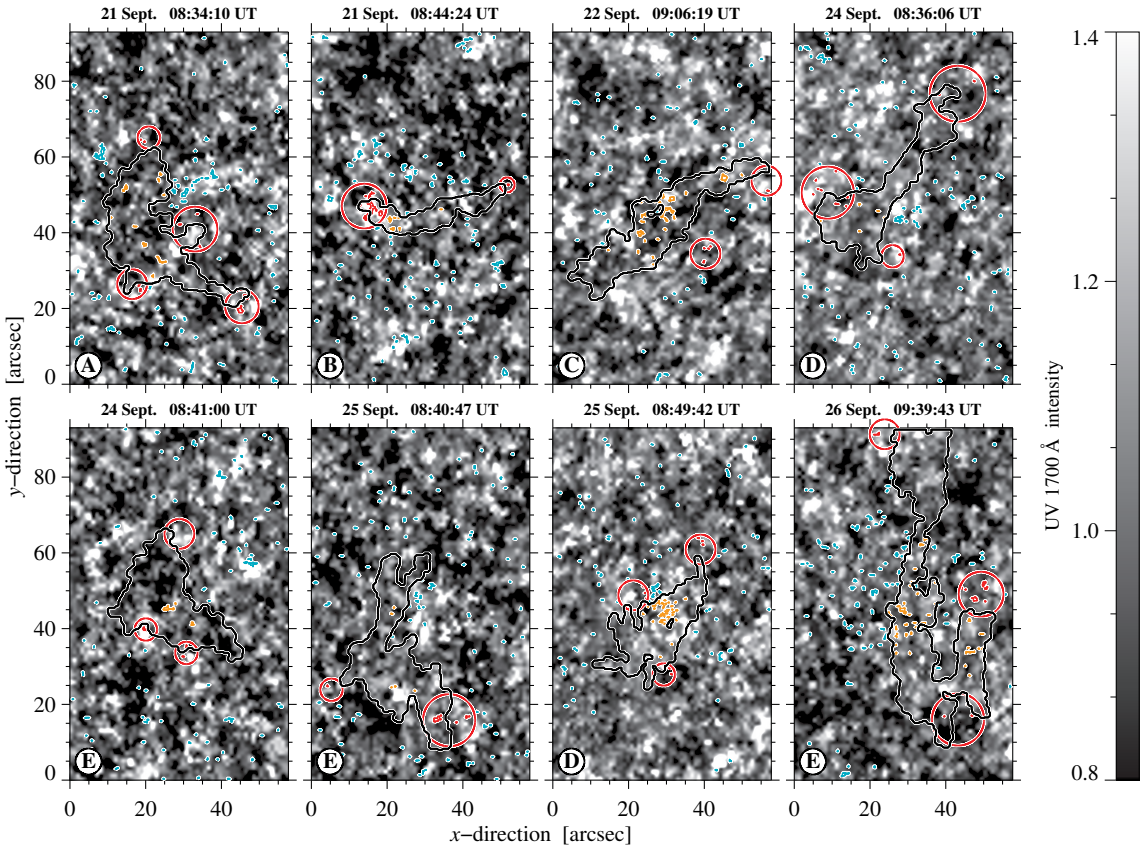

Figure 7.10: UV 1700 Å intensity of AIA normalized to the quiet-Sun intensity with the contours of the filaments (*black*) and Type I (*cyan*), Type II (*orange*), and Type III (*red*) filigree. In addition, the footpoints are marked with red circles. The label of the filaments is noted in a black circle in the lower left corner (see Table 7.1).

is also evident in the large differences for the percentiles. For Type III, 84 % of the bright points have an average magnetic flux density of up to 22.9 G, whereas for Type I and Type II, the values are about half of this with 13.4 G and 11.8 G. In addition, at the percentile $P_{95\%}$, 11 % of the bright points at the footpoints reach magnetic flux densities of up to 33.9 G, whereas only 20.4 G and 18.6 G are reached for Type I and II, respectively. Furthermore, the standard deviation of 17 G for Type III shows a large scatter for the magnetic flux density at the footpoints. The standard deviation for Type I is 10.0 G and for Type II it is only 5.0 G. The maximum values are reached for Type I and III with about 120 G in both categories for individual bright points, whereas the maximum value of Type II bright points is 26.0 G. In summary, Type III bright points, located at footpoints of polar crown and high-latitude filaments, are associated with higher concentrations of magnetic flux.

The box-and-whisker plot of the UV 1700 Å filtergrams (right panel in Figure 7.11,) shows that the median intensity is close to unity for the three types of bright points. The variation of the intensity is very low for Type II bright points, where 95 % of the bright points have an intensity below $1.16\,I/I_c$, whereas for Type III bright points, 95 % have an intensity below $1.51\,I/I_c$. In addition, the minimum intensity for this type is higher compared to the other types, with 5 % of the bright points having values below $0.87\,I/I_c$, whereas for the other types it is about $0.84\,I/I_c$. In summary, Type III bright points at the footpoints are on average brighter than other bright points. This mirrors the relationship already found for the magnetic field.

7.4 Discussion

This rare sample of high-resolution polar crown and high-latitude filaments observed in Hα images and filtergrams offered the opportunity to connect photospheric bright points with chromospheric filaments. We will discuss physical connections between filaments and bright points. Moreover, we address the

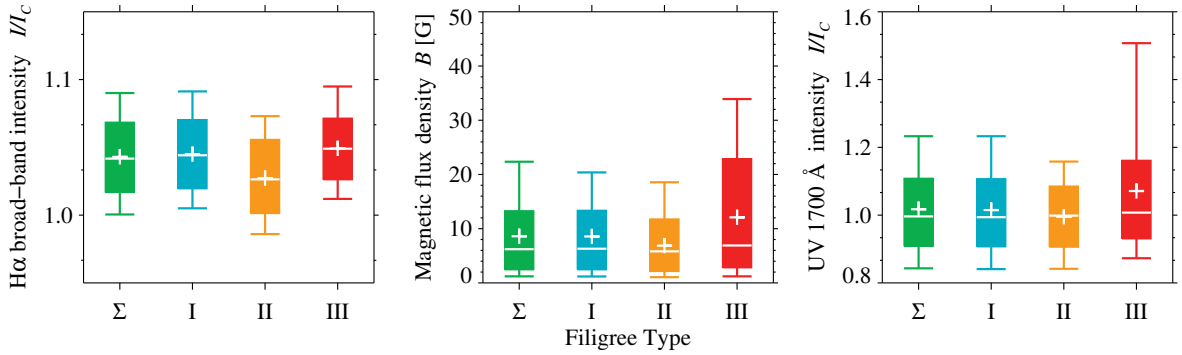

Figure 7.11: Box-and-whisker plot of the broad-band Hα intensity (*left*), magnetic flux density (*middle*), and UV 1700 Å intensity (*right*) for Type I, II, and III filigree (*cyan, orange, and red*) and the aggregate (*green*). The box is between percentiles $P_{16\%}$ and $P_{84\%}$, the whiskers between percentiles $P_{5\%}$ and $P_{95\%}$, the white line is the median value ($P_{50\%}$), and the '+' sign denotes the mean value.

question, if bright points in the weak magnetic fields of polar regions differ from their counterparts in the activity belt, which are well studied.

Morphology of Filaments. We first focus on the morphological description of the polar crown and high-latitude filaments recorded in high-resolution Hα filtergrams. The high-resolution observations resolve many details such as single threads along the spine. In the surroundings, we identified mottles, some clustered around bright cores forming rosettes, and also some mini-filaments. The evolution of Filaments D and E was analyzed by snapshots in time over two and three days. Furthermore, detailed observations of the filaments showed that only one end was contained in the FOV for Filaments A and E, which led to the interpretation that these are fragments of filaments. Density structure and geometric considerations for high-latitude and polar crown filaments were already described in Schmieder et al. (2010) and Dudík et al. (2012), who concluded that the viewing angle favors detecting cool plasma in a filament. Densities along the spine may be too low so that cool plasma escapes observations and leads to a fragmented appearance of filaments. Nonetheless, in full-disk Hα and He I filtergrams more of the spine was visible and we could pinpoint the counterparts for the extreme ends nearby.

Irregular Granulation. The Hα images are dominated by line-wing radiation, displaying photospheric granulation along with filigree. Some granules appeared brighter while other small areas appeared dark, which we attributed to strong absorption features and broad line profiles. In the intergranular lanes, we detected filigree as individual bright points or as clusters thereof. In the vicinity of bright points at lower latitudes, the granulation pattern often seems to be washed-out because of lower contrast and reduced visibility of the intergranular lanes, which is called "abnormal granulation" (Dunn and Zirker, 1973). However, it is often related to strong magnetic flux concentrations in the vicinity of active regions (Simon and Zirker, 1974) close to pores (Nesis, Hammer, and Schleicher, 2005) or sunspots (Sobotka, Bonet, and Vazquez, 1994) with magnetic field strength of more than 100 G (Jin, Wang, and Zhao, 2009; Beck et al., 2017). In this study, the LOS magnetic field does not reach 100 G, except for some single pixels related to bright points, yet the typical pattern of "abnormal granulation" is not encountered.

Morphology of Filigree. The bright points appear in different sizes and shapes and sometimes in clusters. The visual inspection of bright points led to the assumption that most bright points have a circular shape but many are significantly elongated (Muller, 2001). A cursory visual inspection of the sample in the present study supports this assumption but the quantitative analysis of the eccentricity shows a different result. Most of the bright points have an aspect ratio of about 2:1, and only three of the bright points have an eccentricity of nearly zero. Many bright points in Hα form elongated chains, which shows a morphological similarity to bright points in Ca II H (Kuckein et al., 2009). Nonetheless, not all bright points will be resolved. In an extensive statistical study, Yang et al. (2019) analyzed about 75 000 bright points in *Hinode* G-band images using a convolutional neural network. They differentiated between

isolated points, elongated chains, and bright points in the form of a knee. Isolated points and elongated chains exhibited a mean eccentricity and standard deviation of 0.48±0.23 and 0.89±0.01, respectively. The latter is comparable to the median eccentricity in our sample of 0.83 – 0.86 for all three types.

The peak of the length distribution of the bright points resides in the range 0.″5 – 0.″7 with a median of the distribution of about 0.″7. More elongated bright points have a length of up to 2.″0 and only some clusters reach higher values. The median value of the width is about 0.″4 for the three types of bright points. Earlier studies state a length of about 1.″0 – 2.″5 for elongated bright points (Dunn and Zirker, 1973; Tarbell et al., 1990) and diameters of 0.″30 – 0.″35 for circular bright points (Muller, 2001; Kuckein, 2019). Smaller diameters between 0.″13 – 0.″16 are given by Berger and Title (2001). In the study of Yang et al. (2019), bright points have diameters in the range 0.″14 – 0.″43 with a mean diameter of 0.″22 and a standard deviation of 0.″03, whereby the majority of bright points (88 %) have a circular shape. Leenaarts et al. (2006) concludes that bright points in the blue wing of Hα − 0.08 Å are predominantly photospheric and therefore have a similar morphology as G-band bright points. Since the broad-band filter covers the far wings of Hα (Figure 7.1), we expect in these pseudo continuum images even more similarities to G-band bright points. However, our results indicate larger values for length and width of bright points observed at high-latitudes.

The area distribution was compared with the distribution of the perimeter length of bright points. A similar distribution was found for a statistical sample of pores from *Hinode* observations by Verma and Denker (2014). They found that small pores have a tendency towards circular shapes and that larger pores tend to develop corrugated boundaries. A similar behavior is observed for bright points, where small bright points tend to be more circular whereas larger bright points are more elongated as seen in Figure 7.8. This is reasonable because bright points are likely associated with single magnetic elements (*e.g.*, Muller, 2001). Nonetheless, for smaller areas, close to the diffraction limit of the telescope, a reliable determination of the area and shape properties is impossible. On the other side of the scale, bright points with large perimeter length exhibit complicated structures. These are clusters of bright points, which were detected as one structure, *e.g.*, near the left footpoint region of Filament B (Figure 7.6). One problem besides seeing and the telescope's diffraction limit is the tendency of pattern recognition algorithms to link neighboring features (Verma and Denker, 2014).

Crockett et al. (2010) reported area distributions of observed and simulated bright points with a peak at about 0.05 Mm^2 and only a few exceeded 0.20 Mm^2 in these observations obtained with the Dunn Solar Telescope (DST). The peak of the area distribution in our study is higher, *i.e.*, in the range 0.07 – 0.09 Mm^2. In addition, our study shows a large tail in the area distribution, up to about 0.50 Mm^2. The larger area distribution can be attributed to the larger image scale of our observations (0.098″ pixel^{-1} at VTT *vs.* 0.069″ pixel^{-1} at DST) or to the location on the solar disk (high latitude *vs.* disk center) and consequently to projection effects. According to Yang et al. (2019), circular bright points have a small area with a mean of about 0.02 Mm^2, whereas more elongated bright points have mean areas of about 0.07 Mm^2. In our sample, the peak in the area distribution was about 0.08 Mm^2 but covers the range between 0.06 Mm^2 and 0.11 Mm^2 within one standard deviation, indicating a significant variation in size. Again, projection effects at high latitudes have to be considered.

The intensity of most bright points is clearly above the median intensity of the Hα images, *i.e.*, in the range 0.96 – 1.17 I/I_c, whereby Type II bright points at the location of the filament tend to lower intensity values within this range with a median value of 1.03 I/I_c. Type III bright points at the location of footpoints are in general brighter with a median intensity of 1.05 I/I_c. In the studies of Sánchez Almeida et al. (2004) and Yang et al. (2019), bright points reach intensities between 0.8 – 1.8 and 0.7 – 1.9, respectively, with the intensity normalized to the mean intensity of the quiet Sun. In the latter, the mean intensities of the identified bright points are 1.05 for circular bright points and reach higher values for more elongated bright point in the range 1.2 – 1.3.

Dunn and Zirker (1973) raised the question, if there are differences between the bright points in active regions, in the "enhanced network", and the quiet network. Most studies analyzed bright points at disk center (*e.g.*, Leenaarts et al., 2006) or active regions (*e.g.*, Kuckein, 2019). Our study dealt with

bright points at high latitudes in the vicinity of PCFs. The statistical evaluation, after careful geometrical correction to assure a correct interpretation of the morphology of the bright points, reveals that these bright points have very similar morphological properties as their counterparts at low latitudes but with larger length and width compared to lower latitudes.

Relations between Filigree and Filaments. Surveying the evolution of the filigree inside the two Filaments D and E over two and three days, we find that a large number of bright points are present before the decay of the filament. Since filigree are associated with individual magnetic elements, they may play an important role in the decay process by dispersing the remaining cool filament plasma. On the other hand, Li and Zhang (2016) reported bright points in the transition region at the base of filament threads, which potentially inject plasma into these threads. These bright points and the related upflows were quasi-periodic, resulting from small-scale oscillatory magnetic reconnection. In our study, we could not relate Type II or III bright points to single threads. Therefore, there is no basis for claiming a relation with the mass supply via the bright points. Nonetheless, Engvold (2004) and Lin et al. (2005) related the endpoints of single threads and barbs to boundaries of supergranular cells but they could not relate these endpoints to bright points. However, we find that bright points at footpoints of filaments are rooted in strong magnetic elements of the chromospheric network, which often correspond to the vertices of supergranular cell boundaries. The cool plasma is suspended above the weak fields inside supergranular cells, and the length of some predominate absorption structure in the observed filaments match the spatial scale of supergranulation.

Relations between Filigree, Magnetic Field, and UV Intensity. We related the location of filigree to the average magnetic flux density and UV intensity for the three types of bright points. This established that Type III bright points at the footpoints are more likely to be found near higher magnetic flux concentrations and with enhanced UV intensities. About 95 % of the bright points in this category display magnetic flux densities of up to 34 G. This indicates that bright points and filament footpoints are linked. In the first description of filigree, Dunn and Zirker (1973) stated that filigree are related to magnetic footpoints but this was neither followed up or extended to filaments of any type.

Some filigree appear in the vicinity of strong magnetic flux concentrations but they are not always co-spatial. The magnetograms will not show all quiet-Sun small-scale magnetic fields because of sensitivity limitations and the proximity close to the poles. Furthermore, we cannot rule out alignment and projection errors. Zhao et al. (2009) found that G-band and Ca II bright points were close to each other but did not necessarily intersect. Berger and Title (2001) examined the distance of G-band bright points to magnetic elements and found a mean distance of $0\farcs24$ but with most bright points intersecting with corresponding magnetic elements. Many studies stated that bright points are related to individual magnetic elements and that bright points in different wavelength bands are physically the same phenomenon, *i.e.*, G-band, Hα, Ca II H, Ca I λ10839 Å, and the blue wing of Fe I λ5250.5Å and Si I λ10827 Å (*e.g.*, Muller, 2001; Berger and Title, 2001; Leenaarts et al., 2006; Zhao et al., 2009; Utz et al., 2014; Kuckein, 2019).

The magnetic field values are relatively low for all filigree. However, the observations were carried out in quiet-Sun regions close to the poles. Other studies stating magnetic flux densities of bright points mainly focused on the activity belt around pores. Here, values of 200 G to 1500 G are encountered, especially in high-resolution observations of the magnetic field (*e.g.*, Tarbell et al., 1990; Muller, 2001; Beck et al., 2007; Utz et al., 2013; Kuckein, 2019).

Our study supports the scenario that vertices of supergranular cells, *i.e.*, the strongest and long-living magnetic flux concentrations in the quiet-Sun (Giannattasio et al., 2018), are often accompanied by bright points. Bright points are signatures of filament footpoints, which leave an imprint on the spatial scale of small high-latitude or polar-crown filaments or the building blocks of large-scale PCFs. In LOS magnetograms, we find intermittent flux cancellation at some of these sites, which provides energy to stabilize the mass-loaded filaments or to inject plasma into the filament (Chae et al., 2000; Chae, 2003). In addition, we observe an increasing number of bright points along the spine of a filament suggesting flux dispersal and a changing magnetic topology, which destabilizes the filament and initiates the decay of

the filament. In general, morphological differences between bright points at low and high latitudes are small with the exception that high-latitude bright points are larger, which may be related to the weaker magnetic fields in polar regions.

7.5 Conclusions and Outlook

To our knowledge, this is the first high-resolution study examining bright points associated with polar crown and high-latitude filaments. They were extracted from high-resolution Hα broad-band images and compared to their counterpart in Hα narrow-band filtergrams and moderate-resolution magnetograms, UV 1700 Å filtergrams, and ChroTel full-disk filtergrams in Hα, Ca II K, and He I. The main results can be summarized as follows: (i) The filaments and their surroundings could be resolved in great detail with high-resolution Hα observations obtained with a new synchronized, dual-imager CMOS camera system. (ii) Bright points at high latitudes have a similar morphological appearance as bright points at low latitudes close to active regions but are slightly larger. (iii) We found that filigree at the footpoints are more likely located at stronger magnetic flux concentrations and that they exhibit enhanced UV intensities compared to other bright points in the surroundings. (iv) We observed a larger number of bright points at the location of the filament when the filament started to decay. This conclusion is based on the temporal evolution of two filaments followed over the course of two and three days. (v) Bright regions in UV 1700 Å and Ca II K are clearly associated with bright points at the footpoints of filaments, in particular at the border of supergranular cells. Establishing the role of supergranular motions in forming polar crown filaments is a worthwhile scientific endeavor in itself but has to be deferred to a future investigation.

In the future, high-resolution fast cameras such as the M-lite 2M CMOS cameras, which were tested in this study, can be used for a detailed investigation of the temporal evolution of filigree and bright points. Time-series of polar crown filaments in Hα broad- and narrow-band will resolve the interaction of small-scale magnetic features and filament fine structure, especially within the footpoint regions. This may hold clues for formation and decay of filaments and for mass supply and stability of long-lasting polar crown filaments. Additional high-resolution observations in other wavelength bands will provide a more comprehensive picture of bright points in different atmospheric layers. The synchronized M-lite 2M cameras are now part of the GFPI at the GREGOR solar telescope. In combination with the *High-Resolution Fast Imager* (HiFI: Kuckein et al., 2017) and *GREGOR Infrared Spectrograph* (GRIS: Collados et al., 2012), multi-wavelength observations, simultaneous magnetic field observations, and fast time-series become possible. New 4-meter class telescopes, such as the *Daniel K. Inouye Solar Telescope* (DKIST: Tritschler et al., 2016) and the *European Solar Telescope* (EST: Collados et al., 2010; Jurčák et al., 2019), will soon provide data with a spatial resolution to fully resolve bright points facilitating a direct comparison with numerical simulations of small-scale magnetic features.

Chapter 8

Conclusions and Outlook

In the introduction of this thesis (Chap. 1), we described the importance of high-latitude and polar crown filaments for understanding the solar cycle. We addressed two different perspectives to understand the physical properties and the environment of polar crown and high-latitude filaments. First, we analyzed polar crown filaments on large-scales with full-disk ChroTel observations. Second, we studied the connection of polar crown filaments with small-scale bright points in their surroundings with high-spatial resolution VTT observations. Moreover, we explored possible uses of the Hα full-disk data as a tracer for the solar cycle, for both dark regions related to filaments and bright regions related to chromospheric plage. In the following paragraphs, we will summarize the main results obtained in this thesis. Finally, we will provide an outlook on further science, which can be carried-out in the future with new methods and observational capabilities.

Data Preparation and Exploration of Extraction Methods for Filaments. In this thesis, we demonstrated that the preparation of data is of utmost importance to scientifically exploit the data. In Chapter 3, the full-disk ChroTel filtergrams in He I 10830 Å were corrected for the non-uniform intensity variations, which were introduced by the Lyot-filters. The variation was approximated by Zernike polynomials and removed by dividing the filtergrams with the approximated 2D transmission map. This correction was used for the first time on the ChroTel filtergrams and enabled us to create Dopplergrams for the entire Sun from the filtergrams at different spectral positions. Comparisons with high-resolution spectral scans of GRIS, allowed to quantify the results from the Doppler maps. The method using the Zernike polynomial for the correction of intensity variations cannot only be used for He I 10830 Å filtergrams, but also for ChroTel in Hα and Ca II K filtergrams. The method laid the foundation of the subsequent scientific studies using ChroTel data. With accurately corrected Hα filtergrams, the morphological filament extraction from the synoptic maps in Chapter 4 was possible, as well as the subsequently statistical analysis of polar crown filaments and filaments. The data preparation is crucial for the training of deep learning algorithms for object detection and segmentation. The accurately reduced Hα filtergrams enabled obtaining the results presented in Chapter 5. Moreover, in Chapter 6, the non-uniform intensity correction enabled us to extract automatically with morphological image processing the Hα excess dark regions including filaments and bright plage regions. Further applications of the correction method have to be tested, i.e., on other full-disk telescopes using Lyot-filters or for post-processing of artifacts in filtergrams, for example from the Narrowband Filter Imager (NFI) of the Solar Optical Telescope on board Hinode, where bubbles in the birefringent Lyot filter degrade and obscure the images (Tsuneta et al., 2008).

Another aspect, which is important for the further scientific exploration of filaments and the subsequent analysis of the physical parameters, is the automatic extraction of filaments and their properties from the data. We attempted two possible methods: (1) morphological image processing and (2) object detection and segmentation of filaments. We used morphological image processing to easily extract dark features in the synoptic maps that we created from ChroTel Hα filtergrams. The disadvantage of this method is that also other features, apart from filaments, appear dark in these maps. We solved this issue by excluding small-scale structures, which inevitable excluded small-scale filamentary structures, as well. To avoid these problems in the object extraction, we explored another attempt by training a deep neural network to detect the location of filaments and to segment the filaments with a second network. The labeling of

the data was tedious, but the results show that the effort was worthwhile. The trained network predicts filaments in some cases even better as the previously labeled data. The predicted filaments will be used to reproduce the results in the statistical study presented in Chapter 4, in a forthcoming analysis, to prove the scientific value of the newly explored extraction method with deep neural networks.

Large-scale Filament Studies. In a filament survey using ChroTel Hα filtergrams, which were transformed into synoptic maps, we analyzed several physical parameters of the filaments during Solar Cycle 24, e.g, location, area, tilt-angle, and their intensity distribution. We sorted the filaments according to two phases: the maximum phase and the declining activity phase of the solar cycle, and compared the appearance of filaments during these two phases. The observations started in April 2012, just before the magnetic field reversal in the northern hemisphere in November 2012 and about two years before the magnetic field reversal in the southern hemisphere in March 2014. In the histograms, we clearly see a large number of filaments in mid- and high-latitudes in the southern hemisphere in the maximum phase. These filaments also appear to have comparably large areas. At the southern polar regions, even more large filaments are found, which indicates a connection to large-scale polar crown filaments. At lower latitudes, we find only small-scale filaments, related to active region filaments. In the declining phase, only sporadic filaments appear at latitudes above $\pm 70°$. Furthermore, we can identify Joy's law in the tilt-angle of low-latitude active region filaments, which often form at the PIL between bipolar active regions. For high-latitude filaments, the tilt-angle is reversed at latitudes above $\pm 40°$. This study complemented previous studies of Solar Cycle 24 with additional data for the declining phase. The intensity distribution of high-latitude and polar crown filaments in Hα and He I 10830 Å is very different. The distribution in Hα is broader and resembles a bimodal distribution with a strong declining slope toward high intensities and a shallow slope toward low intensities, in both maximum and declining phase, with a sharp peak at about 0.9 $I/I_{\rm qs}$. In the maximum phase, the gradient is high for the curve towards lower intensities. For He I 10830 Å, we find a Gaussian distribution in both phases, which includes quiet-Sun intensity in the distribution from the surroundings of the filament. This indicates that the filaments in He I have smaller extent than in Hα.

With the ChroTel Hα data, we can track the migration of polar crown filaments in the southern hemisphere. Using a cluster analysis and linear regression, we found a migration rate of $0.79° \pm 0.11°$ per Carrington rotation, which is higher than the migration rate found by Xu et al. (2018) with a migration rate of $0.63° \pm 0.08°$. This indicates an even larger discrepancy to the migration rate in the northern hemisphere, which Xu et al. (2018) determined to be $0.55° \pm 0.10°$. In the previous three cycles, the authors found a larger migration rate in the northern hemisphere than in the southern hemisphere.

The object detection algorithm allows us to utilize various data sources to create Big Data studies. Many surveys of Hα full-disk observations led to large data archives, but not all are easily accessible, e.g., the Virtual Solar Observatory (VSO, Hill et al., 2004). Combining these archives will enable more complex studies of polar crown filaments involving many more solar cycles to better understand the connection of polar crown filaments with the solar dynamo.

Connection of Polar Crown Filaments to Photospheric Bright Points Only a few studies exist with high-spatial resolution of polar crown filaments. In this thesis, we provide a high-resolution study of eight polar crown filaments, which were observed in the line-core of Hα and the continuum. This allowed us to study the connection of photospheric bright points, observed in the continuum and the footpoint regions of the filaments. The bright points found in the vicinity of filament footpoints are more likely to be located at strong magnetic flux concentrations and higher UV intensities. Many bright points appear at the border of supergranular cells. We found in continuous observations of a filament on several days that a larger number of bright points is found at the location of the filament, when the filament is decaying. The sparsely sampled time-series of these filaments did not allow to investigate the connection of these bright points to possible flux dispersal in the spine of the filament. In general, high-resolution filament observations under very good seeing conditions, covering longer periods of time, are rare, but they are essential in clarifying the role of bright points in the flux dispersal in decaying filaments.

Hα Excess as Tracer of Solar Activity We explored further capabilities of full-disk Hα observations of the Sun by creating a tracer for solar activity from the imaging Hα excess regions for bright plage regions and dark absorption regions related to filaments and sunspots. The positive Hα excess of the bright regions showed a very high correlation to other tracers of the solar activity, such as Mg II or the F10.7 cm radio flux. The distribution of the mean intensity of Hα excess regions during minimum and maximum exhibit the same shape, but with a lower amplitude. This indicates a stable coronal temperature during the solar cycle. We analyzed the positive Hα excess in comparison to the mean intensity of the Hα excess regions and their coverage fraction and found very high correlations. Both findings are relevant for the modeling of stellar and exoplanet atmospheres. Moreover, we explored the capabilities of a tracer created from the negative Hα excess, which is related to filaments and sunspots, but mainly to filaments since they are the dominating objects in full-disk Hα filtergrams. The tracer shows a correlation with the solar activity cycle. These results can be used for modeling the influence of filaments on stellar spectra of strong chromospheric absorption lines. Longer time-series and an imaging Hα excess derived from filaments, require further exploration and analysis, also on a longer time-scale, covering more than Solar Cycle 24. The new cycle has just begun and holds new fascinating opportunities to pursue research in this direction.

Outlook

Large-scale Filament Observations A uniform VSO-compliant access to various observatories observing the Sun in Hα with full-disk telescopes will give a large variety of new possible applications. With an increased database, a more effective and comprehensive training of deep neural networks will be possible and a detection and segmentation of filaments in near real-time becomes possible. Statistical studies of the migration of polar crown filaments will become more effective and different aspects can be better analyzed such as the appearance of a second "rush-to-the-pole" during the solar cycle or the migration rate of each hemisphere for several solar cycles. In addition, deep neural networks allow us to track polar crown filaments over time and enable a better understanding of their temporal evolution.

Deep neural networks can be exploited even more by using more than one wavelength for the training. Adding continuum data, a better exclusion of sunspots is possible and using Ca II K observations: We can better connect the appearance of low-latitude filaments to the chromospheric network, which is related to the underlying magnetic field. Polar crown filaments form at the border of unipolar field of the poles and the trailing flux of decayed active regions, which is transported polewards (Karna, Zhang, and Pesnell, 2017). According to the the Babcock-Leighton dynamo model, polar crown filaments should disappear with the magnetic field reversal at the poles during maximum (Webb, Davis, and McIntosh, 1984), but observations showed that they completely disappear six month to 1.5 years after the magnetic field reversal. In the study of Webb, Davis, and McIntosh (1984), this is explained by introducing a reversing poloidal component to the solar dynamo. From the observational point of view, the formation of polar crown filaments with respect to the magnetic field observations of SDO/HMI can be studied. At the pole, the magnetic field is weak and the determination of the PIL is complicated. With deep neural networks many applications can improve to infer the LOS magnetic field at the poles, e.g., enhancing the images to Hinode resolution (Díaz Baso and Asensio Ramos, 2018) or in noise reduction and enhancing the signal of the magnetic field with autoencoding techniques (Goodfellow, Bengio, and Courville, 2016). In addition, the magnetic field and polar crown filaments can be linked with high-spatial resolution observations of the polar magnetic field and polar crown filaments, which we will discuss below.

In the end, a more elaborated study including several solar cycles of the positive and negative imaging Hα excess will enhance our understanding of the Sun and solar-like stars. A large database of this tracer will facilitate better comparisons to other stars, where Hα spectral data is easily accessible. On the other hand, the negative Hα excess will enable studying the influence of filaments on Hα absorption lines in contrast to transiting events of exoplanets.

High-resolution Filament Observations As already indicated, only few observations of polar crown filaments are available in high-spatial resolution. The instrument suite of the VTT and the GREGOR solar telescope are both well suited to observe polar crown filaments. We have demonstrated this in Chapter 7 for

imaging observations of polar crown filaments in the Hα broad-band images and narrow-band filtergrams. Observations with the VTT echelle spectrograph will facilitate cloud model inversions (Beckers, 1964; Kuckein, Verma, and Denker, 2016; González Manrique, Bello González, and Denker, 2017; Dineva et al., 2020a) of filaments, which provide additional information on LOS velocity, Doppler width, the source function, and optical depth of filaments. With the echelle spectrograph, up to three wavelengths were observed simultaneously in the past, which enables observations in additional chromospheric lines, such as Hβ. An upgrade camera system at the VTT echelle spectrograph is planned for the year 2021 with the installation of new fast cameras, then, four spectral regions can be scanned simultaneously with a cadence of about one minute and a FOV of $120'' \times 240''$.

The GREGOR telescope is the largest European telescope with a mirror size of 1.5 m. The instruments at the telescope include, e.g., the GRIS, the GFPI, and the HiFI. Spectropolarimetric observations with GRIS in the He I 10830 Å line are possible, which includes the photospheric Si I and Ca I lines. Inversions of these three lines will give magnetic field information of the chromosphere and photosphere, where we can better relate bright points in the vicinity of polar crown filaments to their magnetic field, and we can analyze the LOS velocities in different atmospheric layers. This will enable us to study the connection of the appearance of bright points in the filament spine, while the filament is decaying, and the plasma transport in polar crown filaments. In general, detailed magnetic field observations and analysis of filaments are crucial to understand the overall structure of filaments, their stability, and mass supply. Only few of such studies exist, because of the complicated analysis and interpretation of the results. In the recent years, new inversion codes were developed to derive magnetic field properties from spectral scans of chromospheric lines.

The world's largest solar telescope is the Daniel K. Inouye Solar Telescope (DKIST, Tritschler et al., 2016), which will start with its normal operation in 2021. The 4-meter telescope will give a new perspective on the smallest resolvable features, the bright points. For this purpose, various instruments are available that can observe simultaneously multiple atmospheric layers of the Sun, addressing a broad variety of science cases. The instruments at DKIST are perfectly suited to study the chromosphere and its magnetic field, which is fundamental to understand the nature of filaments and in particular polar crown filaments.

In 2022, the next flight of Sunrise (Solanki et al., 2010) is scheduled – a stratospheric balloon mission with several high-resolution instruments. The major advantage compared to ground-based observations is that the observed data suffers less from effects introduced by the turbulent atmosphere of Earth, which is known as seeing. One instrument on board is the Sunrise Chromospheric Infrared Polarimeter (SCIP, Barthol et al., 2018), which will enable the observations of multiple spectral lines and achieves a very high signal to noise ratio for polarimetric observations. The instrument will allow to inter the magnetic field from lower atmospheric layers up to the chromosphere (Quintero Noda et al., 2017a,b, 2019). Having access to the 3D topology of the magnetic field will expand the results from this thesis and will provide us a much better understanding of bright points in the vicinity of filaments.

Bibliography

Ahmadzadeh, A., Mahajan, S.S., Kempton, D.J., Angryk, R.A., Ji, S.: 2019, Toward Filament Segmentation Using Deep Neural Networks. *arXiv e-prints*, arXiv:1912.02743. ADS.

Alexander, C.E., Walsh, R.W., Régnier, S., Cirtain, J., Winebarger, A.R., Golub, L., Kobayashi, K., Platt, S., Mitchell, N., Korreck, K., DePontieu, B., DeForest, C., Weber, M., Title, A., Kuzin, S.: 2013, Anti-parallel EUV Flows Observed along Active Region Filament Threads with Hi-C. *Astrophys. J., Lett.* **775**, L32. DOI. ADS.

Alvarado-Gómez, J.D., Hussain, G.A.J., Drake, J.J., Donati, J.-F., Sanz-Forcada, J., Stelzer, B., Cohen, O., Amazo-Gómez, E.M., Grunhut, J.H., Garraffo, C., Moschou, S.P., Silvester, J., Oksala, M.E.: 2018, Far beyond the Sun - I. The Beating Magnetic Heart in Horologium. *Mon. Not. R. Astron. Soc.* **473**, 4326. DOI. ADS.

Arlt, R., Vaquero, J.M.: 2020, Historical Sunspot Records. *Liv. Rev. Sol. Phys.* **17**, 1. DOI. ADS.

Arlt, R., Leussu, R., Giese, N., Mursula, K., Usoskin, I.G.: 2013, Sunspot Positions and Sizes for 1825–1867 from the Observations by Samuel Heinrich Schwabe. *Mon. Not. R. Astron. Soc.* **433**, 3165. DOI. ADS.

Armstrong, J.A., Fletcher, L.: 2019, Fast Solar Image Classification Using Deep Learning and Its Importance for Automation in Solar Physics. *Sol. Phys.* **294**, 80. DOI. ADS.

Babcock, H.W.: 1961, The Topology of the Sun's Magnetic Field and the 22-YEAR Cycle. *Astrophys. J.* **133**, 572. DOI. ADS.

Babcock, H.W., Babcock, H.D.: 1955, The Sun's Magnetic Field, 1952 – 1954. *Astrophys. J.* **121**, 349. DOI. ADS.

Baliunas, S.L., Donahue, R.A., Soon, W.H., Horne, J.H., Frazer, J., Woodard-Eklund, L., Bradford, M., Rao, L.M., Wilson, O.C., Zhang, Q., Bennett, W., Briggs, J., Carroll, S.M., Duncan, D.K., Figueroa, D., Lanning, H.H., Misch, T., Mueller, J., Noyes, R.W., Poppe, D., Porter, A.C., Robinson, C.R., Russell, J., Shelton, J.C., Soyumer, T., Vaughan, A.H., Whitney, J.H.: 1995, Chromospheric Variations in Main-Sequence Stars. II. *Astrophys. J.* **438**, 269. DOI. ADS.

Balthasar, H., Vazquez, M., Woehl, H.: 1986, Differential Rotation of Sunspot Groups in the Period from 1874 through 1976 and Changes of the Rotation Velocity within the Solar Cycle. *Astron. Astrophys.* **155**, 87. ADS.

Barthol, P., Katsukawa, Y., Lagg, A., Solanki, S.K., Kubo, M., Riethmueller, T., Martínez Pillet, V., Gandorfer, A., Feller, A., Berkefeld, .T., Orozco Suárez, D., Del Toro Iniesta, J.C., Bernasconi, P., Álvarez-Herrero, A., Quintero Noda, C.: 2018, Getting Ready for the Third Science Flight of SUNRISE. In: *42nd COSPAR Scientific Assembly* **42**, PSB.1. ADS.

Beck, C., Bellot Rubio, L.R., Schlichenmaier, R., Sütterlin, P.: 2007, Magnetic Properties of G-band Bright Points in a Sunspot Moat. *Astron. Astrophys.* **472**, 607. DOI. ADS.

Beck, C., Fabbian, D., Rezaei, R., Puschmann, K.G.: 2017, The Polarization Signature of Photospheric Magnetic Fields in 3D MHD Simulations and Observations at Disk Center. *Astrophys. J.* **842**, 37. DOI. ADS.

Beckers, J.M.: 1964, A Study of the Fine Structures in the Solar Chromosphere. PhD Thesis, Sacramento Peak Observatory, Air Force Cambridge Research Laboratories, Massachusetts, USA.

Bentely, R.D., Freeland, S.L.: 1998, SOLARSOFT – An Analysis Environment for Solar Physics. In: *Crossroads for European Solar and Heliospheric Physics. Recent Achievements and Future Mission Possibilities*, *ESA Special Publication* **417**, 225. ADS.

Berger, T.E., Title, A.M.: 2001, On the Relation of G-Band Bright Points to the Photospheric Magnetic Field. *Astrophys. J.* **553**, 449. DOI. ADS.

Berger, T.E., Liu, W., Low, B.C.: 2012, SDO/AIA Detection of Solar Prominence Formation within a Coronal Cavity. *Astrophys. J., Lett.* **758**, L37. DOI. ADS.

Berger, T., Testa, P., Hillier, A., Boerner, P., Low, B.C., Shibata, K., Schrijver, C., Tarbell, T., Title, A.: 2011, Magneto-Thermal Convection in Solar Prominences. *Nature* **472**, 197. DOI. ADS.

Bertello, L., Pevtsov, A., Tlatov, A., Singh, J.: 2016, Correlation Between Sunspot Number and Ca II K Emission Index. *Sol. Phys.* **291**, 2967. DOI. ADS.

Bethge, C.: 2010, Investigation of Large Scale Structures in the Solar Chromosphere with the Full-disk Telescope ChroTel. PhD Thesis, Albert-Ludwigs-Universität Freiburg.

Bethge, C., Peter, H., Kentischer, T.J., Halbgewachs, C., Elmore, D.F., Beck, C.: 2011, The Chromospheric Telescope. *Astron. Astrophys.* **534**, A105. DOI. ADS.

Böhm-Vitense, E.: 1989, *Introduction to Stellar Astrophysics. Vol.2: Stellar Atmospheres* **2**, Cambridge University Press, Cambridge, UK. ADS.

Brandt, P.: 2001, Solar Photosphere: Granulation. In: Murdin, P. (ed.) *Encyclopedia of Astronomy and Astrophysics*, IOP Publishing Ltd and Nature Publishing Group, London, UK. DOI. ADS.

Brault, J.W.: 1985, Fourier Transform Spectroscopy. In: *High Resolution in Astronomy, Fifteenth Advanced Course of the Swiss Society of Astronomy and Astrophysics. Edited by A.O. Benz, M. Huber, and M. Mayer. Geneva Observatory, Sauverny, Switzerland*, 3.

Brown, T.M., Morrow, C.A.: 1987, Depth and Latitude Dependence of Solar Rotation. *Astrophys. J., Lett.* **314**, L21. DOI. ADS.

Brueckner, G.E., Howard, R.A., Koomen, M.J., Korendyke, C.M., Michels, D.J., Moses, J.D., Socker, D.G., Dere, K.P., Lamy, P.L., Llebaria, A., Bout, M.V., Schwenn, R., Simnett, G.M., Bedford, D.K., Eyles, C.J.: 1995, The Large Angle Spectroscopic Coronagraph (LASCO). *Sol. Phys.* **162**, 357. DOI. ADS.

Cameron, R.H., Dikpati, M., Brandenburg, A.: 2017, The Global Solar Dynamo. *Space Sci. Rev.* **210**, 367. DOI. ADS.

Carrington, R.C.: 1858, On the Distribution of the Solar Spots in Latitudes since the Beginning of the Year 1854, with a Map. *Mon. Not. R. Astron. Soc.* **19**, 1. DOI. ADS.

Carroll, B.W., Ostlie, D.A.: 2017, *An Introduction to Modern Astrophysics*, Pearson Addison-Wesley, San Francisco, USA.

Cauley, P.W., Redfield, S., Jensen, A.G.: 2017, A Decade of Hα Transits for HD 189733 b: Stellar Activity versus Absorption in the Extended Atmosphere. *Astron. J.* **153**, 217. DOI. ADS.

Cauley, P.W., Kuckein, C., Redfield, S., Shkolnik, E.L., Denker, C., Llama, J., Verma, M.: 2018, The Effects of Stellar Activity on Optical High-resolution Exoplanet Transmission Spectra. *Astron. J.* **156**, 189. DOI. ADS.

Chae, J.: 2003, The Formation of a Prominence in NOAA Active Region 8668. II. TRACE Observations of Jets and Eruptions Associated with Canceling Magnetic Features. *Astrophys. J.* **584**, 1084. DOI. ADS.

Chae, J., Denker, C., Spirock, T.J., Wang, H., Goode, P.R.: 2000, High-resolution Hα Observations of Proper Motion in NOAA 8668: Evidence for Filament Mass Injection by Chromospheric Reconnection. *Sol. Phys.* **195**, 333. DOI. ADS.

Chatterjee, S., Hegde, M., Banerjee, D., Ravindra, B.: 2017, Long-term Study of the Solar Filaments from the Synoptic Maps as Derived from H_α Spectroheliograms of the Kodaikanal Observatory. *Astrophys. J.* **849**, 44. DOI. ADS.

Chatzistergos, T., Ermolli, I., Krivova, N.A., Solanki, S.K., Banerjee, D., Barata, T., Belik, M., Gafeira, R., Garcia, A., Hanaoka, Y., Hegde, M., Klimeš, J., Korokhin, V.V., Lourenço, A., Malherbe, J.-M., Marchenko, G.P., Peixinho, N., Sakurai, T., Tlatov, A.G.: 2020, Analysis of Full-disc Ca II K Spectroheliograms. III. Plage Area Composite Series Covering 1892-2019. *Astron. Astrophys.* **639**, A88. DOI. ADS.

Chen, L.-C., Papandreou, G., Schroff, F., Adam, H.: 2017, Rethinking Atrous Convolution for Semantic Image Segmentation. *arXiv e-prints*, arXiv:1706.05587. ADS.

Clette, F., Cugnon, P., Berghmans, D., van der Linden, R., Wauters, L.: 2002, The New Instrumentation of the SIDC/Uccle Station. In: Wilson, A. (ed.) *Solar Variability: From Core to Outer Frontiers*, *ESA Special Publication* **2**, 935. ADS.

Cliver, E.W.: 2014, The Extended Cycle of Solar Activity and the Sun's 22-Year Magnetic Cycle. *Space Sci. Rev.* **186**, 169. DOI. ADS.

Collados, M., Lagg, A., Díaz Garcí A, J.J., Hernández Suárez, E., López López, R., Páez Mañá, E., Solanki, S.K.: 2007, Tenerife Infrared Polarimeter II. In: Heinzel, P., Dorotovič, I., Rutten, R.J. (eds.) *The Physics of Chromospheric Plasmas*, *Astronomical Society of the Pacific Conference Series* **368**, 611. ADS.

Collados, M., Bettonvil, F., Cavaller, L., Ermolli, I., Gelly, B., Pérez, A., Socas-Navarro, H., Soltau, D., Volkmer, R., EST Team: 2010, European Solar Telescope: Progress Status. *Astron. Nachr.* **331**, 615. DOI. ADS.

Collados, M., López, R., Páez, E., Hernández, E., Reyes, M., Calcines, A., Ballesteros, E., Díaz, J.J., Denker, C., Lagg, A., Schlichenmaier, R., Schmidt, W., Solanki, S.K., Strassmeier, K.G., von der Lühe, O., Volkmer, R.: 2012, GRIS: The GREGOR Infrared Spectrograph. *Astron. Nachr.* **333**, 872. DOI. ADS.

Cortes, C., Vapnik, V.: 1995, Support-Vector Networks. *Machine Learning* **20**, 273.

Coulter, R.L., Kuhn, J.R., Lin, H.: 1996, The Precision Solar Photometric Telescopes. In: *American Astronomical Society Meeting Abstracts Nr.188*, 56.04. ADS.

Crockett, P.J., Mathioudakis, M., Jess, D.B., Shelyag, S., Keenan, F.P., Christian, D.J.: 2010, The Area Distribution of Solar Magnetic Bright Points. *Astrophys. J., Lett.* **722**, L188. DOI. ADS.

David, T.J., Petigura, E.A., Luger, R., Foreman-Mackey, D., Livingston, J.H., Mamajek, E.E., Hillenbrand, L.A.: 2019, Four Newborn Planets Transiting the Young Solar Analog V1298 Tau. *Astrophys. J., Lett.* **885**, L12. DOI. ADS.

Del Zanna, G., Mason, H.E.: 2018, Solar UV and X-ray Spectral Diagnostics. *Liv. Rev. Sol. Phys.* **15**, 5. DOI. ADS.

Deng, H., Zhang, D., Wang, T., Ji, K., Wang, F., Liu, Z., Xiang, Y., Jin, Z., Cao, W.: 2015, Objective Image-Quality Assessment for High-Resolution Photospheric Images by Median Filter-Gradient Similarity. *Sol. Phys.* **290**, 1479. DOI. ADS.

Deng, Y.Y., Schmieder, B., Engvold, O., DeLuca, E., Golub, L.: 2000, Emergence of Sheared Magnetic Flux Tubes in an Active Region Observed with the SVST and TRACE. *Sol. Phys.* **195**, 347. DOI. ADS.

Denker, C., Tritschler, A.: 2005, Measuring and Maintaining the Plate Parallelism of Fabry-Pérot Etalons. *Publ. Astron. Soc. Pac.* **117**, 1435. DOI. ADS.

Denker, C., Johannesson, A., Marquette, W., Goode, P.R., Wang, H., Zirin, H.: 1999, Synoptic Hα Full-Disk Observations of the Sun from BigBear Solar Observatory - I. Instrumentation, Image Processing, Data Products, and First Results. *Sol. Phys.* **184**, 87. DOI. ADS.

Denker, C., Balthasar, H., Hofmann, A., Bello González, N., Volkmer, R.: 2010, The GREGOR Fabry-Perot Interferometer: A New Instrument for High-Resolution Solar Observations. In: McLean, I.S., Ramsay, S.K., Takami, H. (eds.) *Ground-Based and Airborne Instrumentation for Astronomy III.*, *Proc. SPIE* **7735**, 77356M. DOI. ADS.

Denker, C., Dineva, E., Balthasar, H., Verma, M., Kuckein, C., Diercke, A., González Manrique, S.J.: 2018, Image Quality in High-resolution and High-cadence Solar Imaging. *Sol. Phys.* **293**, 44. DOI. ADS.

Denker, C., Verma, M., Kuckein, C., Diercke, A., Kamlah, R., Seelemann, T., Balthasar, H., Dineva, E., Kontogiannis, I., Pal, P.: 2020, Synchronized, High-cadence CMOS Cameras for Imaging Spectroscopy and Image Restoration. *Sol. Phys.* submitted.

Díaz Baso, C.J., Asensio Ramos, A.: 2018, Enhancing SDO/HMI Images Using Deep Learning. *Astron. Astrophys.* **614**, A5. DOI. ADS.

Dickens, C.: 1859, *A Tale of Two Cities*, Chapman & Hall, London, UK.

Diercke, A., Denker, C.: 2019, Chromospheric Synoptic Maps of Polar Crown Filaments. *Sol. Phys.* **294**, 152. DOI. ADS.

Diercke, A., Arlt, R., Denker, C.: 2015, Digitization of Sunspot Drawings by Spörer made in 1861–1894. *Astron. Nachr.* **336**, 53. DOI. ADS.

Diercke, A., Kuckein, C., Verma, M., Denker, C.: 2018, Counter-Streaming Flows in a Giant Quiet-Sun Filament Observed in the Extreme Ultraviolet. *Astron. Astrophys.* **611**, A64. DOI. ADS.

Diercke, A., Kuckein, C., Verman, M., Denker, C.: 2020, Filigree in the Surroundings of Polar Crown and High-Latitude Filaments. *Sol. Phys.*, arXiv:2012.04349. ADS.

Dineva, E., Verma, M., González Manrique, S.J., Schwartz, P., Denker, C.: 2020a, Cloud Model Inversions of Strong Chromospheric Absorption Lines Using Principal Component Analysis. *Astron. Nachr.* **341**, 64. DOI. ADS.

Dineva, E., Denker, C., Strassmeier, K.G., Ilyin, I., Pevtsov, A.A.: 2020b, Monitoring Solar Activity with PEPSI. In: *IAU General Assembly*, 351. DOI. ADS.

Domingo, V., Fleck, B., Poland, A.I.: 1995, The SOHO Mission: An Overview. *Sol. Phys.* **162**, 1. DOI. ADS.

Dudík, J., Aulanier, G., Schmieder, B., Zapiór, M., Heinzel, P.: 2012, Magnetic Topology of Bubbles in Quiescent Prominences. *Astrophys. J.* **761**, 9. DOI. ADS.

Dunn, R.B., Zirker, J.B.: 1973, The Solar Filigree. *Sol. Phys.* **33**, 281. DOI. ADS.

Dunn, R.B., Zirker, J.B., Beckers, J.M.: 1974, Properties of the Solar Filigree Structure. In: Athay, R.G. (ed.) *Chromospheric Fine Structure*, *IAU Symposium* **56**, 45. ADS.

Elgendy, M.: 2020, *Deep Learning for Vision Systems*, Manning Publications, Shelter Island, New York, USA. ISBN 9781617296192. https://www.manning.com/books/deep-learning-for-vision-systems.

Elmore, D.F., Card, G.L., Chambellan, C.W., Hassler, D.M., Hull, H.L., Lecinski, A.R., MacQueen, R.M., Streander, K.V., Streete, J.L., White, O.R.: 1998, Chromospheric Helium Imaging Photometer (an Instrument for High Time Cadence 1083-nm Wavelength Solar Observations). *Appl. Opt.* **37**, 4270. DOI. ADS.

Engvold, O.: 1998, Observations of Filament Structure and Dynamics. In: Webb, D.F., Schmieder, B., Rust, D.M. (eds.) *New Perspectives on Solar Prominences*, *ASP Conf. Ser.* **150**, 23. ADS.

Engvold, O.: 2001, Solar Prominence Fine Structure. In: Murdin, P. (ed.) *Encyclopedia of Astronomy and Astrophysics*, IOP Publishing Ltd and Nature Publishing Group, London, UK, 2695. DOI. ADS.

Engvold, O.: 2004, Structures and Dynamics of Solar Filaments – Challenges in Observing and Modeling. In: Stepanov, A.V., Benevolenskaya, E.E., Kosovichev, A.G. (eds.) *Multi-wavelength Investigations of Solar Activity* **223**, 187. DOI. ADS.

Engvold, O.: 2015, Description and Classification of Prominences. In: Vial, J.-C., Engvold, O. (eds.) *Solar Prominences, Astrophys. Space. Sci. Libr.* **415**, Cham, Switzerland, 31. DOI. ADS.

Ermolli, I., Shibasaki, K., Tlatov, A., van Driel-Gesztelyi, L.: 2014, Solar Cycle Indices from the Photosphere to the Corona: Measurements and Underlying Physics. *Space Sci. Rev.* **186**, 105. DOI. ADS.

Evershed, J., Evershed, M.A.: 1917, *Results of Prominence Observations* **1**, Kodaikanal, India, 55.

Fanning, D.W.: 2011, *Coyote's Guide to Traditional IDL Graphics*, Coyote Book Publishing, Fort Collins, Colorado.

Favata, F., Micela, G., Orlando, S., Schmitt, J.H.M.M., Sciortino, S., Hall, J.: 2008, The X-ray Cycle in the Solar-type Star HD 81809. XMM-Newton Observations and Implications for the Coronal Structure. *Astron. Astrophys.* **490**, 1121. DOI. ADS.

Feng, S., Ji, K.-F., Deng, H., Wang, F., Fu, X.-D.: 2012, Automatic Detection and Extraction Algorithm of Inter-Granular Bright Points. *J. Korean Astron. Soc.* **45**, 167. DOI. ADS.

Forveille, T., Shore, S.: 2020, The Solar Orbiter Mission. *Astron. Astrophys.* **642**, E1. DOI. ADS.

Freeland, S.L., Handy, B.N.: 1998, Data Analysis with the SolarSoft System. *Sol. Phys.* **182**, 497. DOI. ADS.

Fröhlich, C.: 2012, Total Solar Irradiance Observations. *Surveys in Geophysics* **33**, 453. DOI. ADS.

Gaizauskas, V.: 2001, Solar Filament Channels. In: Murdin, P. (ed.) *Encyclopedia of Astronomy and Astrophysics*, IOP Publishing Ltd and Nature Publishing Group, London, UK, 2509. DOI. ADS.

Gaizauskas, V., Zirker, J.B., Sweetland, C., Kovacs, A.: 1997, Formation of a Solar Filament Channel. *Astrophys. J.* **479**, 448. DOI. ADS.

Giannattasio, F., Berrilli, F., Consolini, G., Del Moro, D., Gošić, M., Bellot Rubio, L.: 2018, Occurrence and Persistence of Magnetic Elements in the Quiet Sun. *Astron. Astrophys.* **611**, A56. DOI. ADS.

Gibson, S.E., Webb, D., Hewins, I.M., McFadden, R.H., Emery, B.A., Denig, W., McIntosh, P.S.: 2017, Beyond sunspots: Studies using the McIntosh Archive of Global Solar Magnetic Field Patterns. In: Nandy, D., Valio, A., Petit, P. (eds.) *Living Around Active Stars* **328**, 93. DOI. ADS.

Girshick, R.: 2015, Fast R-CNN. In: *2015 IEEE International Conference on Computer Vision (ICCV)*, 1440. DOI.

Girshick, R., Donahue, J., Darrell, T., Malik, J.: 2014, Rich Feature Hierarchies for Accurate Object Detection and Semantic Segmentation. In: *2014 IEEE Conference on Computer Vision and Pattern Recognition*, 580. DOI.

Golub, L., Deluca, E., Austin, G., Bookbinder, J., Caldwell, D., Cheimets, P., Cirtain, J., Cosmo, M., Reid, P., Sette, A., Weber, M., Sakao, T., Kano, R., Shibasaki, K., Hara, H., Tsuneta, S., Kumagai, K., Tamura, T., Shimojo, M., McCracken, J., Carpenter, J., Haight, H., Siler, R., Wright, E., Tucker, J., Rutledge, H., Barbera, M., Peres, G., Varisco, S.: 2007, The X-Ray Telescope (XRT) for the Hinode Mission. *Sol. Phys.* **243**, 63. DOI. ADS.

Gonzalez, R.C., Woods, R.E.: 2002, *Digital Image Processing*, Prentice-Hall, Upper Saddle River, New Jersey, USA.

Gonzalez, R.C., Woods, R.E., Eddins, S.: 2009, *Digital Image Processing using MATLAB*, Gatesmark Publishing, Konxville, USA.

González Manrique, S.J., Bello González, N., Denker, C.: 2017, High-resolution Imaging Spectroscopy of two Micro-pores and an Arch Filament System in a small Emerging-flux Region. *Astron. Astrophys.* **600**, A38. DOI. ADS.

González Manrique, S.J., Kuckein, C., Collados, M., Denker, C., Solanki, S.K., Gömöry, P., Verma, M., Balthasar, H., Lagg, A., Diercke, A.: 2018, Temporal Evolution of Arch Filaments as seen in He I 10830 . *Astron. Astrophys.* **617**, A55. DOI. ADS.

Goodfellow, I., Bengio, Y., Courville, A.: 2016, *Deep Learning*, MIT Press, Cambridge, MA, USA. www.deeplearningbook.org.

Gully-Santiago, M.A., Herczeg, G.J., Czekala, I., Somers, G., Grankin, K., Covey, K.R., Donati, J.F., Alencar, S.H.P., Hussain, G.A.J., Shappee, B.J., Mace, G.N., Lee, J.-J., Holoien, T.W.-S., Jose, J., Liu, C.-F.: 2017, Placing the Spotted T Tauri Star LkCa 4 on an HR Diagram. *Astrophys. J.* **836**, 200. DOI. ADS.

Halbgewachs, C., Bethge, C., Caligari, P., Elmore, D., Kentischer, T.J., Peter, H., Sigwarth, M., Schmidt, W.: 2008, The Control and Data Concept for the Robotic Solar Telescope ChroTel. In: *Advanced Software and Control for Astronomy II*, *Proc. SPIE* **7019**, 70192T. DOI. ADS.

Hale, G.E.: 1908, On the Probable Existence of a Magnetic Field in Sun-Spots. *Astrophys. J.* **28**, 315. DOI. ADS.

Hale, G.E., Ellerman, F., Nicholson, S.B., Joy, A.H.: 1919, The Magnetic Polarity of Sun-Spots. *Astrophys. J.* **49**, 153. DOI. ADS.

Hall, J.C., Lockwood, G.W.: 2004, The Chromospheric Activity and Variability of Cycling and Flat Activity Solar-Analog Stars. *Astrophys. J.* **614**, 942. DOI. ADS.

Hanisch, R.J., Farris, A., Greisen, E.W., Pence, W.D., Schlesinger, B.M., Teuben, P.J., Thompson, R.W., Warnock, A.: 2001, Definition of the Flexible Image Transport System (FITS). *Astron. Astrophys.* **376**, 359. DOI.

Hanslmeier, A.: 2020, *Einführung in Astronomie und Astrophysik*, Springer Spektrum, Berlin, Germany. DOI. ADS.

Hao, Q., Fang, C., Cao, W., Chen, P.F.: 2015, Statistical Analysis of Filament Features Based on the Hα Solar Images from 1988 to 2013 by Computer Automated Detection Method. *Astrophys. J., Suppl. Ser.* **221**, 33. DOI. ADS.

Harvey, J.W.: 1973, Fraunhofer Lines with Large Zeeman Splitting. *Sol. Phys.* **28**, 9. DOI. ADS.

Harvey, J.W., Hill, F., Hubbard, R.P., Kennedy, J.R., Leibacher, J.W., Pintar, J.A., Gilman, P.A., Noyes, R.W., Title, A.M., Toomre, J., Ulrich, R.K., Bhatnagar, A., Kennewell, J.A., Marquette, W., Patron, J., Saa, O., Yasukawa, E.: 1996, The Global Oscillation Network Group (GONG) Project. *Sci* **272**, 1284. DOI. ADS.

Hathaway, D.H.: 2010, The Solar Cycle. *Liv. Rev. Sol. Phys.* **7**, 1. DOI. ADS.

Haywood, R.D., Collier Cameron, A., Unruh, Y.C., Lovis, C., Lanza, A.F., Llama, J., Deleuil, M., Fares, R., Gillon, M., Moutou, C., Pepe, F., Pollacco, D., Queloz, D., Ségransan, D.: 2016, The Sun as a Planet-host Star: Proxies from SDO images for HARPS Radial-velocity Variations. *Mon. Not. R. Astron. Soc.* **457**, 3637. DOI. ADS.

He, K., Zhang, X., Ren, S., Sun, J.: 2016, Deep Residual Learning for Image Recognition. In: *2016 IEEE Conference on Computer Vision and Pattern Recognition (CVPR)*, 770. DOI.

He, K., Gkioxari, G., Dollár, P., Girshick, R.: 2017, Mask R-CNN. In: *2017 IEEE International Conference on Computer Vision (ICCV)*, 2980. DOI.

Hempelmann, A., Schmitt, J.H.M.M., Stępień, K.: 1996, Coronal X-ray Emission of Cool Stars in Relation to Chromospheric Activity and Magnetic Cycles. *Astron. Astrophys.* **305**, 284. ADS.

Hempelmann, A., Robrade, J., Schmitt, J.H.M.M., Favata, F., Baliunas, S.L., Hall, J.C.: 2006, Coronal Activity Cycles in 61 Cygni. *Astron. Astrophys.* **460**, 261. DOI. ADS.

Hill, F., Bogart, R.S., Davey, A., Dimitoglou, G., Gurman, J.B., Hourcle, J.A., Martens, P.C., Suarez-Sola, I., Tian, K., Wampler, S., Yoshimura, K.: 2004, The Virtual Solar Observatory: Status and Initial Operational Experience. In: Quinn, P.J., Bridger, A. (eds.) *Optimizing Scientific Return for Astronomy through Information Technologies*, *Proc. SPIE* **5493**, 163. DOI. ADS.

Hofmeister, S.J., Utz, D., Heinemann, S.G., Veronig, A., Temmer, M.: 2019, Photospheric Magnetic Structure of Coronal Holes. *Astron. Astrophys.* **629**, A22. DOI. ADS.

Holzreuter, R., Solanki, S.K.: 2015, Three-dimensional non-LTE Radiative Transfer Effects in Fe I lines. III. Line Formation in Magneto-hydrodynamic Atmospheres. *Astron. Astrophys.* **582**, A101. DOI. ADS.

Hurlburt, N., Cheung, M., Schrijver, C., Chang, L., Freeland, S., Green, S., Heck, C., Jaffey, A., Kobashi, A., Schiff, D., Serafin, J., Seguin, R., Slater, G., Somani, A., Timmons, R.: 2012, Heliophysics Event Knowledgebase for the Solar Dynamics Observatory (SDO) and Beyond. *Sol. Phys.* **275**, 67. DOI. ADS.

Iazev, S.A., Khmyrov, G.M.: 1988, An Investigation of a Giant Filament as Observed in May – July 1984: Comparison With Characteristics of a Large-scale System of Magnetic Fields. *Adv. Space Res.* **8**, 199. DOI. ADS.

Illarionov, E., Kosovichev, A., Tlatov, A.: 2020, Machine-learning Approach to Identification of Coronal Holes in Solar Disk Images and Synoptic Maps. *Astrophys. J.* **903**, 115. DOI. ADS.

Jansen, F., Lumb, D., Altieri, B., Clavel, J., Ehle, M., Erd, C., Gabriel, C., Guainazzi, M., Gondoin, P., Much, R., Munoz, R., Santos, M., Schartel, N., Texier, D., Vacanti, G.: 2001, XMM-Newton Observatory. I. The Spacecraft and Operations. *Astron. Astrophys.* **365**, L1. DOI. ADS.

Jarolim, R., Veronig, A.M., Pötzi, W., Podladchikova, T.: 2020, Image-quality Assessment for Full-disk Solar Observations with Generative Adversarial Networks. *Astron. Astrophys.* **643**, A72. DOI. ADS.

Jin, C., Wang, J., Zhao, M.: 2009, Vector Magnetic Fields of Solar Granulation. *Astrophys. J.* **690**, 279. DOI. ADS.

Jocher, G., Stoken, A., Borovec, J., NanoCode012, ChristopherSTAN, Changyu, L., Laughing, Hogan, A., lorenzomammana, tkianai, yxNONG, AlexWang1900, Diaconu, L., Marc, wanghaoyang0106, ml5ah, Doug, Hatovix, Poznanski, J., 于力军 Yu, L., changyu98, Rai, P., Ferriday, R., Sullivan, T., Xinyu, W., YuriRibeiro, Claramunt, E.R.n., hopesala, pritul dave, yzchen: 2020, *ultralytics/yolov5: v3.0*, Zenodo. DOI.

Johannesson, A., Marquette, W.H., Zirin, H.: 1998, A 10-Year Set of Ca II K-Line Filtergrams. *Sol. Phys.* **177**, 265. DOI. ADS.

Jurčák, J., Collados, M., Leenaarts, J., van Noort, M., Schlichenmaier, R.: 2019, Recent Advancements in the EST Project. *Adv. Space Res.* **63**, 1389. DOI. ADS.

Karna, N., Zhang, J., Pesnell, W.D.: 2017, The Formation and Maintenance of the Dominant Southern Polar Crown Cavity of Cycle 24. *Astrophys. J.* **835**, 135. DOI. ADS.

Karpen, J.T.: 2015, Plasma Structure and Dynamics. In: Vial, J.-C., Engvold, O. (eds.) *Solar Prominences, Astrophys. Space. Sci. Libr.* **415**, Springer International Publishing, Cham, Switzerland, 237. DOI. ADS.

Keller, C.U., Harvey, J.W., Giampapa, M.S.: 2003, SOLIS: An Innovative Suite of Synoptic Instruments. In: Keil, S.L., Avakyan, S.V. (eds.) *Innovative Telescopes and Instrumentation for Solar Astrophysics*, *Proc. SPIE* **4853**, 194. DOI. ADS.

Kentischer, T.J., Bethge, C., Elmore, D.F., Friedlein, R., Halbgewachs, C., Knölker, M., Peter, H., Schmidt, W., Sigwarth, M., Streander, K.: 2008, ChroTel: A Robotic Telescope to Observe the Chromosphere of the Sun. In: McLean, I.S., Casali, M.M. (eds.) *Ground-Based and Airborne Instrumentation for Astronomy II*, *Proc. SPIE* **7014**, 701413. DOI. ADS.

Kippenhahn, R., Schlüter, A.: 1957, Eine Theorie der solaren Filamente. *Z. Astrophys.* **43**, 36. ADS.

Kontogiannis, I., Dineva, E., Diercke, A., Verma, M., Kuckein, C., Balthasar, H., Denker, C.: 2020, High-resolution Spectroscopy of an Erupting Minifilament and Its Impact on the Nearby Chromosphere. *Astrophys. J.* **898**, 144. DOI. ADS.

Kosugi, T., Matsuzaki, K., Sakao, T., Shimizu, T., Sone, Y., Tachikawa, S., Hashimoto, T., Minesugi, K., Ohnishi, A., Yamada, T., Tsuneta, S., Hara, H., Ichimoto, K., Suematsu, Y., Shimojo, M., Watanabe, T., Shimada, S., Davis, J.M., Hill, L.D., Owens, J.K., Title, A.M., Culhane, J.L., Harra, L.K., Doschek, G.A., Golub, L.: 2007, The Hinode (Solar-B) Mission: An Overview. *Sol. Phys.* **243**, 3. DOI. ADS.

Krucker, S., Hurford, G.J., Grimm, O., Kögl, S., Gröbelbauer, H.-P., Etesi, L., Casadei, D., Csillaghy, A., Benz, A.O., Arnold, N.G., Molendini, F., Orleanski, P., Schori, D., Xiao, H., Kuhar, M., Hochmuth, N., Felix, S., Schramka, F., Marcin, S., Kobler, S., Iseli, L., Dreier, M., Wiehl, H.J., Kleint, L., Battaglia, M., Lastufka, E., Sathiapal, H., Lapadula, K., Bednarzik, M., Birrer, G., Stutz, S., Wild, C., Marone, F., Skup, K.R., Cichocki, A., Ber, K., Rutkowski, K., Bujwan, W., Juchnikowski, G., Winkler, M., Darmetko, M., Michalska, M., Seweryn, K., Białek, A., Osica, P., Sylwester, J., Kowalinski, M., Ścisłowski, D., Siarkowski, M., Stęślicki, M., Mrozek, T., Podgórski, P., Meuris, A., Limousin, O., Gevin, O., Le Mer, I., Brun, S., Strugarek, A., Vilmer, N., Musset, S., Maksimović, M., Fárník, F., Kozáček, Z., Kašparová, J., Mann, G., Önel, H., Warmuth, A., Rendtel, J., Anderson, J., Bauer, S., Dionies, F., Paschke, J., Plüschke, D., Woche, M., Schuller, F., Veronig, A.M., Dickson, E.C.M., Gallagher, P.T., Maloney, S.A., Bloomfield, D.S., Piana, M., Massone, A.M., Benvenuto, F., Massa, P., Schwartz, R.A., Dennis, B.R., van Beek, H.F., Rodríguez-Pacheco, J., Lin, R.P.: 2020, The Spectrometer/Telescope for Imaging X-rays (STIX). *Astron. Astrophys.* **642**, A15. DOI. ADS.

Kuckein, C.: 2012, Study of the Magnetic Structure of Active Region Filaments. PhD Thesis, Universidad de La Laguna, Spain.

Kuckein, C.: 2019, Height Variation of Magnetic Filed and Plasma Flows in Isolated Bright Points. *Astron. Astrophys.* **630**, A139. DOI. ADS.

Kuckein, C., Martínez Pillet, V., Centeno, R.: 2012a, An Active Region Filament Studied Simultaneously in the Chromosphere and Photosphere. I. Magnetic Structure. *Astron. Astrophys.* **539**, A131. DOI. ADS.

Kuckein, C., Martínez Pillet, V., Centeno, R.: 2012b, An Active Region Filament Studied Simultaneously in the Chromosphere and Photosphere. II. Doppler Velocities. *Astron. Astrophys.* **542**, A112. DOI. ADS.

Kuckein, C., Verma, M., Denker, C.: 2016, Giant Quiescent Solar Filament Observed with High-Resolution Spectroscopy. *Astron. Astrophys.* **589**, A84. DOI. ADS.

Kuckein, C., Centeno, R., Martínez Pillet, V., Casini, R., Manso Sainz, R., Shimizu, T.: 2009, Magnetic Field Strength of Active Region Filaments. *Astron. Astrophys.* **501**, 1113. DOI. ADS.

Kuckein, C., Denker, C., Verma, M., Balthasar, H., González Manrique, S.J., Louis, R.E., Diercke, A.: 2017, sTools - a Data Reduction Pipeline for the GREGOR Fabry-Pérot Interferometer and the High-resolution Fast Imager at the GREGOR Solar Telescope. In: Vargas Domínguez, S., Kosovichev, A.G., Antolin, P., Harra, L. (eds.) *Fine Structure and Dynamics of the Solar Atmosphere*, *IAU Symposium* **327**, 20. DOI. ADS.

Kuckein, C., González Manrique, S.J., Kleint, L., Asensio Ramos, A.: 2020, Determining the Dynamics and Magnetic Fields in He I 10830 Å During a Solar Filament Eruption. *Astron. Astrophys.* **640**, A71. DOI. ADS.

Künzel, H.: 1955, Polarisationsinterferenzfilter und ihre Prüfung. *Astron. Nachr.* **282**, 252. DOI. ADS.

Kuperus, M., Raadu, M.A.: 1974, The Support of Prominences Formed in Neutral Sheets. *Astron. Astrophys.* **31**, 189. ADS.

LaVision: 2017, Product Manual for Imager M-lite. Technical report, LaVision GmbH, Göttingen, Germany.

Le Phuong, L.: 2016, Activity Indices Based on Sun-as-a-Star Spectra Obtained with the SOLIS Integrated Sunlight Spectrometer. Master Thesis, Universität Potsdam, Germany.

Lean, J.L., Rottman, G.J., Kyle, H.L., Woods, T.N., Hickey, J.R., Puga, L.C.: 1997, Detection and Parameterization of Variations in Solar Mid- and Near-ultraviolet Radiation (200-400 nm). *J. Geophys. Res.* **102**, 29939. DOI. ADS.

LeCun, Y., Bengio, Y.: 1995, Convolutional Networks for Images, Speech, and Time Series. *The Handbook of Brain Theory and Neural Networks* **3361**, 1995.

Lecun, Y., Bengio, Y., Hinton, G.: 2015, Deep Learning. *Nature* **521**, 436. DOI. ADS.

Leenaarts, J., Carlsson, M., Rouppe van der Voort, L.: 2012, The Formation of the Hα Line in the Solar Chromosphere. *Astrophys. J.* **749**, 136. DOI. ADS.

Leenaarts, J., Rutten, R.J., Sütterlin, P., Carlsson, M., Uitenbroek, H.: 2006, DOT Tomography of the Solar Atmosphere. VI. Magnetic Elements as Bright Points in the Blue Wing of Hα. *Astron. Astrophys.* **449**, 1209. DOI. ADS.

Lemen, J.R., Title, A.M., Akin, P.F. D. J.and Boerner, Chou, C., Drake, J.F., Duncan, D.W., Edwards, C.G., Friedlaender, F.M., Heyman, G.F., Hurlburt, N.E., Katz, N.L., Kushner, G.D., Levay, M., Lindgren, R.W., Mathur, D.P., McFeaters, E.L., Mitchell, S., Rehse, R.A., Schrijver, C.J., Springer, L.A., Stern, R.A., Tarbell, T.D., Wuelser, J.-P., Wolfson, C.J., Yanari, C., Bookbinder, J.A., Cheimets, P.N., Caldwell, D., Deluca, E.E., Gates, R., Golub, L., Park, S., Podgorski, W.A., Bush, R.I., Scherrer, P.H., Gummin, M.A., Smith, P., Auker, G., Jerram, P., Pool, P., Soufli, R., Windt, D.L., Beardsley, S., Clapp, M., Lang, J., Waltham, N.: 2012, The Atmospheric Imaging Assembly (AIA) on the Solar Dynamics Observatory (SDO). *Sol. Phys.* **275**, 17. DOI. ADS.

Leroy, J.L., Bommier, V., Sahal-Brechot, S.: 1983, The Magnetic Field in the Prominences of the Polar Crown. *Sol. Phys.* **83**, 135. DOI. ADS.

Leroy, J.L., Bommier, V., Sahal-Brechot, S.: 1984, New Data on the Magnetic Structure of Quiescent Prominences. *Astron. Astrophys.* **131**, 33. ADS.

Li, K.J.: 2010, Latitude Migration of Solar Filaments. *Mon. Not. R. Astron. Soc.* **405**, 1040. DOI. ADS.

Li, K.J., Li, Q.X., Gao, P.X., Shi, X.J.: 2008, Cyclic Behavior of Solar Full-Disk Activity. *J. Geophys. Res.* **113**, A11108. DOI. ADS.

Li, L., Zhang, J.: 2013, The Evolution of Barbs of a Polar Crown Filament Observed by SDO. *Sol. Phys.* **282**, 147. DOI. ADS.

Li, T., Zhang, J.: 2016, Subarcsecond Bright Points and Quasi-Periodic Upflows Below a Quiescent Filament Observed by IRIS. *Astron. Astrophys.* **589**, A114. DOI. ADS.

Lin, R.P., Dennis, B.R., Hurford, G.J., Smith, D.M., Zehnder, A., Harvey, P.R., Curtis, D.W., Pankow, D., Turin, P., Bester, M., Csillaghy, A., Lewis, M., Madden, N., van Beek, H.F., Appleby, M., Raudorf, T., McTiernan, J., Ramaty, R., Schmahl, E., Schwartz, R., Krucker, S., Abiad, R., Quinn, T., Berg, P., Hashii, M., Sterling, R., Jackson, R., Pratt, R., Campbell, R.D., Malone, D., Landis, D., Barrington-Leigh, C.P., Slassi-Sennou, S., Cork, C., Clark, D., Amato, D., Orwig, L., Boyle, R., Banks, I.S., Shirey, K., Tolbert, A.K., Zarro, D., Snow, F., Thomsen, K., Henneck, R., McHedlishvili, A., Ming, P., Fivian, M., Jordan, J., Wanner, R., Crubb, J., Preble, J., Matranga, M., Benz, A., Hudson, H., Canfield, R.C., Holman, G.D., Crannell, C., Kosugi, T., Emslie, A.G., Vilmer, N., Brown, J.C., Johns-Krull, C., Aschwanden, M., Metcalf, T., Conway, A.: 2002, The Reuven Ramaty High-Energy Solar Spectroscopic Imager (RHESSI). *Sol. Phys.* **210**, 3. DOI. ADS.

Lin, Y., Engvold, O.R., Wiik, J.E.: 2003, Counterstreaming in a Large Polar Crown Filament. *Sol. Phys.* **216**, 109. DOI. ADS.

Lin, Y., Engvold, O., Rouppe van der Voort, L., Wiik, J.E., Berger, T.E.: 2005, Thin Threads of Solar Filaments. *Sol. Phys.* **226**, 239. DOI. ADS.

Lites, B.W.: 2005, Magnetic Flux Ropes in the Solar Photosphere: The Vector Magnetic Field under Active Region Filaments. *Astrophys. J.* **622**, 1275. DOI. ADS.

Liu, W., Berger, T.E., Low, B.C.: 2012, First SDO/AIA Observation of Solar Prominence Formation Following an Eruption: Magnetic Dips and Sustained Condensation and Drainage. *Astrophys. J., Lett.* **745**, L21. DOI. ADS.

Liu, W., Berger, T.E., Low, B.C.: 2014, Coronal Condensation in Funnel Prominences as Return Flows of the Chromosphere-Corona Mass Cycle. In: Schmieder, B., Malherbe, J.-M., Wu, S.T. (eds.) *Nature of Prominences and their Role in Space Weather* **300**, 441. DOI. ADS.

Liu, W., Anguelov, D., Erhan, D., Szegedy, C., Reed, S., Fu, C.-Y., Berg, A.C.: 2016, SSD: Single Shot MultiBox Detector. In: Leibe, B., Matas, J., Sebe, N., Welling, M. (eds.) *Computer Vision – ECCV 2016*, Springer International Publishing, Cham, 21. ISBN 978-3-319-46448-0.

Liu, Y., Hoeksema, J.T., Scherrer, P.H., Schou, J., Couvidat, S., Bush, R.I., Duvall, T.L., Hayashi, K., Sun, X., Zhao, X.: 2012, Comparison of Line-of-sight Magnetograms Taken by the Solar Dynamics Observatory/Helioseismic and Magnetic Imager and Solar and Heliospheric Observatory/Michelson Doppler Imager. *Sol. Phys.* **279**, 295. DOI. ADS.

Livingston, W., Wallace, L., White, O.R., Giampapa, M.S.: 2007, Sun-as-a-Star Spectrum Variations 1974-2006. *Astrophys. J.* **657**, 1137. DOI. ADS.

Llama, J., Shkolnik, E.L.: 2015, Transiting the Sun: the Impact of Stellar Activity on X-Ray and Ultraviolet Transits. *Astrophys. J.* **802**, 41. DOI. ADS.

Löfdahl, M.G.: 2002, Multi-Frame Blind Deconvolution with Linear Equality Constraints. In: Bones, P.J., Fiddy, M.A., Millane, R.P. (eds.) *Image Reconstruction from Incomplete Data*, *Proc. SPIE* **4792**, 146. DOI. ADS.

Löhner-Böttcher, J., Schmidt, W., Doerr, H.-P., Kentischer, T., Steinmetz, T., Probst, R.A., Holzwarth, R.: 2017, LARS: An Absolute Reference Spectrograph for Solar Observations. Upgrade from a Prototype to a Turn-key System. *Astron. Astrophys.* **607**, A12. DOI. ADS.

López Ariste, A., Aulanier, G., Schmieder, B., Sainz Dalda, A.: 2006, First Observation of Bald Patches in a Filament Channel and at a Barb Endpoint. *Astron. Astrophys.* **456**, 725. DOI. ADS.

Louis, R.E., Puschmann, K.G., Kliem, B., Balthasar, H., Denker, C.: 2014, Sunspot Splitting Triggering an Eruptive Flare. *Astron. Astrophys.* **562**, A110. DOI. ADS.

Luna, M., Knizhnik, K., Muglach, K., Karpen, J., Gilbert, H., Kucera, T.A., Uritsky, V.: 2014, Observations and Implications of Large-amplitude Longitudinal Oscillations in a Solar Filament. *Astrophys. J.* **785**, 79. DOI. ADS.

Mackay, D.H., Karpen, J.T., Ballester, J.L., Schmieder, B., Aulanier, G.: 2010, Physics of Solar Prominences. II. Magnetic Structure and Dynamics. *Space Sci. Rev.* **151**, 333. DOI. ADS.

MacTaggart, D., Hood, A.W.: 2010, Simulating the "Sliding Doors" Effect Through Magnetic Flux Emergence. *Astrophys. J., Lett.* **716**, L219. DOI. ADS.

Makarov, V.I., Tlatov, A.G.: 2000, The Large-Scale Solar Magnetic Field and 11-Year Activity Cycles. *Astronomy Reports* **44**, 759. DOI. ADS.

Makarov, V.I., Tlatov, A.G., Callebaut, D.K., Obridko, V.N., Shelting, B.D.: 2001, Large-Scale Magnetic Field and Sunspot Cycles. *Sol. Phys.* **198**, 409. DOI. ADS.

Maldonado, J., Phillips, D.F., Dumusque, X., Collier Cameron, A., Haywood, R.D., Lanza, A.F., Micela, G., Mortier, A., Saar, S.H., Sozzetti, A., Rice, K., Milbourne, T., Cecconi, M., Cegla, H.M., Cosentino, R., Costes, J., Ghedina, A., Gonzalez, M., Guerra, J., Hernández, N., Li, C.-H., Lodi, M., Malavolta, L., Molinari, E., Pepe, F., Piotto, G., Poretti, E., Sasselov, D., San Juan, J., Thompson, S., Udry, S., Watson, C.: 2019, Temporal Evolution and Correlations of Optical Activity Indicators Measured in Sun-as-a-star Observations. *Astron. Astrophys.* **627**, A118. DOI. ADS.

Malherbe, J.-M.: 1989, The Formation of Solar Prominences. In: Priest, E.R. (ed.) *Dynamics and Structure of Quiescent Solar Prominences*, *Astrophys. Space. Sci. Libr.* **150**, 115. DOI. ADS.

Marquette, W.H., Denker, C.: 1999, Full Disk Image of the Sun Observed in the Blue Wing of Hα. *Sol. Phys.* **186**. Frontispiece. DOI.

Marshall, S., Fletcher, L., Hough, K.: 2006, Optimal Filtering of Solar Images using Soft Morphological Processing Techniques. *Astron. Astrophys.* **457**, 729. DOI. ADS.

Martin, S.F.: 1998, Conditions for the Formation and Maintenance of Filaments. *Sol. Phys.* **182**, 107. DOI. ADS.

Martin, S.F.: 2001, Solar Prominence Formation. In: Murdin, P. (ed.) *Encyclopedia of Astronomy and Astrophysics*, IOP Publishing Ltd and Nature Publishing Group, London, UK, 2698. DOI. ADS.

McIntosh, P.S.: 2005, Motions and Interactions among Large-scale Solar Structures on H-alpha Synoptic Charts. In: Sankarasubramanian, K., Penn, M., Pevtsov, A. (eds.) *Large-scale Structures and their Role in Solar Activity* **CS-346**, Astron. Soc. Pacific, San Francisco, 193. ADS.

McIntosh, S.W., Leamon, R.J., Egeland, R., Dikpati, M., Fan, Y., Rempel, M.: 2019, What the Sudden Death of Solar Cycles Can Tell Us About the Nature of the Solar Interior. *Sol. Phys.* **294**, 88. DOI. ADS.

Mehltretter, J.P.: 1974, Observations of Photospheric Faculae at the Center of the Solar Disk. *Sol. Phys.* **38**, 43. DOI. ADS.

Metcalfe, T.S., Basu, S., Henry, T.J., Soderblom, D.R., Judge, P.G., Knölker, M., Mathur, S., Rempel, M.: 2010, Discovery of a 1.6 Year Magnetic Activity Cycle in the Exoplanet Host Star ß Horologii. *Astrophys. J., Lett.* **723**, L213. DOI. ADS.

Meunier, N., Desort, M., Lagrange, A.-M.: 2010, Using the Sun to Estimate Earth-like Planets Detection Capabilities . II. Impact of Plages. *Astron. Astrophys.* **512**, A39. DOI. ADS.

Miesch, M.S.: 2005, Large-Scale Dynamics of the Convection Zone and Tachocline. *Living Rev. Sol. Phys.* **2**, 1. DOI. ADS.

Minaee, S., Boykov, Y., Porikli, F., Plaza, A., Kehtarnavaz, N., Terzopoulos, D.: 2020, Image Segmentation Using Deep Learning: A Survey. *arXiv e-prints*, arXiv:2001.05566. ADS.

Moore, C.E., Minnaert, M.G.J., Houtgast, J., Rowland, H.A.: 1966, *The Solar Spectrum 2935 Å to 8770 Å: Second Revision of Rowland's Preliminary Table of Solar Spectrum Wavelengths* **61**, National Bureau of Standards, Washington, D.C., USA. ADS.

Morris, B.M., Hebb, L., Davenport, J.R.A., Rohn, G., Hawley, S.L.: 2017, The Starspots of HAT-P-11: Evidence for a Solar-like Dynamo. *Astrophys. J.* **846**, 99. DOI. ADS.

Müller, E.: 2001, Fluid Dynamics. In: Murdin, P. (ed.) *Encyclopedia of Astronomy and Astrophysics*, IOP Publishing Ltd and Nature Publishing Group, London, UK. DOI. ADS.

Muller, R.: 2001, Solar Photosphere: Filigree. In: Murdin, P. (ed.) *Encyclopedia of Astronomy and Astrophysics*, IOP Publishing Ltd and Nature Publishing Group, London, UK. DOI. ADS.

Naqvi, M.F., Marquette, W.H., Tritschler, A., Denker, C.: 2010, The Big Bear Solar Observatory Ca II K-line Index for Solar Cycle 23. *Astron. Nachr.* **331**, 696. DOI. ADS.

Nesis, A., Hammer, R., Schleicher, H.: 2005, Topology and Dynamics of Abnormal Granulation. *Astron. Nachr.* **326**, 305. DOI. ADS.

Neubeck, A., Van Gool, L.: 2006, Efficient Non-Maximum Suppression. In: *18th International Conference on Pattern Recognition (ICPR'06)* **3**, 850. DOI.

Newton, E.R., Mann, A.W., Tofflemire, B.M., Pearce, L., Rizzuto, A.C., Vanderburg, A., Martinez, R.A., Wang, J.J., Ruffio, J.-B., Kraus, A.L., Johnson, M.C., Thao, P.C., Wood, M.L., Rampalli, R., Nielsen, E.L., Collins, K.A., Dragomir, D., Hellier, C., Anderson, D.R., Barclay, T., Brown, C., Feiden, G., Hart, R., Isopi, G., Kielkopf, J.F., Mallia, F., Nelson, P., Rodriguez, J.E., Stockdale, C., Waite, I.A., Wright, D.J., Lissauer, J.J., Ricker, G.R., Vanderspek, R., Latham, D.W., Seager, S., Winn, J.N., Jenkins, J.M., Bouma, L.G., Burke, C.J., Davies, M., Fausnaugh, M., Li, J., Morris, R.L., Mukai, K., Villaseñor, J., Villeneuva, S., De Rosa, R.J., Macintosh, B., Mengel, M.W., Okumura, J., Wittenmyer, R.A.: 2019, TESS Hunt for Young and Maturing Exoplanets (THYME): A Planet in the 45 Myr Tucana-Horologium Association. *Astrophys. J., Lett.* **880**, L17. DOI. ADS.

Nielsen, M.B., Gizon, L., Cameron, R.H., Miesch, M.: 2019, Starspot Rotation Rates Versus Activity Cycle Phase: Butterfly Diagrams of Kepler Stars are Unlike that of the Sun. *Astron. Astrophys.* **622**, A85. DOI. ADS.

Noll, R.J.: 1976, Zernike Polynomials and Atmospheric Turbulence. *J. Opt. Soc. Am.* **66**, 207. ADS.

Noyes, R.W., Hartmann, L.W., Baliunas, S.L., Duncan, D.K., Vaughan, A.H.: 1984, Rotation, Convection, and Magnetic Activity in Lower Main-sequence Stars. *Astrophys. J.* **279**, 763. DOI. ADS.

Okamoto, T.J., Tsuneta, S., Berger, T.E.: 2010, A Rising Cool Column as a Signature of Helical Flux Emergence and Formation of Prominence and Coronal Cavity. *Astrophys. J.* **719**, 583. DOI. ADS.

Okamoto, T.J., Tsuneta, S., Lites, B.W., Kubo, M., Yokoyama, T., Berger, T.E., Ichimoto, K., Katsukawa, Y., Nagata, S., Shibata, K., Shimizu, T., Shine, R.A., Suematsu, Y., Tarbell, T.D., Title, A.M.: 2008, Emergence of a Helical Flux Rope under an Active Region Prominence. *Astrophys. J., Lett.* **673**, L215. DOI. ADS.

Okamoto, T.J., Tsuneta, S., Lites, B.W., Kubo, M., Yokoyama, T., Berger, T.E., Ichimoto, K., Katsukawa, Y., Nagata, S., Shibata, K., Shimizu, T., Shine, R.A., Suematsu, Y., Tarbell, T.D., Title, A.M.: 2009, Prominence Formation Associated with an Emerging Helical Flux Rope. *Astrophys. J.* **697**, 913.

Orlando, S., Favata, F., Micela, G., Sciortino, S., Maggio, A., Schmitt, J.H.M.M., Robrade, J., Mittag, M.: 2017, Fifteen Years in the High-energy Life of the Solar-Type Star HD 81809. XMM-Newton Observations of a Stellar Activity Cycle. *Astron. Astrophys.* **605**, A19. DOI. ADS.

Otruba, W.: 1999, High Cadence Digital Full Disk Hα Patrol Device at Kanzelhöhe. In: *Third Advances in Solar Physics Euroconference: Magnetic Fields and Oscillations* **184**, 314. ADS.

Otruba, W., Pötzi, W.: 2003, The New High-speed Hα Imaging System at Kanzelhöhe Solar Observatory. *Hvar Obs. Bull.* **27**, 189. ADS.

Otsu, N.: 1979, A Threshold Selection Method from Gray-Level Histograms. *IEEE Transactions on Systems, Man, and Cybernetics* **9**, 62. DOI.

Padinhatteeri, S., Sridharan, R., Sankarasubramanian, K.: 2010, Seeing-Induced Errors in Solar Doppler Velocity Measurements. *Sol. Phys.* **266**, 195. DOI. ADS.

Palacios, J., Utz, D., Hofmeister, S., Krikova, K., Gömöry, P., Kuckein, C., Denker, C., Verma, M., González Manrique, S.J., Campos Rozo, J.I., Koza, J., Temmer, M., Veronig, A., Diercke, A., Kontogiannis, I., Cid, C.: 2020, Magnetic Flux Emergence in a Coronal Hole. *Sol. Phys.* **295**, 64. DOI. ADS.

Panesar, N.K., Innes, D.E., Schmit, D.J., Tiwari, S.K.: 2014, On the Structure and Evolution of a Polar Crown Prominence/Filament System. *Sol. Phys.* **289**, 2971. DOI. ADS.

Paszke, A., Gross, S., Massa, F., Lerer, A., Bradbury, J., Chanan, G., Killeen, T., Lin, Z., Gimelshein, N., Antiga, L., et al.: 2019, Pytorch: An Imperative Style, High-performance Deep Learning Library. In: *Advances in Neural Information Processing Systems*, 8026.

Perona, P., Malik, J.: 1990, Scale-Space and Edge Detection Using Anisotropic Diffusion. *IEEE Trans. Pattern Anal. Mach. Intell.* **12**, 629.

Pesnell, W.D., Thompson, B.J., Chamberlin, P.C.: 2012, The Solar Dynamics Observatory (SDO). *Sol. Phys.* **275**, 3. DOI. ADS.

Pevtsov, A.A.: 2016, The Need for Synoptic Solar Observations from the Ground. In: Dorotovic, I., Fischer, C.E., Temmer, M. (eds.) *Coimbra Solar Physics Meeting: Ground-based Solar Observations in the Space Instrumentation Era*, *Astronomical Society of the Pacific Conference Series* **504**, 71. ADS.

Plavchan, P., Barclay, T., Gagné, J., Gao, P., Cale, B., Matzko, W., Dragomir, D., Quinn, S., Feliz, D., Stassun, K., Crossfield, I.J.M., Berardo, D.A., Latham, D.W., Tieu, B., Anglada-Escudé, G., Ricker, G., Vanderspek, R., Seager, S., Winn, J.N., Jenkins, J.M., Rinehart, S., Krishnamurthy, A., Dynes, S., Doty, J., Adams, F., Afanasev, D.A., Beichman, C., Bottom, M., Bowler, B.P., Brinkworth, C., Brown, C.J., Cancino, A., Ciardi, D.R., Clampin, M., Clark, J.T., Collins, K., Davison, C., Foreman-Mackey, D., Furlan, E., Gaidos, E.J., Geneser, C., Giddens, F., Gilbert, E., Hall, R., Hellier, C., Henry, T., Horner, J., Howard, A.W., Huang, C., Huber, J., Kane, S.R., Kenworthy, M., Kielkopf, J., Kipping, D., Klenke, C., Kruse, E., Latouf, N., Lowrance, P., Mennesson, B., Mengel, M., Mills, S.M., Morton, T., Narita, N., Newton, E., Nishimoto, A., Okumura, J., Palle, E., Pepper, J., Quintana, E.V., Roberge, A., Roccatagliata, V., Schlieder, J.E., Tanner, A., Teske, J., Tinney, C.G., Vanderburg, A., von Braun, K., Walp, B., Wang, J., Wang, S.X., Weigand , D., White, R., Wittenmyer, R.A., Wright, D.J., Youngblood,

A., Zhang, H., Zilberman, P.: 2020, A Planet within the Debris Disk Around the Pre-main-sequence Star AU Microscopii. *Nature* **582**, 497. DOI. ADS.

Pötzi, W., Veronig, A.M., Riegler, G., Amerstorfer, U., Pock, T., Temmer, M., Polanec, W., Baumgartner, D.J.: 2015, Real-time Flare Detection in Ground-Based Hα Imaging at Kanzelhöhe Observatory. *Sol. Phys.* **290**, 951. DOI. ADS.

Press, W.H., Teukolsky, S.A., Vetterling, W.T., Flannery, B.P.: 2002, *Numerical Recipes in C++: The Art of Scientific Computing*, 2nd edn. Cambridge University Press, Cambridge, UK. ISBN 0 521 75033 4.

Priest, E.: 2014, *Magnetohydrodynamics of the Sun*, Cambridge University Press, Cambridge, UK. DOI. ADS.

Priest, E.R., van Ballegooijen, A.A., Mackay, D.H.: 1996, A Model for Dextral and Sinistral Prominences. *Astrophys. J.* **460**, 530. DOI. ADS.

Puschmann, K.G., Denker, C., Kneer, F., Al Erdogan, N., Balthasar, H., Bauer, S.M., Beck, C., Bello González, N., Collados, M., Hahn, T., Hirzberger, J., Hofmann, A., Louis, R.E., Nicklas, H., Okunev, O., Martínez Pillet, V., Popow, E., Seelemann, T., Volkmer, R., Wittmann, A.D., Woche, M.: 2012, The GREGOR Fabry-Pérot Interferometer. *Astron. Nachr.* **333**, 880. DOI. ADS.

Qu, M., Shih, F.Y., Jing, J., Wang, H.: 2005, Automatic Solar Filament Detection Using Image Processing Techniques. *Sol. Phys.* **228**, 119. DOI. ADS.

Quintero Noda, C., Shimizu, T., Katsukawa, Y., de la Cruz Rodríguez, J., Carlsson, M., Anan, T., Oba, T., Ichimoto, K., Suematsu, Y.: 2017a, Chromospheric Polarimetry through Multiline Observations of the 850-nm Spectral Region. *Mon. Not. R. Astron. Soc.* **464**, 4534. DOI. ADS.

Quintero Noda, C., Kato, Y., Katsukawa, Y., Oba, T., de la Cruz Rodríguez, J., Carlsson, M., Shimizu, T., Orozco Suárez, D., Ruiz Cobo, B., Kubo, M., Anan, T., Ichimoto, K., Suematsu, Y.: 2017b, Chromospheric Polarimetry through Multiline Observations of the 850-nm Spectral Region - II. A Magnetic Flux Tube Scenario. *Mon. Not. R. Astron. Soc.* **472**, 727. DOI. ADS.

Quintero Noda, C., Iijima, H., Katsukawa, Y., Shimizu, T., Carlsson, M., de la Cruz Rodríguez, J., Ruiz Cobo, B., Orozco Suárez, D., Oba, T., Anan, T., Kubo, M., Kawabata, Y., Ichimoto, K., Suematsu, Y.: 2019, Chromospheric Polarimetry through Multiline Observations of the 850 nm Spectral Region III: Chromospheric Jets driven by Twisted Magnetic Fields. *Mon. Not. R. Astron. Soc.* **486**, 4203. DOI. ADS.

Rackham, B.V., Apai, D., Giampapa, M.S.: 2018, The Transit Light Source Effect: False Spectral Features and Incorrect Densities for M-dwarf Transiting Planets. *Astrophys. J.* **853**, 122. DOI. ADS.

Redmon, J., Farhadi, A.: 2016, *YOLO9000: Better, Faster, Stronger*.

Redmon, J., Farhadi, A.: 2018, *YOLOv3: An Incremental Improvement*.

Redmon, J., Divvala, S., Girshick, R., Farhadi, A.: 2016, *You Only Look Once: Unified, Real-Time Object Detection*.

Reinhold, T., Cameron, R.H., Gizon, L.: 2017, Evidence for Photometric Activity Cycles in 3203 Kepler Stars. *Astron. Astrophys.* **603**, A52. DOI. ADS.

Ren, S., He, K., Girshick, R., Sun, J.: 2017, Faster R-CNN: Towards Real-Time Object Detection with Region Proposal Networks. *IEEE Transactions on Pattern Analysis and Machine Intelligence* **39**, 1137. DOI.

Rezatofighi, H., Tsoi, N., Gwak, J.Y., Sadeghian, A., Reid, I., Savarese, S.: 2019, Generalized intersection over union: A metric and a loss for bounding box regression. In: *Proceedings of the IEEE Conference on Computer Vision and Pattern Recognition*, 658.

Robbrecht, E., Berghmans, D.: 2004, Automated Recognition of Coronal Mass Ejections (CMEs) in Near-real-time Data. *Astron. Astrophys.* **425**, 1097. DOI. ADS.

Robrade, J., Schmitt, J.H.M.M., Favata, F.: 2012, Coronal Activity Cycles in Nearby G and K Stars. XMM-Newton Monitoring of 61 Cygni and α Centauri. *Astron. Astrophys.* **543**, A84. DOI. ADS.

Ronneberger, O., Fischer, P., Brox, T.: 2015, U-Net: Convolutional Networks for Biomedical Image Segmentation. In: Navab, N., Hornegger, J., Wells, W.M., Frangi, A.F. (eds.) *Medical Image Computing and Computer-Assisted Intervention – MICCAI 2015*, Springer International Publishing, Cham, 234. ISBN 978-3-319-24574-4.

Russell, S.J., Norvig, P.: 2010, *Artificial Intelligence: A Modern Approach*, 3rd edn. Pearson, Upper Saddle River, New Jersey, USA.

Rutten, R., Hagenaar, H.: 2001, Chromosphere: Network. In: Murdin, P. (ed.) *Encyclopedia of Astronomy and Astrophysics*, IOP Publishing and Nature Publishing Group, London, UK, 1994. DOI. ADS.

Rutten, R.J., Uitenbroek, H.: 1991, Ca II H_{2v} and K_{2v} Cell Grains. *Sol. Phys.* **134**, 15. DOI. ADS.

Sánchez Almeida, J., Márquez, I., Bonet, J.A., Domínguez Cerdeña, I., Muller, R.: 2004, Bright Points in the Internetwork Quiet Sun. *Astrophys. J., Lett.* **609**, L91. DOI. ADS.

Sanz-Forcada, J., Stelzer, B., Metcalfe, T.S.: 2013, ßHorologi, the First Coronal Activity Cycle in a Young Solar-like Star. *Astron. Astrophys.* **553**, L6. DOI. ADS.

Scherrer, P.H., Bogart, R.S., Bush, R.I., Hoeksema, J.T., Kosovichev, A.G., Schou, J., Rosenberg, W., Springer, L., Tarbell, T.D., Title, A., Wolfson, C.J., Zayer, I., MDI Engineering Team: 1995, The Solar Oscillations Investigation - Michelson Doppler Imager. *Sol. Phys.* **162**, 129. DOI. ADS.

Scherrer, P.H., Schou, J., Bush, R.I., Kosovichev, A.G., Bogart, R.S., Hoeksema, J.T., Liu, Y., Duvall, T.L., Zhao, J., Title, A.M., Schrijver, C.J., Tarbell, T.D., Tomczyk, S.: 2012, The Helioseismic and Magnetic Imager (HMI) Investigation for the Solar Dynamics Observatory (SDO). *Sol. Phys.* **275**, 207. DOI. ADS.

Schmidt, W., Soltau, D.: 1987, Construction of the German Solar Telescopes in the Observatorio del Teide, Tenerife: The Vacuum Tower Telescope. *Mitt. Astron. Ges.* **68**, 184. ADS.

Schmidt, W., von der Lühe, O., Volkmer, R., Denker, C., Solanki, S.K., Balthasar, H., Bello Gonzalez, N., Berkefeld, T., Collados, M., Fischer, A., Halbgewachs, C., Heidecke, F., Hofmann, A., Kneer, F., Lagg, A., Nicklas, H., Popow, E., Puschmann, K.G., Schmidt, D., Sigwarth, M., Sobotka, M., Soltau, D., Staude, J., Strassmeier, K.G., Waldmann , T.A.: 2012, The 1.5 Meter Solar Telescope GREGOR. *Astron. Nachr.* **333**, 796. DOI. ADS.

Schmieder, B.: 2001, Chromosphere. In: Murdin, P. (ed.) *Encyclopedia of Astronomy and Astrophysics*, IOP Publishing Ltd and Nature Publishing Group, London, UK. DOI. ADS.

Schmieder, B., Chandra, R., Berlicki, A., Mein, P.: 2010, Velocity Vectors of a Quiescent Prominence Observed by Hinode/SOT and the MSDP (Meudon). *Astron. Astrophys.* **514**, A68. DOI. ADS.

Schrijver, C.J., Siscoe, G.L.: 2009, *Heliophysics: Plasma Physics of the Local Cosmos*, Cambridge University Press, Cambridge, UK. ADS.

Schrijver, C.J., Siscoe, G.L.: 2010, *Heliophysics: Evolving Solar Activity and the Climates of Space and Earth*, Cambridge University Press, Cambridge, UK. ADS.

Schwabe, H.: 1844, Sonnenbeobachtungen im Jahre 1843. Von Herrn Hofrath Schwabe in Dessau. *Astron. Nachr.* **21**, 233. DOI. ADS.

Senthamizh Pavai, V., Arlt, R., Diercke, A., Denker, C., Vaquero, J.M.: 2016, Sunspot Group Tilt Angle Measurements from Historical Observations. *Advances in Space Research* **58**, 1468. DOI. ADS.

Shen, Z., Diercke, A., Denker, C.: 2018, Calibration of Full-disk He I 10830 Å Filtergrams of the Chromospheric Telescope. *Astron. Nachr.* **339**, 661. DOI. ADS.

SILSO World Data Center: 2008 – 2019, The International Sunspot Number. *International Sunspot Number Monthly Bulletin and Online Catalogue*. www.sidc.be/silso/.

Simões, P.J.A., Reid, H.A.S., Milligan, R.O., Fletcher, L.: 2019, The Spectral Content of SDO/AIA 1600 and 1700 Å Filters from Flare and Plage Observations. *Astrophys. J.* **870**, 114. DOI. ADS.

Simon, G.W., Zirker, J.B.: 1974, A Search for the Footpoints of Solar Magnetic Fields. *Sol. Phys.* **35**, 331. DOI. ADS.

Sobotka, M., Bonet, J.A., Vazquez, M.: 1994, A High-resolution Study of the Structure of Sunspot Light Bridges and Abnormal Granulation. *Astrophys. J.* **426**, 404. DOI. ADS.

Solanki, S.K., Barthol, P., Danilovic, S., Feller, A., Gandorfer, A., Hirzberger, J., Riethmüller, T.L., Schüssler, M., Bonet, J.A., Martínez Pillet, V., del Toro Iniesta, J.C., Domingo, V., Palacios, J., Knölker, M., Bello González, N., Berkefeld, T., Franz, M., Schmidt, W., Title, A.M.: 2010, SUNRISE: Instrument, Mission, Data, and First Results. *Astrophys. J., Lett.* **723**, L127. DOI. ADS.

Spörer, F.W.G.: 1879, Beobachtung der Sonnenflecken etc. *Astron. Nachr.* **96**, 23. DOI. ADS.

Spörer, F.W.G.: 1889, Von den Sonnenflecken des Jahres 1888 und von der Verschiedenheit der nördlichen und südlichen Halbkugel der Sonne seit 1883. *Astron. Nachr.* **121**, 105. DOI. ADS.

Spruit, H.: 2001, Solar Photosphere. In: Murdin, P. (ed.) *Encyclopedia of Astronomy and Astrophysics*, IOP Publishing Ltd and Nature Publishing Group, London, UK. DOI. ADS.

Staiger, J.: 2012, HELLRIDE: A New Multiline Spectrometer for the Vacuum Tower Telescope, Tenerife. In: Rimmele, T.R., Tritschler, A., Wöger, F., Collados Vera, M., Socas-Navarro, H., Schlichenmaier, R., Carlsson, M., Berger, T., Cadavid, A., Gilbert, P.R., Goode, P.R., Knölker, M. (eds.) *Second ATST-EAST Meeting: Magnetic Fields from the Photosphere to the Corona.*, *Astronomical Society of the Pacific Conference Series* **463**, 445. ADS.

Steinegger, M., Denker, C., Goode, P.R., Marquette, W.H., Varsik, J., Wang, H., Otruba, W., Freislich, H., Hanslmeier, A., Luo, G., Chen, D., Zhang, Q.: 2000, The New Global High-Resolution Hα Network: First Observations and First Results. In: Wilson, A. (ed.) *The Solar Cycle and Terrestrial Climate, Solar and Space Weather*, *ESA Special Publication* **463**, 617. ADS.

Stix, M.: 2004, *The Sun: An Introduction*, Springer, Berlin, Germany. ADS.

Strassmeier, K.G., Ilyin, I., Steffen, M.: 2018, PEPSI Deep Spectra. I. The Sun-as-a-star. *Astron. Astrophys.* **612**, A44. DOI. ADS.

Sun, X., Hoeksema, J.T., Liu, Y., Zhao, J.: 2015, On Polar Magnetic Field Reversal and Surface Flux Transport During Solar Cycle 24. *Astrophys. J.* **798**, 114. DOI. ADS.

Svalgaard, L., Kamide, Y.: 2013, Asymmetric Solar Polar Field Reversals. *Astrophys. J.* **763**, 23. DOI. ADS.

Tapping, K.F., Charrois, D.P.: 1994, Limits to the Accuracy of the 10.7 cm Flux. *Sol. Phys.* **150**, 305. DOI. ADS.

Tarbell, T., Ferguson, S., Frank, Z., Shine, R., Title, A., Topka, K., Scharmer, G.: 1990, High-Resolution Observations of Emerging Magnetic Fields and Flux Tubes in Active Region Photosphere. In: Stenflo, J.O. (ed.) *Solar Photosphere: Structure, Convection, and Magnetic Fields*, *IAU Symposium* **138**, 147. ADS.

Taylor, M.E., Stone, P.: 2009, Transfer Learning for Reinforcement Learning Domains: A Survey. *Journal of Machine Learning Research* **10**, 1633.

Tlatov, A.G., Kuzanyan, K.M., Vasil'yeva, V.V.: 2016, Tilt Angles of Solar Filaments over the Period of 1919 – 2014. *Sol. Phys.* **291**, 1115. DOI. ADS.

Toriumi, S., Airapetian, V.S., Hudson, H.S., Schrijver, C.J., Cheung, M.C.M., DeRosa, M.L.: 2020, Sun-as-a-star Spectral Irradiance Observations of Transiting Active Regions. *Astrophys. J.* **902**, 36. DOI. ADS.

Tritschler, A., Rimmele, T.R., Berukoff, S., Casini, R., Kuhn, J.R., Lin, H., Rast, M.P., McMullin, J.P., Schmidt, W., Wöger, F., DKIST Team: 2016, Daniel K. Inouye Solar Telescope: High-resolution Observing of the Dynamic Sun. *Astron. Nachr.* **337**, 1064. DOI. ADS.

Tsiropoula, G., Tziotziou, K., Kontogiannis, I., Madjarska, M.S., Doyle, J.G., Suematsu, Y.: 2012, Solar Fine-scale Structures. I. Spicules and Other Small-scale, Jet-like Events at the Chromospheric Level: Observations and Physical Parameters. *Space Sci. Rev.* **169**, 181. DOI. ADS.

Tsuneta, S., Ichimoto, K., Katsukawa, Y., Nagata, S., Otsubo, M., Shimizu, T., Suematsu, Y., Nakagiri, M., Noguchi, M., Tarbell, T., Title, A., Shine, R., Rosenberg, W., Hoffmann, C., Jurcevich, B., Kushner, G., Levay, M., Lites, B., Elmore, D., Matsushita, T., Kawaguchi, N., Saito, H., Mikami, I., Hill, L.D., Owens, J.K.: 2008, The Solar Optical Telescope for the Hinode Mission: An Overview. *Sol. Phys.* **249**, 167. DOI. ADS.

Tull, R.: 2001, Spectrographs: High-Resolution Spectrographs. In: Murdin, P. (ed.) *Encyclopedia of Astronomy and Astrophysics*, IOP Publishing Ltd and Nature Publishing Group, London, UK, 2894. DOI. ADS.

Unsöld, A.: 1974, *Der neue Kosmos*, Springer, Berlin, Germany. ADS.

Utz, D., Jurčák, J., Hanslmeier, A., Muller, R., Veronig, A., Kühner, O.: 2013, Magnetic Field Strength Distribution of Magnetic Bright Points Inferred from Filtergrams and Spectro-polarimetric Data. *Astron. Astrophys.* **554**, A65. DOI. ADS.

Utz, D., del Toro Iniesta, J.C., Bellot Rubio, L.R., Jurčák, J., Martínez Pillet, V., Solanki, S.K., Schmidt, W.: 2014, The Formation and Disintegration of Magnetic Bright Points Observed by Sunrise/IMaX. *Astrophys. J.* **796**, 79. DOI. ADS.

van Ballegooijen, A.A.: 2001, Solar Prominence Models. In: Murdin, P. (ed.) *Encyclopedia of Astronomy and Astrophysics*, IOP Publishing Ltd and Nature Publishing Group, London, UK, 2703. DOI. ADS.

van Ballegooijen, A.A., Martens, P.C.H.: 1989, Formation and Eruption of Solar Prominences. *Astrophys. J.* **343**, 971. DOI. ADS.

van der Lühe, O., Soltau, D., Berkefeld, T., Schelenz, T.: 2003, KAOS: Adaptive optics system for the Vacuum Tower Telescope at Teide Observatory. In: Keil, S.L., Avakyan, S.V. (eds.) *Innovative Telescopes and Instrumentation for Solar Astrophysics*, *Proc. SPIE* **4853**, 187. DOI. ADS.

van Driel-Gesztelyi, L., Green, L.M.: 2015, Evolution of Active Regions. *Living Rev. Sol. Phys.* **12**, 1. DOI. ADS.

van Noort, M., Rouppe van der Voort, L., Löfdahl, M.G.: 2005, Solar Image Restoration by Use of Multi-Frame Blind De-Convolution with Multiple Objects and Phase Diversity. *Sol. Phys.* **228**, 191. DOI. ADS.

Verma, M., Denker, C.: 2011, Horizontal Flow Fields Observed in Hinode G-Band Images. I. Methods. *Astron. Astrophys.* **529**, A153. DOI. ADS.

Verma, M., Denker, C.: 2014, Horizontal Flow Fields observed in Hinode G-band Images. IV. Statistical Properties of the Dynamical Environment around Pores. *Astron. Astrophys.* **563**, A112. DOI. ADS.

Viereck, R.A., Puga, L.C.: 1999, The NOAA Mg II Core-to-wing Solar Index: Construction of a 20-year Time Series of Chromospheric Variability from Multiple Satellites. *J. Geophys. Res.* **104**, 9995. DOI. ADS.

von der Lühe, O.: 1998, High-Resolution Observations with the German Vacuum Tower Telescope on Tenerife. *New Astron. Rev.* **42**, 493. DOI. ADS.

Štěpán, J., Trujillo Bueno, J., Leenaarts, J., Carlsson, M.: 2015, Three-dimensional Radiative Transfer Simulations of the Scattering Polarization of the Hydrogen Lyα Line in a Magnetohydrodynamic Model of the Chromosphere-Corona Transition Region. *Astrophys. J.* **803**, 65. DOI. ADS.

Waldmeier, M.: 1973, A Secondary Polar Zone of Solar Prominences. *Sol. Phys.* **28**, 389. DOI. ADS.

Wang, J., Li, W., Denker, C., Lee, C., Wang, H., Goode, P.R., McAllister, A., Martin, S.F.: 2000, Minifilament Eruption on the Quiet Sun. I. Observations at Hα Central Line. *Astrophys. J.* **530**, 1071. DOI. ADS.

Wang, S., Jenkins, J.M., Martinez Pillet, V., Beck, C., Long, D.M., Prasad Choudhary, D., Muglach, K., McAteer, J.: 2020, Magnetic Structure of an Erupting Filament. *Astrophys. J.* **892**, 75. DOI. ADS.

Wang, Y.-M.: 1999, The Jetlike Nature of He II λ304 Prominences. *Astrophys. J., Lett.* **520**, L71. DOI. ADS.

Warmuth, A., Önel, H., Mann, G., Rendtel, J., Strassmeier, K.G., Denker, C., Hurford, G.J., Krucker, S., Anderson, J., Bauer, S.-M., Bittner, W., Dionies, F., Paschke, J., Plüschke, D., Sablowski, D.P., Schuller, F., Senthamizh Pavai, V., Woche, M., Casadei, D., Kögl, S., Arnold, N.G., Gröbelbauer, H.-P., Schori, D., Wiehl, H.J., Csillaghy, A., Grimm, O., Orleanski, P., Skup, K.R., Bujwan, W., Rutkowski, K., Ber, K.: 2020, The STIX Aspect System (SAS): The Optical Aspect System of the Spectrometer/Telescope for Imaging X-Rays (STIX) on Solar Orbiter. *Sol. Phys.* **295**, 90. DOI. ADS.

Webb, D.F., Davis, J.M., McIntosh, P.S.: 1984, Observations of the Reappearance of Polar Coronal Holes and the Reversal of the Polar Magnetic Field. *Sol. Phys.* **92**, 109. DOI. ADS.

Weisskopf, M.C., Brinkman, B., Canizares, C., Garmire, G., Murray, S., Van Speybroeck, L.P.: 2002, An Overview of the Performance and Scientific Results from the Chandra X-Ray Observatory. *Publ. Astron. Soc. Pac.* **114**, 1. DOI. ADS.

Wells, D.C., Greisen, E.W., Harten, R.H.: 1981, FITS – A Flexible Image Transport System. *Astron. Astrophys. Suppl. Ser.* **44**, 363. ADS.

White, O.R., Livingston, W.C.: 1981, Solar Luminosity Variation. III - Calcium K Variation from Solar Minimum to Maximum in Cycle 21. *Astrophys. J.* **249**, 798. DOI. ADS.

Wilson, P.R.: 1981, Faculae, Filigree and Calcium Bright Points. *Sol. Phys.* **69**, 9. DOI. ADS.

Xu, Y., Pötzi, W., Zhang, H., Huang, N., Jing, J., Wang, H.: 2018, Collective Study of Polar Crown Filaments in the Past Four Solar Cycles. *Astrophys. J.* **862**, L23. DOI. ADS.

Xue, Z., Yan, X., Cheng, X., Yang, L., Su, Y., Kliem, B., Zhang, J., Liu, Z., Bi, Y., Xiang, Y., Yang, K., Zhao, L.: 2016, Observing the Release of Twist by Magnetic Reconnection in a Solar Filament Eruption. *Nature Communications* **7**, 11837. DOI. ADS.

Yang, Y., Li, X., Bai, X., Zhou, H., Liang, B., Zhang, X., Feng, S.: 2019, Morphological Classification of G-band Bright Points Based on Deep Learning. *Astrophys. J.* **887**, 129. DOI. ADS.

Yelles Chaouche, L., Kuckein, C., Martínez Pillet, V., Moreno-Insertis, F.: 2012, The Three-dimensional Structure of an Active Region Filament as Extrapolated from Photospheric and Chromospheric Observations. *Astrophys. J.* **748**, 23. DOI. ADS.

Zhao, M., Wang, J.-X., Jin, C.-L., Zhou, G.-P.: 2009, Magnetic Non-potentiality on the Quiet Sun and the Filigree. *Res. Astron. and Astrophys.* **9**, 933. DOI. ADS.

Zhu, G., Lin, G., Wang, D., Liu, S., Yang, X.: 2019, Solar Filament Recognition Based on Deep Learning. *Sol. Phys.* **294**, 117. DOI. ADS.

Zirker, J.B., Engvold, O., Martin, S.F.: 1998, Counter-Streaming Gas Flows in Solar Prominences as Evidence for Vertical Magnetic Fields. *Nature* **396**, 440. DOI. ADS.

Acknowledgments

'It was the best of times, it was the worst of times,
it was the age of wisdom, it was the age of foolishness,
it was the epoch of belief, it was the epoch of incredulity,
it was the season of Light, it was the season of Darkness,
it was the spring of hope, it was the winter of despair,
we had everything before us, we had nothing before us,
we were all going direct to Heaven,
we were all going direct the other way.

Dickens (1859) – *A Tale of Two Cities*

I would like to express my special appreciation and thanks to my doctoral supervisor Prof. Dr. Carsten Denker. Without his support, suggestions, and scientific advice, the thesis would not be same. I am very grateful that I had the opportunity to work since my Bachelor studies in the Solar Physics Group. I honestly appreciate the possibilities to participate in several summer schools and scientific exchanges with Slovakia, and that I had the opportunity to gain observing experience at VTT and GREGOR on Tenerife. I gained all my knowledge on solar physics during these great nine years at AIP. Furthermore, I want to thank my co-advisor Prof. Dr. Klaus Strassmeier for fruitful discussions in our meetings. My sincere thanks to my mentor Prof. Dr. Claudia Stolle for the support during the last four years.

I want to give a special thanks to all the members of the Solar Physics Group at AIP. It was a pleasure to work with you. I honestly do not know how to thank Dr. Christoph Kuckein for all his support in the last years, not only scientifically, but as a real friend, to whom I always could come with all my problems. I would have not survived the last four years without your support. I enjoyed also the scientific discussions we had and thank you for all the advice I got from you on my scientific work. I would like to thank Dr. Sergio J. González Manrique for all his support. Sergio, you were always there, when I needed a nice word and encouragement, but also as an advisor in my scientific research. Many thanks to Dr. Horst Balthasar for his support and encouragement. I always enjoyed the nice conversations with you and I learned a lot from you. I want to thank Robert Kamlah for the great tea and coffee breaks we spend together and the nice conversations we had during this time. I miss you in our office. I appreciate the support I received from Prof. Dr. Gottfried Mann, Dr. Alexander Warmuth, Dr. Christian Vocks, Dr. Senthamizh Pavai Valliappan, and M. Bröse, who were always very kind and interested in work. Many thanks also to Dr. Hakan Önel, who had always an open ear and good advice during our occasional car rides to Berlin. I also want to thank Dr. Jürgen Rendtel for the possibility to observe at the Einstein Tower and for his support during the observing campaigns on Tenerife. Thank you for checking always at Tenerife if ChroTel was running. Many thanks to Dr. Ioannis Kontogiannis for great scientific discussions and his helpful comments on the manuscripts related to the thesis. I want to thank Dr. Meetu Verma for her support when I started in the solar physics group, pleasant observing campaigns we spend together on Tenerife, and some very good book recommendation. Thank you also to the other members of the solar physics group Ö. Adebali, E. Dineva, D. Lehmann, Dr. P. Pal, Dr. F. Schuller, and Dr. Y. Wu.

A special thank you to all, who took the time to read my doctoral thesis and send me comments to improve it: Dr. C. Kuckein, Dr. S. J. González Manrique, Dr. H. Balthasar, Dr. S. P. Valliappan, R. Jarolim, U. Niemann, M. Ziener. I really appreciate the figures, which were created by S. Schrottke.

There are many more people at AIP, I want to thank, which I met doing my time there. A very special thank you goes to Melissa. It was always great to meet you at the bus and later to have lunch with you and speak with you about all possible topics. You were very supportive during my time here at AIP. Furthermore, I want to thank Anika for teaching with me at university, Dalal for a great time in Vienna and also later at AIP. Thank you to Ekaterina, Engin, Vada, Anke, Dario, Katrin, Adriane, and many other how I forgot to mention. Zili, thank you for the nice time I had during your internship at AIP. It was a pleasure to have you here and to work with you.

Many thanks to Robert Jarolim and Prof. Dr. Astrid Veronig for their support during the SOLARNET mobility program. The short time in Graz was great. Robert, I am still very sorry that I watered and killed the cactus. Keep the new one alive!

My appreciation to all the scientists involved in the manuscripts, observations, and which I met and who supported me during the time of my thesis project: Dr. Peter Gömöry, Dr. Ales Kucera, Dr. Wilson Cauley, Prof. Dr. Katja Poppenhäger, Dr. Julián Alverado-Goméz, Dr. Carlos Quintero Noda, Dr. Alexandra Tritschler, Dr. Christian Bethge, Dr. Stefan Hofmeister, Dr. Domenik Utz, Dr. Judith Palacios, and many more.

A great thanks to all my friends, who supported me during the doctoral thesis, in particular Stuff, Ulli, Phili, Karo, and Emilie for shearing me up when I was down. The chats with you are wonderful, also when they escalate sometimes. The week-end trips are irreplaceable and we have to continue these trips when traveling is again possible. Die Sonne scheint immer! I also appreciate the online games, the online reading evenings, and all the great other things we are doing together. A special thank you goes to Hella how was supporting me in all possible ways and strolled with me through Berlin and Hongkong to discover new places and have long conversations. Vicky, thank you that always cheered me up during our train rides to Berlin and during our meetings in Golm. Thank you to Simon and Daniel for the great time during summers and new year, and our weekly online evenings. Thank you also to all the other friends, who supported me and always listened to my complains: Daniel K., Saskia, Thomas, Lydia, Niels, Sebastian, Nicole, Jana, Maren, Marcus, Stephan, Julia, and many more.

Furthermore, I want to thank my family for their support and their encouragement. Especially, I want to thank my mother Sabine Diercke and my mother-in-law Tatjana Ziener for their great support. Thank you to my sister Michi and my brother-in-law Denis and their children Benni, Fine, and Lotti. Above all I want to thank my boyfriend Marco Ziener, who is always at my side, listens to me, cooking for me, and cheering me up when I was frustrated. Without all the love and support you gave me, I would not have managed to finish the thesis.

Thank you for further technical support by Dr. Jürgen Rendtel, Godehard Monecke and Karin Gerber during the observing campaign at VTT and the nice evenings at the observatory. ChroTel is operated by the Leibniz-Institut für Sonnenphysik (KIS) in Freiburg, Germany, at the Spanish Observatorio del Teide on Tenerife (Spain). The ChroTel filtergraph was developed by the KIS in cooperation with the High Altitude Observatory (HAO) in Boulder, Colorado. This research has made use of NASA's Astrophysics Data System. Additional Hα full-disk data were provided by the Kanzelhöhe Solar Observatory, University of Graz, Austria. The Vacuum Tower Telescope (VTT) at the Spanish Observatorio del Teide of the Instituto de Astrofísica de Canarias is operated by the German consortium of the Leibniz-Institut für Sonnenphysik (KIS) in Freiburg, the Leibniz-Institut für Astrophysik Potsdam (AIP), and the Max-Planck-Institut für Sonnensystemforschung (MPS) in Göttingen. The Solar Dynamics Observatory is developed and launched by NASA. The SDO data are provided by the Joint Science Operations Center – Science Data Processing at Stanford University. This thesis has made use of NASA's Astrophysics Data System. SolarSoftWare is a public-domain software package for analysis of solar data written in the Interactive Data Language by Harris Geospatial Solutions. The thesis made use of various Python packages, in particular, PyTorch, numpy, matplotlib, and pandas.

Appendix A – Abstracts

Refereed articles

Classification of High-resolution Solar Hα Spectra using t-distributed Stochastic Neighbor Embedding

M. Verma, G. Matijevič, C. Denker, A. Diercke, E. Dineva, H. Balthasar, R. Kamlah, I. Kontogiannis, C. Kuckein, P. S. Pal, 2020, Astrophysical Journal, accepted for publication

The Hα spectral line is a well-studied absorption line revealing properties of the highly structured and dynamic solar chromosphere. Typical features with distinct spectral signatures in Hα include filaments and prominences, bright active-region plages, superpenumbrae around sunspots, surges, flares, Ellerman bombs, filigree, and mottles and rosettes, among others. This study is based on high-spectral resolution Hα spectra obtained with the echelle spectrograph of the Vacuum Tower Telescope (VTT) located at Observatorio del Teide (ODT), Tenerife, Spain. The t-distributed Stochastic Neighbor Embedding (t-SNE) is a machine learning algorithm, which is used for nonlinear dimensionality reduction. In this application, it projects Hα spectra onto a two-dimensional map, where it becomes possible to classify the spectra according to results of Cloud Model (CM) inversions. The CM parameters optical depth, Doppler width, line-of-sight velocity, and source function describe properties of the cloud material. Initial results of t-SNE indicate its strong discriminatory power to separate quiet-Sun and plage profiles from those that are suitable for CM inversions. In addition, a detailed study of various t-SNE parameters is conducted, the impact of seeing conditions on the classification is assessed, results for various types of input data are compared, and the identified clusters are linked to chromospheric features. Although t-SNE proves to be efficient in clustering high-dimensional data, human inference is required at each step to interpret the results. This exploratory study provides a framework and ideas on how to tailor a classification scheme towards specific spectral data and science questions.

Wavelength Dependence of Image Quality Metrics and Seeing Parameters and their Relation to Adaptive Optics Performance

R. Kamlah, M. Verma, A. Diercke, C. Denker, 2020, Solar Physics, accepted for publication

Ground-based solar observations are severely affected by Earth's turbulent atmosphere. As a consequence, observed image quality and prevailing seeing conditions are closely related. Partial correction of image degradation is nowadays provided in real-time by adaptive optics (AO) systems. In this study, different metrics of image quality are compared with parameters characterizing the prevailing seeing conditions, i.e., Median Filter Gradient Similarity (MFGS), Median Filter Laplacian Similarity (MFLS), Helmli-Scherer mean, granular rms-contrast, differential image motion, and Fried-parameter r0. The quiet-Sun observations at disk center were carried out at the Vacuum Tower Telescope (VTT), Observatorio del Teide (OT), Izana, Tenerife, Spain. In July and August 2016, time-series of short-exposure images were recorded with the High-resolution Fast Imager (HiFI) at various wavelengths in the visible and near-infrared parts of the spectrum. Correlation analysis yields the wavelength dependence of the image quality metrics and seeing parameters, and Uniform Manifold Approximation and Projection (UMAP) is employed to characterize the seeing on a particular observing day. In addition, the image quality metrics and seeing parameters are used to determine the field-dependence of the correction provided by the AO system. Management of high-resolution imaging data from large-aperture, ground-based telescopes demands reliable image quality metrics and meaningful characterization of prevailing seeing conditions and AO performance. The present study offers guidance how to retrieve such information ex post facto.

High-resolution Spectroscopy of an Erupting Minifilament and Its Impact on the Nearby Chromosphere

I. Kontogiannis, E. Dineva, A. Diercke, M. Verma, C. Kuckein, H. Balthasar, C. Denker, 2020, Astrophysical Journal 898, 144

We study the evolution of a minifilament eruption in a quiet region at the center of the solar disk and its impact on the ambient atmosphere. We used high spectral resolution imaging spectroscopy in Hα acquired by the echelle spectrograph of the Vacuum Tower Telescope, Tenerife, Spain; photospheric magnetic field observations from the Helioseismic Magnetic Imager; and UV/EUV imaging from the Atmospheric Imaging Assembly of the Solar Dynamics Observatory. The Hα line profiles were noise-stripped using principal component analysis and then inverted to produce physical and cloud model parameter maps. The minifilament formed between small-scale, opposite-polarity magnetic features through a series of small reconnection events, and it erupted within an hour after its appearance in Hα. Its development and eruption exhibited similarities to large-scale erupting filaments, indicating the action of common mechanisms. Its eruption took place in two phases, namely, a slow rise and a fast expansion, and it produced a coronal dimming, before the minifilament disappeared. During its eruption, we detected a complicated velocity pattern, indicative of a twisted, thread- like structure. Part of its material returned to the chromosphere, producing observable effects on nearby low-lying magnetic structures. Cloud model analysis showed that the minifilament was initially similar to other chromospheric fine structures, in terms of optical depth, source function, and Doppler width, but it resembled a large-scale filament on its course to eruption. High spectral resolution observations of the chromosphere can provide a wealth of information regarding the dynamics and properties of minifilaments and their interactions with the surrounding atmosphere.

High-resolution spectroscopy of a surge in an emerging flux region

M. Verma, C. Denker, A. Diercke, C. Kuckein, H. Balthasar, E. Dineva, I. Kontogiannis, P. S. Pal, M. Sobotka, 2020, Astronomy & Astrophysics, 639, A19

Aims: The regular pattern of quiet-Sun magnetic fields was disturbed by newly emerging magnetic flux, which led a day later to two homologous surges after renewed flux emergence, affecting all atmospheric layers. Hence, simultaneous observations in different atmospheric heights are needed to understand the interaction of rising flux tubes with the surrounding plasma, in particular by exploiting the important diagnostic capabilities provided by the strong chromospheric Hα line regarding morphology and energetic processes in active regions.
Methods: A newly emerged active region NOAA 12722 was observed with the Vacuum Tower Telescope (VTT) at Observatorio del Teide, Tenerife, Spain, on 11 September 2018. High spectral resolution observations using the echelle spectrograph in the chromospheric Hα λ 6562.8 Å line were obtained in the early growth phase. Noise-stripped Hα line profiles yield maps of line-core and bisector velocities, which were contrasted with velocities inferred from Cloud Model inversions. A high-resolution imaging system recorded simultaneously broad- and narrowband Hα context images. The Solar Dynamics Observatory provided additional continuum images, line-of-sight (LOS) magnetograms, and UV and extreme UV (EUV) images, which link the different solar atmospheric layers.
Results: The active region started as a bipolar region with continuous flux emergence when a new flux system emerged in the leading part during the VTT observations, resulting in two homologous surges. While flux cancellation at the base of the surges provided the energy for ejecting the cool plasma, strong proper motions of the leading pores changed the magnetic field topology making the region susceptible to surging. Despite the surge activity in the leading part, an arch filament system in the trailing part of the old flux remained stable. Thus, stable and violently expelled mass-loaded ascending magnetic structures can coexist in close proximity. Investigating the height dependence of LOS velocities revealed the existence of neighboring strong up- and downflows. However, downflows occur with a time lag. The opacity of the ejected cool plasma decreases with distance from the base of the surge, while the speed of the ejecta increases. The location at which the surge becomes invisible in Hα corresponds to the interface where the surge brightens in He IIλ304 Å. Broad-shouldered and duallobed Hα profiles suggests

accelerated or decelerated and highly structured LOS plasma flows. Significantly broadened Hα profiles imply significant heating at the base of the surges, which is also supported by bright kernels in UV and EUV images uncovered by swaying motions of dark fibrils at the base of the surges.
Conclusions: The interaction of newly emerging flux with pre-existing flux concentrations of a young, diffuse active region provided suitable conditions for two homologous surges. High-resolution spectroscopy revealed broadened and dual-lobed Hα profiles tracing accelerated or decelerated flows of cool plasma along the multi-threaded structure of the surge.

Magnetic Flux Emergence in a Coronal Hole

J. Palacios, D. Utz, S. Hofmeister, K. Krikova, P. Gömöry, C. Kuckein, C. Denker, M. Verma, S. J. González Manrique, J. I. Campos Rozo, J. Koza, M. Temmer, A. Veronig, A. Diercke, I. Kontogiannis, C. Cid, 2020, Solar Physics 295, 64

A joint campaign of various space-borne and ground-based observatories, comprising the Japanese Hinode mission (Hinode Observing Plan 338, 20 - 30 September 2017), the GREGOR solar telescope, and the Vacuum Tower Telescope (VTT), investigated numerous targets such as pores, sunspots, and coronal holes. In this study, we focus on the coronal hole region target. On 24 September 2017, a very extended non-polar coronal hole developed patches of flux emergence, which contributed to the decrease of the overall area of the coronal hole. These flux emergence patches erode the coronal hole and transform the area into a more quiet-Sun-like area, whereby bipolar magnetic structures play an important role. Conversely, flux cancellation leads to the reduction of opposite-polarity magnetic fields and to an increase in the area of the coronal hole.

Tracking Downflows from the Chromosphere to the Photosphere in a Solar Arch Filament System

S. J. González Manrique, C. Kuckein, A. Pastor Yabar, A. Diercke, M. Collados, P. Gömöry, S. Zhong, Y. Hou, C. Denker, 2020, Astrophysical Journal 890, 82

We study the dynamics of plasma along the legs of an arch filament system (AFS) from the chromosphere to the photosphere, observed with high-cadence spectroscopic data from two ground-based solar telescopes: the GREGOR telescope (Tenerife) using the GREGOR Infrared Spectrograph in the He I 10830 Å range and the Swedish Solar Telescope (La Palma) using the CRisp Imaging Spectro-Polarimeter to observe the Ca II 8542 Å and Fe I 6173 Å spectral lines. The temporal evolution of the draining of the plasma was followed along the legs of a single arch filament from the chromosphere to the photosphere. The average Doppler velocities inferred at the upper chromosphere from the He I 10830 Å triplet reach velocities up to 20–24 km s^{-1}, and in the lower chromosphere and upper photosphere the Doppler velocities reach up to 11 km s^{-1} and 1.5 km s^{-1} in the case of the Ca II 8542 Å and Si I 10827 Å spectral lines, respectively. The evolution of the Doppler velocities at different layers of the solar atmosphere (chromosphere and upper photosphere) shows that they follow the same line-of-sight (LOS) velocity pattern, which confirms the observational evidence that the plasma drains toward the photosphere as proposed in models of AFSs. The Doppler velocity maps inferred from the lower photospheric Ca I 10839 Å or Fe I 6173 Å spectral lines do not show the same LOS velocity pattern. Thus, there is no evidence that the plasma reaches the lower photosphere. The observations and the nonlinear force-free field (NLFFF) extrapolations demonstrate that the magnetic field loops of the AFS rise with time. We found flow asymmetries at different footpoints of the AFS. The NLFFF values of the magnetic field strength help us to explain these flow asymmetries.

Temporal Evolution of Arch Filaments as seen in He I 10 830 Å

S. J. González Manrique, C. Kuckein, M. Collados, C. Denker, S. K. Solanki, P. Gömöry, M. Verma, H. Balthasar, A. Lagg, A. Diercke, 2019, Astronomy & Astrophysics 617, A55

Aims: We study the evolution of an arch filament system (AFS) and of its individual arch filaments to learn about the processes occurring in them.
Methods: We observed the AFS at the GREGOR solar telescope on Tenerife at high cadence with the

very fast spectroscopic mode of the GREGOR Infrared Spectrograph (GRIS) in the He I 10 830 Å spectral range. The He I triplet profiles were fitted with analytic functions to infer line-of-sight (LOS) velocities to follow plasma motions within the AFS.
Results: We tracked the temporal evolution of an individual arch filament over its entire lifetime, as seen in the He I 10 830 Å triplet. The arch filament expanded in height and extended in length from 13″to 21″. The lifetime of this arch filament is about 30 min. About 11 min after the arch filament is seen in He I, the loop top starts to rise with an average Doppler velocity of 6 km s^{-1}. Only two minutes later, plasma drains down with supersonic velocities towards the footpoints reaching a peak velocity of up to 40 km s^{-1} in the chromosphere. The temporal evolution of He I 10 830 Å profiles near the leading pore showed almost ubiquitous dual red components of the He I triplet, indicating strong downflows, along with material nearly at rest within the same resolution element during the whole observing time.
Conclusions: We followed the arch filament as it carried plasma during its rise from the photosphere to the corona. The material then drained toward the photosphere, reaching supersonic velocities, along the legs of the arch filament. Our observational results support theoretical AFS models and aids in improving future models.

Dynamics and connectivity of an extended arch filament system

A. Diercke, C. Kuckein, C. Denker, 2019, Astronomy & Astrophysics 629, A48

Aims: In this study, we analyzed a filament system, which expanded between moving magnetic features (MMFs) of a decaying sunspot and opposite flux outside of the active region from the nearby quiet-Sun network. This configuration deviated from a classical arch filament system (AFS), which typically connects two pores in an emerging flux region. Thus, we called this system an extended AFS. We contrasted classical and extended AFSs with an emphasis on the complex magnetic structure of the latter. Furthermore, we examined the physical properties of the extended AFS and described its dynamics and connectivity.
Methods: The extended AFS was observed with two instruments at the Dunn Solar Telescope (DST). The Rapid Oscillations in the Solar Atmosphere (ROSA) imager provided images in three different wavelength regions, which covered the dynamics of the extended AFS at different atmospheric heights. The Interferometric Bidimensional Spectropolarimeter (IBIS) provided spectroscopic Hα data and spectropolarimetric data that was obtained in the near-infrared (NIR) Ca II λ8542 Å line. We derived the corresponding line-of-sight (LOS) velocities and used He II λ304 Å extreme ultraviolet (EUV) images of the Atmospheric Imaging Assembly (AIA) and LOS magnetograms of the Helioseismic and Magnetic Imager (HMI) on board the Solar Dynamics Observatory (SDO) as context data.
Results: The NIR Ca II Stokes-V maps are not suitable to definitively define a clear polarity inversion line and to classify this chromospheric structure. Nevertheless, this unusual AFS connects the MMFs of a decaying sunspot with the network field. At the southern footpoint, we measured that the flux decreases over time. We find strong downflow velocities at the footpoints of the extended AFS, which increase in a time period of 30 min. The velocities are asymmetric at both footpoints with higher velocities at the southern footpoint. An EUV brigthening appears in one of the arch filaments, which migrates from the northern footpoint toward the southern one. This activation likely influences the increasing redshift at the southern footpoint.
Conclusions: The extended AFS exhibits a similar morphology as classical AFSs, for example, threaded filaments of comparable length and width. Major differences concern the connection from MMFs around the sunspot with the flux of the neighboring quiet-Sun network, converging footpoint motions, and longer lifetimes of individual arch filaments of about one hour, while the extended AFS is still very dynamic.

High-resolution Imaging and Near-infrared Spectroscopy of Penumbral Decay

M. Verma, C. Denker, H. Balthasar, C. Kuckein, R. Rezaei, M. Sobotka, N. Deng, H. Wang, A. Tritschler, M. Collados, A. Diercke, S. J. González Manrique, 2018, Astronomy & Astrophysics 614, A2

Aims: Combining high-resolution spectropolarimetric and imaging data is key to understanding the decay process of sunspots as it allows us to scrutinize the velocity and magnetic fields of sunspots and their

surroundings.
Methods: Active region NOAA 12597 was observed on 2016 September 24 with the 1.5-meter GREGOR solar telescope using high-spatial-resolution imaging as well as imaging spectroscopy and near-infrared (NIR) spectropolarimetry. Horizontal proper motions were estimated with local correlation tracking, whereas line-of-sight (LOS) velocities were computed with spectral line fitting methods. The magnetic field properties were inferred with the "Stokes Inversions based on Response functions" (SIR) code for the Si I and Ca I NIR lines.
Results: At the time of the GREGOR observations, the leading sunspot had two light bridges indicating the onset of its decay. One of the light bridges disappeared, and an elongated, dark umbral core at its edge appeared in a decaying penumbral sector facing the newly emerging flux. The flow and magnetic field properties of this penumbral sector exhibited weak Evershed flow, moat flow, and horizontal magnetic field. The penumbral gap adjacent to the elongated umbral core and the penumbra in that penumbral sector displayed LOS velocities similar to granulation. The separating polarities of a new flux system interacted with the leading and central part of the already established active region. As a consequence, the leading spot rotated 55° clockwise over 12 h.
Conclusions: In the high-resolution observations of a decaying sunspot, the penumbral filaments facing the flux emergence site contained a darkened area resembling an umbral core filled with umbral dots. This umbral core had velocity and magnetic field properties similar to the sunspot umbra. This implies that the horizontal magnetic fields in the decaying penumbra became vertical as observed in flare-induced rapid penumbral decay, but on a very different time-scale.

High-cadence Imaging and Imaging Spectroscopy at the GREGOR Solar Telescope — A Collaborative Research Environment for High-resolution Solar Physics

C. Denker, C. Kuckein, M. Verma, S. J. González Manrique, A. Diercke, H. Enke, J. Klar, H. Balthasar, R. E. Louis, E. Dineva, 2018, Astrophysical Journal Supplementary 236, 5

In high-resolution solar physics, the volume and complexity of photometric, spectroscopic, and polarimetric ground-based data significantly increased in the last decade, reaching data acquisition rates of terabytes per hour. This is driven by the desire to capture fast processes on the Sun and the necessity for short exposure times "freezing" the atmospheric seeing, thus enabling ex post facto image restoration. Consequently, large-format and high-cadence detectors are nowadays used in solar observations to facilitate image restoration. Based on our experience during the "early science" phase with the 1.5 m GREGOR solar telescope (2014-2015) and the subsequent transition to routine observations in 2016, we describe data collection and data management tailored toward image restoration and imaging spectroscopy. We outline our approaches regarding data processing, analysis, and archiving for two of GREGOR's post-focus instruments (see http://gregor.aip.de), i.e., the GREGOR Fabry-Pérot Interferometer (GFPI) and the newly installed High-Resolution Fast Imager (HiFI). The heterogeneous and complex nature of multidimensional data arising from high-resolution solar observations provides an intriguing but also a challenging example for "big data" in astronomy. The big data challenge has two aspects: (1) establishing a workflow for publishing the data for the whole community and beyond and (2) creating a collaborative research environment (CRE), where computationally intense data and postprocessing tools are colocated and collaborative work is enabled for scientists of multiple institutes. This requires either collaboration with a data center or frameworks and databases capable of dealing with huge datasets based on virtual observatory (VO) and other community standards and procedures.

Image Quality in High-resolution and High-cadence Solar Imaging

C. Denker, E. Dineva, H. Balthasar, M. Verma, C. Kuckein, A. Diercke, S. J. González Manrique, 2018, Solar Physics 293, 44

Broad-band imaging and even imaging with a moderate bandpass (about 1 nm) provides a photon-rich environment, where frame selection (lucky imaging) becomes a helpful tool in image restoration, allowing us to perform a cost-benefit analysis on how to design observing sequences for imaging with high spatial resolution in combination with real-time correction provided by an adaptive optics (AO) system. This

study presents high-cadence (160 Hz) G-band and blue continuum image sequences obtained with the High-resolution Fast Imager (HiFI) at the 1.5-meter GREGOR solar telescope, where the speckle-masking technique is used to restore images with nearly diffraction-limited resolution. The HiFI employs two synchronized large-format and high-cadence sCMOS detectors. The median filter gradient similarity (MFGS) image-quality metric is applied, among others, to AO-corrected image sequences of a pore and a small sunspot observed on 2017 June 4 and 5. A small region of interest, which was selected for fast-imaging performance, covered these contrast-rich features and their neighborhood, which were part of Active Region NOAA 12661. Modifications of the MFGS algorithm uncover the field- and structure-dependency of this image-quality metric. However, MFGS still remains a good choice for determining image quality without a priori knowledge, which is an important characteristic when classifying the huge number of high-resolution images contained in data archives. In addition, this investigation demonstrates that a fast cadence and millisecond exposure times are still insufficient to reach the coherence time of daytime seeing. Nonetheless, the analysis shows that data acquisition rates exceeding 50 Hz are required to capture a substantial fraction of the best seeing moments, significantly boosting the performance of post-facto image restoration.

Counter-streaming Flows in a Giant Quiet-Sun Filament Observed in the Extreme Ultraviolet

A. Diercke, C. Kuckein, M. Verma, C. Denker, 2018, Astronomy & Astrophysics 611, A64

Aim: The giant solar filament was visible on the solar surface from 2011 November 8–23. Multiwavelength data from the Solar Dynamics Observatory (SDO) were used to examine counter-streaming flows within the spine of the filament.
Methods: We use data from two SDO instruments, the Atmospheric Imaging Assembly (AIA) and the Helioseismic and Magnetic Imager (HMI), covering the whole filament, which stretched over more than half a solar diameter. Hα images from the Kanzelhöhe Solar Observatory (KSO) provide context information of where the spine of the filament is defined and the barbs are located. We apply local correlation tracking (LCT) to a two-hour time series on 2011 November 16 of the AIA images to derive horizontal flow velocities of the filament. To enhance the contrast of the AIA images, noise adaptive fuzzy equalization (NAFE) is employed, which allows us to identify and quantify counter-streaming flows in the filament. We observe the same cool filament plasma in absorption in both Hα and EUV images. Hence, the counter-streaming flows are directly related to this filament material in the spine. In addition, we use directional flow maps to highlight the counter-streaming flows.
Results: We detect counter-streaming flows in the filament, which are visible in the time-lapse movies in all four examined AIA wavelength bands (λ171 Å, λ193 Å, λ304 Å, and λ211 Å. In the time-lapse movies we see that these persistent flows lasted for at least two hours, although they became less prominent towards the end of the time series. Furthermore, by applying LCT to the images we clearly determine counter-streaming flows in time series of λ171 Å and λ193 Å images. In the λ304 Å wavelength band, we only see minor indications for counter-streaming flows with LCT, while in the λ211 Å wavelength band the counter-streaming flows are not detectable with this method. The diverse morphology of the filament in Hα and EUV images is caused by different absorption processes, i.e., spectral line absorption and absorption by hydrogen and helium continua, respectively. The horizontal flows reach mean flow speeds of about 0.5 km s^{-1} for all wavelength bands. The highest horizontal flow speeds are identified in the λ171 Å band with flow speeds of up to 2.5 km s^{-1}. The results are averaged over a time series of 90 minutes. Because the LCT sampling window has finite width, a spatial degradation cannot be avoided leading to lower estimates of the flow velocities as compared to feature tracking or Doppler measurements. The counter-streaming flows cover about 15-20% of the whole area of the EUV filament channel and are located in the central part of the spine.
Conclusions: Compared to the ground-based observations, the absence of seeing effects in AIA observations reveal counter-streaming flows in the filament even with a moderate image scale of 0.″6 pixel^{-1}. Using a contrast enhancement technique, these flows can be detected and quantified with LCT in different wavelengths. We confirm the omnipresence of counter-streaming flows also in giant quiet-Sun filaments.

Ca II 8542 Å Brightenings Induced by a Solar Microflare

C. Kuckein, A. Diercke, S. J. González Manrique, M. Verma, J. Löhner-Böttcher, H. Socas-Navarro, H. Balthasar, M. Sobotka, C. Denker, 2017, Astronomy & Astrophysics 608, A117

Aims: We study small-scale brightenings in Ca II 8542 Å line-core images to determine their nature and effect on localized heating and mass transfer in active regions.
Methods: High-resolution two-dimensional spectroscopic observations of a solar active region in the near- infrared Ca II 8542 Å line were acquired with the GREGOR Fabry-Pérot Interferometer attached to the 1.5-m GREGOR telescope. Inversions of the spectra were carried out using the NICOLE code to infer temperatures and line-of-sight (LOS) velocities. Response functions of the Ca II line were computed for temperature and LOS velocity variations. Filtergrams of the Atmospheric Imaging Assembly (AIA) and magnetograms of the Helioseismic and Magnetic Imager (HMI) were coaligned to match the ground-based observations and to follow the Ca II brightenings along all available layers of the atmosphere.
Results: We identified three brightenings of sizes up to $2'' \times 2''$that appeared in the Ca II 8542 Å line-core images. Their lifetimes were at least 1.5 min. We found evidence that the brightenings belonged to the footpoints of a microflare (MF). The properties of the observed brightenings disqualified the scenarios of Ellerman bombs or Interface Region Imaging Spectrograph (IRIS) bombs. However, this MF shared some common properties with flaring active-region fibrils or flaring arch filaments (FAFs): (1) FAFs and MFs are both apparent in chromospheric and coronal layers according to the AIA channels; and (2) both show flaring arches with lifetimes of about 3.0–3.5 min and lengths of $20''$next to the brightenings. The inversions revealed heating by 600 K at the footpoint location in the ambient chromosphere during the impulsive phase. Connecting the footpoints, a dark filamentary structure appeared in the Ca II line-core images. Before the start of the MF, the spectra of this structure already indicated average blueshifts, meaning upward motions of the plasma along the LOS. During the impulsive phase, these velocities increased up to $-2.2\,\mathrm{km\,s^{-1}}$. The structure did not disappear during the observations. Downflows dominated at the footpoints. However, in the upper photosphere, slight upflows occurred during the impulsive phase. Hence, bidirectional flows are present in the footpoints of the MF.
Conclusions: We detected Ca II brightenings that coincided with the footpoint location of an MF. The MF event led to a rise of plasma in the upper photosphere, both before and during the impulsive phase. Excess mass, previously raised to at most chromospheric layers, slowly drained downward along arches toward the footpoints of the MF.

Wings of the Butterfly: Sunspot Groups for 1826 – 2015

R. Leussu, I. G. Usoskin, V. Senthamizh Pavai **A. Diercke**, R. Arlt, C. Denker, and K. Mursula, 2017, Astronomy & Astrophysics, 599, A131

The spatio-temporal evolution of sunspot activity, the so-called Maunder butterfly diagram, has been continously available since 1874 using data from the Royal Greenwich Observatory, extended by SOON network data after 1976. Here we present a new extended butterfly diagram of sunspot group occurrence since 1826, using the recently digitized data from Schwabe (1826-1867) and Spörer (1866–1880). The wings of the diagram are separated using a recently developed method based on an analysis of long gaps in sunspot group occurrence in different latitude bands. We define characteristic latitudes, corresponding to the start, end, and the largest extent of the wings (the F, L, and H latitudes). The H latitudes (30°–45°) are highly significantly correlated with the strength of the wings (quantified by the total sum of the monthly numbers of sunspot groups). The F latitudes (20°–30°) depict a weak tendency, especially in the southern hemisphere, to follow the wing strength. The L latitudes (2°–10°) show no clear relation to the wing strength. Overall, stronger cycle wings tend to start at higher latitudes and have a greater wing extent. A strong (5–6)-cycle periodic oscillation is found in the start and end times of the wings and in the overlap and gaps between successive wings of one hemisphere. While the average wing overlap is zero in the southern hemisphere, it is two to three months in the north. A marginally significant oscillation of about ten solar cycles is found in the asymmetry of the L latitudes. The new long database of butterfly wings provides new observational constraints to solar dynamo models that discuss the spatio-temporal distribution of sunspot occurrence over the solar cycle and longer.

Conference Proceedings

Revisiting the building blocks of solar magnetic fields by GREGOR

D. Utz, C. Kuckein, J. I. Campos Rozo, S. J. González Manrique, H. Balthasar, P. Gömöry, J. Hernández Palacios, C. Denker, M. Verma, I. Kontogianni, K. Krikova, S. Hofmeister, A. Diercke, 2019, in *Solar and Stellar Magnetic Fields: Origins and Manifestations*, Kosovichev, Strassmeier, & Jardine (eds), Proc. IAU Symposium No. 354

The Sun is our dynamic host star due to its magnetic fields causing plentiful of activity in its atmosphere. From high energetic flares and coronal mass ejections (CMEs) to lower energetic phenomena such as jets and fibrils. Thus, it is of crucial importance to learn about formation and evolution of solar magnetic fields. These fields cover a wide range of spatial and temporal scales, starting on the larger end with active regions harbouring complex sunspots, via isolated pores, down to the smallest yet resolved elements - so-called magnetic bright points (MBPs). Here, we revisit the various manifestations of solar magnetic fields by the largest European solar telescope in operation, the 1.5-meter GREGOR telescope. We show images from the High-resolution Fast Imager (HiFI) and spectropolarimetric data from the GREGOR Infrared Spectrograph (GRIS). Besides, we outline resolved convective features inside the larger structures - so-called light-bridges occurring on large to mid-sized scales.

Synoptic maps in three wavelengths of the Chromospheric Telescope

A. Diercke, C. Denker, 2018, in *Astronomy in Focus*, A. Shapiro and G. Kopp (eds.), Proc. of XXXth IAU General Assembly, Vienna AUstria, Proc. IAU, 339

The Chromospheric Telescope (ChroTel) observes the entire solar disk since 2011 in three different chromospheric wavelengths: Hα, Ca II K, and He I. The instrument records full-disk images of the Sun every three minutes in these different spectral ranges. The ChroTel observations cover the rising and decaying phase of solar cycle 24. We started analyzing the ChroTel time-series and created synoptic maps of the entire observational period in all three wavelength bands. The maps will be used to analyze the poleward migration of quiet-Sun filaments in solar cycle 24.

Photospheric Magnetic Fields of the Trailing Sunspots in Active Region NOAA 12396

M. Verma, H. Balthasar, C. Denker, F. Böhm, C. E. Fischer, C. Kuckein, S. J. González Manrique, M. Sobotka, N. Bello González, A. Diercke, T. Berkefeld, M. Collados, A. Feller, A. Hofmann, A. Lagg, H. Nicklas, D. Orozco Suárez, A. Pastor Yabar, R. Rezaei, R. Schlichenmaier, D. Schmidt, W. Schmidt, M. Sigwarth, S. K. Solanki, D. Soltau, J. Staude, K. G. Strassmeier, R. Volkmer, O. von der Lühe, T. Waldmann, 2018, in Solar Polarization Workshop 8, L. Belluzzi (eds.),

The solar magnetic field is responsible for all aspects of solar activity. Sunspots are the main manifestation of the ensuing solar activity. Combining high-resolution and synoptic observations has the ambition to provide a comprehensive description of the sunspot growth and decay processes. Active region NOAA 12396 emerged on 2015 August 3 and was observed three days later with the 1.5-meter GREGOR solar telescope on 2015 August 6. High-resolution spectropolarimetric data from the GREGOR Infrared Spectrograph (GRIS) are obtained in the photospheric Si I λ 1082.7 nm and Ca I λ1083.9 nm lines, together with the chromospheric He I λ1083.0 nm triplet. These near-infrared spectropolarimetric observations were complemented by synoptic line-of-sight magnetograms and continuum images of the Helioseismic and Magnetic Imager (HMI) and EUV images of the Atmospheric Imaging Assembly (AIA) on board the Solar Dynamics Observatory (SDO).

Flows along arch filaments observed in the GRIS 'very fast spectroscopic mode'

S. J. González Manrique, C. Denker, C. Kuckein, A. Pastor, M. Collados, M. Verma, H. Balthasar, A. Diercke, C. E. Fischer, P. Gömöry, N. Bello González, R. Schlichenmaier, M. Cubas Armas, T. Berkefeld, A> Feller, S. Hoch, A. Hofmann, A.Lagg, H. Nicklas, D. Orozco Suárez, D. Schmidt, W. Schmidt, M. Sigwarth, M. Sobotka, S. K. Solanki, D. Soltau, J. Staude, K. G. Strassmeier, R. Volkmer, O. von der Lühe, T. Waldmann, 2017, in *Fine Structure and Dynamics of the Solar Atmosphere*, S. Vargas Domínguez, A. G. Kosovichev, L. Harra, and P. Antolin (eds.), Proc. IAU Symp., 327, 28

A new generation of solar instruments provides improved spectral, spatial, and temporal resolution, thus facilitating a better understanding of dynamic processes on the Sun. High-resolution observations often reveal multiple-component spectral line profiles, e.g., in the near-infrared He I 10830 Å triplet, which provides information about the chromospheric velocity and magnetic fine structure. We observed an emerging flux region, including two small pores and an arch filament system, on 2015 April 17 with the 'very fast spectroscopic mode' of the GREGOR Infrared Spectrograph (GRIS) situated at the 1.5-meter GREGOR solar telescope at Observatorio del Teide, Tenerife, Spain. We discuss this method of obtaining fast (one per minute) spectral scans of the solar surface and its potential to follow dynamic processes on the Sun. We demonstrate the performance of the 'very fast spectroscopic mode' by tracking chromospheric high-velocity features in the arch filament system.

sTools – a Data Reduciton Pipeline for the GREGOR Fabry-Pérot Interferometer (GFPI) and the High-resolution Fast Imager (HiFI) at the GREGOR solar telescope

C. Kuckein, C. Denker, M. Verma, S. J. González Manrique, R. E. Louis, and A. Diercke, 2017, in *Fine Structure and Dynamics of the Solar Atmosphere*, S. Vargas Domínguez, A. G. Kosovichev, L. Harra, and P. Antolin (eds.), Proc. IAU Symp., 327, 20

A huge amount of data has been acquired with the GREGOR Fabry-Pérot Interferometer (GFPI), large-format facility cameras, and since 2016 with the High-resolution Fast Imager (HiFI). These data are processed in standardized procedures with the aim of providing science-ready data for the solar physics community. For this purpose, we have developed a user-friendly data reduction pipeline called "sTools" based on the Interactive Data Language (IDL) and licensed under creative commons license. The pipeline delivers reduced and image-reconstructed data with a minimum of user interaction. Furthermore, quick-look data are generated as well as a webpage with an overview of the observations and their statistics. All the processed data are stored online at the GREGOR GFPI and HiFI data archive of the Leibniz Institute for Astrophysics Potsdam (AIP). The principles of the pipeline are presented together with selected high-resolution spectral scans and images processed with sTools.

Appendix B – List of Acronyms

AIA	Atmospheric Imaging Assembly
AIP	Leibniz-Institut für Astrophysik Potsdam
AO	Adaptive Optic
AP	Average Precision
AU	Astronomical Unit
BBSO	Big Bear Solar Observatory
BCE	Binary Crossentropy
CCD	Charge-Coupled Device
ChIP	Chromospheric Helium Imaging Photometer
ChroTel	Chromospheric Telescope
CME	Coronal Mass Ejection
CMOS	Complementary Metal-Oxid-Semiconductor
CNN	Convolutional Neural Network
COG	Center-of-Gravity
DKIST	Daniel K. Inouye Solar Telescope
EST	European Solar Telescope
EUV	Extrem Ultra-Violet
FCN	Fully Concolutional Network
FDP	Full-Disk Patrol
FITS	Flexible Image Transport System
FOV	Field-of-View
FPS	Frames per Second
FTS	Fourier Transform Spectroscopy
FWHM	Full Width at Half Maximum
GFPI	GREGOR Fabry-Pérot Interferometer
GHN	Global Hα Network
GIoU	Generalized Intersection over Union
GONG	Global Oscillation Network Group
GPS	Global Positioning System
GRIS	GREGOR Infrared Spectrograph
HAO	High Altitude Observatory
HEK	Heliophysics Events Knowledgebase
HELLRIDE	HELioseismological Large Regions Interferometric DEvice
HiFI	High-resolution Fast Imager
HMI	Helioseismic and Magnetic Imager
IAA	Indian Institute of Astrophysics
IDL	Interactive Data Language
IoU	Intersection over Union
ISS	Integrated Sunlight Spectrometer

JPEG Joint Photospheric Experts Group

K Kelvin
KAOS Kiepenheuer Adaptive Optics System
KHI Kelvin-Helmholtz Instability
KIS Leibniz-Institut für Sonnenphysik
KO Kodaikanal Observatory
KSO Kanzelhöhe Solar Observatory

LARS Laser-based Absolute Reference Spectrograph
LASCO Large Angle Spectroscopic Coronagraph
LCVR Liquid Crystal Variable Retarders
LOS Line-of-Sight
LTE Local Thermodynamic Equilibrium
LWS Living with a Star

mAP mean Average Precision
MDI Michalson Doppler Imager
MFGS Median Filter-Gradient Similarity
MHD Magnetohydrodynamics
MHz Mega Hertz
MK Million Kelvin
MLSO Mauna Loa Solar Observatory
Mm Megameter
MOMFBD Multi-Object Multi-Frame Blind Deconvolution
MPS Max-Planck Institut für Sonnensystemforschung

NASA National Aeronautics and Space Administration
NFI Narrowband Filter Imager
NIR Near-Infrared
NMS Non-Maximum Suppression
NLTE Non-LTE
NOAA National Ocianic and Atmospheric Administration
NSO National Solar Observatory

PCF Polar Crown Filament
PEPSI Potsdam Echelle Polarimetric and Spectroscopic Instrument
PI Principle Investigator
PIL Polarity-Inversion-Line
PSPT Precision Solar Photometric Telescope
PTU Programmable Timing Unit

R-CNN Region-based Convolutional Neural Network
RHESSI Reuven Ramaty High-Energy Solar Spectroscopic Imager
ROI Region-of-Interest
RTE Radiative Transfer Equation
RTI Rayleigh-Taylor instabilities

SCIP Sunrise Chromospheric Infrared Polarimeter
SDI Solar Disk-Integrated Telescope
SDO Solar Dynamics Observatory
SGD Stochastic Gradient Descent
SIDC Solar Influence Data Analysis Center
SOLIS Synoptic Optical Long-term Inverstigation of the Sun
SOT Solar Optical Telescope
SSD Single-Shot Detector
SSW SolarSoft
STIX Spectrometer/Telescope for Imaging X-Rays
SVD Singular Value Decomposition
SVM Support Vector Machine

TIP II Tenerife Infrared Polarimeter II
TSI Total Solar Irradiance

USA United States of America
USET Uccle Solar Equatorial Telescope
UT Universal Time
UV Ultra-Violet

VSO Virtual Solar Observatory
VTT Vacuum Tower Telescope

WWW World Wide Web

XRT X-Ray Telescope

YNAO Yunnan Astronomical Observatory
YOLO You Only Look Once